8-29-2017 12:00 AM

Estimation of Turbulence Effects on Wind-Induced Suctions on the Roof of a Low-Rise Building

Chieh-Hsun Wu
The University of Western Ontario

Supervisor
Gregory A. Kopp
The University of Western Ontario

Graduate Program in Civil and Environmental Engineering
A thesis submitted in partial fulfillment of the requirements for the degree in Doctor of Philosophy

Abstract

The effects of turbulence in the atmospheric boundary layer (ABL) on surface pressures of a typical low-rise building roof are investigated in this thesis. A 1/50 geometrically-scaled model of the Texas Tech University Wind Engineering Field Research Lab (WERFL) building model is used for pressure measurements in wind tunnel experiments. ABL wind turbulence intensities ranging from about 10% to 30%, and length scales ranging from 6 to 12 times of the building height (*H*) are generated.

The effects of ABL turbulence on the mean roof pressures within the separated flow are explained from the time-averaged Navier-Stokes equations. The pressure fields are reconstructed by integrating the pressure gradients using an analytic interpolation approach. For high turbulence intensity levels, the maximum suction coefficient on the roof surface was found to be increased. Such increasing magnitudes are directly related to reduced sizes of mean separation bubbles, more rapid variation of the velocity magnitude near the leading edge and enhanced variation of the turbulence stresses. On the other hand, higher surface pressure recovery found in the leeward portion of the separation bubble is mainly due to the more rapid variation of the turbulence stresses.

The effects of ABL turbulences on the fluctuating roof surface pressures are explained by the quasi-steady (QS) theory. Basically, the QS model assumes that the instantaneous roof surface pressure is induced by a modified local mean flow field. The selection of the mean flow pattern and the amplification of the velocity magnitudes are determined so that the resulted instantaneous velocity vector is matched to the measurement at the reference location, i.e., 1*H* above the roof leading edge in this thesis. The QS model is found to explain the effects of large length scale turbulences very well. Better QS-predictions are observed if vertical component of the velocities are included. A statistical method for estimating the surface pressure probability distribution, based on the assumptions from the QS model, is derived and validated. This method relates the probability density function (pdf) of building surface pressures to the joint pdf of wind speed, azimuth angle, and elevation angle.

Keywords

Wind loads, Low-rise building aerodynamics, Turbulence, Separated-reattached flow, Mean pressures, Fluctuating pressures, Pressure integration technique, Quasi-steady theory.

Co-Authorship Statement

This thesis summarized the experimental investigations of atmospheric boundary layer turbulence effects on the wind induced suction on a low-rise building roof. The particle image velocimetry (PIV) measurements, along with the planar mean flow and turbulence fields used in this thesis are provided by Dr. Abul Fahad Akon. These PIV measurements provide valuable data for this thesis in order to link the wind field and pressure field near the low-rise building roof from theoretical aspect. The paper entitled 'Effects of turbulence on the mean pressure field in the separated-reattaching flow above a low-rise building', which is co-authored with Abul Fahad Akon and Gregory A. Kopp, is recently submitted to Journal of Wind Engineering and Industrial Aerodynamics for peer review. Part of this thesis include the results of this paper.

Professor Gregory A. Kopp is my advisor in the PhD program. His guidance's and feedbacks on my experimental works, methods of analyses, and eventually the writing of this thesis and other papers have been appreciated. The paper entitled 'Estimation of wind-induced pressures on a low-rise building using quasi-steady theory', which is co-authored by Gregory A. Kopp, is published on the journal of Frontiers in Built Environment. Part of this thesis include the results published in this paper as well.

Acknowledgments

The greatest thank is delivered to my PhD advisor, Professor Gregory A. Kopp, for his supports on many aspects of my PhD studies. His offer of paid position as a student research assistant is very appreciated for my four years of studies and researches. This opportunity allows me to focus on my academic work without worrying about the basic living expense issue. On the academic aspect, he provides valuable guidance's and feedbacks on my research throughout the constant meetings during my PhD program. However, his allowance of my free thinking enables me to explore the research topics via different approaches. Within this culture I have been able to learn more and, in fact, been entranced by the physics embedded in wind engineering. All of his efforts as an advisor greatly influence me and will be appreciated throughout my life.

It has been a great opportunity to have experiences in conducting measurements in the Boundary Layer Wind Tunnel (BLWT) in University of Western Ontario. In addition to its long history in wind engineering and highly automated control system nowadays, the most attractable thing is that the group of expertise is gathered here and willing to help. Mr. Gerry Dafoe, Mr. Anthony Burggraaf and other technicians in the BLWT are sincerely acknowledged for their help on my testing setups. Without their help my measured data may not be accurate and reliable. Dr. Abul Fahad Akon is also acknowledged in sharing his PIV and pressure measurement data for my investigations. About one third of the discussion in this thesis are based on his data. Dr. Sarah Stenabaugh is gratefully appreciated for her help on introducing the Cobra probe instrumentation. In my memory that was my first year in the program and she was in the last year and had been pregnant for few months. Finally I wish to thank my parents, for their constant support for my pursing graduate education.

Table of Contents

List of Tables

List of Figures

List of Nomenclature

A	Area of a roof surface panel.
Cp	Pressure coefficient.
Cp_{avg}	Area averaged pressure coefficient.
Cp_e	Estimated pressure coefficient.
Cp_{inst}	Instantaneous function used in the quasi-steady theory.
f	Frequency.
f_s	Sampling rate.
H	Height of the low-rise building model, $H = 8\,\text{cm}$.
$H(f)$	Frequency response function at frequency f.
I_u	Turbulence intensity of longitudinal velocity component.
L_c	Cut-off length for moving average.
L_{ux}	Integral length scale of longitudinal velocity component.
N_s	Window size for moving average.
$\mathbf{n}$	Outward normal vector on the control volume surface, $\mathbf{n} = n_x\mathbf{i} + n_y\mathbf{j} + n_z\mathbf{k}$
$\mathbf{n_1}$	Outward normal vector on the control volume surface docked at the roof panel.
p	Pressure.
p_∞	Ambient static pressure.
r	Radial distance on the xz-plane, i.e., $r = \sqrt{x^2 + z^2}$.
S	Bounding surfaces of the control volume except S_1.

S_1	Bounding surface of the control volume that is docked with the roof panel.
S_{uu}	Auto-spectra of longitudinal velocity component.
u	Longitudinal velocity component (with direction parallel to x-coordinate).
$\mathbf{u}$	Velocity vector, $\mathbf{u} = u\mathbf{i} + v\mathbf{j} + w\mathbf{k}$.
u_{H}	Upstream longitudinal velocity at roof height.
u_{ref}	Reference velocity.
v	Transverse velocity component with direction parallel to y-coordinate.
w	Vertical velocity component with direction parallel to z-coordinate.
x	x-coordinate of the space.
x_r	Reattachment length of the mean separation bubble.
$\mathbf{x}$	Space vector. $\mathbf{x} = x\mathbf{i} + y\mathbf{j} + z\mathbf{k}$
z	Vertical coordinate of the space.
ν	Kinematic viscosity of air.
α_1	Coefficient associated with x-derivative of the analytic support, Φ .
α_3	Coefficient associated with z-derivative of the analytic support, Φ .
β	Elevation angle of wind velocity vector.
θ	Azimuth angle of wind velocity vector.
Φ	Analytic support.
ρ	Density of air.
σ	Support size of the radial analytic function Φ .
$\boldsymbol{\tau}$	Turbulence stress tensor with component $\tau_{ij} = \overline{u_i' u_j'}$
$\langle a \rangle, \bar{a}$	Estimate or (temporal) mean or of a.
$\langle a \mid b \rangle$	Estimate of mean of a based on the condition of b.

a'	Temporal fluctuation of a, i.e., $a' = a - \overline{a}$.
$\min(a)$	Minimum value of a.
$\mathrm{rms(a)}$	Toot mean square (or standard deviation) of a.
Re[a]	Real part of a.

Chapter 1

1 Introduction

1.1 Background

Understanding the wind effects on structures can help engineers to design for assess the wind-induced risk caused by severe wind storms. In the Enhanced Fujita Scale (WSEC, 2016), for example, the typical types damages that are observed are shown in Figure 1-1 (a) for typical residential houses in severe storms. The Degrees of Damage (DOD) provide the typical sequence of damage observations as a function of wind speed. These types of damages have been commonly observed in post-disaster surveys in both hurricanes (e.g., Hurricane Katrina, van de Lindt et al., 2007) and tornadoes (e.g., Tornado in Tuscaloosa, Alabama, van de Lindt et al., 2013). Among these damages, roofs have been found to be particularly vulnerable to wind-induced uplift. For example, the uplift failures of asphalt shingles (DOD 2, Figure 1-1 (b)), roof sheathing panels (DOD 4, Figure 1-1 (c)) and even the entire roof (DOD 6, Figure 1-1 (d)) have been observed in Angus Tornado (Kopp et al., 2016). Once a portion of the roof has blown off, the subsequent rain-water penetration can immediately accumulate the loss of the house contents (Sparks et al., 1994). Failed sheathing panels can also become flying debris (Kordi et al., 2010) and impact other buildings (Minor, 1994). Hence, the wind-induced roof surface pressures, and the consequent roof failures, have been a focus of attention for low-rise buildings and houses.

a

DOD	Damage description	Wind speed (mph)		
		Expected	Lower	Upper
1	Threshold of visible damage	65	53	80
2	Loss of roof covering material (< 20%), gutters and/or awning; loss of vinyl or metal siding	79	63	97
3	Broken glass in doors and windows	96	79	114
4	Uplift of roof deck and loss of significant roof covering material (>20%); collapse of chimney; garage doors collapse inward; failure of parch or carport	97	81	116
5	Entire house shifts off foundation	121	103	141
6	Large sections of roof structure removed; most walls remain standing	122	104	142

b

c

d

Figure 1-1: (a) Degree of damages (DOD) and the corresponding range of failure wind speeds for typical one- and two-family residences (WSEC, 2006) (b) Examples of DOD 2. (c) Example of DOD 4. (d) Example of DOD 6.

Construction quality can greatly affect the resistance to wind-induced loads. For example, He and Hong (2012) show that the typical toe-nailed, roof-to-wall connection are prone to error, leading to possible reductions of the uplift resistance of the roofs. However, using hurricane clips for the roof-to-wall connections can significantly increase the resistance of the entire roof (e.g., Amini and van de Lindt, 2014). Building shape, on the other hand, can affect the aerodynamics of the roof significantly. Hip roofs are found to receive less wind uplift than that of gable or flat roofs (Gavanski et al., 2013), although adding parapets (e.g., Kopp et al., 2005) or using rounded corners for the roof edges (e.g., Roberston, 1991) may reduce the wind induced suction. In contrast, a large opening on the windward wall can pressurize the internal volume of the building and significantly increase the net uplift for the roof (e.g., Oh et al., 2007). Changing the plan dimensions of the roof (e.g., Ho et al., 2005; Gavanski et al., 2013) or side walls (e.g., Akon and Kopp, 2016) can alter the flow pattern on roof and, hence, affect the wind induced suctions.

The upstream flow and turbulence conditions in the atmospheric boundary layer (ABL) play important roles on the roof surface pressures. In order to quantify the effects of turbulence on wind loading, the vertical profiles of the turbulence characteristics have been varied, along with separate measurements of building surface pressures (e.g., Tieleman, 1993; Tieleman et al., 1994). Although this type of methodology (i.e., non-simultaneous measurement of wind speed and surface pressures) is straightforward for typical engineering practice, the studying of the inherent physical mechanisms is limited. For example, Tieleman (1993) and Tieleman et al. (1994) observed significant dependence of the mean roof surface pressure to the upstream turbulence intensity for all wind directions. However, because the interaction between the upstream turbulence and the local flow field cannot be observed directly with this type of measurement, the detailed physical mechanism causing the variation of the mean pressure variations cannot be directly explained.

One benefit of modern flow field measurement technologies, such as particle image velocimetry (PIV), is that these tools can be used to investigate the detailed flow field near the building surfaces (e.g., Pratt and Kopp, 2014). For example, Akon and Kopp

(2016), examined the mean flow field above the roof of a geometrically-scaled model of the Texas Tech University Wind Engineering Research Field Laboratory building (i.e., TTU WERFL, see Levitan and Mehta, 1992a). For wind directions normal to the building walls, they found that increased upstream turbulence intensity reduces the sizes of the mean separation bubbles, with relatively little influence of the turbulence length scales over the range of their measurements. The distribution of the mean roof surface pressures was found to be strongly related to the dimension of the separation bubbles and, hence, the upstream turbulence intensity. Similar effects of the intensity (e.g., Kiya and Sasaki, 1983b; Saathoff and Melbourne, 1997) and length scales (e.g., Hillier and Cherry, 1981; Nakamura and Ozono, 1987) of the free stream turbulence have also been observed for flow passing 2D rectangular prisms in uniform flow. Although the mean surface pressure distribution is strongly related to the reattachment lengths, Akon and Kopp (2016) did not find a self-similar pressure distribution after applying a normalization based on the reattachment length and extreme value of the mean pressure coefficient. Thus, turbulence fundamentally alters the mean separation bubble in a way that changes in body geometry for a smooth free stream do not (Roshko and Lau, 1965).

The fluctuating component of the roof surface pressures are strongly dependent on the upstream turbulence as well. Increasing upstream turbulence intensity, in general, has been found to increase the fluctuations of the wind-induced suctions on roofs (e.g., Tieleman, 1993; Tieleman et al., 1994; Tieleman, 2003; Akon, 2017). In addition to the intensity, the integral length scale of the upstream turbulence has been found to affect the pressure fluctuations. For the flow passing a 2D rectangular prism, surface pressure measurements show that the pressure fluctuation can be amplified by increasing the length scale of the upstream turbulence without changing the turbulence intensity (e.g., Hiller and Cherry, 1981; Saathoff and Melbourne, 1997). In addition, the largest magnitude fluctuations move closer to the leading edge because of the earlier transition to turbulence of the separated shear layer. Similar trends had been observed on roof surface pressure fluctuation by Akon (2017) for ABL flow normal to the low-rise building wall.

When the upstream flow is laminar (i.e., smooth), a laminar shear layer is formed by the flow separation at the leading edge. Due to small disturbances, the laminar shear layer

rolls up into discrete Kevin-Helmholtz (KH) vortices. These KH vortices can pair, forming larger vortices and further impinging the roof surface or shedding downstream, breaking into random turbulent eddies. The fluctuating pressures under such separated flows are governed by the flow characteristics described above (e.g., Kiya and Sasaki, 1983a). The effects of turbulence on the separated shear layer have been investigated by. Gartshore (1973), who found that the turbulence on the stagnation streamline controlled the primary changes to the separated flow. Lander et al. (2017) found that the separated flow becomes turbulent immediately after separation due to a by-pass transition mechanism. Increased upstream turbulence intensity is reported to increase perturbation of the shear layer and, hence, the growth rate of roll up vortices in the shear layer (Kiya and Saski, 1983b; Saathoff and Melbourne, 1997). Increased length scale of the free stream turbulence, on the other hand, is found to increase the span-wise (normal to the flow direction) coherence of the vortex roll up while decreasing the perturbation from the small scale turbulence (Saathoff and Melbourne, 1997). Hence, the increased surface pressure fluctuations can be, in part, explained by these enhanced vortices generated from the leading edge.

Relatively large length scales of the ABL turbulence are usually encountered for typical low-rise buildings. For example, the integral length scale of the ABL turbulence can be as large as 30 times the building height for the full scale TTU WERFL building (Levitan and Mehta, 1992b), with a turbulence intensity is of about 20%. These large scale turbulent eddies are expected to produce a ‘buffeting’ type of effect (Tieleman, 2003). Hence, on top of its interaction on the building-generated turbulence (i.e., the separating-reattached flow above the roof) discussed earlier, large scale turbulence is expected to produce more overall changes of the load. Turbulent eddies of large length scales also imply significant transverse and vertical velocity fluctuations in the ABL. The fluctuations of roof surface pressures may be influenced by the transverse (e.g., Tieleman et al, 1996) and vertical velocity component as well. For example, the wind azimuth angle changes due to large scale turbulence can sway the axis of the conical vortices (e.g., Banks and Meroney, 2001; Wu et al., 2001), influencing the location of maximum instantaneous suction on roof. Large-scale upward wind can lift the axis of the conical

vortex so that its structure is better developed (i.e., more rounded vortex pattern) and, hence, enhance the suction beneath it (Wu et al., 2001).

Therefore, in wind tunnel modelling of turbulent flow, the best approach is to match both the intensity and length scale of the turbulence, due to the awareness of their effects on roof surface pressures mentioned earlier. However, the dimension of typical wind tunnels can limit its capability in simulating turbulences of very large length scale for structure models that are also large enough to resolve geometric details of interest. For example, the wind tunnel study of cavity pressure between roof and roof top solar panels requires the length scale ratio of at least 1:20 (e.g., Stenabaugh and Kopp, 2015). Consider placing Stenabaugh and Kopp's (2015) model (with full scale roof height being 8 m) and assuming the integral length scale of turbulence being 30 times the building height as that measured in TTU WERFL site (see Levitan and Mehta, 1992b), this would require the model integral length scale of 12 m being simulated in the wind tunnel, which is generally not achievable in typical wind tunnels.

After noticing the inadequacy of wind tunnel simulation of large length scale turbulence, Irwin (2008) argued that this issue may be resolved if the wind loading problems can be separated into the influences due to small and large length scale turbulence. Following the argument of Irwin (2008), Asghari-Mooneghi et al. (2016) proposed to use the 'partial turbulence simulation method' in wind tunnel to study the aerodynamic effect on the low-rise building roofs due to small length scale of turbulence. For the missing portion of large length scale turbulence, they proposed to use Quasi-Steady theory for correcting the effect. Although the Qausi-Steady model are not explicitly used in the approach of Asghari Mooneghi et al. (2016), the concept behind is worth for consideration.

The objective of this research is to estimate or correct the ABL turbulence effects on roof surface pressures, particularly with respect to the large scale of turbulence. In order to reach this goal, detailed understanding of the mechanisms between the near roof turbulent flow and roof surface pressure is required. This is done through a more detailed investigation on relationship between the flow field near the roof and surface pressures

on roof. For flow directions normal to the low-rise building wall, Akon (2017) conducted particle image velocimetry (PIV) measurements to study the flow within a vertical plane parallel to the stream direction near roof, along with the roof surface pressure measurements. Part of his experimental data are used in this thesis to study the effect of turbulence on the mean roof surface pressures. The momentum equations (i.e., the Navier-Stokes equations), which specify the relationship between the wind field and pressure field, offer a promising tool from the theoretical point of view. This thesis shows an example of connecting the mean roof surface pressures to the mean flow and turbulence fields near the roof via the differential momentum equations. Through this process, effects of the upstream turbulence on the mean surface pressure distributions observed in Akon and Kopp (2016) are further explained.

For the pressure fluctuation on roof, however, three-dimensional and temporal flow field measurements of high resolution are usually required (e.g., de Kat and van Oudheusden, 2012), if the instantaneous pressure is to be evaluated theoretically. Such high cost in the flow field measurement, however, are generally not applicable for typical wind engineering applications and, hence, lead to impractical use of direct theoretical approaches. On the other hand, the quasi-steady (QS) theory, which requires less cost in measurement and calculation, offers a convenient tool in relating the wind speed and roof surface pressures. Basically, the QS method estimates the instantaneous building surface pressure analytically using vector information of the wind measured at a point location near the building. Because the analytical function is established via building surface pressure measurements, the QS approach is of a semi-empirical approach. For turbulence with length scales larger than the building dimension, the QS method are expected to be particular useful in relating wind field and building surface pressures (e.g., Tieleman, 2003; Asghari Mooneghi et al., 2016). Hence, in this thesis the effect of the ABL turbulence on the roof surface pressure fluctuation are explained via the QS theory.

1.2 Time-averaged momentum equations

As mentioned in Section 1.1, Akon and Kopp (2016) found that the mean roof surface pressure distribution is strongly related to the intensity but less to the length scale of the upstream ABL turbulence, through their PIV and roof surface pressure measurements.

With the capability of PIV measurements, the goal now is to look into more detailed influences of the ABL turbulence on the pressure field variation near the roof. From the differential momentum equations (i.e., the Navier-Stokes equations), the flow fields can be directly connected to the pressure field so that the influence of turbulence on the pressure field can be examined. By defining the pressure coefficient, Cp, as

$$Cp = \frac{p - p_\infty}{0.5\,\rho u_{\text{ref}}^2}, \tag{1-1}$$

and normalizing the velocity vector, **u**, by the reference velocity, u_{ref}, the gradient of the mean pressure coefficient can be written as:

$$\nabla\overline{Cp} = -2\left[\left(\frac{\overline{\mathbf{u}}}{u_{\text{ref}}}\right)\cdot\nabla\left(\frac{\overline{\mathbf{u}}}{u_{\text{ref}}}\right) + \nabla\cdot\left(\frac{\boldsymbol{\tau}}{u_{\text{ref}}^2}\right) - \frac{\nu}{u_{\text{ref}}}\nabla^2\left(\frac{\overline{\mathbf{u}}}{u_{\text{ref}}}\right)\right]. \tag{1-2}$$

Here p denotes the pressure, p_∞ is the ambient static pressure and ν is the kinematic viscosity. The overbars in Eq. (1-2) denote the time average, while $\boldsymbol{\tau}$ denotes the turbulent stress tensor with components $\tau_{ij} = \overline{u_i' u_j'}$ and the prime denoting a fluctuating component.

This Eulerian approach to pressure gradient evaluation, along with methods of pressure integration have been explored by many researchers as recently reviewed by van Oudheusden (2013). The central difference scheme, which is of second order accuracy and relatively simple in operation, is usually used in determining the velocity gradients on the right hand side of Eq. (1-2) (e.g., Murai et al., 2007; de Kat and van Oudhuesden, 2012). On the side of pressure integration, however, more attention is needed. Space-marching techniques for pressure integration are relatively straightforward and fast (e.g., Baur and Kőngeter, 1999; van Oudheusden et al., 2007). However sometimes the 'memory' effects of integrated results along the integration path can occur (e.g., de Kat et al., 2008), which means the pressure integration can be path dependent with errors from either discretization or measurement (e.g., Sciacchitano and Wieneke, 2016) being accumulated along the integration path (Ettl et al., 2008). Because of these drawbacks

for space-marching schemes, other types of optimization methods for pressure integration may be preferable. The most common approach is to solve the Poisson equation for pressure with standard numerical techniques (e.g., Gurka et al., 1999; de Kat and van Oudheusden, 2012). Note that boundary conditions of mixed type, i.e., a combination of Dirichlet and Neumann, are required for solving Poisson equations (van Oudheusden, 2013). In addition to these techniques, algorithms in CFD have also been used to determine pressure from velocity data. For example, Jaw et al. (2009) calculated the pressure distribution through the SIMPLER algorithm, in which continuity is satisfied and no boundary condition is required. In contrast to these methods, the current work applies the analytic interpolation approach proposed by Ettl et al. (2008). The goal of this method is to keep the local details of integration while providing a globally optimized solution. It has other advantages, such as no requirements for entire boundary conditions and the ability to remove bad gradient data.

The area-averaged pressure is an important quantity in wind engineering applications for determination of cladding loads on, for example, roof panels (e.g., Gavanski et al., 2013). Instead of taking the average of integrated pressure from the differential momentum equation in Eq. (1-2), we use the integral momentum approach with a control volume (CV) docked at the target surface (e.g., a CV attached on top of a specified area on the roof surface). By recalling the definition of pressure coefficient in Eq. (1-1) and neglecting the viscous terms (e.g., Kurtulus et al., 2007), the area-averaged mean pressure coefficient, $\overline{Cp}_{\text{avg}}$, on the target surface, S_1, of area, A, can be represented as:

$$\begin{aligned}\overline{Cp}_{\text{avg}}\,\mathbf{n}_1\,A &\equiv \iint_{S_1}\overline{Cp}\,\mathbf{n}_1\,ds \\ &= -2\iint_{S}\left[\left(\frac{\overline{\mathbf{u}}}{u_{\text{ref}}}\right)\cdot\mathbf{n}\right]\left(\frac{\overline{\mathbf{u}}}{u_{\text{ref}}}\right)ds - 2\iint_{S}\left(\frac{\boldsymbol{\tau}}{u_{\text{ref}}^2}\right)\cdot\mathbf{n}\,ds - \iint_{S}\overline{Cp}\,\mathbf{n}ds\end{aligned}, \tag{1-3}$$

where S denotes the bounding surface of the CV, excluding the target surface S_1; $\mathbf{n}$ and $\mathbf{n}_1$ denote the outward normal vector for CV bounding surfaces S and S_1, respectively. Note that instead of evaluating the total force acting on an object enclosed by the CV, as can be seen in the typical applications (e.g., Kurtulus et al., 2007; van Oudheusden,

2007), the current work applies the integral momentum equation to estimate the area-averaged surface pressures. The applications of time-averaged differential momentum of Eq. (1-2) and integral mention of Eq. (1-3) will be presented in Chapter 3 and Chapter 4, respectively.

1.3 Quasi steady (QS) theory

The quasi-steady theory (QS) has been a common approach in wind engineering for determination of instantaneous wind loads, either on low-rise buildings (e.g., Letchford et al., 1993) or tall buildings (e.g., Kawai, 1983). A summary of recent applications of QS models is shown in Table 1-1. This is a relatively simple approach as compared to the full momentum equations in terms of estimating instantaneous roof surface pressure coefficients, p , from instantaneous velocity vector, $\mathbf{u}_{\mathrm{m}}$, measured at point *m*:

$$p - p_{\infty} = 0.5\,\rho \left|\mathbf{u}_{\mathrm{m}}\right|^2 Cp_{\mathrm{inst}}\,, \tag{1-4a}$$

or alternatively in the form of pressure coefficient, according to Eq. (1-1), that

$$Cp = \frac{\left|\mathbf{u}_{\mathrm{m}}\right|^2}{u_{\mathrm{ref}}^2} Cp_{\mathrm{inst}} \tag{1-4b}$$

Note that the velocity vector used here is composed of the three components in Cartesian coordinate so that the magnitude of **u** satisfies

$$\left|\mathbf{u}\right|^2 = u^2 + v^2 + w^2\,, \tag{1-5a}$$

and the corresponding azimuth, θ, and elevation, β , angles of the wind velocity vector are defined respectively as

$$\theta = \tan^{-1}\left(\frac{v}{u}\right) \quad \text{and} \quad \beta = \tan^{-1}\left(\frac{w}{\sqrt{u^2 + v^2}}\right). \tag{1-5b, c}$$

On the right hand side of Eq. (1-4b), the ratio $|\mathbf{u}_m|^2 / u_{ref}^2$ accounts for the contribution of instantaneous dynamic pressure, whereas Cp_{inst} denotes the 'instantaneous function'. One of the advantages in considering the QS formulation in Eq. (1-4) is that the instantaneous building surface pressure is separated into the contribution from the instantaneous dynamic pressure and the contribution from other aerodynamic effects, such as the body-generated turbulence, embedded in Cp_{inst}.

The variation of Cp_{inst} plays a crucial role in QS theory in estimating surface pressures based on the formulation in Eq. (1-4). Some of the earlier researches applied QS theory (e.g., Kawai, 1983; Letchford et al., 1993) by considering the effects of wind azimuth variations. To model the effects of wind azimuth variations, linear functions for $Cp_{inst}(\theta)$ had been often used for simplicity. In particular, the slope and intercept of the linear function are evaluated from the mean values of pressure coefficients such that

$$Cp_{inst}(\theta) = \overline{Cp}(\bar{\theta}) + \frac{d\,\overline{Cp}}{d\,\theta}(\theta - \bar{\theta}). \tag{1-6}$$

Richards et al. (1995) proposed treating the wind azimuth effects non-linearly by representing $Cp_{inst}(\theta)$ as a Fourier series with experimentally determined coefficients. These authors found that the instantaneous function is generally different than the mean pressure coefficients because of smoothing effects caused by the averaging of the mean wind direction in the mean pressure coefficients. This has the effect of lowering the magnitudes of the peak values (Richards et al., 1995). Banks and Meroney (2001) later compared the conditionally-averaged instantaneous function, $\langle Cp_{inst} \,|\, \theta \rangle$, with a non-linear QS model similar to that proposed by Richards et al. (1995). They found that their non-linear model worked well for point pressures near the roof corner of a low-rise building, except for cases when the mean wind direction is approximately perpendicular to the roof edge.

Cook (1990) mentioned that the most comprehensive way to apply QS theory is to include both wind azimuth and elevation-angle variations in the instantaneous function, $Cp_{\text{inst}}(\theta,\beta)$. The effects of wind elevation angle have been investigated by several researchers (e.g., Letchford and Marwood, 1997; Sharma and Richards, 1999). In these experimental studies, building models were tilted so that the surface pressures were altered by winds at different mean elevation angles. Richards and Hoxey (2004) used a similar approach in their full-scale field study of roof point pressures by tilting the 6-meter-tall Silsoe cube into the wind. Based on these studies, it has been found that an upwardly directed wind angle is generally associated with higher magnitude instantaneous functions for locations on roof surfaces, with rates of change which are approximately linear with angle. Although these works have revealed the relationships between instantaneous pressure coefficients and three-dimensional wind directions, experiments that include both rotating and tilting of buildings are cumbersome and are not routinely implemented in practice.

Part of this thesis applies the QS vector model to include both wind azimuth and elevation angles in order to relate the instantaneous wind vector to instantaneous surface pressures. The effects of wind azimuth variations are treated as non-linear functions and handled in a similar way as suggested by Richards et al. (1995). Wind elevation-angle effects are also considered such that the instantaneous pressure coefficient will be a function of three-dimensional wind directions, i.e., $Cp_{\text{inst}}(\theta,\beta)$. The appropriate estimate of Cp_{inst}, is obtained through conditional averaging, as suggested by Banks and Meroney (2001), i.e.,

$$Cp_{\text{inst}}(\theta,\beta) = \langle Cp_{\text{inst}} \mid \theta,\beta \rangle \tag{1-7}$$

where $\langle \bullet \rangle$ represents the expected value, in this case conditioned on the instantaneous values of both θ and β. Wind elevation-angle effects on Cp_{inst} are obtained through synchronized surface pressure and local three-dimensional wind-velocity vector measurements. Through this type of measurement technique, there are two main

advantages: (i) the method offers a relatively simpler alternative to measuring elevation-angle effects when compared to what is required to tilt building models and (ii) a QS model can be used to predict time series of building surface pressures given an appropriate wind speed time history.

A statistical method based on the QS vector model is also derived. This method relates the joint probability of the three-dimensional wind-velocity components with the probability of surface pressures. There are a few differences between the current formulation of the statistical method used in this thesis and the formulation proposed by Richards and Hoxey (2004). By using a similar analytical form of the instantaneous functions for the QS model, the joint probability of measured wind turbulence is directly used in the current formulation. This may offer an easier alternative when compared to the formulation proposed by Richards and Hoxey (2004) (from Eqs. 19–22 in their paper), where the joint probability between wind speed and wind elevation angle were simulated by superimposing a (negatively correlated) Reynolds stresses portion with the randomly generated portion. Also, mutual independence is not found between wind velocity, azimuth, and elevation angles in our data. So, in the present work, the original form of the joint probability of wind turbulence is retained and is not reduced to individual multiplication. This is different to the formulation used by Richards and Hoxey (2004), where the individual multiplication is used and, therefore, mutual independence is implied.

Although the QS method is not able to account for every aerodynamic effect on the building surface pressures (e.g., the building generated turbulence, Akon, 2017), it is able to explain some portion of point pressure fluctuations (Richards and Hoxey, 2012), and is probably more appropriate for turbulence of large length scale (e.g., Asghari Mooneghi et al., 2016) and for area-averaged pressures (e.g., Letchford et al., 1993). In addition, the QS method would appear to be a useful tool in explaining building surface pressures for severe transient storms. For example, buildings in such storms undergo intense wind that changes rapidly in both magnitude and direction due to the translation of the storm past the building. The wind elevation angle may also be important for tornadoes (e.g., Blanchard, 2013), since this type of storm may produce more upwardly directed winds,

compared to typical atmospheric boundary layer winds. Such rapid changes of wind are coupled with turbulence, resulting in a complex flow field.

As mentioned earlier, the QS theory belongs to a semi-empirical approach because the instantaneous function is usually established on the measurements of the mean pressure coefficients. Although the QS theory has been shown to be an efficient (and sufficient for some cases) method in wind engineering applications, little has been known about its theoretical background. In order to bridge this gap, the inherent physical assumption of the QS approach is presented through simple algebraic manipulations of mean integral momentum equation, Eq. (1-3). Through further comparisons to the instantaneous integral momentum equations, the missing physical mechanism on roof surface pressure estimation are further identified for the QS theory. These physical assumptions are derived in Chapter 4 for a simpler QS model that counts for wind azimuth variation only. Applications and extensions of the QS model including both azimuth and elevation variations are further presented in Chapters 5 and 6.

Table 1-1: Summary of previous applications of quasi-steady models.

Author	Formulation in calculating $p - p_\infty$	Notes of application
QS models considering magnitude of the wind		
Uematsu & Isyumov, 1998	$\frac{1}{2}\rho\left[\left(\bar{u}^2 + 2\bar{u}u'\right)\overline{Cp}\left(\bar{\theta}\right)\right]$	RMS of area-averaged pressures on low-building models.
QS models considering magnitude and azimuth of the wind		
Kawai, 1983	$\frac{1}{2}\rho\left[\left(\bar{u}^2 + 2\bar{u}u'\right)\overline{Cp}\left(\bar{\theta}\right) + \bar{u}v'\frac{\partial\overline{Cp}(\theta')}{\partial\theta}\right]$	Probability and spectra of point pressures on tall building walls.
Letchford et al., 1993	$\frac{1}{2}\rho\left(\bar{u}^2 + 2\bar{u}u'\right)\left[\overline{Cp}\left(\bar{\theta}\right) + \frac{v'}{\bar{u}}\frac{\partial\overline{Cp}(\theta')}{\partial\theta}\right]$	Probability and spectra of point and area average pressures on TTU WERFL roof.
Uematsu & Isyumov, 1999		RMS of pressures of low-buildings.

Richards et al., 1995	$\frac{1}{2}\rho\|\mathbf{u}\|^2 Cp_{\text{inst}}(\theta)$, where $Cp_{\text{inst}}(\theta)$ is obtained from $\overline{Cp}(\bar{\theta})$ and fitted nonlinearly (by Fourier Series or polynomial). Smoothing effects of azimuth fluctuation on $Cp_{\text{inst}}(\theta)$ are considered.	RMS of point pressures on full scale Silsoe cube.
Banks & Meroney, 2001		Synchronized velocity and pressure signals. Comparing time series, RMS and probability of the QS-predicted pressures.
QS models considering magnitude, azimuth and elevation of the wind		
Letchford & Marwood, 1997	$\frac{1}{2}\rho\left(\bar{u}^2+2\bar{u}u'\right)\left[\begin{array}{l}\overline{Cp}(\bar{\theta})+\frac{v'}{\bar{u}}\frac{\partial\overline{Cp}(\theta')}{\partial\theta}+\\ \frac{w'}{\bar{u}}\frac{\partial\overline{Cp}(\beta')}{\partial\beta}\end{array}\right]$, where the gradient $\frac{\partial\overline{Cp}(\beta')}{\partial\beta}$ is obtained from tilted models.	Synchronized velocity and pressure measurements. RMS of point pressures along a line on a low-building roof below corner vortices
Sharma & Richards, 1999		Spectra of pressures on roof.
Sharma & Richards, 2004		Spectra of point and area-averaged of the 1/50 TTU windward wall.
Richards & Hoxey, 2004	$\frac{1}{2}\rho\|\mathbf{u}\|^2\left[\begin{array}{l}Cp_{\text{inst}}(\theta)+\frac{\partial Cp_{\text{inst}}(\theta,\beta)}{\partial\beta}\left(\frac{-u_*^2}{\overline{u'}^2}\cdot\frac{\|\mathbf{u}\|-\bar{u}}{\|\mathbf{u}\|}\right)\\ +\frac{\partial Cp_{\text{inst}}(\theta,\beta)}{\partial\beta}\left(\beta'_{\text{random}}\right)\end{array}\right]$, where $Cp_{\text{inst}}(\theta)$'s are obtained from the similar way by Richards et al. (1995) ; $\frac{\partial\overline{Cp}(\beta)}{\partial\beta}$'s are obtained by tilting the building; u_* denotes the Reynolds stresses between stream-wise and vertical velocities and β'_{random} is the randomly generated elevation angle fluctuations.	Probability of the point pressures on the full scale Silsoe cube.
Asghari Mooneghi et al., 2016	Implicit use of formulation $\frac{1}{2}\rho\|\mathbf{u}\|^2 Cp_{\text{inst}}(\theta,\beta)$, where extreme value analyses were conducted on $Cp_{\text{inst}}(\theta,\beta)$. Effects of wind elevations are obtained by tilting the model.	Peak point pressure values on TTU WERFL building and Silsoe Cube in both model and full scale.

1.4 Thesis layout

The layout of this this thesis is presented as follows. Six roughness terrain conditions were set up in the boundary layer wind tunnel in order to simulate the atmospheric boundary layer flows with a range of turbulence intensities and length scales. The upstream wind characteristics, the surface pressure measurements of the geometrically-scaled building model and wind field measurements near the roof are presented in Chapter 2. The effects of upstream turbulence on the mean pressure distribution along the centerline of the roof are explained via differential momentum equations in Chapter 3. The integral momentum approach is introduced in Chapter 4 and applied for calculating the area-averaged roof surface pressures. The inherent physical assumption in a traditional QS theory is also derived in this chapter through algebraic manipulations of the integral momentum equations. In Chapter 5, the QS model that accounts for instantaneous wind speed vector of three-dimensions is established and validated for a single terrain roughness condition. Chapter 6 further looks at the applicability of the QS model in estimating the roof surface pressure fluctuations for different upstream turbulence conditions. The overall conclusions and suggestions for further research are presented in Chapter 7.

Chapter 2

2 Experimental setup

This chapter describes the experimental setup for the simulation of the atmospheric boundary layer flows. The related surface pressure measurements on the geometrically-scaled building model, along with the planar field and point measurements of velocity near the building, are also presented.

2.1 Atmospheric boundary layer (ABL) flow simulation with various terrain roughness conditions

Six upstream terrain roughness conditions created in Boundary Layer Wind Tunnel II in University of Western Ontario (UWO) are used in order to generate the turbulence with a range of intensities and length scales. These ABL turbulent flows are simulated in the high speed section of the wind tunnel, which offers a fetch of 39 m for flow development and a cross-section of 3.36 m in width and 2.05 m in height at the test location. At the upstream end, three spires with a height of 1.22 m and a base width of 0.1 m are placed. Sets of roughness blocks are distributed along the floor between the upstream end and test location. By altering the heights of the roughness blocks, three distinct ABL turbulent flows, which are called ‘Flat’, ‘Open’ and ‘Suburban’ in this paper, are generated. By further placing a barrier of 0.38 m (15 inch) height immediately after the spires, along with the same sets of roughness blocks mentioned earlier, another three sets of ABL flow are generated with altered integral scales. In summary, the measurements were conducted with a total of six terrain roughness conditions. Three of them with 15 inch barrier at the upstream end are labelled as ‘F15’, ‘O15’and ‘S15’ for Flat, Open and Suburban roughness distributions, respectively; The remaining three, without upstream barriers, are labelled as ‘F0’, ‘O0’ and ‘S0’, correspondingly. Note that these six upstream terrain conditions were also used for discussions by Akon and Kopp (2016) and Akon (2017).

Vertical profiles of the mean longitudinal velocity component, $\bar{u}$, are measured using Cobra probes (TFI, Model no. 900, 311) without the building model in place for the six terrain conditions. These mean longitudinal velocities are normalized by the mean

longitudinal velocity at the roof height, i.e., $\overline{u}/\overline{u}_H$, and are shown in Figure 2-1 (a) as a function of normalized height, z/H. Here z denotes the vertical distance from the wind tunnel floor and $H = 8\,\text{cm}$ is the building height of the (geometrically-scaled) model. Near the roof, i.e., $z/H \le 3$, similar vertical distributions of $\overline{u}/\overline{u}_H$ can be found for the Flat and Open terrains (i.e., 'F0', 'F15', 'O0' and 'O15') while a significant increase of shear can be observed in the Suburban terrains (i.e., 'S0' and 'S15'). The ratios of building height to roughness length, known as the Jensen number, are 540, 600, 290, 600, 56 and 71 for terrains 'F0', 'F15', 'O0', 'O15', 'S0' and 'S15' respectively, as reported by Akon and Kopp (2016). Figure 2-1 (b) shows the vertical profile for the corresponding turbulence intensity, I_u, of six terrains. Clear increases in turbulence intensities can be observed for increased roughness along the wind tunnel floor. Adding the 15-inch barrier at the upstream end has less effect on turbulence intensity. Hence the relative intensity of turbulence near the roof height can be a summarized as $I_{u,\text{F0}} \cong I_{u,\text{F15}} < I_{u,\text{O0}} \cong I_{u,\text{O15}} < I_{u,\text{S0}} < I_{u,\text{S15}}$, where the terrains are labelled in the subscripts.

The power spectral densities of the longitudinal velocity fluctuations were also obtained at the roof height for the six terrains. Instead of using the typical normalization, $fS_{uu}/\overline{u'u'}$, for the spectra, we have non-dimensionalized it using $fS_{uu}/\overline{u}^2$, where f denotes the frequency and S_{uu} is the auto-spectral density. This normalization is similar to the conventional one, but with additional information on turbulence intensity, since $\int_{f=0}^{\infty} S_{uu}/\overline{u}^2\, df$ is in fact equal to I_u^2. So, the clear increases of turbulence intensity due to increased roughness that is observed in Figure 2-1 (b) are reflected in the magnitude changes in the reduced spectra in Figure 2-1 (c). In addition to the magnitude of the fluctuations, the associated length scales can also be observed for the six upstream turbulence conditions. The terrains with the 15-inch barrier at the upstream end produce turbulent flows of larger length scales as compared to terrains without the barrier. For example, the reduced spectra obtained from F15 and O15 generally shift the F0 and O0 counterparts toward the larger length scale side (Figure 2-1 (c)). However S15 terrain not

only produces more large scale turbulence but maintains small scale turbulence equivalent to S0, leading to total increase of turbulence intensity shown in Figure 2-1 (b). These measured spectra are found to reasonably match the von-Karman spectrum. Akon and Kopp (2016) reported the ratio of integral length scale to building height, L_{ux}/H , as being 6, 8, 7, 13, 11 and 12 for terrains F0, O0, S0, F15, O15 and S15, respectively, where $L_{ux} = \bar{u}\int_0^{\infty} u'(t)u(t+t_*)/\overline{u'}^2\, dt_*$ and t_* is the time lag. Note that these ABL flows produced from the six terrains are generally applicable for wind tunnel simulation of the real wind environment (Akon and Kopp, 2016).

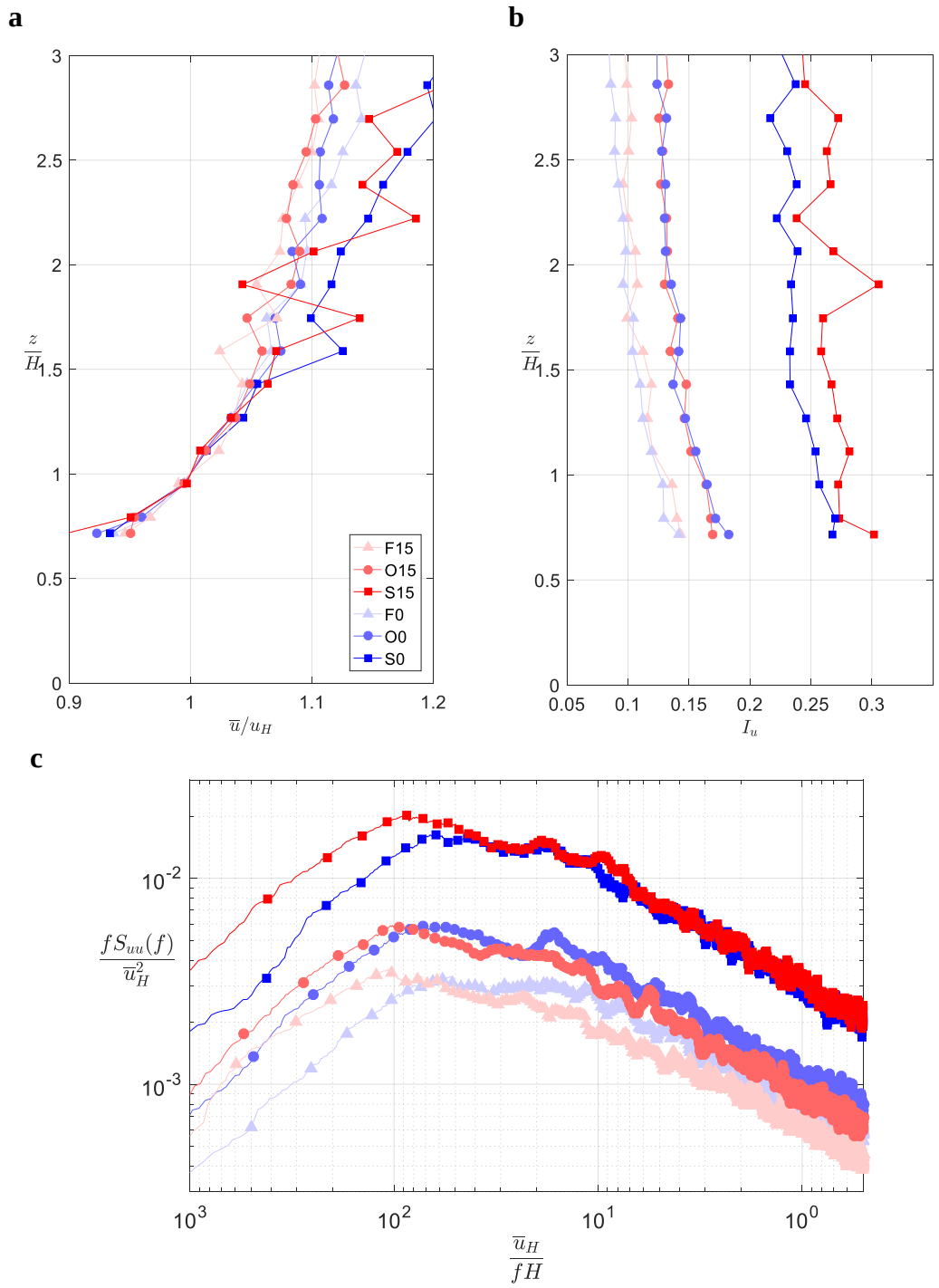

Figure 2-1: (a) Mean u-component velocity profiles, (b) turbulence intensity profiles and (c) reduced spectral density of u component at roof height distribution for 6 terrains.

2.2 Surface pressure measurement on a low-rise building model

The surface pressure measurements on the 1/50 geometrically-scaled model of Texas Tech University 'WERFL' Building (Levitan and Mehta, 1992a) are used throughout this thesis. The modelled building has a plane dimension of 18.3 cm × 27.5 cm and an eave height of 7.8 cm. Figure 2-2 (a) shows the total 204 uniformly distributed taps on the model surface. A Cartesian coordinate used to define the space and velocity components are also included in this figure. The origin of the coordinate system is located at the middle bottom of the building model longer wall. Based on this definition, wind direction normal to the longer wall is 0˚ in azimuth, whereas the wind direction normal to the shorter wall is 90˚ in azimuth. The building model was placed in the high speed test section of the wind tunnel, where the six upstream terrain roughness conditions described in Section 2.1 can be applied. Detailed tubing system and frequency responses for the pressure measurement can be found in Ho et al. (2005).

a

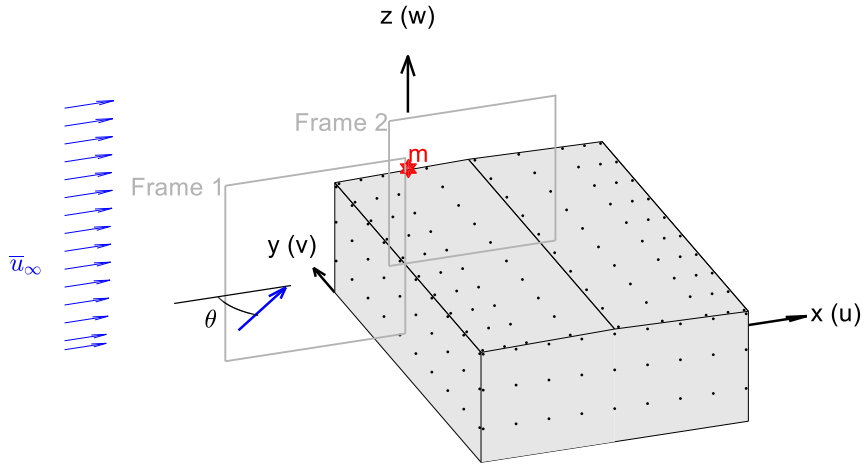

b

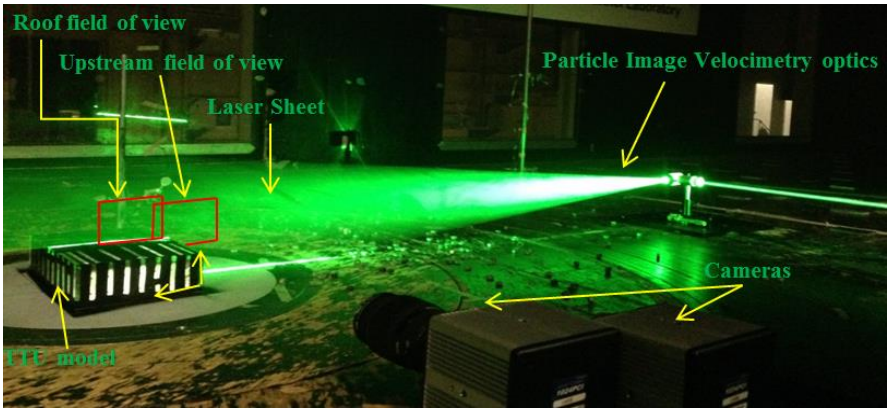

c

Figure 2-2: (a) Pressure tap locations for the 1/50 TTU building along with the Cartesian coordinate of the space and wind azimuth definition. (b) The planar image frames of PIV measurement near the TTU building model by Akon and Kopp (2016) (also indicated in plot (a)); (c) The point location *m* of the cobra probe velocity measurement (Wu and Kopp, 2016) (also indicated in plot (a)).

2.3 Velocity measurements above the roof

The planar flow field above the roof centerline of the TTU model was measured by Akon (Akon and Kopp, 2016; Akon, 2017) using the Time-Resolved Particle Image Velocimetry (TR-PIV) system for the upstream mean wind direction of 0˚ azimuth. The schematic setup in Figure 2-2 (a) and the example of exact setup photo in Figure 2-2 (b). The TR-PIV measurements are synchronized with the building surface pressure measurement. The building surface pressure measured at the 9 taps along the roof centerline were sampled at a rate of 1108 Hz for 180 seconds and low-pass filtered to about 200 Hz due to the frequency response of the pressure measurement system. The sampling rate of the TR-PIV system is 500 Hz. Details about the TR-PIV system can be found in Akon (2017) and Taylor et al. (2010). Figure 2-2 (a) shows the two fields of view, i.e., upstream field (Frame 1) and roof field (Frame 2), taken by the PIV system, along with the building model. Also note that the planar PIV measurement only captures u-w velocity components in the x-z plane. The final grid spacing between data points is $\Delta x = \Delta z = 0.2\,\text{cm}$ for Frame 1 and $\Delta x = \Delta z = 0.18\,\text{cm}$ for Frame 2 due to the slightly different fields of view used with the two cameras. The resulting mean velocity, turbulence stresses and mean surface pressures (Akon, 2017) are used for analyses in Chapter 3 and Chapter 4 in this thesis.

Simultaneous measurements of building surface pressures and wind velocity vectors at a point location (see Appendix B) were also conducted by the author in Boundary Layer Wind Tunnel II at UWO (see example of setup in Figure 2-2 (c)). A Cobra probe (TFI Corp., model 900, probe #289) was placed at one building height above the leading edge of the roof surface at the mid-plane of the long wall. This point location of the velocity measurement, which is denoted as *m* and shown in Figure 2-2 (a), was selected to obtain the velocities representative of the flow at the building location, while minimizing the effects on the building pressures (see Appendix D). In addition, two additional simultaneous cobra probe measurements were made in these experiments. However, preliminary analyses (see Appendix A) shows that the correlation of measured velocities between probes decreases significantly as the transverse separation distance increases. Hence, the velocities measured above the roof are mainly used for analyses throughout

this thesis. These synchronized velocity and pressure measurements (see Appendix B for details) were conducted for mean wind azimuth angles varied from 0˚ to 90˚, in increments of 5˚ (Figure 2-2 (a)). Furthermore, the measurement point *m* above roof was made fixed with respect to the building for each mean wind azimuth angle in order to analyze the velocity-pressure data using quasi-steady theory. The synchronized pressure and velocity time series were sampled at 625 Hz for 200 seconds for each mean wind direction in these experiments. These data are involved in quasi-steady analyses shown in Chapters 4, 5 and 6.

Chapter 3

3 Evaluation of mean pressure field using time-averaged differential momentum equation

In this chapter, a method to obtain the pressure field from the measured velocity field is developed by applying the differential momentum equations (i.e., the Navier-Stokes equations). It is also used to explain the effects of the mean flow and turbulence fields to the mean pressure fields above the roof of the TTU WERFL model (see Section 2.2). The mean flow and turbulence fields were measured by Akon (2017) via planar TR-PIV mentioned in Section 2.3. Synchronized roof surface pressure measurements by Akon (2017) are also used for discussion.

3.1 Integration of planar pressure gradient data using the analytic interpolation technique

The analytic interpolation technique proposed by Ettl et al. (2008) for surface reconstruction is explained and applied for integrating mean pressure gradient data in this section. The Navier-Stokes equations, represented in Eq. (1-2), are used to determine the mean pressure gradient using planar PIV measurement data. For wind normal to the building and a measurement plane above the centerline (see Figure 2-2 (b)), the mean flow field can be treated as symmetric and, hence, the gradients associated with out-of-plane component are negligible. The exact components used in Eq. (1-2) for evaluation of mean pressure gradient are:

$$\frac{\partial \overline{Cp}}{\partial x} = -2\left[\frac{\bar{u}}{u_{\text{ref}}}\frac{\partial}{\partial x}\left(\frac{\bar{u}}{u_{\text{ref}}}\right)+\frac{\bar{w}}{u_{\text{ref}}}\frac{\partial}{\partial z}\left(\frac{\bar{u}}{u_{\text{ref}}}\right)+\frac{\partial}{\partial x}\left(\frac{\overline{u'u'}}{u_{\text{ref}}^2}\right)+\frac{\partial}{\partial z}\left(\frac{\overline{u'w'}}{u_{\text{ref}}^2}\right)-\frac{\nu}{u_{\text{ref}}}\left(\frac{\partial^2}{\partial x^2}\left(\frac{\bar{u}}{u_{\text{ref}}}\right)+\frac{\partial^2}{\partial z^2}\left(\frac{\bar{u}}{u_{\text{ref}}}\right)\right)\right] \quad \text{(3-1a)}$$

$$\frac{\partial \overline{Cp}}{\partial z} = -2\left[\frac{\bar{u}}{u_{\text{ref}}}\frac{\partial}{\partial x}\left(\frac{\bar{w}}{u_{\text{ref}}}\right)+\frac{\bar{w}}{u_{\text{ref}}}\frac{\partial}{\partial z}\left(\frac{\bar{w}}{u_{\text{ref}}}\right)+\frac{\partial}{\partial x}\left(\frac{\overline{u'w'}}{u_{\text{ref}}^2}\right)+\frac{\partial}{\partial z}\left(\frac{\overline{w'w'}}{u_{\text{ref}}^2}\right)-\frac{\nu}{u_{ref}}\left(\frac{\partial^2}{\partial x^2}\left(\frac{\bar{w}}{u_{\text{ref}}}\right)+\frac{\partial^2}{\partial z^2}\left(\frac{\bar{w}}{u_{\text{ref}}}\right)\right)\right] \quad \text{(3-1b)}$$

On the right hand side of Eq. (3-1), the 1st and 2nd terms are associated with the mean convection, the 3rd and 4th terms are associated with turbulence and the 5th and 6th terms are associated with viscous stresses.

The analytic interpolation approach developed by Ettl et al. (2008) offers an effective tool for topological surface reconstruction by integrating measured gradient data. Because the differential momentum equation offers gradient information of pressure, as shown in Eq. (3-1), the reconstruction method of Ettl et al. (2008) will be applicable to pressure reconstruction. In this approach, the estimated pressure coefficient, Cp_e, at location $\mathbf{x}$ is assumed as linear spatial superposition of analytic functions, i.e.,

$$Cp_e(\mathbf{x}) = \sum_{j=1}^{N}\left[\alpha_{1j}\frac{\partial}{\partial x}\Phi(\mathbf{x}-\mathbf{x}_j)+\alpha_{3j}\frac{\partial}{\partial z}\Phi(\mathbf{x}-\mathbf{x}_j)\right], \tag{3-2}$$

where α_{1j} and α_{3j} are the appropriate coefficients for the *x* and *z* derivatives of analytic support centred at the *j*-th grid point, respectively; N denotes total number of grid points. Wenland's function was selected by Ettl et al. (2008), and also here, for the analytic support, Φ. This function is symmetric about its centre and resembles a bell-shaped surface for the radial distance $r \le 1$ and is zero for regions of $r > 1$, i.e.,

$$\Phi(r) = \begin{cases} \frac{1}{3}(1-r)^6(35r^2+18r+3) & \text{for} \quad r \le 1 \\ 0 \quad \text{for} \quad r > 1 \end{cases} \quad \text{with} \quad r = \sqrt{x^2+z^2}\,. \tag{3-3}$$

The support size, which is denoted as σ, describes the range of influence of the radial support Φ. As can be seen in Eq. (3-3), the support size is unity for the original Wenland's function. Adjustment of the support size may be needed in order to render smooth integration results for various grid spacing. Such adjustment can be simply achieved by replacing original grid location, $\mathbf{x}$, in Eq. (3-2) by the normalized one, $\mathbf{x}/\sigma$. Thus, the Cp_e in Eq. (3-2) is directly related to *j*-th support if $|\mathbf{x}-\mathbf{x_j}| \le \sigma$, while supports outside the influence region can be neglected in Eq. (3-2). In order to determine the coefficients α and β, the gradient of Cp_e represented by Eq. (3-2) is taken at grid point $\mathbf{x}_i$ and matched with the measured gradient data obtained from the Navier-Stokes equations, Eq.(3-1), such that

$$\underbrace{\begin{bmatrix} \frac{\partial^2}{\partial x^2}\Phi(\mathbf{x}_i-\mathbf{x}_j) & \frac{\partial^2}{\partial x\partial z}\Phi(\mathbf{x}_i-\mathbf{x}_j) \\ \frac{\partial^2}{\partial x\partial z}\Phi(\mathbf{x}_i-\mathbf{x}_j) & \frac{\partial^2}{\partial z^2}\Phi(\mathbf{x}_i-\mathbf{x}_j) \end{bmatrix}}_{\mathbf{A},\ 2N\times 2N} \underbrace{\begin{bmatrix} \alpha_j \\ \beta_j \end{bmatrix}}_{\mathbf{c},\ 2N\times 1} = \underbrace{\begin{bmatrix} \frac{\partial}{\partial x}\overline{Cp}(\mathbf{x}_i) \\ \frac{\partial}{\partial z}\overline{Cp}(\mathbf{x}_i) \end{bmatrix}}_{\mathbf{d},\ 2N\times 1}. \tag{3-4}$$

Once the linear system described in Eq. (3-4) is established, the coefficients can be solved by matrix inversion.

There are a few notes regarding the application. First, since the integration scheme is based on gradient data, the integrated values resulting from Eq.(3-2) only offer information of relative difference. Therefore it is necessary to specify a constant of integration at a specified location within the domain of measurement. Second, if a normalized grid location, $\mathbf{x}/\sigma$, is used in Eq. (3-2), the measured gradient data must be pre-multiplied by σ before putting into vector **d** in Eq.(3-4), in order to account for the chain rule.

The current interpolation method allows users to treat bad data points with two options because of the advantages of the mathematical nature of Eq. (3-2). Assuming that there are a total of N_b bad gradient data points, scattered at locat1ions $\mathbf{x}_b$ within the measurement plane. The first option is to exclude the radial basis supports located at $\mathbf{x}_b$ in Eq. (3-2) while keeping full gradient data in **d** in Eq. (3-4). In this case, $\mathbf{A}$ becomes a non-square matrix of dimension $2N\times 2(N-N_b)$ and $\mathbf{d}$ is still a vector of dimension $2N\times 1$. Then, a least-squares method can be used to solve for the coefficient vector **c** in Eq. (3-4), as mentioned in Ettl et al. (2008). The second option is to remove both the supports at $\mathbf{x}_b$ in Eq. (3-2) and bad gradient data in vector **d** in Eq. (3-4). The corresponding dimensions of matrices $\mathbf{A}$ and **d** have sizes of $2(N-N_b)\times 2(N-N_b)$ and $2(N-N_b)\times 1$, respectively, in this case. Therefore, direct matrix inversion can be used again to solve the coefficient vector. The reconstruction at bad gradient data locations can then be treated as extrapolation by simply evaluating $Cp_e(\mathbf{x}_b)$ in Eq. (3-2).

Interested readers are referred to Ettl et al. (2008) for more useful techniques for application.

A review of the details used in current pressure integration is as follows. Once the mean velocities and turbulence stresses are captured from the two PIV image frames in Figure 2-2, a smoothing technique mentioned is applied to remove unreasonable data. Due to the laser reflection near the model surface, some erroneous velocity and turbulence stresses can be found in the measurement in this region, especially for terrains that produce high upstream turbulence intensity. These erroneous data are identified and replaced by the mean value of its neighbors. This process can effectively reduce the number erroneous pressure gradient in the first place. After that, the central difference scheme is applied to calculate the pressure gradient vectors according to differential momentum in Eq. (3-1). Bad pressure gradient data are identified and removed in the reconstruction process if the magnitude or direction deviates extremely from that of its neighbors. The size of the analytic support is chosen to be about 14 times that of the PIV data grid spacing in order to render reconstruction smoothness. The mean pressure is assumed to be the same as the ambient value, i.e., $\overline{Cp} = 0$, at the roof height, upstream end of frame 1, i.e., $\{x = -1.56H,\ z = H\}$. Reconstructed pressures in frame 2 are then adjusted by an integration constant through minimizing the difference of integrated pressures within the overlapped region between frames 1 and 2 (see Figure 2 and Ettl et al. (2008)).

3.2 Application of the pressure integration technique in determination of pressure field due to a steady 2D vortical flow field

This section provides a quick comparison of the pressure fields obtained from a simple line-wise integration and analytic interpolation approach introduced in 3.2. In order to demonstrate the ideas, three identical 2D steady flow fields of elliptical pattern are created on the x-z plane and shown in Figure 3-1 (a). Such flow fields are generated by placing the two vortex blobs (which can be think of two Rankine vortices, see Spalart, 1998) near the origin along a line of different angles, i.e., 0˚ (horizontal), 45˚ (oblique) and 90˚ (vertical). Note that the flow fields creating by this methods satisfied continuity

as well (Spalart, 1998). Each of the two have a core radius of 2 m (i.e., the radial distance from center to location of maximum velocity) and are 4 m apart from each other. The resulting pressure gradient are shown in Figure 3-1 (b), which are calculated by only including the convection terms in Eq. (3-1). Note that the three fields of pressure gradients are near identical and aligned with the lines of 0˚, 45˚ and 90˚. For the regions where curvature of the streamlines are large (Figure 3-1 (a)), the magnitudes of pressure gradient are higher as well (see Figure 3-1 (b)).

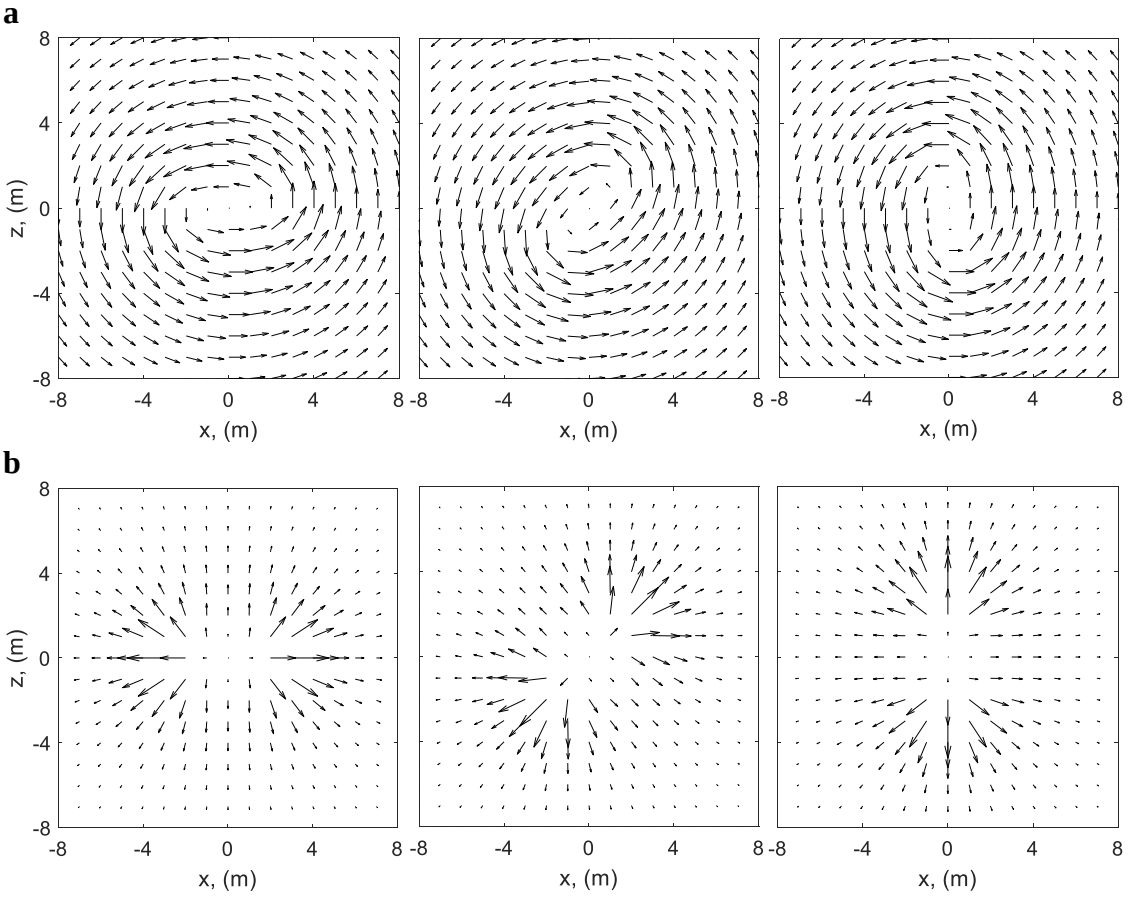

Figure 3-1: (a) Three identical steady flow fields generated by placing the two vortex blobs along different axes; (b) The corresponding gradient fields of Cp.

In order show the value of the analytical interpolation approach for pressure integration, a simple line-wise integration technique is also used for comparison. For the line-wise integration technique, the pressure along the bottom boundary of the field, i.e., $\{z = -8\,\mathrm{m}\}$, is first prescribed by Bernoulli's equation. The fields of Cp's are obtained by integrating the pressure gradients (shown in Figure 3-1 (b)) along the z-axis in the

upward direction. Note that only vertical component of the gradient, i.e., dCp/dz, is required for the line-wise integration because the integration path is parallel to the z-axis. The results of integrated pressure fields, which correspond to the flow fields shown in Figure 3-1 (a), obtained from the simple line-wise integration and the analytical interpolation technique are shown in Figure 3-2 (a) and (b), respectively. As can be clearly seen in Figure 3-2 (a), the use of the simple line-wise integration leads to inconsistent results of integrated pressures. The error can also be accumulated along the integration path as well (see the middle plot in Figure 3-2 (a)). By using the analytic interpolation approach, however, the results are more consistent and the integration error appeared in middle graph in Figure 3-2 (a) are removed. Hence, the use of the analytic interpolation approach for pressure integration is asserted for the following application on the PIV data.

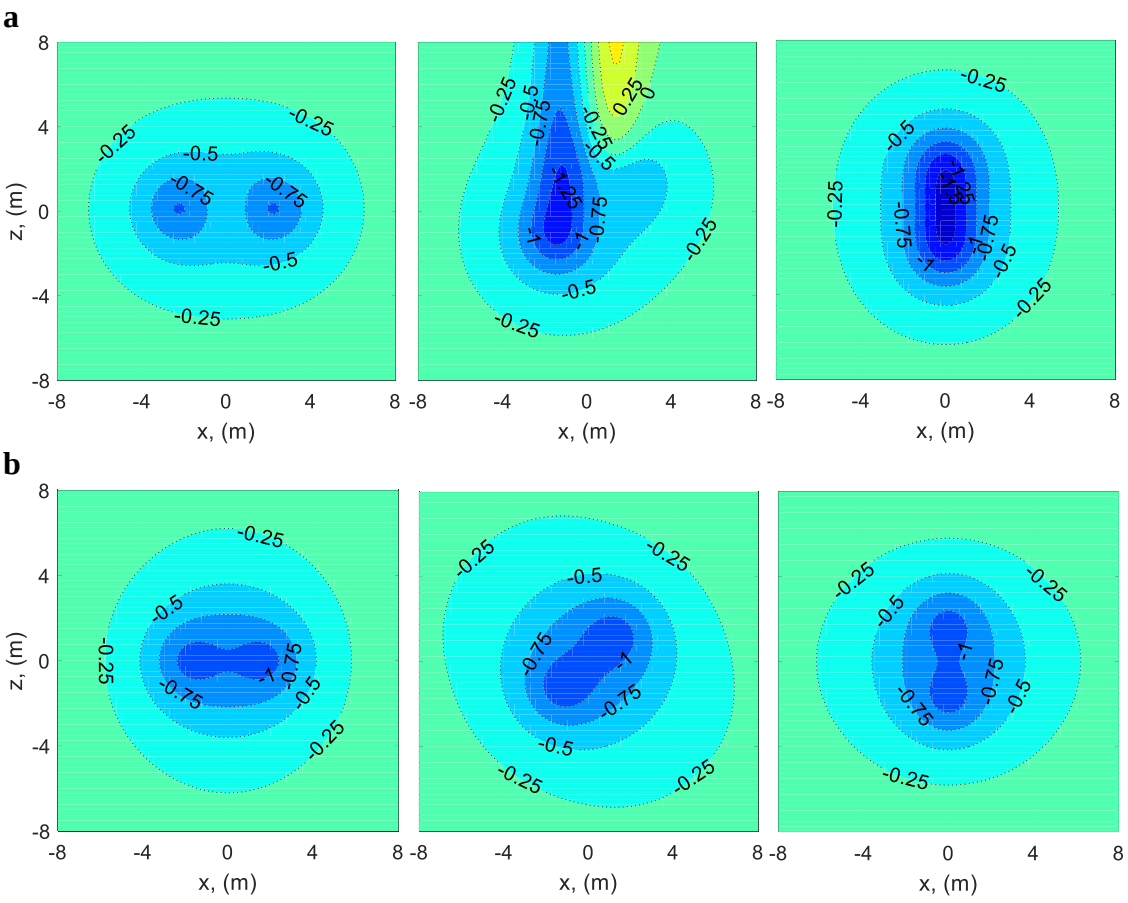

Figure 3-2: Cp fields obtained from: (a) simple line-wise integration and (b) the analytical interpolation approach.

3.3 Application of the pressure integration technique in planar flow fields measured near the low-rise building roof

3.3.1 Pressure gradients of the convection terms

Planar PIV measurements were conducted near the building roof under six upstream terrain conditions mentioned in Section 2.3. Figure 3-3 shows the ratio of the mean velocity magnitude, $|\overline{\mathbf{u}}|$, to a reference velocity, u_{ref}, for all six terrains. Generally, a speed-up ratio of $\approx 1.0/0.7 = 1.4$ can be found when comparing the mean upstream velocity at the roof height to the velocity on top of the roof of the same streamline. Low velocities can be found within the stagnation region in front of the wall and in the recirculation region above the roof. The contribution of the convection terms to the pressure gradient in Navier-Stokes equations, i.e., the 1st and 2nd terms on the right hand side of Eq. (3-1), is shown in Figure 3-4 for all six upstream terrain conditions. Generally the gradient vectors are found to radiate from the windward corner, with the magnitudes being the largest near the leading edge and reduced above the mean separation bubbles (which are also shown in Figure 3-4). Over the regions further away from the leading edge and within the separation bubbles, relatively small gradient vectors can be observed.

As already noted by Akon and Kopp (2016), the size of separation bubbles is much more sensitive to the intensity than the scale of the upstream turbulence, being smaller for greater values of turbulence intensity. Their observation can be easily verified by reviewing the turbulence intensities in Figure 2-1 (b) and the mean separation bubbles in Figure 3-4. Because the curvature of the streamlines increases as the size of separation bubbles is reduced, the convection-contributed pressure gradients above the separation bubbles are intensified for rougher terrains. The terrain effects on relative mean velocity magnitude (see Figure 3-3) is not significant in general, although details of velocity variation near the leading edge are different when comparing the results in Figure 3-3 for terrains ‘F0’ and ‘S15’. Lower velocity magnitude variation near the leading edge can be found for terrain ‘F0’ while higher variation can be observed for terrain ‘S15’. More rapid spatial variations of velocity magnitude increases the convection-contributed

pressure gradients as well, so that the pressure gradients of terrain ‘S15’ are larger than that in terrain ‘F0’ near the leading edge (see Figure 3-4).

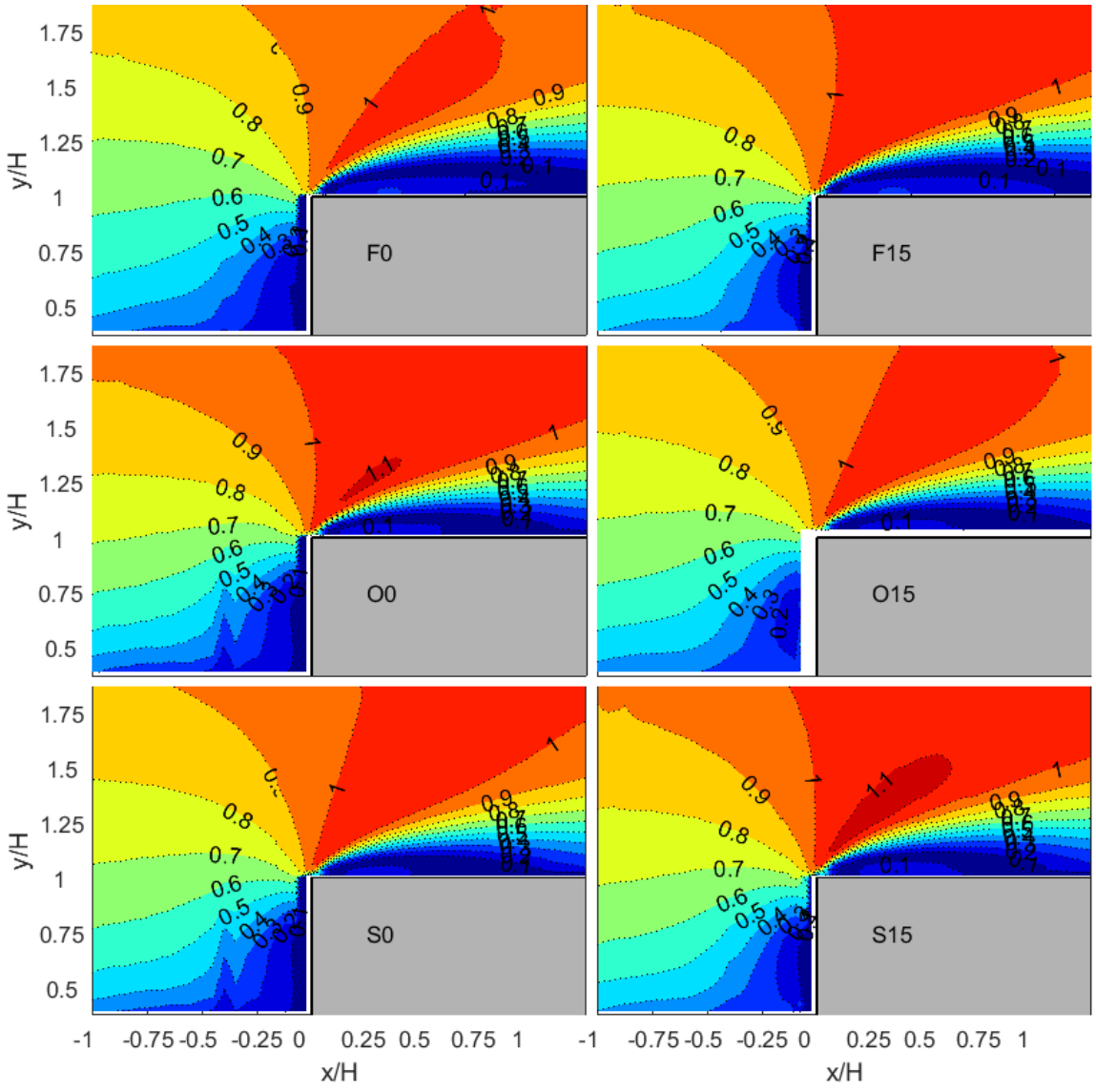

Figure 3-3: Mean velocity ratio, $|\overline{\mathbf{u}}|/u_{\mathrm{ref}}$, near roof obtained for the six terrains.

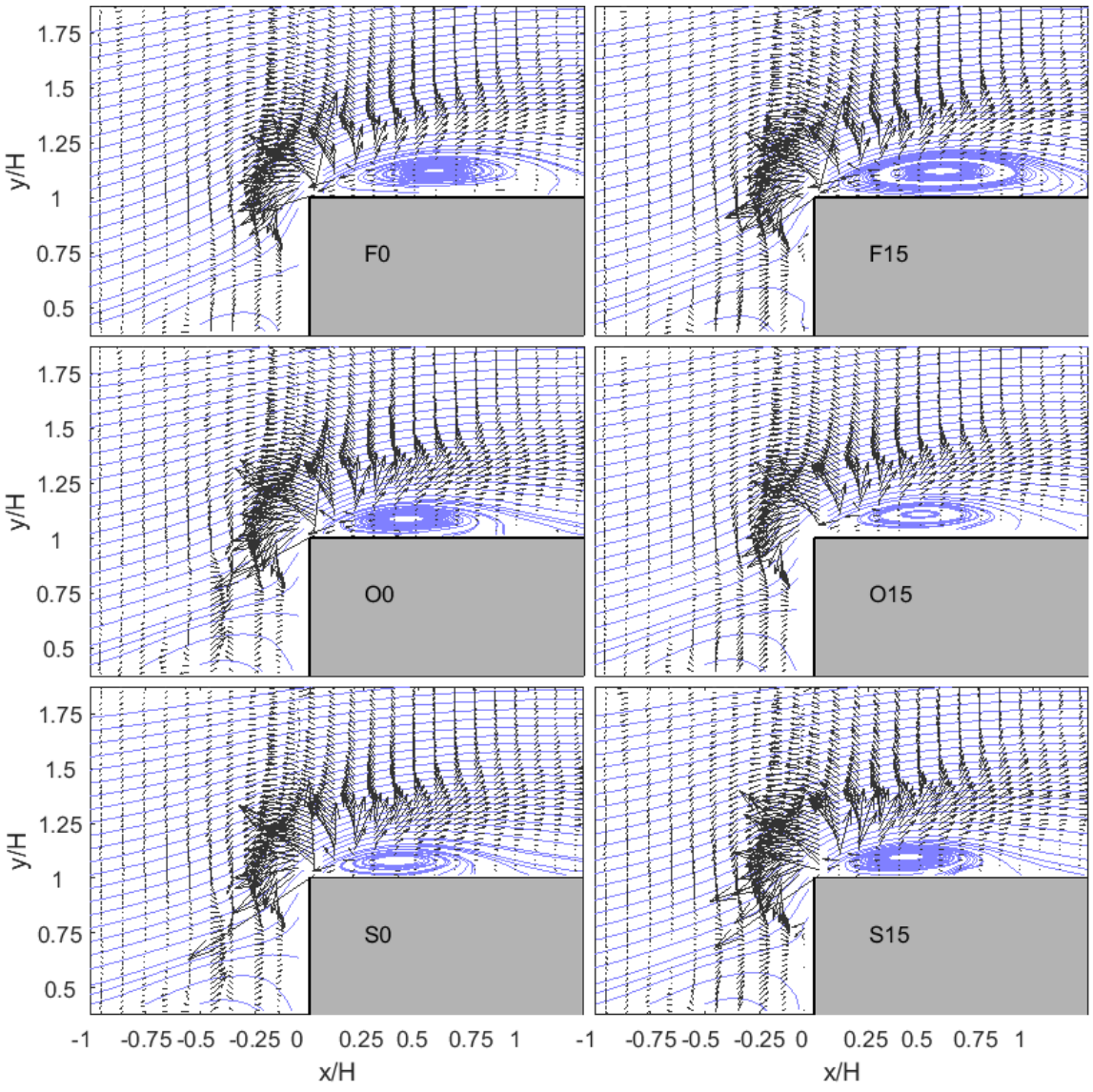

Figure 3-4: Vectors of gradient $\overline{Cp}$ of the mean convection term in the Navier-Stokes equations for the six terrains along with streamlines.

3.3.2 Pressure gradients of the turbulence terms

The three distinct components of turbulence stress tensors, $\overline{u'u'}$, $\overline{w'w'}$ and $\overline{u'w'}$, are normalized by reference velocity and shown respectively in Figures 3-5, 3-6 and 3-7. Once these turbulence stresses are measured, the turbulence contribution to the mean pressure gradient vectors, which is shown in Figure 3-8, can be obtained by evaluating the 3rd and 4th terms of Eq. (3-1). For the distribution of $\overline{u'u'}/u_{ref}^2$ shown in Figure 3-5,

maximum values are found to coincide with the shear layer region while decreasing values can be found for the regions away from the shear layers. By further comparing Figure 3-5 to Figures 3-6 and 3-7, it is observed that the $\overline{u'u'}$ component dominates the turbulence stress tensor, with maximum magnitudes around 4 times that of the other two. Hence, according to Eq. (3-1a), the turbulence-contributed pressure gradient vectors generally radiate from the shear layer in a nearly horizontal direction. For the distribution of $\overline{w'w'}/u_{\text{ref}}^2$ shown in Figure 3-6, larger magnitudes are found over the leeward half of the separation bubbles. The spatial variation of $\overline{w'w'}/u_{\text{ref}}^2$ is responsible for the pressure gradients in the vertical direction, according to Eq. (3-1b). For the distribution of $\overline{u'w'}/u_{\text{ref}}^2$ shown in Figure 3-7, a spatial migration of the positive peaks near the roof leading edge to the negative peaks over the leeward half of the separation bubbles can be found. According to Eq. (3-1), the vertical gradient of $\overline{u'w'}/u_{\text{ref}}^2$ is associated with the horizontal pressure gradient while the horizontal gradient of $\overline{u'w'}/u_{\text{ref}}^2$ is associated with the vertical pressure gradient.

The effects of upstream terrain conditions on the turbulence-contributed pressure gradients are described here. As shown in Figure 3-5, the maximum values of $\overline{u'u'}/u_{\text{ref}}^2$ increase by about 0.03 for changing a terrain to the next rougher level in these experiments, i.e. from ‘F0’ to ‘O0’, ‘O0’ to ‘S0’ and ‘O15’ to ‘S15’. For the $\overline{u'w'}/u_{\text{ref}}^2$ distribution shown in Figure 3-7, higher positive peak values are found for rougher terrains, while negative peak values appear to be mostly independent from the terrain effects. However, the distances between the high and low peak values of $\overline{u'w'}/u_{\text{ref}}^2$ shrink as the sizes of separation bubbles reduce. For the distribution of $\overline{w'w'}/u_{\text{ref}}^2$ shown in Figure 3-6, reduced effects of the upstream terrain conditions can be observed. As a result of these variations, larger turbulence-contributed pressure gradients can be found for rougher terrains in Figure 3-8, for regions near the shear layers and roof surface. Overall, rougher terrains that produce higher intensities of upstream turbulence (see

Figure 2-1 (b)) and induce higher turbulence-contributed pressure gradients. The effects of the turbulence length scales are observed to be less significant.

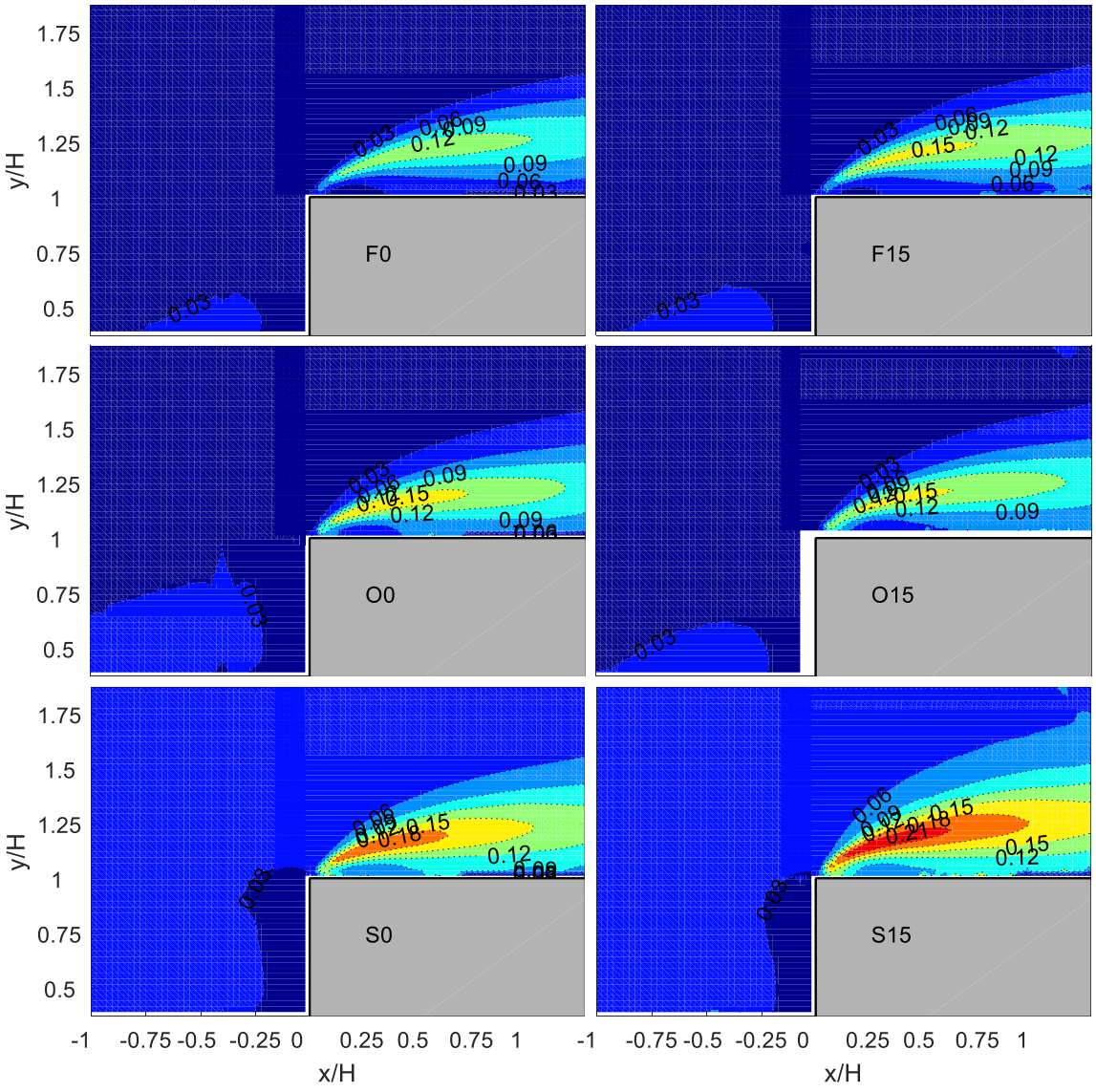

Figure 3-5: Turbulent stress ratio, $\overline{u'u'}/u_{\mathrm{ref}}^2$, obtained for the six terrains.

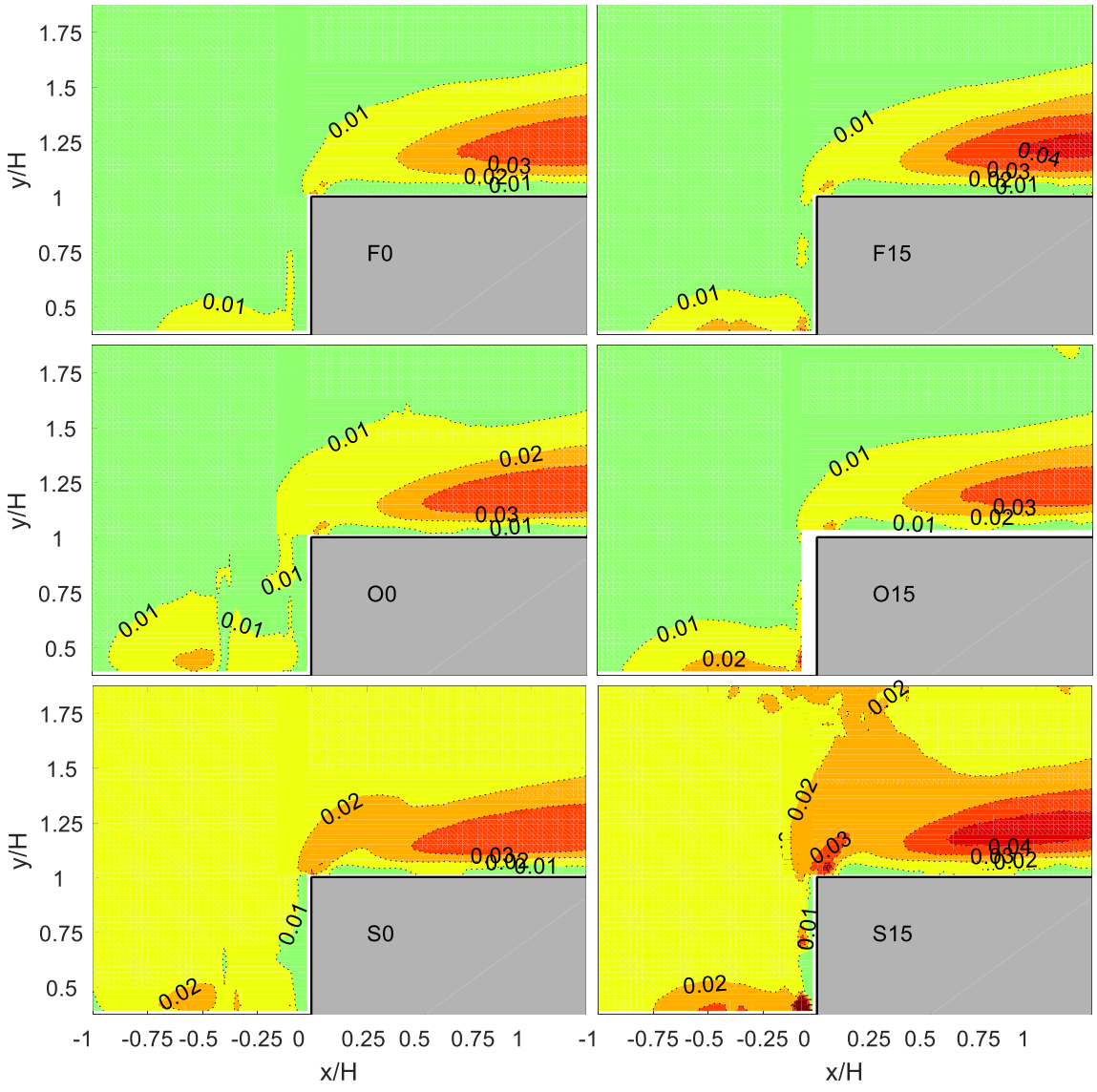

Figure 3-6: Turbulent stress ratio, $\overline{w'w'}/u_{\mathrm{ref}}^2$, obtained for the six terrains.

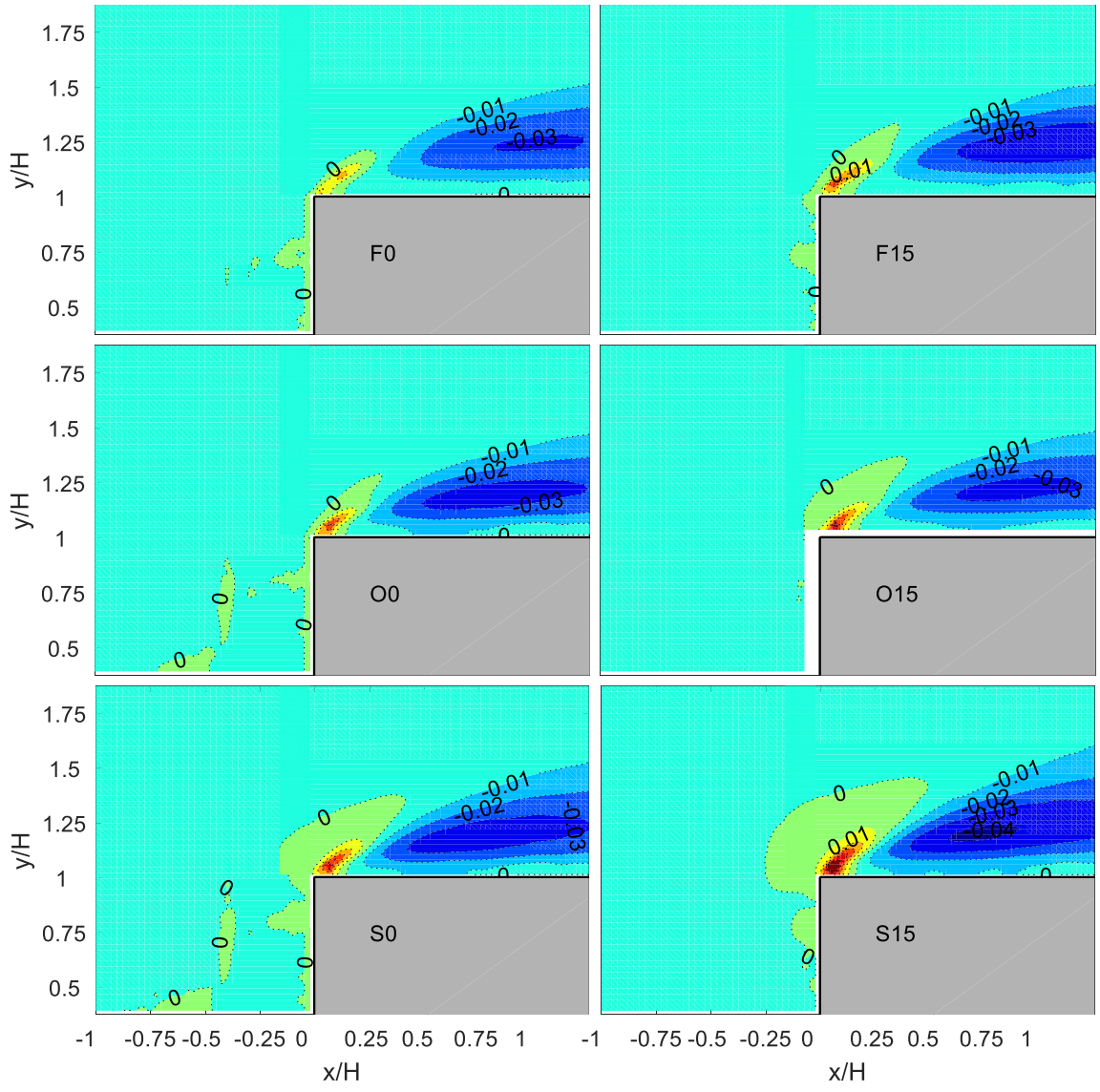

Figure 3-7: Turbulent stress ratio, $\overline{u'w'}/u_{ref}^2$, obtained for the six terrains.

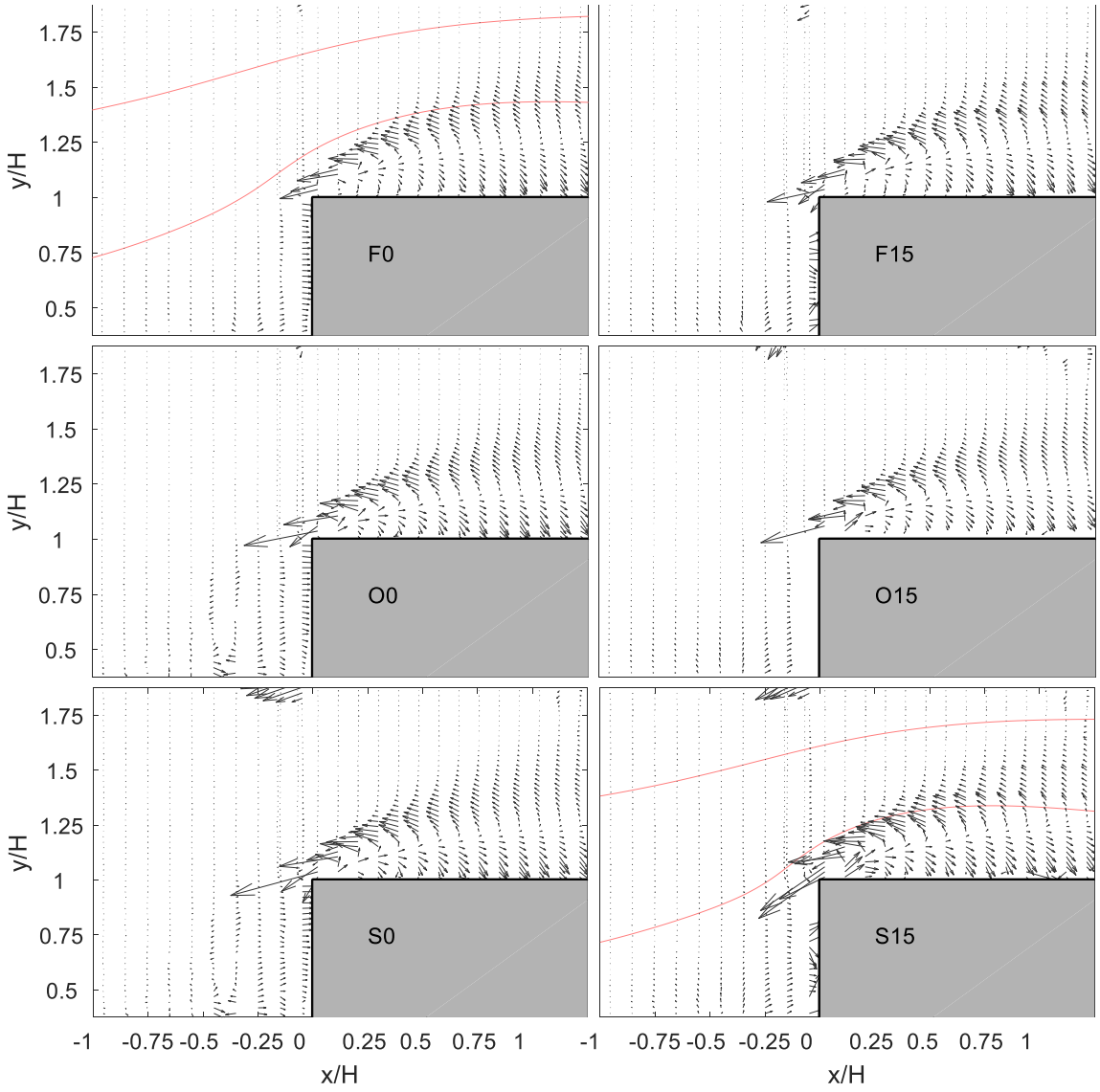

Figure 3-8: Vectors of gradient $\overline{Cp}$ of turbulence term in the Navier-Stokes equations obtained for the six terrains.

3.3.3 Integrated pressure field

For high Reynolds number flow, the viscous contribution is relatively small (e.g., van Oudheusden et al., 2007). The contribution of the viscosity terms to the final integrated pressures are less than 1% for all the cases of our measurements. By summing the contributions of convection, turbulence and viscosity in the Navier-Stokes equations, the total gradient of $\overline{Cp}$ can be obtained, and is shown in Figure 3-9 for the six terrains.

The analytic interpolation technique introduced in Section 3.1 is applied to integrate the total mean pressure gradients shown in Figure 3-9. The reconstructed $\overline{Cp}$ fields are shown in Figure 3-10 for the six terrain conditions. Smooth distributions of the integrated $\overline{Cp}$'s can be observed for all terrains, with the lowest negative values centered at the windward portion of the mean separation bubbles (see Figure 3-10). For regions far upstream of the building, relatively little variation of integrated pressures can be observed. Hence, by assuming the pressure at an upstream point is equivalent to the ambient pressure, Bernoulli's equation, i.e.,

$$\overline{Cp}_{\text{roof top}} = \overline{Cp}_{\text{upstream}} + \frac{\left|\overline{\mathbf{u}}_{\text{upstream}}\right|^2}{u_{\text{ref}}^2} - \frac{\left|\overline{\mathbf{u}}_{\text{roof top}}\right|^2}{u_{\text{ref}}^2}, \tag{3-5}$$

can also be applied to evaluate the pressure along the streamlines and, therefore, serve as a crosscheck for the integrated results. In Eq. (3-5), $\overline{Cp}_{\text{upstream}}$ and $\overline{\mathbf{u}}_{\text{upstream}}$ denote, respectively, the mean pressure coefficients and velocity at an upstream location for the selected streamline, while $\overline{Cp}_{\text{roof top}}$ and $\overline{\mathbf{u}}_{\text{roof top}}$ denote, respectively, the mean pressure coefficient and velocity at a downstream location above the roof on the same streamline. Two streamlines are selected, in terrains 'F0' and 'S15', for this purpose (see Figures 3-8 and 3-10): The upper streamline starts at an upstream point near $\{x=-H; y=1.375H\}$ while the lower one starts at an upstream point near $\{x=-H; y=0.75H\}$. Figure 3-11 shows the comparison of Bernoulli-estimated $\overline{Cp}$'s to the integrated results extracted from the upper and lower streamlines in Figure 3-10. Good agreement of $\overline{Cp}$'s can be

found between Bernoulli's estimations and integrated results for the upper streamlines under the two selected terrain conditions. Such agreement manifest the applicability of the analytic interpolation technique for pressure reconstruction introduced in Section 3.1. However, for the lower streamlines in both terrains, Bernoulli's equation begins to undershoot the suction at $\{x/H \approx 0.25\}$ and continues accumulating the underestimation for the rest of downstream region. Such accumulating underestimation of Bernoulli's equation is due to the absence of the turbulence-contributed pressure gradients near the shear layers. By reviewing the sub-plots in Figure 3-8 for terrains 'F0' and 'S15', both of the lower streamlines are found to enter the region of large turbulence-contributed pressure gradients near $\{x/H \approx 0.25\}$. Because these turbulence-contributed pressure gradient vectors point in the direction opposite to the flow direction, the missing accumulation of these vectors along the positive flow direction leads to an underestimation of Bernoulli-estimated $\overline{Cp}$'s along the lower streamlines.

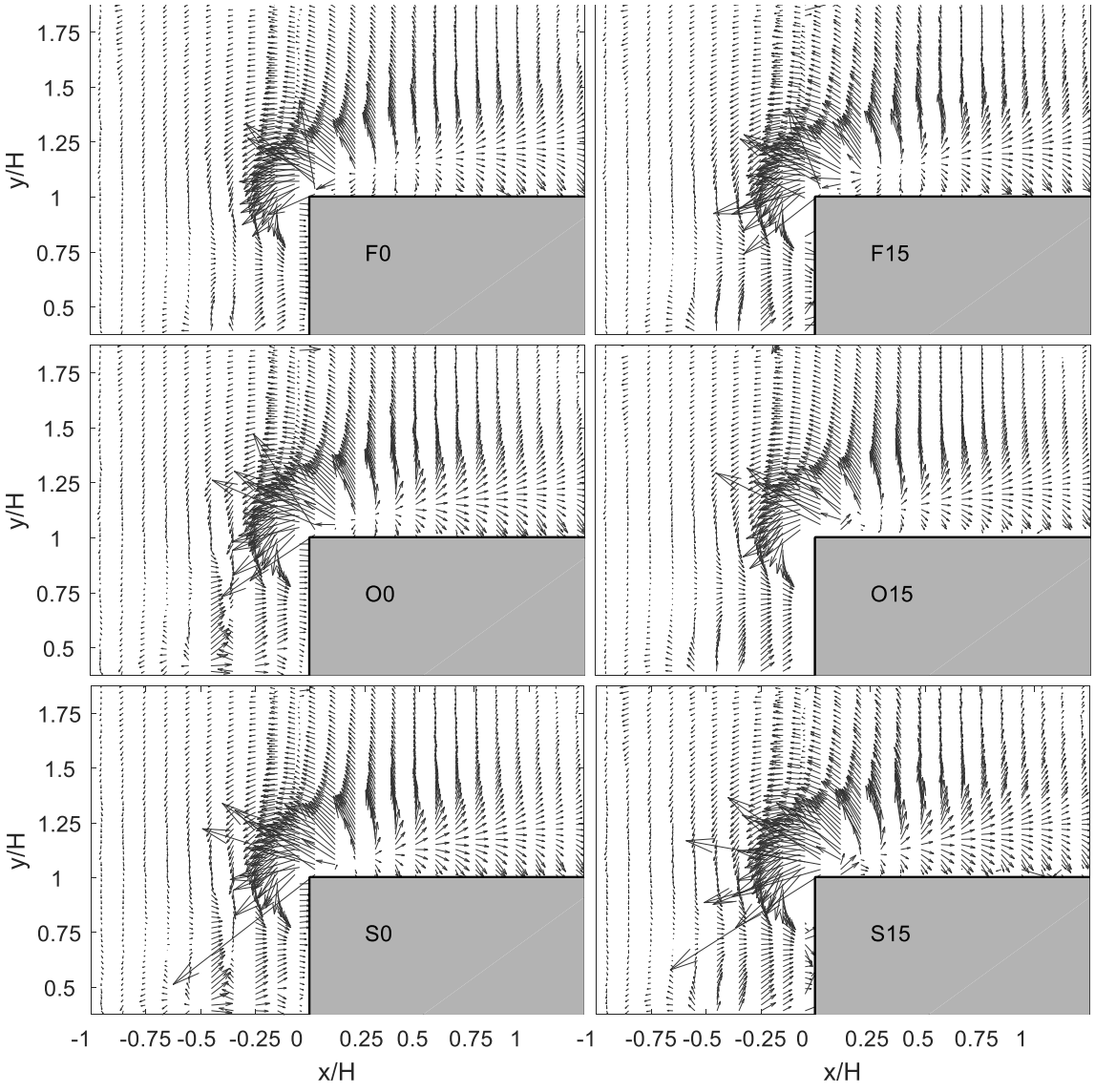

Figure 3-9: Vectors of total gradient $\overline{Cp}$ obtained for the six terrains.

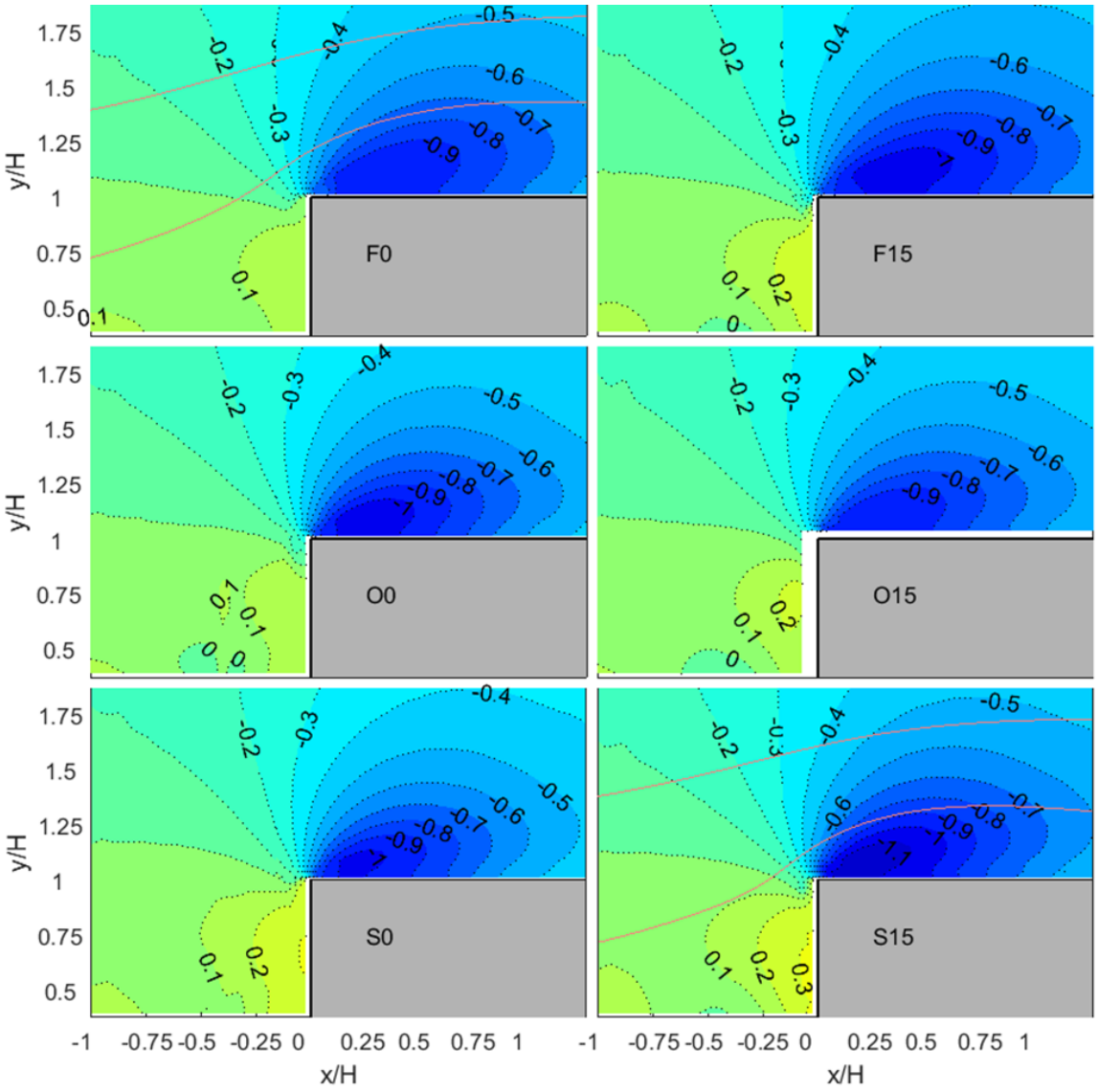

Figure 3-10: The $\overline{Cp}$ field integrated from the gradient data using the analytical interpolation technique for the six terrains.

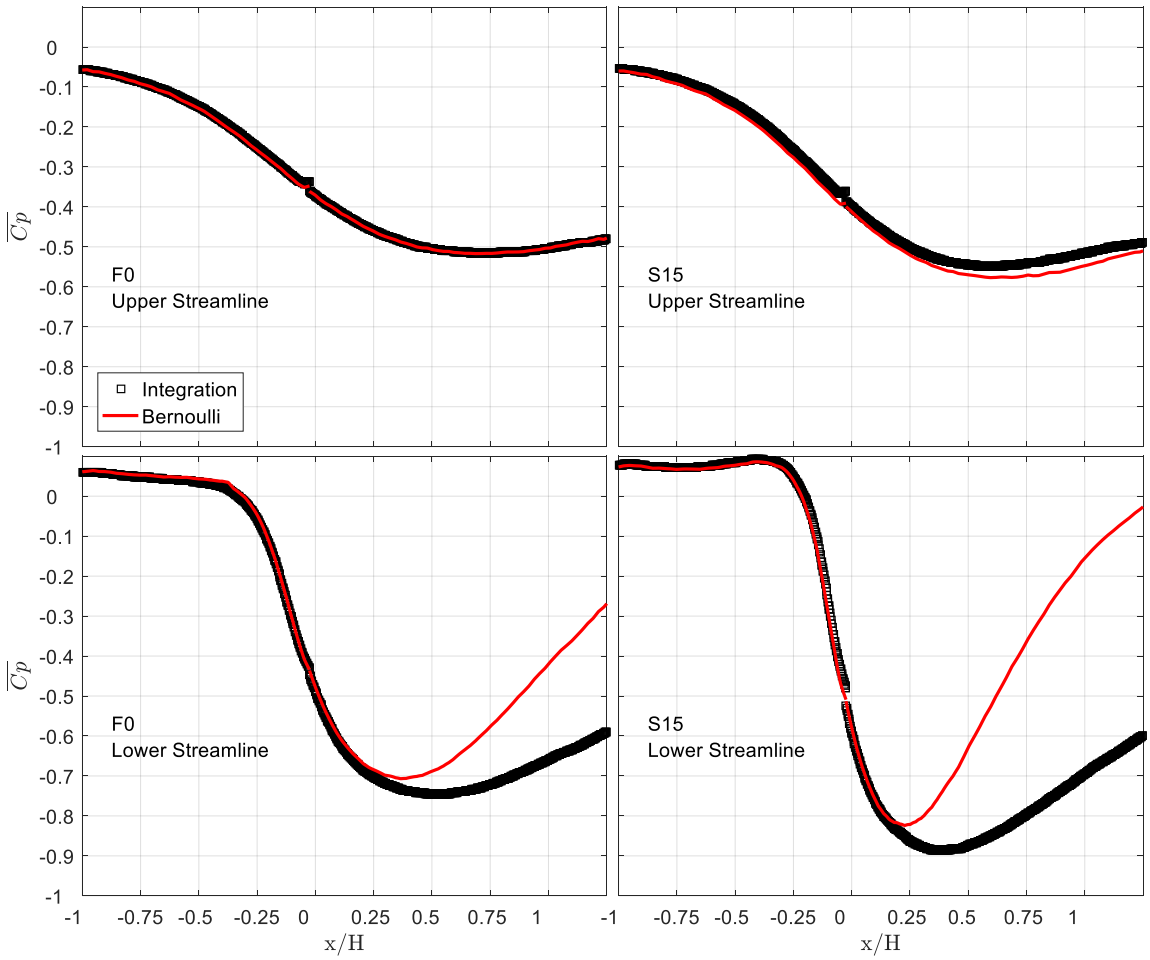

Figure 3-11: $\overline{Cp}$ obtained from the integration technique and Bernoulli's equation along upper and lower streamlines in terrains 'F0' and 'S15'.

3.3.4 Surface pressures

The mean roof surface pressure coefficients measured by Akon and Kopp (2016) are shown in Figure 3-12 for six upstream terrain conditions and compared to the integrated $\overline{Cp}$'s extracted from a horizontal line near the roof height in Figure 3-10. As the upstream turbulence intensity increases, progressive variations of the $\overline{Cp}$ distributions can be observed in the roof surface pressure measurements. For terrains producing lower turbulence intensity, the $\overline{Cp}$ distributions resemble a plateau for the windward portion of the separation bubbles. As the upstream turbulence intensity increases, the plateau reduces to a prominent peak as a result of reduced size of the separation bubble. The minimum $\overline{Cp}$ can also be found to gradually decrease as the upstream turbulence intensity increases (Akon and Kopp, 2016). For example, the $\min\left(\overline{Cp}\right) = -0.9$ is observed for roof height $I_u = 13\%$ (see Figure 1 (b)) while $\min\left(\overline{Cp}\right) = -1.3$ is observed for roof height $I_u = 27\%$. However, as the distance from the leading edge increases, these minimum $\overline{Cp}$'s gradually recover to a common value of $\overline{Cp} = -0.2$. Hence, higher rates of pressure recovery can be found for rougher terrains that produce higher turbulence intensities. Because the $\overline{Cp}$ distributions are strongly dependent on the sizes of the separation bubbles, Akon and Kopp (2016) also examined the universality of the mean pressure distributions by plotting Roshko and Lau's (1965) reduced form of mean pressure coefficients, i.e.,

$$Cp^* = \frac{\overline{Cp} - \min\left(\overline{Cp}\right)}{1 - \min\left(\overline{Cp}\right)}, \tag{3-6}$$

against reduced distance, x/x_r. Here Cp^* denotes the reduced pressure coefficients and x_r denotes the reattachment length. From the results shown in Figure 3-13, Akon and Kopp (2016) found that, although the minimum mean pressures generally locate at $x/x_r = 0.25$ for these six terrains, the distribution of mean pressure coefficients is not self-similar.

The reconstructed field of $\overline{Cp}$'s are extracted from a horizontal line near roof height and compared to the roof surface measurements in Figure 3-12. Good agreements between the results obtained from the Navier-Stokes equations and the roof surface measurement can be observed for terrains 'F0', 'F15' and 'O0'. However, some underestimation of the integrated results can be found near the leading edge for terrains 'O15', 'S0' and 'S15'. These underestimations may be due to some missing details of velocity and turbulence information in this region near the leading edge surfaces (due to the reflections from the laser). Despite this uncertainty, the trend of $\overline{Cp}$ variation observed from surface measurements for the six terrains can also be observed from the integrated results to some extent. As the upstream turbulence intensity increases, the minimum $\overline{Cp}$ obtained from integration also decreases (see Figures 3-10 and 3-12). By reviewing what has been discussed so far, for the gradient fields of the mean pressures, the decreasing minimum mean pressure is due to the increased pressure gradient obtained from both convection (Figure 3-4) and turbulence (Figure 3-8) terms in the Navier-Stokes equations of Eq. (3-1). Higher rates of pressure recovery can be found in the integrated results as well. However, only the turbulence terms governs the pressure recovery for the region just above the roof (see Figure 3-8) and higher turbulence-contributed pressure gradients can be found in this region for rougher terrains that produce higher turbulence intensities. These increased pressure gradients, which lead to both the decreased minimum value and higher recovery rate of mean pressure, can be further linked back to the flow fields. As mentioned earlier, the increased convection-contributed pressure gradient is attributed to the reduced size of separation bubble (Figure 3-4) and more rapid spatial variation of velocity magnitude near the leading edge (Figure 3-3). On the other hand, the increased turbulence-contributed pressure gradients are attributed to the increased spatial variation of $\overline{u'u'}/u_{\text{ref}}^2$ in Figure 3-5 and $\overline{u'w'}/u_{\text{ref}}^2$ in Figure 3-7. The summary of these effects for both the mean velocity and turbulence fields explains the variation of the $\overline{Cp}$ distribution on the roof shown in Figures 3-12 and 3-13. However, the turbulence-induced pressure gradients are not large enough to allow the reduced pressure coefficient distribution to be self-similar (see Figure 3-13). As a result, the reduced pressure coefficient of Eq. (3-6) has a larger magnitude at reattachment for higher turbulence flows.

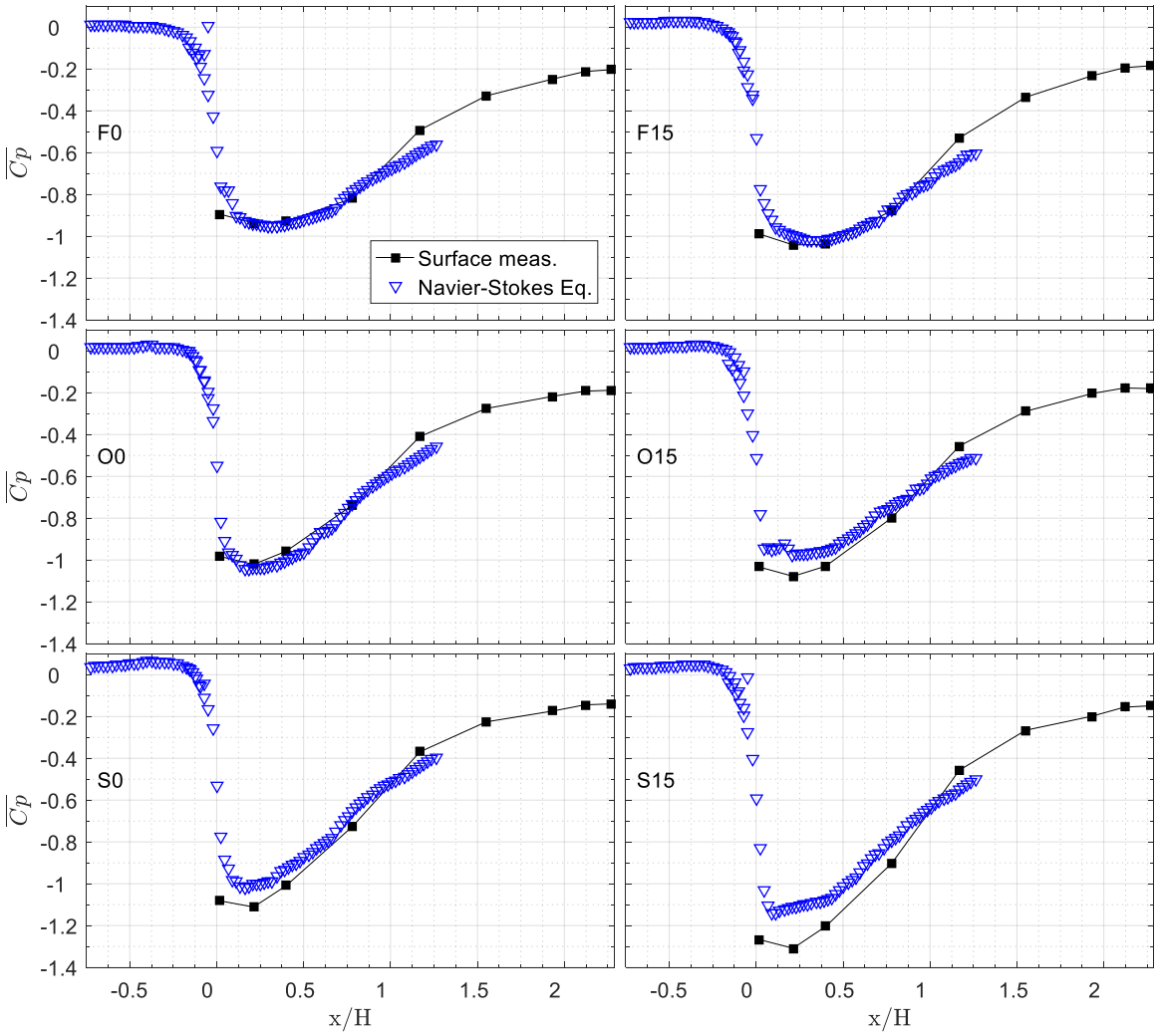

Figure 3-12: Roof surface $\overline{Cp}$ obtained from measurement and integration for the six terrains.

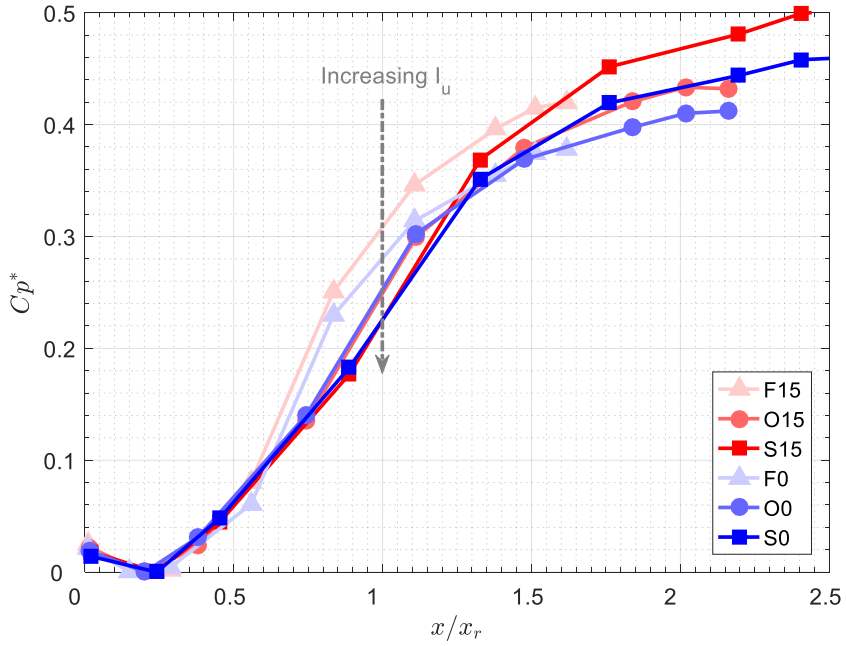

Figure 3-13: Reduced coefficient Cp^* obtained from surface pressure measurements for the six terrains (Akon and Kopp, 2016).

3.4 Summary

The effects of the atmospheric boundary layer (ABL) turbulence intensity and length scales on the mean separated and reattached flow and roof surface pressure were examined by Akon and Kopp (2016). The goal of the current work is to extend the understanding of their observations by further linking the velocity and turbulence fields to the pressure fields. Time-resolved particle image velocimetry (TR-PIV) data were used to measure the flow field near a typical low-rise building, where surface pressure measurements were also synchronized. Experiments were conducted under the six upstream terrain conditions, in which a range of turbulence intensities and length scales were simulated. The main contributions and findings are summarized as follows.

(i) The Navier-Stokes equations are used to determine the gradient vectors of the mean pressure field from the planar PIV data. The convection-contributed pressure gradients are identified by evaluating the terms associated with mean velocities in the Navier-Stokes equations. The turbulence-contributed pressure gradients, on the other

hand, are identified by terms associated with the Reynolds stresses. Effects of upstream turbulence on both of the convection- and turbulence-contributed pressure gradients can, hence, be examined.

(ii) In order to obtain the pressure field from the velocity field, the analytical interpolation technique of Ettl et al. (2008) is applied to integrate the mean pressure gradient. The reconstructed pressure fields match the Bernoulli's equation well along a streamline away from the body and direct pressure measurement on the surface of the body. Hence, the evaluation of pressure gradient using the Navier-Stokes equations and the corresponding pressure integration technique are validated.

(iii) Akon and Kopp (2016) found that the minimum mean roof surface pressure coefficient, $\min\left(\overline{Cp}\right)$, decreases as the upstream turbulence intensity increases. In the current work, these decreasing $\min\left(\overline{Cp}\right)$'s are directly related to both increased convection- and turbulence-contributed pressure gradients over the windward region of the mean separation bubbles.

(iv) As the upstream turbulence intensity increases, a more rapid pressure recovery can be found for the portion of roof surface on the leeward side of the location of $\min\left(\overline{Cp}\right)$. Such increased surface pressure recovery rates are mainly due to the increased turbulence-contributed pressure gradients near the roof surface.

Chapter 4

4 Use of integral momentum equation and quasi-steady theory on evaluation of the area-averaged roof surface pressures

In this chapter, the time-averaged integral momentum equation is used to relate the mean flow and turbulence field above the roof to the mean area-averaged roof surface pressure. The fluctuations of area-averaged roof surface pressures, on the other hand, are related to the instantaneous velocity measurements at a point location above the roof via a simple QS model. The QS model established in this chapter accounts for the magnitudes of the azimuth angles of the wind vectors. Furthermore, the inherent physical assumptions of the QS model is explained via the integral momentum equation.

4.1 Estimation of area-averaged mean pressure using integral momentum

4.1.1 Background

The integral momentum of Eq. (1-3) is now considered for the determination of area-averaged mean roof surface pressure:

$$\begin{aligned}\overline{Cp}_{\text{avg}}\,\mathbf{n}_1\,A &\equiv \iint_{S_1}\overline{Cp}\,\mathbf{n}_1\,ds \\ &= -2\iint_S\left[\left(\frac{\overline{\mathbf{u}}}{u_{\text{ref}}}\right)\cdot\mathbf{n}\right]\left(\frac{\overline{\mathbf{u}}}{u_{\text{ref}}}\right)ds - 2\iint_S\left(\frac{\boldsymbol{\tau}}{u_{\text{ref}}^2}\right)\cdot\mathbf{n}\,ds - \iint_S\overline{Cp}\,\mathbf{n}ds\end{aligned}. \tag{1-3}$$

(Recall that the terms in Eq. (1-3) are defined in Chapter 1). Similar to the differential momentum equation, the first and second term on the right hand side of Eq. (1-3) are associated with the contributions of mean convection and turbulence, respectively. The third term on the right hand side of Eq. (1-3) is associated with the pressure contribution, which is not explicitly shown in differential momentum in Eq. (1-2) because of the definition of control volume here. For the integral momentum approach, the first step is to specify a control volume (CV). Here, the lower boundary surface (i.e., S_1 in Eq. (1-3)) is attached to the roof surface, where the area-averaged mean pressure is to be calculated.

Because the PIV is a planar measurement of wind velocity field, as shown in Figure 2-2 (b), the ideal three-dimensional CV (as denoted by the red dashed lines in Figure 4-1 (a)) is reduced to the two-dimensional area (as denoted by the red solid lines in Figure 4-1(a)) and, hence, the area-averaging of pressure becomes the line-averaging of pressure. On the right hand side of Eq. (1-3), the integrations are conducted for the remaining CV surfaces, S, excluding the bottom face, S_1.

The reduced two-dimensional CV on top of the target roof surface is schematically shown in Figure 4-1 (b). Although the model mimics a gable-roof building, the roof is treated as an uniform horizontal surface in calculation because of its negligible slope. Therefore, the outward normal of the bottom face of CV, i.e. face ① in Figure 4-1 (b), is $\mathbf{n}_1 = -\mathbf{k}$ for Eq. (1-3). Because the bottom CV face ① is assumed to be very close to the roof surface, the velocity and turbulence quantities are assumed to be zero and, hence, only the pressure term is involved in Eq. (1-3) for this face. Note that the resulted force obtained from integrating the mean pressure acting on face ①, as defined by the left hand side of Eq. (1-3), has a direction parallel to the z-axis.

For the CV boundaries normal to the free stream direction, i.e., faces ② and ④ in Figure 4-1 (b), the surfaces are exactly aligned with the z-axis and, hence, their outward normal vectors are parallel to the x-axis. As a result, the pressure along these two vertical boundaries are not involved in calculating the area-averaged pressure on face ① because of the orthogonality. For the top face ③ shown in Figure 4-1 (b), a portion of the streamline is selected as the upper boundary CV face in order to facilitate the calculation. In this manner, there is no mass flux across the upper boundary and, hence, the mean convection term vanishes for this face. This summarizes the terms that need to be considered in the momentum equilibrium of Eq. (1-3) for each of the four CV boundary faces.

a

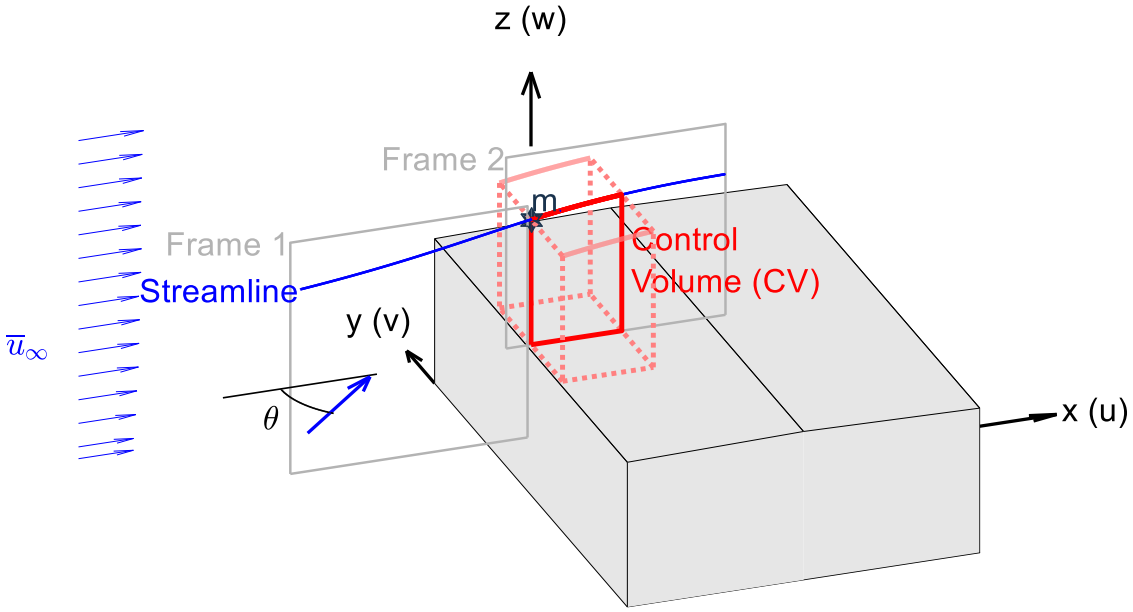

b

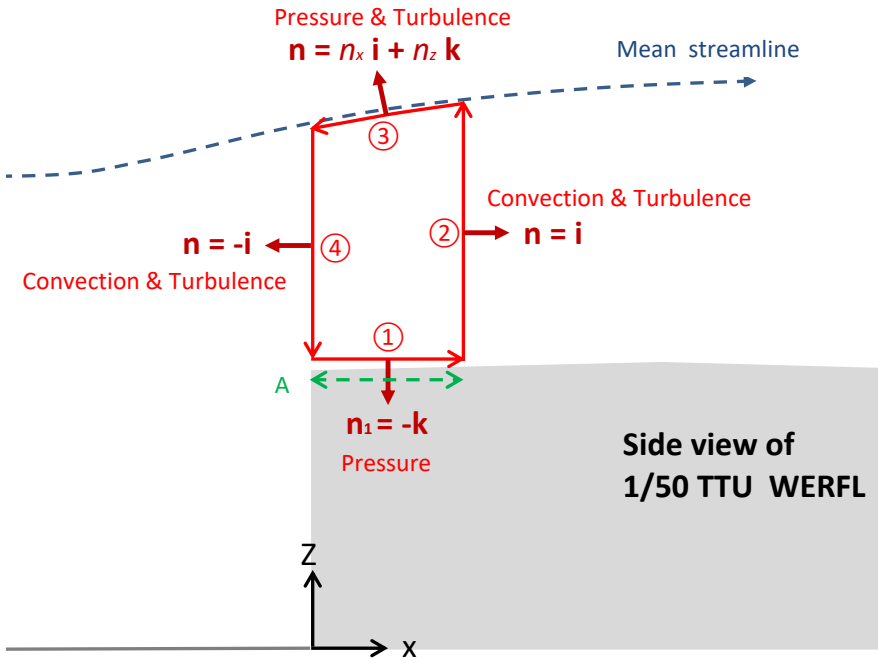

Figure 4-1: (a) Mean flow field around the low-rise building along with planar image frames of PIV measurement and control volume; (b) Reduced 2D control volume on top of the roof surface where line-averaged pressure is calculated.

The integration of Eq. (1-3) can be calculated systematically by starting from the roof leading edge along the bottom CV border, progressing in a counter clockwise manner along the remaining CV boundaries (as indicated by the red arrows in Figure 4-1 (b)). The final form of time averaged momentum equation, as the result of reductions of Eq. (1-3) for the 2D CV shown in Figure 4-1 (b), can be shown as

$$\begin{aligned}
&\overline{Cp}_{\text{avg}}\, A = \\
&2\left(\int_{S_2} \frac{\overline{u}}{u_{\text{ref}}} \frac{\overline{w}}{u_{\text{ref}}} ds - \int_{S_4} \frac{\overline{u}}{u_{\text{ref}}} \frac{\overline{w}}{u_{\text{ref}}} ds \right) \\
&+ 2\left(\int_{S_2} \frac{\overline{u'w'}}{u_{\text{ref}}^2} ds + \int_{S_3} \left(n_x \frac{\overline{u'w'}}{u_{\text{ref}}^2} + n_z \frac{\overline{w'w'}}{u_{\text{ref}}^2} \right) ds - \int_{S_4} \frac{\overline{u'w'}}{u_{\text{ref}}^2} ds \right) \\
&+ \left(\int_{S_3} Cp\, n_z\, ds \right)
\end{aligned} \tag{4-1}$$

Note that the dimension of A is length now for Eq. (4-1), instead of length square for the ideal calculation of Eq. (1-3); The S 's in Eq. (4-1) denote the CV boundary surfaces with subscript indicating the specific face labeled in Figure 4-1 (b), whereas n_x and n_z denote the components of the outward normal unit vector along the *x* and *z* direction, respectively.

The contribution of mean convection and turbulence stresses to the line-averaged mean roof pressure can be directly evaluated from the measured PIV data. The contribution of pressure on the top face of the CV, however, is not explicitly measured. Fortunately Bernoulli equation along a streamline far away from the body can be used to relate the pressure at an upstream location and the pressure above the roof, as shown in Eq. (3-5) and demonstrated in Section 3.3.3. Once the required parameters are obtained along the CV boundaries, multiple area-averaged pressures can be calculated by traversing the CV along the roof surface. The calculated results will be compared in Section 4.1.2 to the surface pressure measurement and the estimations obtained from differential momentum. Another important reason of adding integral momentum approach, in addition to the differential momentum approach, is its explicit relation to the QS theory. In order to

further address this argument, the integral momentum approach of Eq. (1-3) needs to be first validated.

4.1.2 Results and discussion

The integral momentum approach described in Section 4.1.1 is applied to estimate the area-averaged mean roof surface pressure for a mean wind azimuth of 0˚. The control volume (CV) used in the current calculation has a bottom width of $0.25H$ (or 2 cm), as schematically indicated by the 2D solid red box in Figure 4-1. Based on the applicability of Bernoulli's estimation of mean pressure discussed in Section 3.3.3, the main criteria of selecting a streamline as the top CV boundary is to avoid its passage through the region of the high-turbulence-induced pressure gradients. Hence, streamlines far above the separated shear layer would be appropriate for this purpose. Here, we select the streamlines starting from the upstream point near $\{x=-H; z=1.375H\}$, which are consistent with the upper ones labeled 'F0' and 'S15' in Figures 3-8 and 3-10, respectively. The area-averaged mean pressures can be obtained once the information of velocity, pressure and turbulence can be extracted on the CV boundaries. Figure 4-2 shows the integral momentum results at the center of the five non-overlapped segments of CV bottom boundaries for a $1.25H$ (or 10 cm) fetch of roof surface. The measured roof surface $\overline{Cp}$, along with the results integrated from the differential momentum equation (see Figures 3-10 and 3-12), are also attached for comparison in Figure 4-2.

The distribution of $\overline{Cp}_{\text{avg}}$'s estimated from the integral momentum equation are consistent with both the measurements and differential momentum results, as can be observed in Figure 4-2 for terrains 'F0', 'F15' and 'O0'. Hence, the integral momentum approach of Eq. (1-3) is validated, at least for these terrains. However, it is important to note that there is some underestimation of both momentum approaches near leading edge for terrains 'O15', 'S0' and 'S15'. Perhaps, these underestimations are, again, due to the missing details of velocity and turbulence information close to the roof surface. The contributions of convection, pressure, and turbulence to the area-averaged pressure estimated using integral momentum equation are plotted in Figure 4-3 for all six terrain conditions. Generally, the convection term dominates the estimated $\overline{Cp}_{\text{avg}}$'s for areas

near the leading edge, with highest contribution of around 60% of the total. For roof surfaces further downstream, the contribution of the pressure term to the estimated $\overline{Cp}_{avg}$ increased near linearly, being up to 80% for panels $\{H \le x < 1.25H\}$. The contributions of turbulence terms are generally less than 5% and are found to be negative values for most of the locations. Note that these negative contributions of turbulence term are consistent to the pressure recovery observed along the leeward region of the separation bubbles described in the differential momentum approach (i.e., Figure 3-8 and Section 3.3.2).

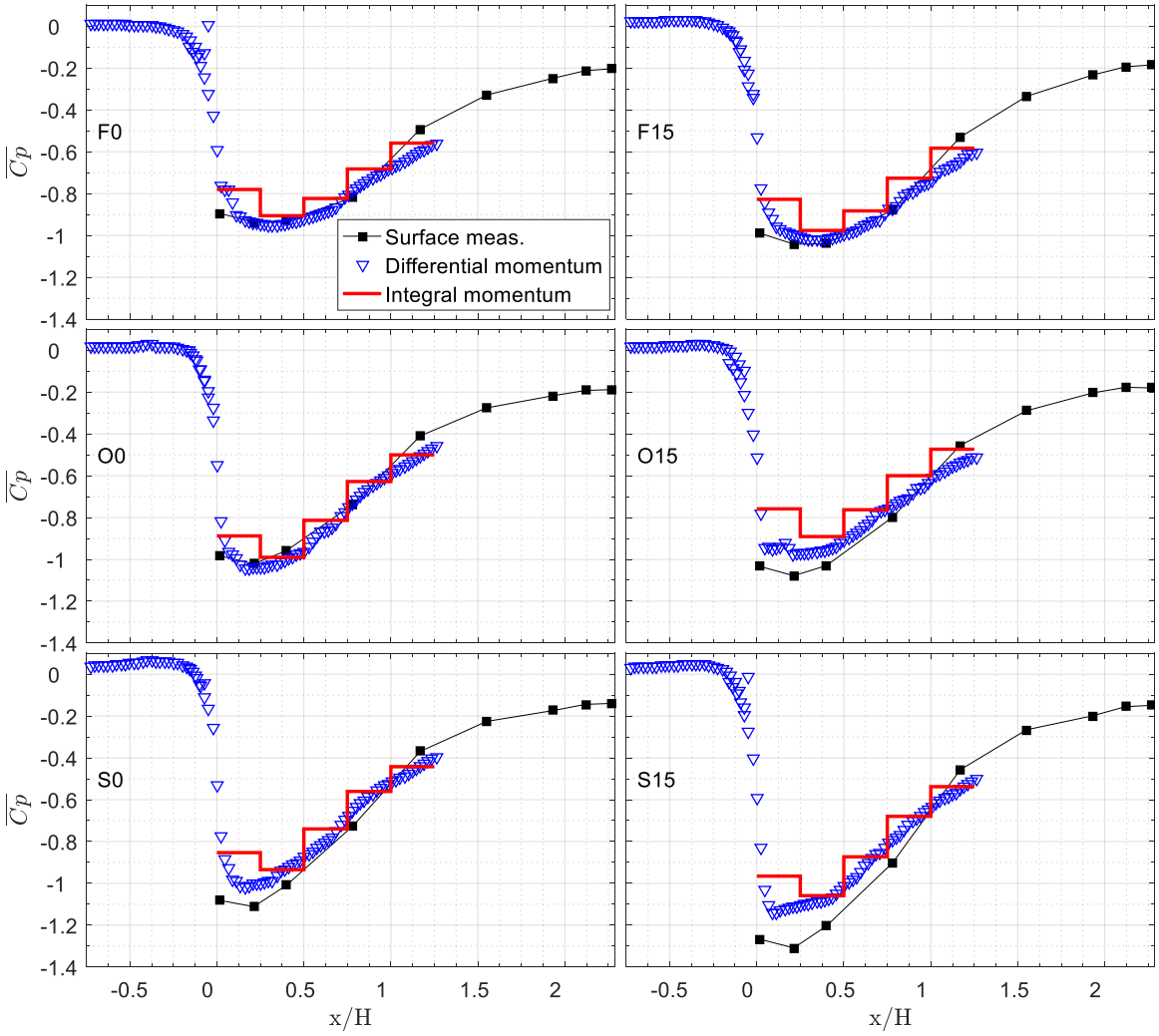

Figure 4-2: Surface pressure measurement and estimations for the six terrains.

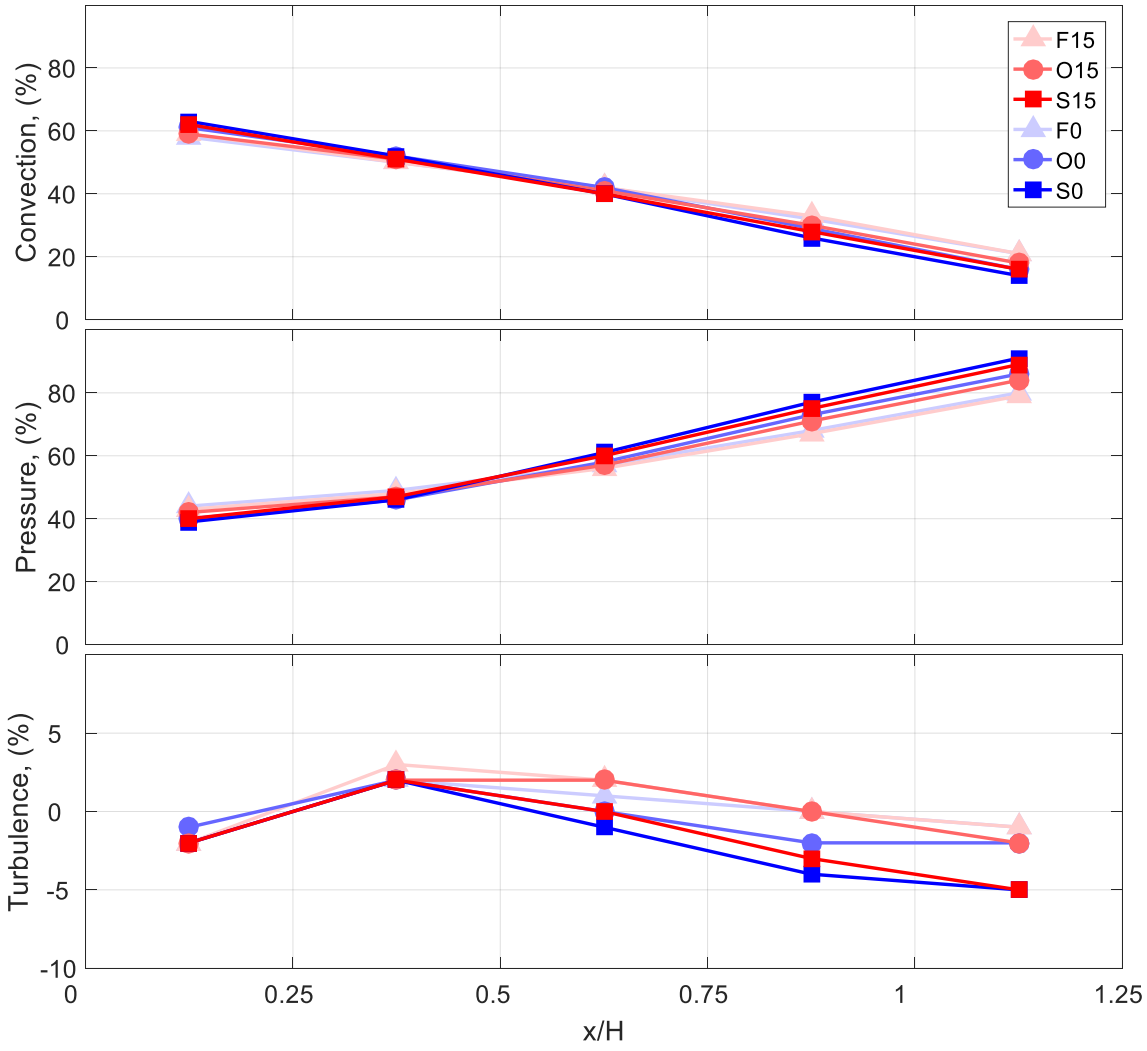

Figure 4-3: Contribution of convection, pressure and turbulence terms in integral momentum equation to the area-averaged mean roof surface pressure.

4.2 A quasi-steady model incorporating magnitude and azimuth angle of instantaneous wind velocity

4.2.1 Background

A relatively simple version of quasi-steady (QS) theory is introduced in this section to incorporate both of the magnitude and azimuth angle of the velocity vectors as variables in the model. By recalling the QS formulation introduced in Eq. (1-4) and Section 1.3, the wind azimuth is treated as an input variable in the instantaneous function, i.e., $Cp_{\text{inst}} = Cp_{\text{inst}}(\theta)$, so that the instantaneous pressures estimated by the QS model become

$$p - p_{\infty} = 0.5\,\rho \left|\mathbf{u}_{\mathrm{m}}\right|^2 Cp_{\mathrm{inst}}(\theta), \tag{4-2a}$$

or alternatively,

$$Cp = \frac{\left|\mathbf{u}_{\mathrm{m}}\right|^2}{u_{\mathrm{ref}}^2} Cp_{\mathrm{inst}}(\theta). \tag{4-2b}$$

A straightforward estimation of the instantaneous function can be obtained by taking the average of Cp_{inst} in Eq. (4-2) under the condition of a specific wind azimuth, i.e.,

$$Cp_{\mathrm{inst}}(\theta) = \langle Cp_{\mathrm{inst}} \,|\, \theta \rangle = \frac{u_{\mathrm{ref}}^2}{\left\langle \left|\mathbf{u}_{\mathrm{m}}\right|^2 \,\middle|\, \theta \right\rangle} \langle Cp \,|\, \theta \rangle = \frac{u_{\mathrm{ref}}^2}{\overline{\left|\mathbf{u}_{\mathrm{m}}\right|^2}} \overline{Cp} \quad \text{evaluated at} \quad \theta = \bar{\theta}\,. \tag{4-3}$$

Here $\left\langle \left|\mathbf{u}_{\mathrm{m}}\right|^2 \,\middle|\, \theta \right\rangle$ and $\langle Cp \,|\, \theta \rangle$ denote the averaged velocity squared and roof surface pressure, respectively, under the condition of specific wind azimuth. Because of the existence of the statistical independence between velocity magnitude and wind azimuth for an ABL turbulent wind, the conditional average of velocity squared, $\left\langle \left|\mathbf{u}_{\mathrm{m}}\right|^2 \,\middle|\, \theta \right\rangle$, can be replaced by the mean value $\overline{\left|\mathbf{u}_{\mathrm{m}}\right|^2}$ obtained from the measurement of the specific mean wind azimuth $\bar{\theta} = \theta$. On the other hand, roof surface Cp's may be statistically dependent on θ. However, the conditional average of roof surface pressure coefficient, $\langle Cp \,|\, \theta \rangle$, is assumed to be equivalent to the mean pressure coefficient, $\overline{Cp}$, obtained from a measurement for the specific mean wind azimuth $\bar{\theta} = \theta$. This assumption is similar to those presented in earlier applications (e.g., Kawai, 1983; Letchford et al., 1993) and is easier for manipulations in later discussions.

By using Eq. (4-3), discrete estimations of the instantaneous function can be obtained for each mean wind azimuth and for each surface pressure tap location. Because of the periodicity of $Cp_{\mathrm{inst}}(\theta)$, the continuous form of the instantaneous function can be conveniently established by fitting the discrete values with a Fourier series (e.g., Richards et al., 1995), i.e.,

$$Cp_{\text{inst}}(\theta) = \sum_{k=0}^{N} a_{1k}\cos(k\theta) + a_{2k}\sin(k\theta), \tag{4-4}$$

where a_{1k} and a_{2k} are the *k*-th order coefficients to be determined while *N* denotes the maximum order being used. Such fitting can be done by minimizing the residual between fitted and measured values while keeping the maximum order *N* as low as possible.

Although it is applicable for pressure estimation at a single tap location, the QS theory has been found to perform better for area-averaged pressures (e.g., Letchford et al., 1993). Therefore, the averaged roof surface pressures over a selected area are chosen for analyses and discussions. Acquiring the instantaneous function for the area-averaged pressure is relatively straightforward. Once the instantaneous function, $Cp_{\text{inst},i}$, is established for each of the individual *i*-th taps within the specified area, the corresponding instantaneous function for an area-averaged pressure, i.e., $Cp_{\text{inst,avg}}$, is simply the weighted average of the individual instantaneous functions, i.e., $Cp_{\text{inst,avg}} = \sum_i Cp_{\text{inst},i}\, A_i/A$, because of the fact that

$$Cp_{\text{avg}} = \sum_i \frac{A_i}{A} Cp_i = \frac{|\mathbf{u}_{\text{m}}|^2}{u_{\text{ref}}^2} \sum_i \frac{A_i}{A} Cp_{\text{inst},i} = \frac{|\mathbf{u}_{\text{m}}|^2}{u_{\text{ref}}^2} Cp_{\text{inst,avg}}, \tag{4-5}$$

where Cp_{avg} denotes the area-averaged pressure coefficient for the total specified area *A* while Cp_i denotes the pressure coefficient at the *i*-th tap location of the tributary area A_i.

4.2.2 The model

Here a portion of roof surface area near the leading edge of the longer wall covering a total of 9 pressure taps is selected for the following analyses regarding the QS theory. Note that the selected roof surface area is covered by the 3D CV, as shown in Figure 4-1 (a). Only the terrain S15 (see Section 2.1) is selected for the following discussions. Because of the symmetrical distribution of the pressure taps, the mean pressures measured at a point on the building within a quadrant of wind directions can be extended

to the full range of wind directions (see Appendix C). These mean pressure coefficients are then used to obtain the discrete estimations of the instantaneous function via Eq. (4-5), which are further fitted using a Fourier series in Eq. (4-4) to generate the continuous form. Note that the mean upstream longitudinal velocity at roof height is used as u_{ref} for defining the pressure coefficients (see Eq. (4-2b)). Figure 4-4 shows both of the discrete estimations and the resulting continuous form of the instantaneous function for the roof surface area. Note that the magnitudes of the Cp_{inst}'s are the largest for wind direction near 0˚ and are reduced for wind directions normal to the shorter walls. It can be also found that the slightly larger magnitudes are skewed to $\theta = 30$ because the selected area is slightly closer to the smaller wall facing the 90˚ azimuth wind.

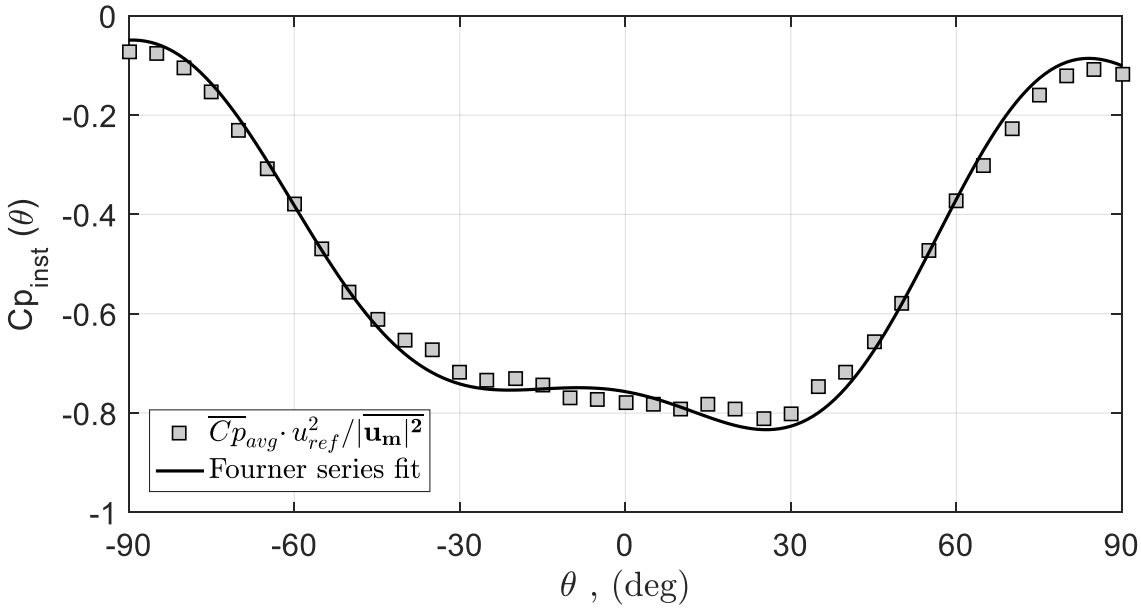

Figure 4-4: Fourier series fit of the instantaneous function for the selected roof surface area in terrain S15.

4.3 Explanation of the physical assumptions in the quasi-steady model with respect to the integral momentum equations

4.3.1 The physical assumptions

As shown in Section 4.2 and Figure 4-4, the QS-estimation of the instantaneous roof surface pressure is essentially done by multiplying the instantaneous dynamic pressure by the mean roof surface pressure coefficient measured at an instantaneous wind azimuth angle, i.e., $\bar{\theta} = \theta$. This statement becomes clear if the instantaneous function in Eq. (4-5) is replaced by the representation of the mean area-averaged pressure coefficient, as shown in Eq. (4-3), i.e., $Cp_{\text{inst,avg}}(\theta) = \overline{Cp}_{\text{avg}}(\bar{\theta} = \theta) \cdot u_{\text{ref}}^2 \Big/ \overline{|\mathbf{u}_{\text{m}}|^2}$, so that the Eq. (4-5) becomes

$$Cp_{\text{avg}}(\theta) = \frac{|\mathbf{u}_{\text{m}}|^2}{u_{\text{ref}}^2}\left(\frac{u_{\text{ref}}^2}{\overline{|\mathbf{u}_{\text{m}}|^2}}\overline{Cp}_{\text{avg}}(\bar{\theta} = \theta)\right) = \frac{|\mathbf{u}_{\text{m}}|^2}{\overline{|\mathbf{u}_{\text{m}}|^2}}\overline{Cp}_{\text{avg}}(\bar{\theta} = \theta). \tag{4-6}$$

In order to understand the inherent physical assumptions in the QS-theory, the mean area-averaged roof surface pressure coefficient, $\overline{Cp}_{\text{avg}}(\bar{\theta} = \theta)$, on the right hand side of Eq. (4-6) are further replaced by the integral momentum estimation shown in Eq. (1-3) so that Eq. (4-5) becomes

$$Cp_{\text{avg}}(\theta = \bar{\theta}) = \left(\frac{|\mathbf{u}_{\text{m}}|^2}{\overline{|\mathbf{u}_{\text{m}}|^2}}\right)\left(\frac{\mathbf{n}_1}{A}\right)\cdot\left[-2\iint_S\left[\left(\frac{\bar{\mathbf{u}}}{u_{\text{ref}}}\right)\cdot\mathbf{n}\right]\left(\frac{\bar{\mathbf{u}}}{u_{\text{ref}}}\right)ds - 2\iint_S\left(\frac{\boldsymbol{\tau}}{u_{\text{ref}}^2}\right)\cdot\mathbf{n}\,ds - \iint_S\overline{Cp}\,\mathbf{n}ds\right]\cdot \tag{4-7}$$

for flow field measured at $\bar{\theta}$

Note that the integral momentum approach in Eq. (4-7) implies placing a 3D CV on top of the selected roof area (see the dashed box in Figure 4-1 (a)) with upper boundary CV face defined by the stream surface (i.e. a collection of the streamlines) passing through the measurement point *m*. The use of this 3D CV is to explain the conceptual ideas for the following discussions instead of direct evaluation of Eq. (4-7). Also recall that the

integral momentum approach used here is already validated in Section 4.1.2 for the 2D flow scenario.

By distributing the instantaneous velocity ratio, $|\mathbf{u}_m|^2 \Big/ \overline{|\mathbf{u}_m|^2}$, into each part of the convection term in Eq. (4-7), i.e.,

$$
\begin{aligned}
&-2\frac{|\mathbf{u}_m|^2}{\overline{|\mathbf{u}_m|^2}}\left(\frac{\mathbf{n}_1}{A}\right)\cdot\iint_S\left[\left(\frac{\bar{\mathbf{u}}}{u_{ref}}\right)\cdot\mathbf{n}\right]\left(\frac{\bar{\mathbf{u}}}{u_{ref}}\right)ds \\
&=-2\left(\frac{\mathbf{n}_1}{A}\right)\cdot\iint_S\left[\left(\frac{|\mathbf{u}_m|}{\sqrt{\overline{|\mathbf{u}_m|^2}}}\frac{\bar{\mathbf{u}}}{u_{ref}}\right)\cdot\mathbf{n}\right]\left(\frac{|\mathbf{u}_m|}{\sqrt{\overline{|\mathbf{u}_m|^2}}}\frac{\bar{\mathbf{u}}}{u_{ref}}\right)ds, \qquad \text{(4-8a)} \\
&\qquad\qquad (\text{for } \bar{\mathbf{u}} \text{ measured at } \bar{\theta})
\end{aligned}
$$

it becomes clear that the QS approach assumes two scenarios for this term:

(i) The direction of the instantaneous flow field is assumed to be the same as the direction of the mean flow field measured at the mean wind azimuth of the same value, i.e., $\bar{\theta} = \theta$. Note that a reference location such as *m* in Figure 4-1 (a) is used to measure the instantaneous wind azimuth, θ.

(ii) The magnitude of the instantaneous velocity is obtained by amplifying the corresponding mean velocity with an uniform rate, $|\mathbf{u}_m| \Big/ \sqrt{\overline{|\mathbf{u}_m|^2}}$, throughout the field. In other words, the gust is uniform and of large size (with respect to the building).

For the pressure term in Eq. (4-7), the goal now is to see if the two assumptions stated for the convection term are further applicable. As discussed in Section 4.1.1, only the pressure on the upper CV boundary face is required for evaluating the area-averaged mean surface pressure of the horizontal roof area (i.e., the bottom face of the 3D CV shown in Figure 4-1 (a)). Recall that the Bernoulli's Eq. (3-5) along streamlines is used for calculating the mean pressure coefficient on the upper CV boundary, i.e.,

$$\overline{Cp}_{\text{CV top}} = \overline{Cp}_{\text{upstream}} + \frac{\left|\overline{\mathbf{u}}_{\text{upstream}}\right|^2}{u_{\text{ref}}^2} - \frac{\left|\overline{\mathbf{u}}_{\text{CV top}}\right|^2}{u_{\text{ref}}^2} \quad (\text{for } \overline{\mathbf{u}} \text{ measured at } \bar{\theta}). \tag{3-5}$$

Hence, by substituting the top CV boundary $\overline{Cp}$ in Eq. (4-7) by the Bernoulli's Eq. (3-5) and assuming ambient upstream pressure, i.e., $\overline{Cp}_{\text{upstream}} = 0$, the pressure contribution in Eq. (4-7) becomes

$$\begin{aligned} &-\left(\frac{\left|\mathbf{u}_{\text{m}}\right|^2}{\left|\overline{\mathbf{u}}_{\text{m}}\right|^2}\right)\left(\frac{\mathbf{n}_1}{A}\right)\cdot \iint_{S_{\text{CV top}}} \overline{Cp}\,\mathbf{n} ds \\ &= -\left(\frac{\mathbf{n}_1}{A}\right)\cdot \iint_{S_{\text{CV top}}} \left[\left(\frac{\left|\mathbf{u}_{\text{m}}\right|}{\sqrt{\left|\overline{\mathbf{u}}_{\text{m}}\right|^2}}\frac{\left|\overline{\mathbf{u}}_{\text{upstream}}\right|}{u_{\text{ref}}}\right)^2 - \left(\frac{\left|\mathbf{u}_{\text{m}}\right|}{\sqrt{\left|\overline{\mathbf{u}}_{\text{m}}\right|^2}}\frac{\left|\overline{\mathbf{u}}_{\text{CV Top}}\right|}{u_{\text{ref}}}\right)^2\right]\mathbf{n}\, ds\,. \end{aligned} \tag{4-8b}$$

(for $\overline{\mathbf{u}}$ measured at $\bar{\theta}$)

As can be clearly seen on the right hand side of Eq. (4-8b), the two physical assumptions of the QS model stated for the convection term are also valid for the pressure term.

Similar QS assumptions can be found for the turbulence contribution by again distributing the velocity ratio in Eq. (4-7) into each component of the turbulence stress tensor, i.e.,

$$\begin{aligned} &-2\left(\frac{\left|\mathbf{u}_{\text{m}}\right|^2}{\left|\overline{\mathbf{u}}_{\text{m}}\right|^2}\right)\left(\frac{\mathbf{n}_1}{A}\right)\cdot \iint_{S}\left(\frac{\boldsymbol{\tau}}{u_{\text{ref}}^2}\right)\cdot\mathbf{n}\, ds \\ &= -2\left(\frac{\mathbf{n}_1}{A}\right)\cdot \iint_{S}\overline{\left(\frac{\left|\mathbf{u}_{\text{m}}\right|}{\sqrt{\left|\overline{\mathbf{u}}_{\text{m}}\right|^2}}\frac{u_i'}{u_{\text{ref}}}\right)\left(\frac{\left|\mathbf{u}_{\text{m}}\right|}{\sqrt{\left|\overline{\mathbf{u}}_{\text{m}}\right|^2}}\frac{u_j'}{u_{\text{ref}}}\right)}\cdot\mathbf{n}\, ds\,. \end{aligned} \tag{4-8c}$$

(For $\overline{u_i'u_j'}$ meausred at $\bar{\theta}$)

Note that because the turbulence contribution may not be as significant as the convection or pressure terms, as already shown in Figure 4-3 for the 2D separated-reattached flow

scenario, the amplification of the turbulence term in QS theory is expected to give relatively minor contribution as well.

In order to illustrate the two physical assumptions of the QS model, imagine two snapshots of the 3D flow fields near the roof are taken at instants t_1 and t_2, in which the instantaneous azimuths of the velocity vector measured at location *m* (Figure 4-1 (a)) are $\theta(t_1) = 0$ and $\theta(t_2) = -30$. For the unknown 3D flow field near the roof, the QS model assumes the instantaneous flow pattern, i.e., the direction of the instantaneous flow field, to be the same as the mean flow pattern so that the mean azimuth at location *m* is equivalent to the instantaneous value. This is the first assumption. Therefore, for time t_1 the instantaneous flow pattern is assumed to be identical to the mean separated-reattached type of flow, as that measured at $\bar{\theta} = \theta(t_1) = 0$ (see Figure 4-5 (a)). Similarly, the instantaneous flow at time t_2 is assumed to be the mean conical-vortex type of pattern, exactly the same as that measured at $\bar{\theta} = \theta(t_2) = -30$ (see Figure 4-5 (b)).

Although the instantaneous flow direction is assumed to be identical to the mean, it is not necessarily the case for the instantaneous magnitude of the velocities. In the QS model, the instantaneous magnitudes of the velocities are assumed to be the amplified version of the mean velocity magnitude with a uniform rate determined by the instantaneous velocity ratio measured at location *m*, i.e., $|\mathbf{u}_m| \Big/ \sqrt{\overline{|\mathbf{u}_m|^2}}$. Hence, for time t_1 the instantaneous flow field is assumed to be the same as the mean separated-reattached flow shown in Figure 4-5 (a) but with mean velocity magnitudes amplified by a uniform rate, $|\mathbf{u}_m(t_1)| \Big/ \sqrt{\overline{|\mathbf{u}_m|^2}}$; Similarly, the velocity magnitudes of mean conical-vortex flow shown in Figure 4-5 (b) are amplified by a rate of $|\mathbf{u}_m(t_2)| \Big/ \sqrt{\overline{|\mathbf{u}_m|^2}}$ for constructing the instantaneous flow field at time t_2 .

a

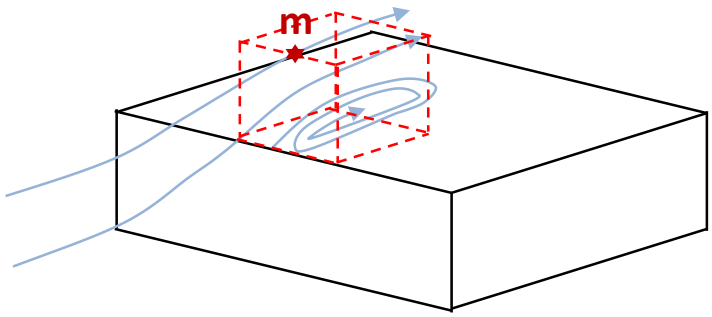

b

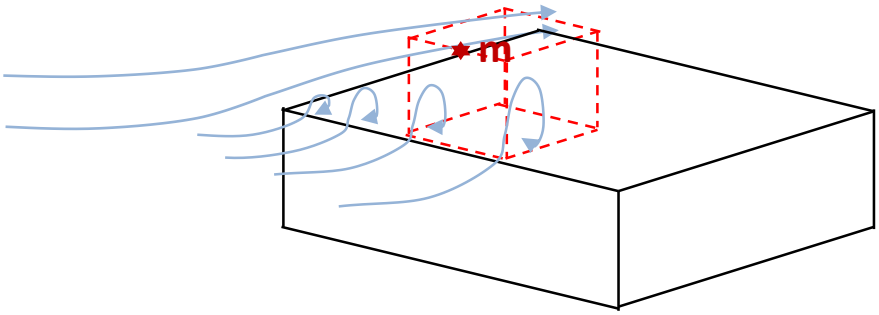

Figure 4-5: Schematic control volume and mean streamlines on top of the roof for mean wind azimuths: (a) $\bar{\theta} = 0$ **and (b)** $\bar{\theta} = -30$ **.**

4.3.2 Missing physical mechanism in the QS model

Since the QS model is usually established on the velocity measurements at a point such as *m* in Figure 4-1 (a), it is impossible to accurately capture the detailed volumetric flow field required for direct evaluation of instantaneous momentum equation. However, missing physical considerations, may be identified by comparing the QS assumptions of Eq. (4-6) to the exact instantaneous integral momentum equation:

$$Cp_{\text{avg}} = \left(\frac{\mathbf{n}_1}{A}\right)\cdot\left[-\frac{2}{u_{\text{ref}}}\underset{\text{CV}}{\iiint}\frac{\partial}{\partial t}\left(\frac{\mathbf{u}}{u_{\text{ref}}}\right)dV - 2\underset{S}{\iint}\left[\left(\frac{\mathbf{u}}{u_{\text{ref}}}\right)\cdot\mathbf{n}\right]\left(\frac{\mathbf{u}}{u_{\text{ref}}}\right)ds - \underset{S}{\iint}Cp\,\mathbf{n}ds\right]. \qquad (4\text{-}9)$$

Acceleration term; Convection (& Turbulence) term; Pressure term

In order to make the QS assumptions for the convection and pressure terms as close as possible to the real scenarios of an instantaneous flow field, local deviations of the instantaneous flow pattern from the mean flow pattern needs to be minimized and the amplification rate, $|\mathbf{u}_{\text{m}}|\Big/\sqrt{\overline{|\mathbf{u}_{\text{m}}|^2}}$, measured at location *m* needs to be representative for the region near the roof. This requirement may be better achieved if the QS model is applied in the ABL flow of large turbulence length scale, e.g., the upstream flow cases generated with 15" barrier (see Figure 2-1 (c)).

For point velocities measured using an instrument like a Cobra probe (TFI Inc.), the instantaneous static pressure can be directly measured at point *m*. This information may be used to approximate the instantaneous upper CV boundary pressure instead of using the QS assumption in Eq. (4-7). In order to apply such a correction, the QS assumption on the pressure contribution is re-written using the mean static pressure coefficient measured at point *m*, $\overline{Cp}_{\text{m}}$, i.e.,

$$-\left(\frac{|\mathbf{u}_{\text{m}}|^2}{\overline{|\mathbf{u}_{\text{m}}|^2}}\right)\left(\frac{\mathbf{n}_1}{A}\right)\cdot\underset{S_{\text{CV top}}}{\iint}\overline{Cp}\,\mathbf{n}ds \approx \left(\frac{|\mathbf{u}_{\text{m}}|^2}{\overline{|\mathbf{u}_{\text{m}}|^2}}\right)\overline{Cp}_{\text{m}} \quad (\text{for } \bar{\mathbf{u}} \text{ and } \overline{Cp}_{\text{m}} \text{ measured at } \bar{\theta}). \qquad (4\text{-}10)$$

Then, the correction is done by removing the QS assumption in the pressure term represented in Eq. (4-10) and compensating with the instantaneous static pressure coefficient measured at point *m*, Cp_{m}. In this manner, a 'static pressure corrected' QS model can be derived from the original one in Eq. (4-5), i.e.,

$$Cp_{\text{avg}}(\theta) = \frac{|\mathbf{u}_{\text{m}}|^2}{u_{\text{ref}}^2}Cp_{\text{inst,avg}}(\theta) - \left(\frac{|\mathbf{u}_{\text{m}}|^2}{\overline{|\mathbf{u}_{\text{m}}|^2}}\right)\overline{Cp}_{\text{m}}(\bar{\theta}=\theta) + Cp_{\text{m}}. \qquad (4\text{-}11)$$

The missing flow acceleration term in the QS model can also be identified by comparing Eq. (4-7) to Eq. (4-9). Note that because the acceleration contribution is a volume integral (over the entire CV), the coherence of the flow structure needs to be high so that the flow acceleration measured at point *m*, $\partial \mathbf{u}_{\mathrm{m}}/\partial t$, can be used to represent the overall flow acceleration within the CV. Furthermore, because of the roof surface is horizontal (see Figure 4-1), only the acceleration of vertical velocity component plays a role. Hence, by adding the acceleration term to the static pressure corrected QS model of Eq. (4-10), the modified version becomes

$$Cp_{\mathrm{avg}}(\theta) = \underbrace{\frac{|\mathbf{u}_{\mathrm{m}}|^2}{u_{\mathrm{ref}}^2} Cp_{\mathrm{inst,avg}}(\theta)}_{\text{Basic QS model}} - \underbrace{\left(\frac{|\mathbf{u}_{\mathrm{m}}|^2}{\overline{|\mathbf{u}_{\mathrm{m}}|^2}}\right)\overline{Cp}_{\mathrm{m}}(\bar{\theta}) + Cp_{\mathrm{m}}}_{\text{Static pressure correction}} + \underbrace{\left(\frac{2}{u_{\mathrm{ref}}}\right)\left(\frac{\Delta \mathrm{V}_{\mathrm{CV}}}{A}\right)\frac{\partial}{\partial t}\left(\frac{w_{\mathrm{m}}}{u_{\mathrm{ref}}}\right)}_{\text{Vertical velocity acceleration}}, \qquad (4\text{-}12)$$

where the last term on the right hand side adds the contribution of vertical velocity acceleration measured at point *m* and $\Delta \mathrm{V}_{\mathrm{CV}}$ denotes the volume of the CV.

4.3.3 Application of the QS models

In this section the use of QS-model (denoted as 'QS-Θ') established in Section 4.2.2 (see also Figure 4-4 and Eq. (4-5)) for prediction of roof surface pressure fluctuation is demonstrated for the ABL turbulent flow generated by the S15 terrain condition (see Figure 2-1). The ideas of static pressure corrected QS model of Eq. (4-11) (denoted as 'QS-Θ-*p*') and further acceleration corrected version of Eq. (4-12) (denoted as 'QS-Θ-*p*-*a*') are also included for the discussion. The comparison is done for measurements of mean wind azimuths $\bar{\theta}$ = 0˚, 30˚, 60˚ and 90˚. The estimated time series of instantaneous Cp_{avg}'s are compared to the measurements via the spectra ratio, coherence and probability density function (PDF). The spectra ratio is used to compare the magnitudes of the predicted and measured fluctuations of Cp_{avg} in frequency domain and

is defined as the ratio of the spectra of the QS-estimated Cp_{avg}, $S_{CpQS}(f)$, to the spectra of measured Cp_{avg}, $S_{\text{CpM}}(f)$, at frequency f, i.e.,

$$\text{Spectra ratio} = \frac{S_{\text{CpQS}}(f)}{S_{\text{CpM}}(f)}. \tag{4-13}$$

On the other hand, the coherence is used to evaluate the correlation between the predicted and measured Cp_{avg} in the frequency domain and is defined as the real part of the normalized cross spectra between QS-estimation and measurement, i.e.,

$$\text{Coherence} = \frac{\text{Re}\left[S_{\text{CpQS,CpM}}(f)\right]}{\sqrt{S_{\text{CpQS}}(f)}\sqrt{S_{\text{CpM}}(f)}}, \tag{4-14}$$

where $\text{Re}\left[S_{\text{CpQS, CpM}}(f)\right]$ is the real part of cross spectra between QS-estimation and measurement.

For mean wind azimuths of 0˚ and 30˚, near unity spectra ratio and high coherence (between 0.8 and 0.9) can be found respectively in Figures 4-6 and 4-7 for the large length scale fluctuations i.e., $\bar{u}_{\text{ref}} / f \geq 13H$. This validates the QS-$\Theta$ estimation of fluctuating Cp_{avg} due to large length scale turbulence, i.e., $\bar{u}_{\text{ref}} / f \geq 13H$. On the other hand, some under- and over-estimated spectra ratios (Figure 4-5), and near zero coherence (Figure 4-6), indicate poor QS-Θ-predicted fluctuating Cp_{avg} due to the small length scale turbulence, i.e., $\bar{u}_{\text{ref}} / f < 13H$. However, because the spectra of Cp_{avg} is relatively small for the small length scale fluctuations and is monotonically decreasing as the length scale reduces, the overall effect of the small length scale fluctuations is limited such that the overall QS-Θ -estimated PDF's of Cp_{avg} shown in Figure 4-8 match well to the measurements (for $\bar{\theta}$ = 0˚ and 30˚). For mean wind azimuth of $\bar{\theta} = 60$, both of the spectra ratio and coherence are slightly reduced for large length scale ($\bar{u}_{\text{ref}} / f \geq 13H$) as compared to cases of $\bar{\theta}$ = 0˚ and 30˚, while the conclusions of QS-Θ-estimation on small length scale ($\bar{u}_{\text{ref}} / f < 13H$) remains the same. A slightly underestimated Cp_{avg} obtained

from QS-Θ model can be found in the tail regions of PDF in Figure 4-7 for $\bar{\theta} = 60^{\circ}$. As the mean wind azimuth approaches to 90˚, both of the spectra ratio and coherence are further reduced for large length scale fluctuations. A significant reduction of the spectra ratio (to around 0.3) for the large length scale fluctuations leads to the apparent underestimation of QS-Θ model near the tail region of the PDF.

By adding the instantaneous correction of the static pressure to the original QS-Θ model of Eq. (4-5), the application of QS-Θ-p model in Eq. (4-11) is also included for comparison in Figures 4-6, 4-7 and 4-8. For mean wind azimuths of 0˚ and 30˚, observations from Figures 4-6 to 4-8 show that the performances of QS-Θ-p model are near equivalent to QS-Θ model. Improved performance of using QS-Θ-p model starts to appear for the case of $\bar{\theta} = 60^{\circ}$, as slightly better matches of spectra ratio and PDF tail values can be observed. The most apparent improvement for using QS-Θ-p model can be observed for mean wind azimuth of 90˚. In this case, the spectra ratio is near unity and good matches of PDF tail values can be observed for the QS-Θ-p model. Significant improvement of the coherence for using QS-Θ-p model can also be observed for the middle range of Cp_{avg} fluctuation, i.e., $2H \le \bar{u}_{\text{ref}} / f < 13H$. Apparent improvement of QS-Θ-p prediction may be expected for the re-attached flow region (i.e., the selected roof surface area for $\bar{\theta} = 90$) because the roof surface Cp_{avg} is more significantly controlled by the static pressure on the upper CV boundary in this situation, as can be seen in Figure 4-3.

The further correction of the QS-Θ-p model by adding the acceleration of vertical velocity does not improve the prediction performance for all analyzed cases. Direct use of vertical acceleration measured at point *m*, i.e., $\partial w_{\text{m}} / \partial t$ in Eq. (4-12), leads to unreasonably large overestimation of small length scale Cp_{avg} fluctuation. This poor estimation implies low spatial coherence of vertical velocity field within the CV. However because it is impossible to fully resolve the spatial coherence of velocity field using a point velocity instrument, the vertical acceleration corrected QS model of Eq. (4-11) is not practical for our current applications.

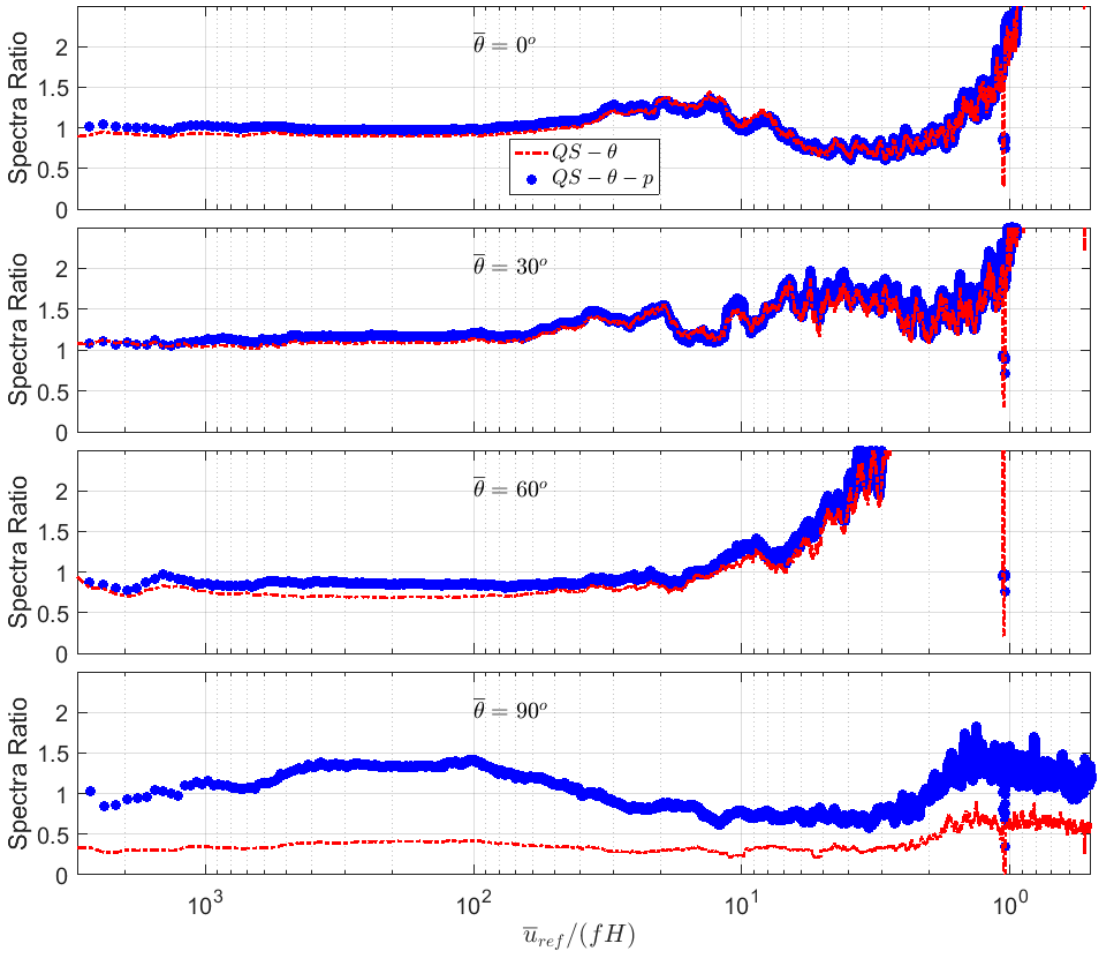

Figure 4-6: The ratio of QS-estimated spectra to measured spectra of Cp_{avg} for various mean wind azimuths in terrain S15.

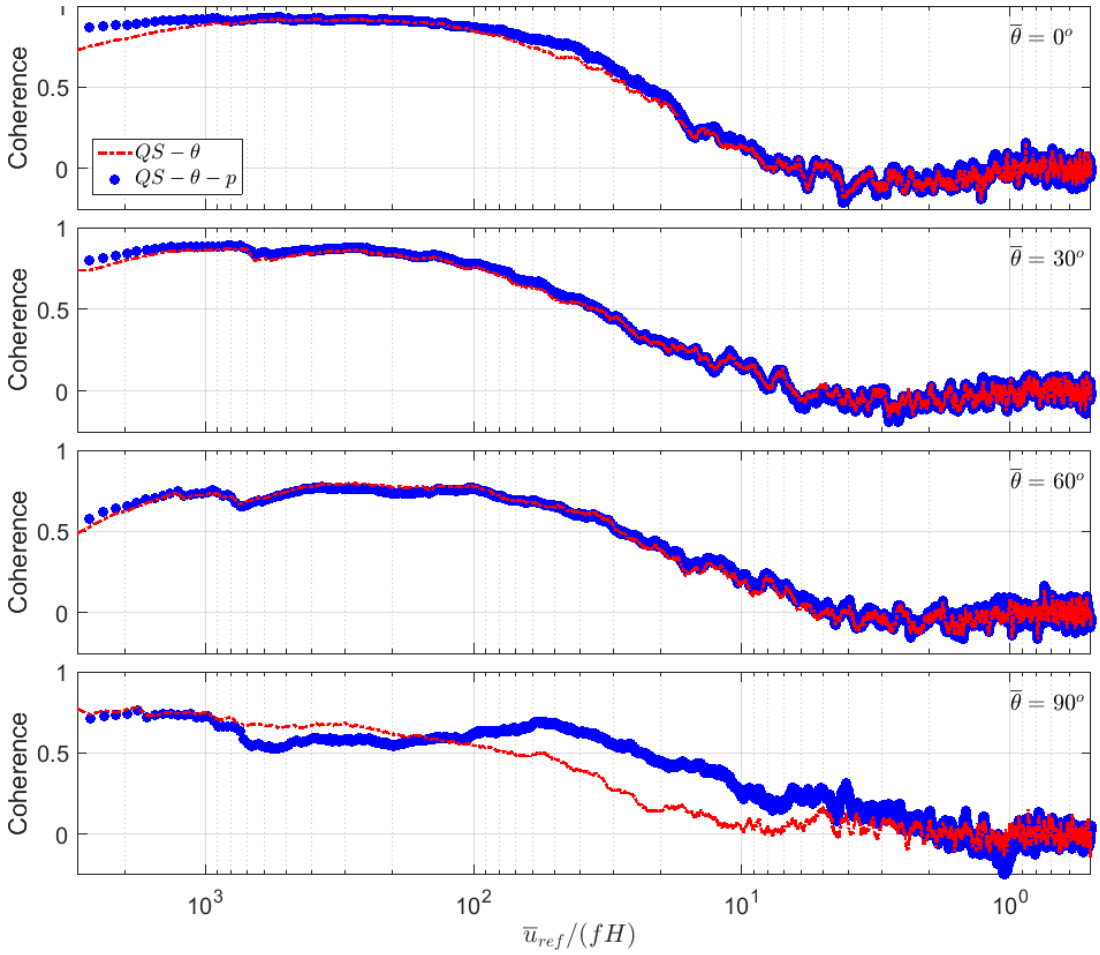

Figure 4-7: The coherence between QS-estimated and measured Cp_{avg} for various mean wind azimuths in terrain S15.

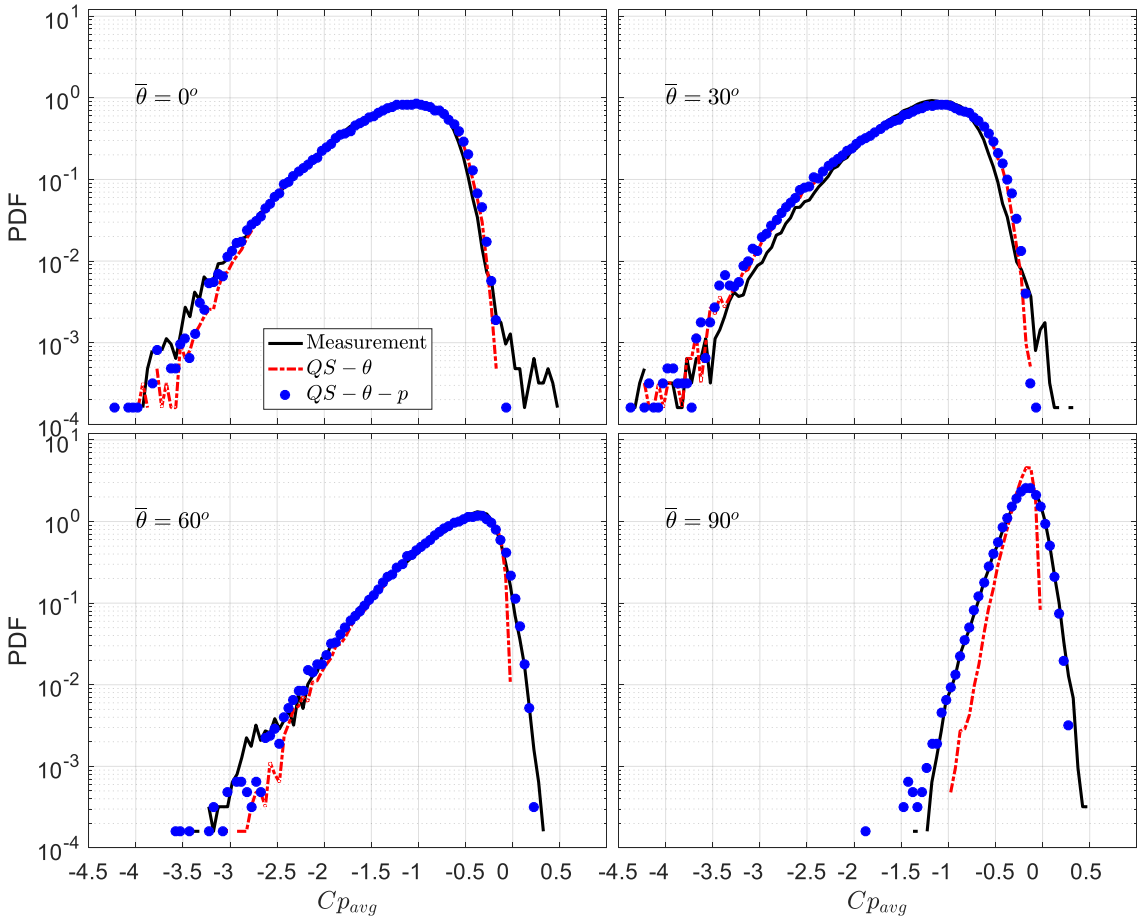

Figure 4-8: Probability density function (PDF) of QS-estimated and measured Cp_{avg} for various mean wind azimuths in terrain S15.

4.4 Summary

In this chapter, the effects of the upstream turbulence on the area-averaged mean and fluctuating pressures are investigated. The time-averaged integral momentum equations are used to relate the near-roof flow fields to the mean area-averaged pressures. On the other hand, a simple quasi-steady model is established for estimating pressure fluctuations. The main goal of this chapter is to derive the physical assumptions embedded in the QS model and investigate possible corrections based on these observations. The main findings are summarized as follows:

- A time-averaged integral momentum approach is proposed to relate the mean flow and turbulence fields to the mean area-averaged roof surface pressures. This is done by placing a control volume (CV) directly above the target roof panel, where the mean area-averaged pressure needs to be calculated. This approach is validated by good agreements between the estimations and measured values (with maximum underestimation of 15%).
- From the time-averaged perspective, the convection term (i.e., the net momentum flux through the CV) dominates the area-averaged pressures for panels beneath the separated flows. For panels under the reattached flows, the static pressure just above the roof dominates the mean surface pressures. The effects of turbulence stresses seem to be relatively minor.
- A simple QS model is established to estimate the instantaneous area-averaged roof surface pressures. This model accounts for the variation of magnitudes and azimuth angles of the instantaneous wind speed measured at the reference location, i.e., one building height above the leading edge. Satisfactory performance of the typical QS model is found for region under flow separation.
- The physical assumptions embedded in the QS model are explained from simple algebraic manipulation of the time-averaged integral momentum equation. Two main finding are revealed:
    - The direction of the instantaneous flow field is assumed to be the same as the direction of the mean flow field. This statements holds when the instantaneous wind azimuth measured at the reference point is equivalent to the mean wind azimuth.
    - The magnitude of the instantaneous velocity field is obtained by amplifying the mean velocity field with an uniform rate, $\left|\mathbf{u}_{\mathrm{m}}\right| \Big/ \sqrt{\overline{\left|\mathbf{u}_{\mathrm{m}}\right|^2}}$, where $\mathbf{u}_{\mathrm{m}}$ is the velocity vector measured at the reference location.
- By further comparing the QS assumptions to the instantaneous integral momentum equation, the missing mechanisms of the QS-model can be elucidated:

- The best scenario for the QS assumption to be true is that the instantaneous flow pattern near the roof exactly matches the mean flow pattern. This ideal scenario may be better approximated if the gusts have a very large scale.

- By using a point velocity measurement, like a Cobra probe, the instantaneous static pressure can be directly measured. Such information may be used to correct the QS assumptions associated with the static pressure above the roof. The pressure-corrected QS model is found to work better for the region of flow re-attachment. However for a roof region under flow separation, little improvement can be found by using the pressure-corrected QS model. This is due to the fact that the static pressure on top of the roof dominates the roof surface pressure for the flow following the re-attachment point, while momentum flux contributes more for the flow separation region.

- A missing acceleration term of vertical velocity is identified in the QS assumption. However, due to little spatial coherence of vertical velocities within the control volume (CV) on top of the roof, the use of the vertical velocity acceleration measured at the reference point overestimated the overall acceleration within the CV. Therefore, adding the acceleration correction to the QS model via a point velocity measurement is not suggested for the practice.

Chapter 5

5 Estimation of instantaneous roof surface pressures using quasi steady model and three-dimensional wind velocity vectors

In this chapter, a quasi-steady (QS) model including the three-dimensionality of the wind speed vector is constructed and validated for the terrain condition S15. The statistical version of the QS model is also introduced in order to calculate the roof pressure statistics based on a given set of turbulence statistics.

5.1 Model construction

For regions of building surfaces where the wind azimuth is the only significant variable for the instantaneous function, $Cp_{\text{inst}}(\theta,\beta)$ can be reduced to $Cp_{\text{inst}}(\theta)$. This means that the estimation of $Cp_{\text{inst}}(\theta)$ is obtained from $Cp_{\text{inst}}(\theta,\langle\beta|\theta\rangle)$, based on the definition given in Eq. (1-7),

$$Cp_{\text{inst}}(\theta,\beta)=\langle Cp_{\text{inst}}|\theta,\beta\rangle, \tag{1-7}$$

where $\langle\beta|\theta\rangle$ denotes the averaged value of β for the given wind azimuth condition, θ. Richards et al. (1995) proposed a method for estimating $Cp_{\text{inst}}(\theta)$ from the mean pressure coefficients. They first assumed that the building surface pressures respond to the incident wind in a way that exactly follows the QS assumption, such that the measured $\langle Cp_{\text{inst}}|\theta\rangle$ are assumed to fall on the predefined $Cp_{\text{inst}}(\theta)$ curve. Based on this assumption, the mean instantaneous function obtained from the measurements of each mean azimuth, $\bar{\theta}$, can be represented as

$$\overline{Cp_{\text{inst}}}(\bar{\theta})=\int_{\theta=-180^{\circ}}^{180^{\circ}} Cp_{\text{inst}}(\theta)f(\theta-\bar{\theta})d\theta, \tag{5-1}$$

where $f(\theta)$ is the probability density function (PDF) of the wind azimuth.

Based on Eq. (1-4a), i.e.,

$$p - p_\infty = 0.5\,\rho\left|\mathbf{u}_\mathrm{m}\right|^2 Cp_\mathrm{inst}\,, \tag{1-4a}$$

the $\overline{Cp_\mathrm{inst}}\left(\bar{\theta}\right)$ on the left-hand side of Eq. (5-1) can be represented as $\left(\bar{p} - \bar{p}_\infty\right)\Big/\left(0.5\rho\left|\mathbf{u}_\mathrm{m}\right|^2\right)$, a quantity that is equivalent to $\overline{Cp}\cdot u_\mathrm{ref}^2\Big/\overline{\left|\mathbf{u}_\mathrm{m}\right|^2}$, based on Eq. (1-4b), i.e.,

$$Cp = \frac{\left|\mathbf{u}_\mathrm{m}\right|^2}{u_\mathrm{ref}^2} Cp_\mathrm{inst}\,, \tag{1-4b}$$

which is relatively easy to obtain from wind tunnel measurements of each $\bar{\theta}$. A least-squares method can be used to fit the measured the discrete $\overline{Cp_\mathrm{inst}}\left(\bar{\theta}\right)$ data with a Fourier series. Richards et al. (1995) suggested that the fitting should minimize the error and the order of Fourier coefficients being used. Once the fitting is done, finer resolution of $\overline{Cp_\mathrm{inst}}\left(\bar{\theta}\right)$ data points can be generated between the measured $\bar{\theta}$ values, and the $Cp_\mathrm{inst}\left(\theta\right)$ on the right-hand side of Eq. (5-1) can be solved by applying the iterative method suggested by Banks and Meroney (2001). For the iterative method, the $Cp_\mathrm{inst}\left(\theta\right)$ are first assumed to be equal to $\overline{Cp_\mathrm{inst}}\left(\bar{\theta}\right)$, then the left-hand side of Eq. (5-1) is updated. The residual, ε, obtained by subtracting the updated value from the original value of $\overline{Cp_\mathrm{inst}}\left(\bar{\theta}\right)$, can be calculated. The solution is then updated by replacing $Cp_\mathrm{inst}\left(\theta\right)$ with $Cp_\mathrm{inst}^\mathrm{old}\left(\theta\right) + 0.5\varepsilon$ for the next iteration. The procedure is repeated until $\left|\varepsilon\right|$ is minimized. The final set of $Cp_\mathrm{inst}\left(\theta\right)$ is, again, obtained by the Fourier series of order N_1,

$$Cp_\mathrm{inst}\left(\theta\right) = \sum_{k=0}^{N_1} a_{1k}\cos\left(k\theta\right) + a_{2k}\sin\left(k\theta\right) \tag{5-2}$$

where a_{1k} and a_{2k} are the appropriate Fourier coefficients.

The wind elevation angle has been found to affect the variation of the instantaneous functions Cp_{inst} for regions on the roof (Letchford and Marwood, 1997; Sharma and Richards, 1999; Wu et al., 2001; Richards and Hoxey, 2004). If a specific value of θ is selected and, thus, $\langle \beta | \theta \rangle$ is fixed and denoted as $\overline{\beta}$, the variation of Cp_{inst} due to changing β has been found to be approximately linear (for the atmosphere boundary layers) by various researchers (Letchford and Marwood, 1997; Sharma and Richards, 1999; Richards and Hoxey, 2004). Therefore, it can be written as

$$Cp_{\text{inst}}(\theta,\beta) = Cp_{\text{inst}}(\theta,\overline{\beta}) + B(\theta)\beta' \tag{5-3}$$

where $B(\theta)$ denotes the gradient, $dCp_{\text{inst}}/d\beta$, at specific θ while β' represents the fluctuating elevation angle, $\beta - \overline{\beta}$. Note that the $Cp_{\text{inst}}(\theta,\overline{\beta})$ in Eq. (5-3) is represented by the Fourier series shown in Eq. (5-2). In the current work, the changes of Cp_{inst} due to the changes of β are found by subtracting $Cp_{\text{inst}}(\theta,\overline{\beta})$, defined in Eq. (5-2), from the conditional averaged values of $Cp_{\text{inst}}(\theta,\beta)$, obtained from Eq. (1-7). Because the gradient, $dCp_{\text{inst}}/d\beta$, may also vary with respect to θ, $B(\theta)$ can also be represented by a Fourier series,

$$B(\theta) = \sum_{k=0}^{N_2} a_{3k}\cos(k\theta) + a_{4k}\sin(k\theta) \tag{5-4}$$

5.2 Statistical version of the quasi-steady model

The surface pressure coefficients can be directly estimated by using QS theory using Eq. (1-4b) if the time series of the measured wind vector, $\mathbf{u}_{\text{m}}$, is known, i.e.,

$$Cp = \frac{|\mathbf{u}_{\text{m}}|^2}{u_{\text{ref}}^2} Cp_{\text{inst}}(\theta,\beta). \tag{1-4b}$$

For situations where the time series is not available, the statistical method based on QS formulation may be an alternative to estimate the statistics of surface pressures. The objective here is to relate the PDF of the pressure coefficients, $f(Cp)$, to the joint PDF of the wind turbulence $f(|\mathbf{u}_{\mathrm{m}}|/u_{\mathrm{ref}}, \theta, \beta)$.

By using the concept of auxiliary variables described by Papoulis and Pillai (2002), $f(Cp)$ can be obtained by integrating the joint PDF, $f(Cp, y_1, y_2)$, over two assumed variables,

$$y_1 = \frac{|\mathbf{u}_{\mathrm{m}}|}{u_{\mathrm{ref}}} \quad \text{and} \quad y_2 = \theta. \tag{5-5}$$

Then, $f(Cp, y_1, y_2)$ can be connected to the joint PDF of wind turbulence through

$$f(Cp, y_1, y_2) = \sum_{r=1}^{Nr} \frac{f\left(\left(|\mathbf{u}_{\mathrm{m}}|/u_{\mathrm{ref}}\right)_r, \theta_r, \beta'_r\right)}{\left|J\left(\left(|\mathbf{u}_{\mathrm{m}}|/u_{\mathrm{ref}}\right)_r, \theta_r, \beta'_r\right)\right|}, \tag{5-6}$$

where the subscript, *r*, denotes each root of the set $\{|\mathbf{u}_{\mathrm{m}}|/u_{\mathrm{ref}}, \theta, \beta\}$ for a given input set $\{Cp, y_1, y_2\}$. Because a one-to-one relationship exists between $\{y_1, y_2\}$ and $\{|\mathbf{u}_{\mathrm{m}}|/u_{\mathrm{ref}}, \theta\}$, as assumed in Eq. (5-5), β' is the only root to be solved from Eqs. (1-4b) and (5-3), i.e.,

$$\beta'_r = \frac{1}{B(\theta)}\left[\left(\frac{u_{\mathrm{ref}}}{|\mathbf{u}_{\mathrm{m}}|}\right)^2 Cp - Cp_{\mathrm{inst}}(\theta, \bar{\beta})\right]. \tag{5-7}$$

Based on this formulation, only one root can be found for a given set of $\{Cp, y_1, y_2\}$ such that $N_r = 1$ in Eq. (5-6). The denominator on the right-hand side of Eq. (5-6) is the absolute value of the Jocobian, where

$$J\left(\left(\left|\mathbf{u}_{\mathrm{m}}\right|/u_{\mathrm{ref}}\right),\theta,\beta'\right)=\begin{vmatrix}\dfrac{\partial Cp}{\partial\left(\left|\mathbf{u}_{\mathrm{m}}\right|/u_{\mathrm{ref}}\right)} & \dfrac{\partial Cp}{\partial\theta} & \dfrac{\partial Cp}{\partial\beta'}\\ \dfrac{\partial y_1}{\partial\left(\left|\mathbf{u}_{\mathrm{m}}\right|/u_{\mathrm{ref}}\right)} & \dfrac{\partial y_1}{\partial\theta} & \dfrac{\partial y_1}{\partial\beta'}\\ \dfrac{\partial y_2}{\partial\left(\left|\mathbf{u}_{\mathrm{m}}\right|/u_{\mathrm{ref}}\right)} & \dfrac{\partial y_2}{\partial\theta} & \dfrac{\partial y_2}{\partial\beta'}\end{vmatrix}. \tag{5-8}$$

Substituting Cp by Eq. (1-4b) and $Cp_{\mathrm{inst}}(\theta,\beta)$ by Eq. (5-3) for the right hand side of Eq. (5-8), then the absolute value of Jocobian can be obtained, i.e.,

$$\left|J\left(\left(\left|\mathbf{u}_{\mathrm{m}}\right|/u_{\mathrm{ref}}\right),\theta,\beta'\right)\right|=\left(\frac{\left|\mathbf{u}_{\mathrm{m}}\right|}{u_{\mathrm{ref}}}\right)^2\left|B(\theta)\right|. \tag{5-9}$$

The PDF of Cp can be obtained by integrating the joint PDF, $f(Cp,y_1,y_2)$, over y_1 and y_2, i.e.,

$$f(Cp)=\int_{y_1=-\infty}^{\infty}\int_{y_2=-\infty}^{\infty}f(Cp,y_1,y_2)dy_2dy_1 \tag{5-10}$$

By replacing $f(Cp,y_1,y_2)$ by Eq. (5-6) and using the Jocobian in Eq. (5-9), the PDF of Cp can be re-written as

$$f(Cp)=\int_{\frac{\left|\mathbf{u}_{\mathrm{m}}\right|}{u_{\mathrm{ref}}}=0}^{\infty}\int_{\theta=-180^\circ}^{180^\circ}\frac{f\left(\left(\left|\mathbf{u}_{\mathrm{m}}\right|/u_{\mathrm{ref}}\right),\theta,\beta_r'\right)}{\left(\left|\mathbf{u}_{\mathrm{m}}\right|/u_{\mathrm{ref}}\right)^2\left|B(\theta)\right|}d\theta\,d\left(\frac{\left|\mathbf{u}_{\mathrm{m}}\right|}{u_{\mathrm{ref}}}\right) \tag{5-11}$$

where β_r' is the solution of the given set of $\left\{Cp,\left|\mathbf{u}_{\mathrm{m}}\right|/u_{\mathrm{ref}},\theta\right\}$, which is solved earlier in Eq. (5-7). If the three wind turbulence variables are mutually independent, the joint PDF in Eq. (5-11) can be reduced to individual multiplication (Papoulis and Pillai, 2002), i.e., $f\left(\left|\mathbf{u}_{\mathrm{m}}\right|/u_{\mathrm{ref}},\theta,\beta\right)=f\left(\left|\mathbf{u}_{\mathrm{m}}\right|/u_{\mathrm{ref}}\right)f(\theta)f(\beta)$. In Eq. (5-11), the joint PDF of wind speed to calculate the pressure statistics is directly used in the current work, instead of simulating the negatively correlated relationship between velocity and elevation angle, as proposed

in Richards and Hoxey (2004) (Eqs. 19–22 in their paper). Once $f(Cp)$ is obtained, the PDF of the surface pressure can also be calculated by using the definition in Eq. (1-4a), i.e.,

$$f(p-p_\infty)=\frac{f(Cp)}{\left(\partial(p-p_\infty)/\partial Cp\right)}=\frac{f(Cp)}{0.5\rho\, u_{\text{ref}}^2} \tag{5-12}$$

5.3 Results and discussion

5.3.1 Studied cases

In this section the data obtained from the synchronized cobra probe and surface pressure measurements (see Appendix B) in terrain S15 described in Chapter 2 are used for discussion. Pressures measured at various corner regions of the roof are selected for analyses. The selected single tap in the corner region is denoted as case C1 and shown in Figure 5-1. Various portion of roof area-averaged pressures are also shown in Figure 5-1. These regions include 4, 9, 16 and 36 pressures taps, which are denoted as C4, C9, C16 and C36, respectively.

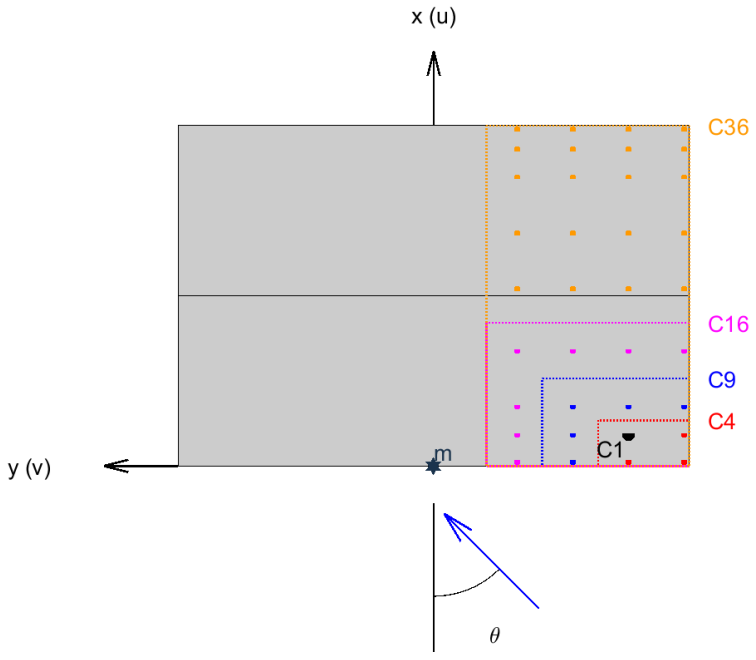

Figure 5-1: Pressure taps within specified regions on roof used for area-averaging analyses.

5.3.2 The quasi-steady model

In this section, the QS coefficients are obtained, using the methods described in Section 5.1. Because of the symmetric shape of the building and the pressure tap layout (see Figure 2-2 a), the measurements between $\bar{\theta} = 0$ and 90° can be extended to the full range of mean wind directions (see Appendix C). Figure 5-2 shows the measured and Fourier-fitted values of $\overline{Cp_{\text{inst}}}$ for a pressure tap near the roof corner, C1. By specifying an error threshold for fitting of $R^2 = 99.5\%$, a total of nine orders of Fourier coefficients were used to fit the measured values of $\overline{Cp_{\text{inst}}}$. Using the continuous form of $\overline{Cp_{\text{inst}}}$ from the fit, the instantaneous function, $Cp_{\text{inst}}(\theta)$, is determined by the iteration procedure described in Section 5.1 and fitted using Eq. (5-2). The resulting fitted function of $Cp_{\text{inst}}(\theta)$ is also shown in Figure 5-2 for the point tap location C1. As found by Richards et al. (1995), differences in magnitudes of $Cp_{\text{inst}}(\theta)$ and $\overline{Cp_{\text{inst}}}(\bar{\theta} = \theta)$ are observed, particularly for wind directions that cause peak pressures (e.g., for θ near 15° in Figure 5-2). This is attributed to the averaging process described by Eq. (5-1), i.e., the instantaneous azimuth sways about the mean value lead to a smoothing for the $\overline{Cp_{\text{inst}}}$ curve.

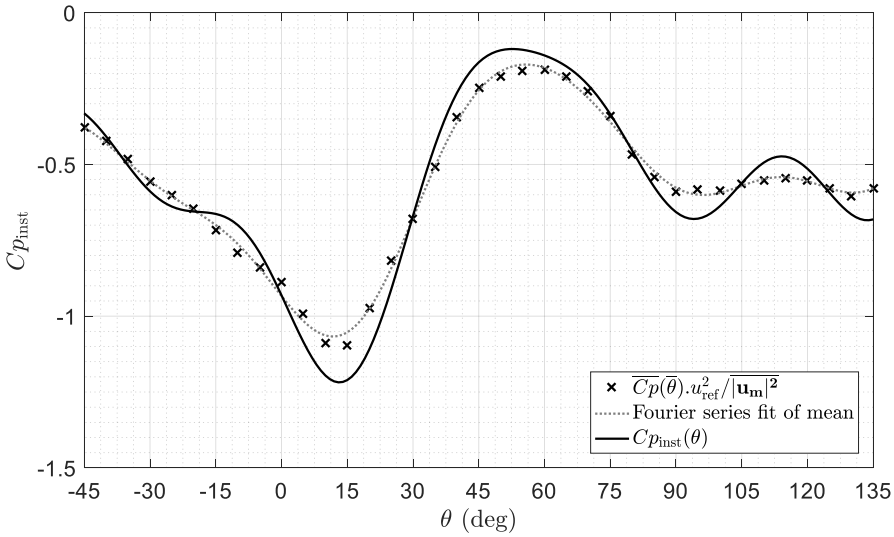

Figure 5-2: $\overline{Cp_{\text{inst}}}$ obtained from each mean wind azimuth $\bar{\theta}$ along with the resulting $Cp_{\text{inst}}(\theta)$ described by Eq. (5-2) for pressure tap, C1.

Once the instantaneous functions are obtained, it is useful to investigate the effects of elevation angle. By using a similar approach as that of Banks and Meroney (2001), the wind-pressure data were first sorted and the data associated with the elemental instantaneous wind azimuth band were identified, i.e., $\theta - d\theta/2 \le \theta < \theta + d\theta/2$. These data were further separated into three bands associated with the fluctuating elevation angles, i.e., $-50 \le \beta' < -2.5$, $-2.5 \le \beta' < 2.5$, and $2.5 \le \beta' < 50$, where $\beta' = \beta - \overline{\beta}$. Note that the $\pm 50^\circ$ is set by the measurement limitations of cobra probes. These three ranges were chosen for plotting and represent downward-acting, nearly horizontal, and upward acting wind angles, respectively. The measured $Cp_{\text{inst}}(\theta, \beta)$ were obtained by averaging for the condition of these three elevation angle bands, as indicated by Eq. (1-7). The conditional averaging was repeated for the elemental azimuth band for several mean wind directions. Figure 5-3 shows the resulting measured values of $\langle Cp_{\text{inst}} | \theta, \beta \rangle$ in discrete symbols along with the fit-$Cp_{\text{inst}}(\theta)$ curve (described by Eq. (5-2)) for pressure tap C1 for four mean azimuths $\overline{\theta} = 45$, 30°, 15° and 0°. Because the total number of data points used for each $Cp_{\text{inst}}(\theta, \beta)$ value are different, the attached color-scale denotes an example for the equivalent duration used in conditional averaging the data (i.e., number of accumulated data points divided by sampling rate), since there are relatively few data points for large excursions from the mean.

As can be seen in Figure 5-3, both of the conditional averaged and the analytical instantaneous function are dependent on the azimuth angle for pressure tap C1. Regarding the functional variations, the $\langle Cp_{\text{inst}} | \theta, \beta \rangle$ variations are found to follow the fit-$Cp_{\text{inst}}(\theta)$ curve from Figure 5-3 for $\overline{\theta} \ge 15$, while keeping the same trend but with much milder slopes for $\overline{\theta} < 15$. Banks and Meroney (2001) first reported similar effects. These authors attributed it to a hysteresis effect such that the instantaneous pressures could not respond to the fluctuations in the wind (azimuth) direction. For example, conical (or corner) vortices dominate the flow structure and the corresponding low pressures at the tap C1 for mean wind azimuth $\overline{\theta} = 15$. When the instantaneous wind suddenly sways to $\theta = 0$, this flow structure does not change to separation bubble type

of flow found observed at $\theta = 0$ and, therefore, retrieve the instantaneous pressure. The reverse situation is true for $\bar{\theta} = 0$, as shown in Figure 5-3.

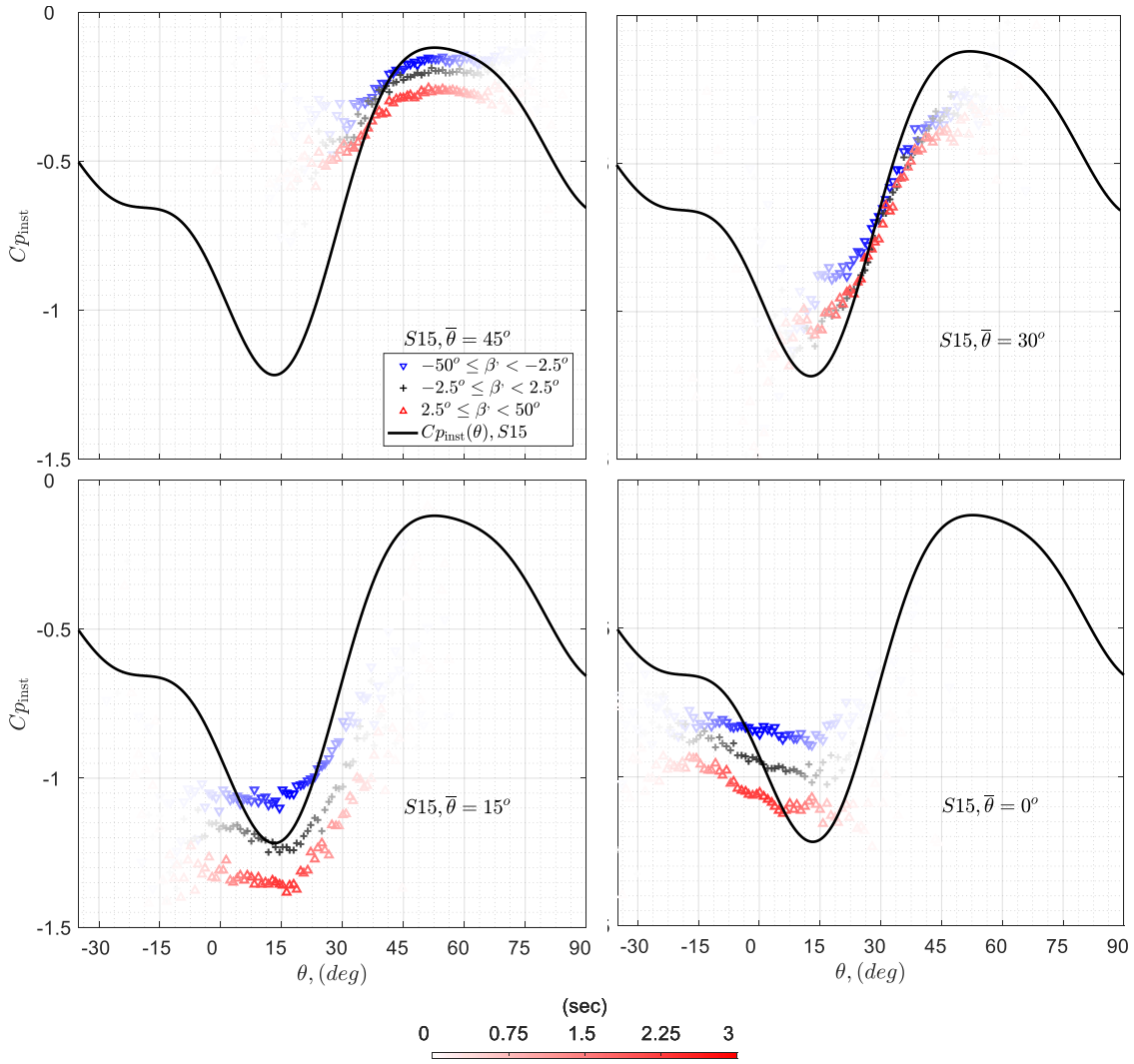

Figure 5-3: $\langle Cp_{\text{inst}} | \theta, \beta \rangle$ and $Cp_{\text{inst}}(\theta)$ (represented by Eq. (5-2)) for case C1, mean wind azimuths $\bar{\theta} = 45$, 30 , 15 and 0 .

The fluctuating wind elevations also play a role in affecting the magnitude of the pressures at tap, C1. In general, an upward wind (i.e., $\beta' > 0$) leads to higher magnitudes of Cp_{inst} , while a downward wind (i.e., $\beta' < 0$) leads to lower magnitudes of Cp_{inst} , with the degree of influence depending on the wind azimuth. Similar observations were also presented by Letchford and Marwood (1997), Sharma and Richards (1999), Wu et al., (2001) and Richards and Hoxey (2004). As expected, the measured values of

$Cp_{\text{inst}}(\theta,\beta)$ tend to be closest to the fit-$Cp_{\text{inst}}(\theta)$ curve (from Figure 5-3) for horizontal winds (i.e., $\beta' \approx 0$), at least for $\theta = \bar{\theta}$. In order to further investigate the elevation-angle effects on the magnitude of $Cp_{\text{inst}}(\theta,\beta)$, the measured differences of the coefficients, $Cp_{\text{inst}}(\theta,\beta) - Cp_{\text{inst}}(\theta,\bar{\beta})$, are examined. Figure 5-4 shows the results, which were obtained for a 5°-band of wind azimuth around the mean (i.e., $-2.5 \le \theta' < -2.5$, where $\theta' = \theta - \bar{\theta}$). As in Figure 5-3, the gray-scale in the figure denotes the total number of data points used in conditional averaging as an effective duration.

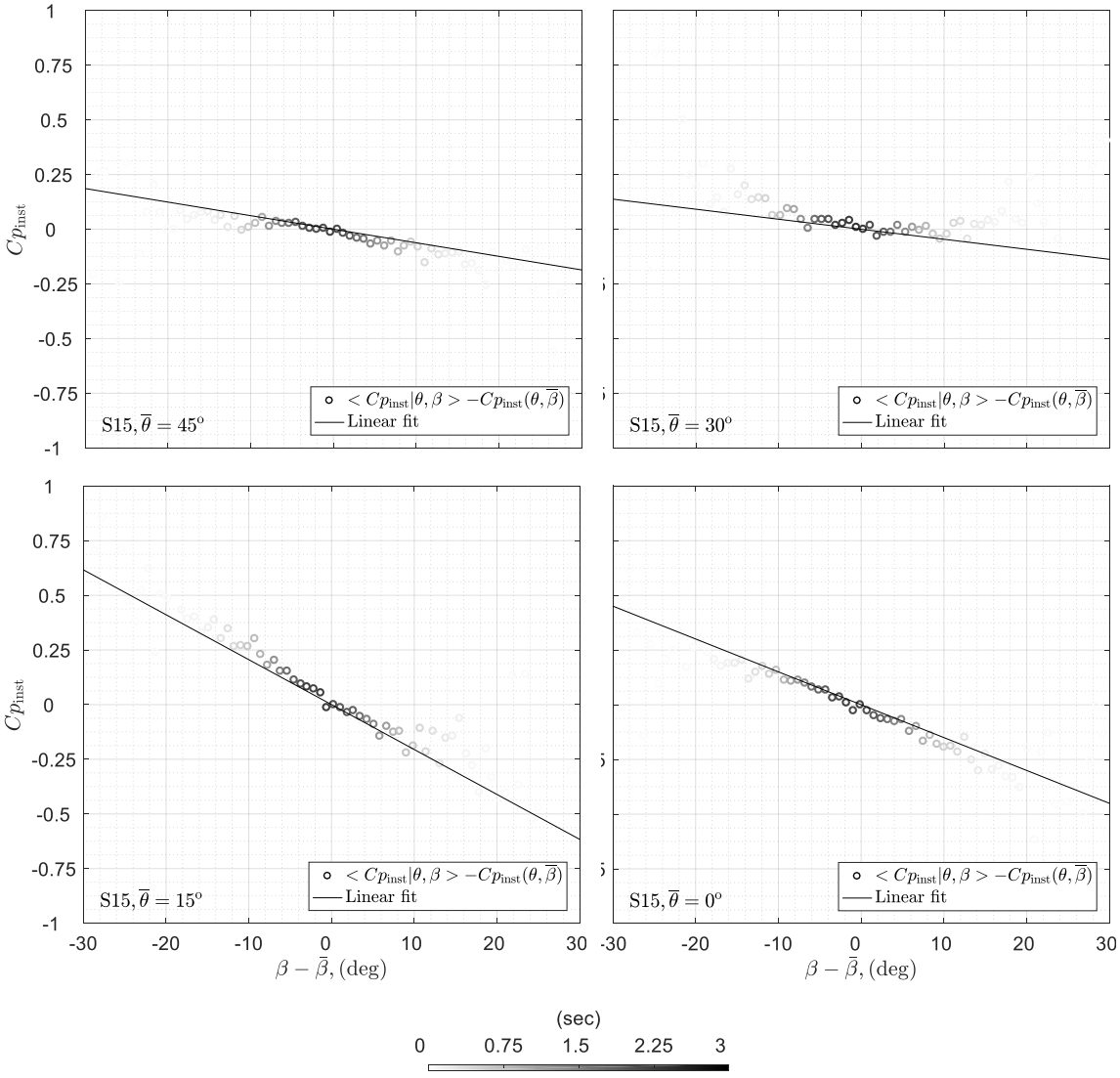

Figure 5-4: The variation of Cp_{inst} versus β' obtained from data points within azimuth band $-2.5 \le \theta' < 2.5$ for case C1, mean azimuths $\bar{\theta} = 45$, 30 , 15 and 0 .

Because the changes caused by the elevation angles to the instantaneous pressure coefficients are found to be linear (in most cases), a linear fit with zero intercept at $\beta' = 0$ is also plotted in the figure. This fitting procedure was conducted for each mean wind azimuth and the corresponding gradients, $B = dCp_{\text{inst}}/d\beta$, were calculated. Figure 5-5 depicts the resulting gradients for each mean azimuth, along with a Fourier-series fit described by Eq. (5-4).

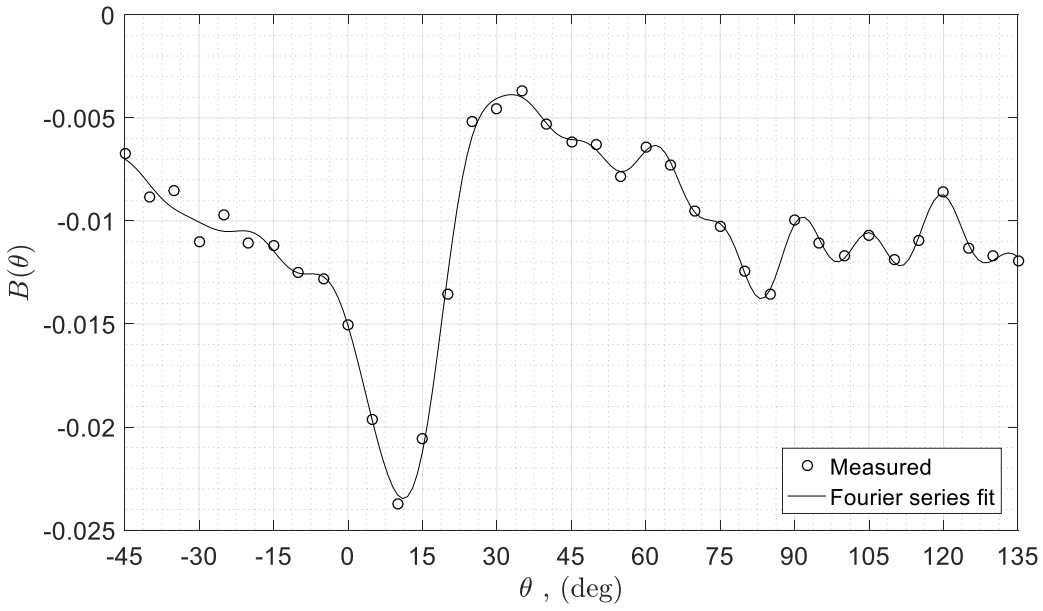

Figure 5-5: The $B(\theta)$ obtained from data points within azimuth band $-2.5 \le \theta' < 2.5$ for each mean wind azimuths for case C1.

Since there are clear variations of $Cp_{\text{inst}}(\theta, \beta)$ for different ranges of wind elevation angle, it is worthwhile to look at the corresponding conditionally averaged elevation angles, $\langle \beta' | \theta \rangle$, for each elemental azimuth band $\theta' - d\theta/2 \le \theta' < \theta' + d\theta/2$ for wind vector time series obtained without the building in place. Figure 5-6 (a) shows the joint PDF for the fluctuating azimuth and fluctuating elevation angle, $f(\theta', \beta')$. The nearly concentric shape of probability distribution data indicates a low correlation between θ' and β'. Therefore, the $\langle \beta' | \theta \rangle$ locus is quite uniform and nearly equal to +7°, 0°, and -7° for the upward, horizontal, and downward bins of elevation angle, respectively, as shown

in Figure 5-6 (b). Although the upward-acting winds increase $\left|Cp_{\text{inst}}\right|$ at pressure tap C1, as shown by Figures 5-3 and 5-4, the existence of Reynolds stresses, $-\overline{u'w'}$, in the atmosphere boundary layer has been reported by Sharma and Richards (1999) to suppress such fluctuations. Basically, the Reynolds shear stresses imply that the positive gusts (i.e., increasing horizontal wind speeds) are generally associated with negative elevation angles. This can be observed by Figure 5-6 (c), where the joint PDF between velocity square ratio, $\left|\mathbf{u}_{\text{m}}\right|^2(\beta')/\left|\mathbf{u}_{\text{m}}\right|^2(\overline{\beta})$, and fluctuating elevation angle, β', were obtained with the building removed from the wind tunnel. A clear negative correlation between $\left|\mathbf{u}_{\text{m}}\right|^2(\beta')/\left|\mathbf{u}_{\text{m}}\right|^2(\overline{\beta})$ and β' can be observed. Thus, based on Eq. (1-4), instantaneously high values of dynamic pressure are generally offset by instantaneous pressure coefficients of lower magnitude, leading to the suppression process of the surface pressures. For events such as tornadoes, however, Reynolds stresses effects, and, in fact, the role of the vertical component of the wind, in general, is a largely unexplored issue. Thus, upward wind directions produced by these types of storms may induce roof pressures beyond the expectations obtained from typical boundary layer wind tunnel experiments.

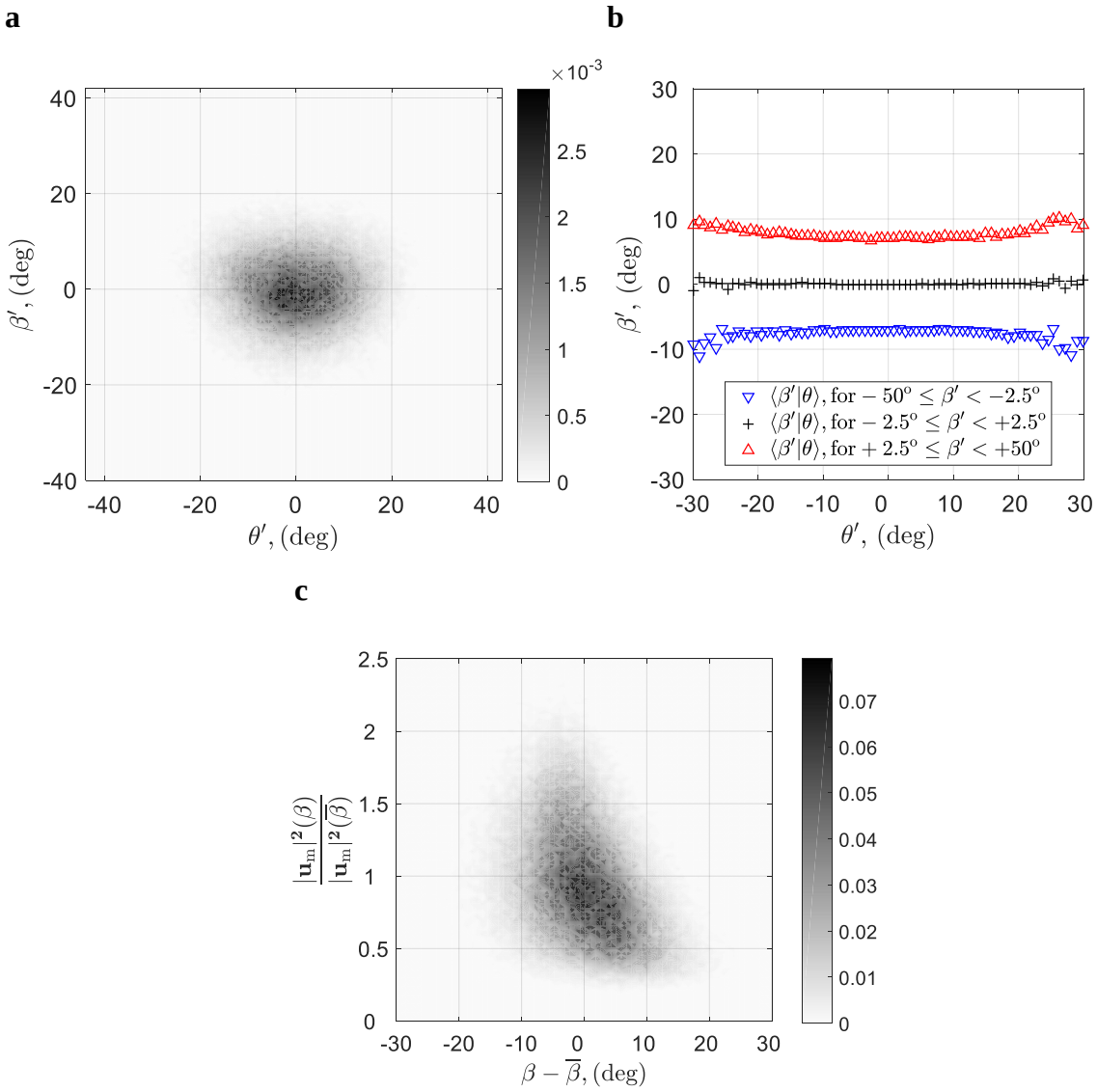

Figure 5-6: (a) $f(\theta', \beta')$, (b) $\langle\beta'|\theta\rangle$ loci for given ranges of β, and (c) $f\left(\left|\mathbf{u}_m\right|^2(\beta')/\left|\mathbf{u}_m\right|^2(\overline{\beta}), \beta'\right)$ obtained from velocity measurement without building in place.

5.3.3 Comparison of measured pressures and quasi-steady theory predictions

In this section, the QS model described in Eq. (1-4b) is used to calculate the pressure coefficients, Cp , and compare them to measurements. Two forms of the model are used: one that only accounts for the instantaneous wind azimuth contribution (QS-θ), which utilizes only the $Cp_{\text{inst}}\left(\theta, \overline{\beta}\right)$ term in Eq. (5-3), and the other that includes both azimuth and elevation angles (QS-θ-β), i.e., the full model defined in Eq. (5-3). The analysis involves four cases, including single point pressures (C1) and area-averaged pressures (C4, C9, and C16, as defined in Figure 5-1).

Figure 5-7 shows the spectra of measured and QS estimates of Cp for the four areas and the mean wind azimuth of 15°. Generally, both the distribution and magnitude of the spectra obtained from QS models are similar to measurements. The spectra obtained via the QS-θ model are found to be slightly higher in magnitude than the QS-θ-β prediction, which can be explained by the suppression process of pressure fluctuation when the wind elevation is included, as discussed by Sharma and Richards (1999) and in Section 5.3.2. The QS-θ-β model generally gives spectra of slightly lower magnitude compared to the measurements.

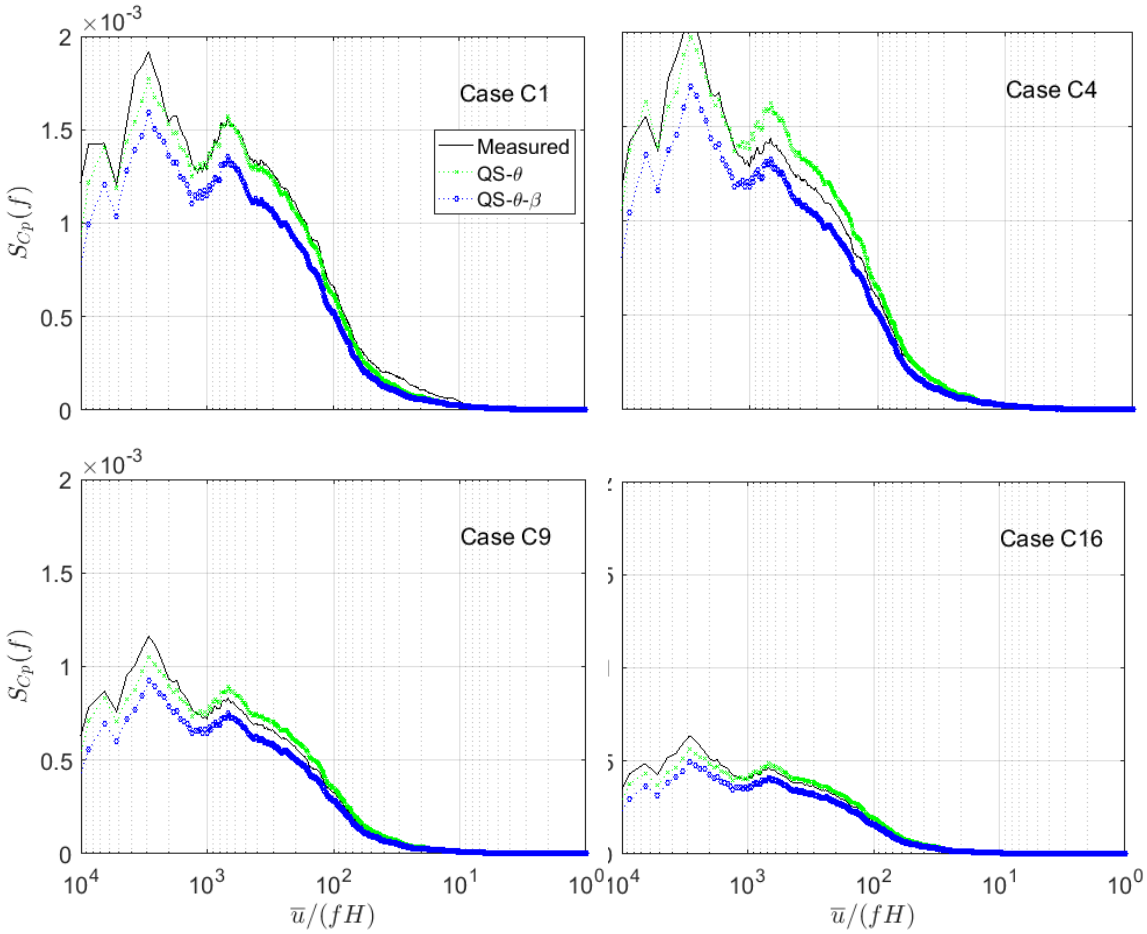

Figure 5-7: Spectra of measured and quasi-steady predicted Cp for cases C1, C4, C9, and C16, mean wind azimuth $\overline{\theta} = 15$.

The frequency-dependent correlation coefficient between the measured and QS-predicted values of Cp is also of interest. For this purpose, the coherence, which is defined here as the real part of the normalized cross-spectra between measured and QS-predicted Cp values, i.e., Eq. (4-13), are obtained (see also Section 4.3.2),

$$\text{Coherence} = \frac{\text{Re}\left[S_{\text{CpQS,CpM}}(f)\right]}{\sqrt{S_{\text{CpQS}}(f)}\sqrt{S_{\text{CpM}}(f)}} \tag{4-13}$$

is calculated, where $S_{\text{CpQS}}(f)$ and $S_{\text{CpM}}(f)$ denote the auto-spectra of QS-predicted and measured Cp at frequency, f, respectively, and $S_{\text{CpQS, CpM}}(f)$ is the cross-spectra between the prediction and the measurement. Figure 5-8 shows the calculated values of

coherence for the four areas and a mean wind azimuth of 15°. Generally, the QS predicted Cp fluctuations are a better match for larger gusts, with coherence ≈ 0.9 for $\bar{u}/f > 125H$, noting that the integral scale is about 12.5H and the largest building length is 3.475H. The level of correlation begins to decrease for $\bar{u}/f \leq 125H$ and is near zero for $\bar{u}/f < 10H$. Although low coherences are found for small gust sizes, the Cp fluctuations are relatively low over this region, as can be seen in the auto-spectra plots (Figure 5-7). Furthermore, the QS-θ-β predictions are seen to have better correlations with the measured values, especially in middle range of frequencies $(10H \leq \bar{u}/f < 125H)$, when compared to the QS-θ estimates.

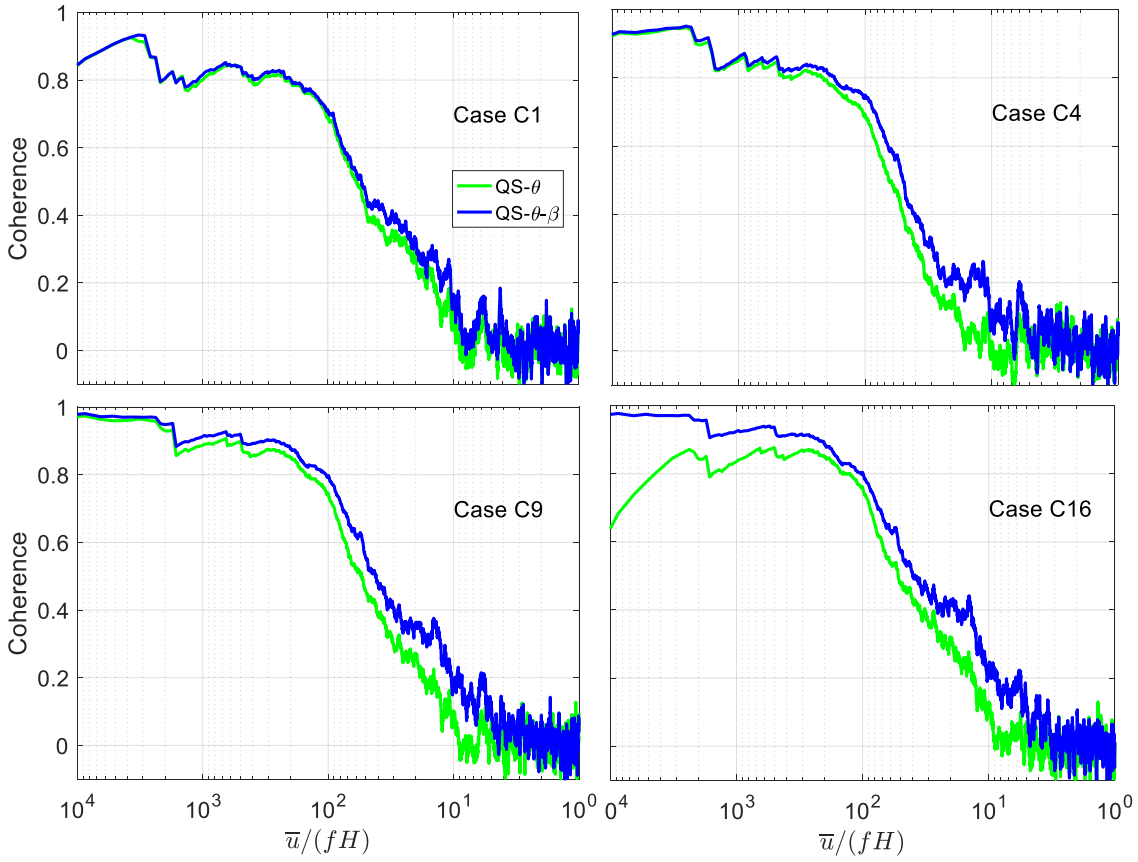

Figure 5-8: Coherence between measured and QS-predicted Cp for cases C1, C4, C9, and C16, mean wind azimuth $\bar{\theta} = 15$.

To better understand the impact of the results depicted in Figures 5-7 and 5-8, Figure 5-9 shows the measured and (QS-θ-β)-predicted time series for 3 sec around a selected peak denoted as time, $t = t_p$. The figure indicates that the low-frequency portion of the fluctuations follow the measurements for case C1, while the tracking of the time series at higher frequencies is clearly lacking, leading to mismatches of the predicted peak values, with differences up to 30% are observed. The better correlation of low frequency portion is a reflection of case C1 of Figure 5-8, while the underestimation of peaks may be attributed to underestimation of the spectral content for both the low and median frequency ranges of Figure 5-7. The mismatch of QS-predicted pressures of small length fluctuations are partially due to the location of wind speed measurements, which is 1*H* above the roof leading edge (see Figure 2-2 (a) and Figure 5-1). Because the small scale turbulences measured at point *m* are expected have little correlations to that just above the tap C1, the inclusion of these small scale turbulences in the QS model are expected to give little interpretation of pressure fluctuation measured at C1. On the other hand, the point roof pressures may be better correlated to the strengths of shed vortices (from the leading edge), as shown by Akon (2017). In order to account for these small scale, local, building generated vortices, a modified model that better captures the effects of these vortices is required for predicting point pressures near the roof leading edges.

When more points were included in area-averaging, a gradual improvement in the QS-θ-β predictions can be observed for cases C4, C9, and C-16 in Figure 5-9. This may be because of the fact that the area-averaging of closely spaced point pressures acts like a low-pass filter of the individual point pressures, which removes the low-correlation/high-frequency portion of Cp predicted by the model. This observation of low-pass spatial filtering process was first discussed by Letchford et al. (1993) from their analysis of full-scale measurements (noting that a linear QS-θ model was used in their work).

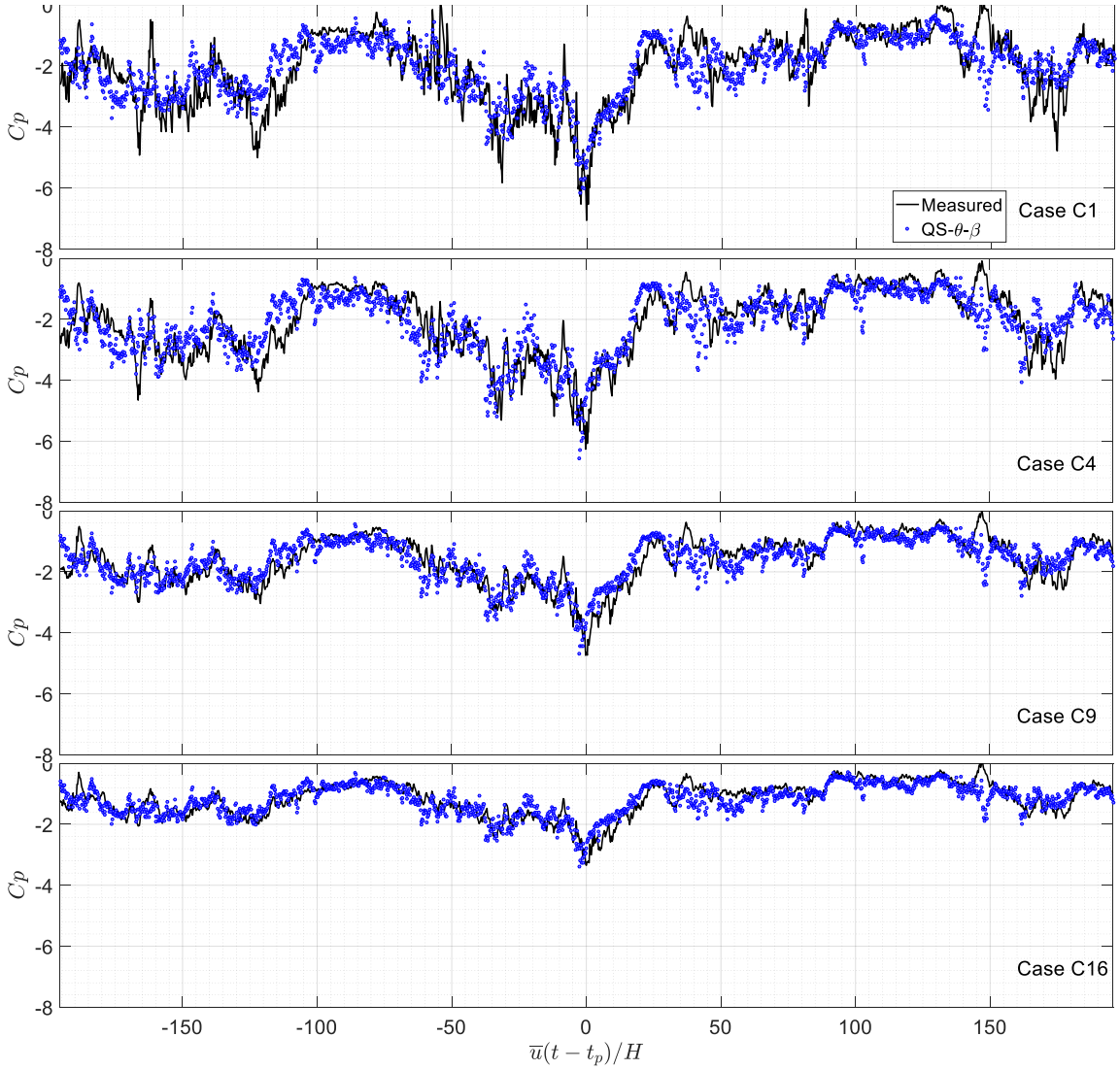

Figure 5-9: Time series of measured and QS-predicted Cp around a selected peak for cases C1, C4, C9, and C16, mean wind azimuth $\overline{\theta} = 15$.

Finally, the zero-time-lag correlation coefficients between the measured and predicted pressure coefficients are shown in Figure 5-10, for the four areas and all mean wind azimuths. For pressure tap C1, the correlation coefficients were found to be nearly uniform with wind direction and approximately equal to 50%, except for mean wind azimuths $35 \le \overline{\theta} \le 75$. For area-averaged cases, the correlation coefficients are nearly uniform across all of the measured mean wind azimuths and gradually increases as the number of pressure taps included in the average increase, reaching 65% for the QS-θ-β model over the interval, $0 \le \overline{\theta} \le 50$. Such improvements, again, can be explained by

the low-pass filtering induced by the area-averaging process and indicate that the QS models are more appropriate for area-averaged pressures (see also Letchford et al., 1993).

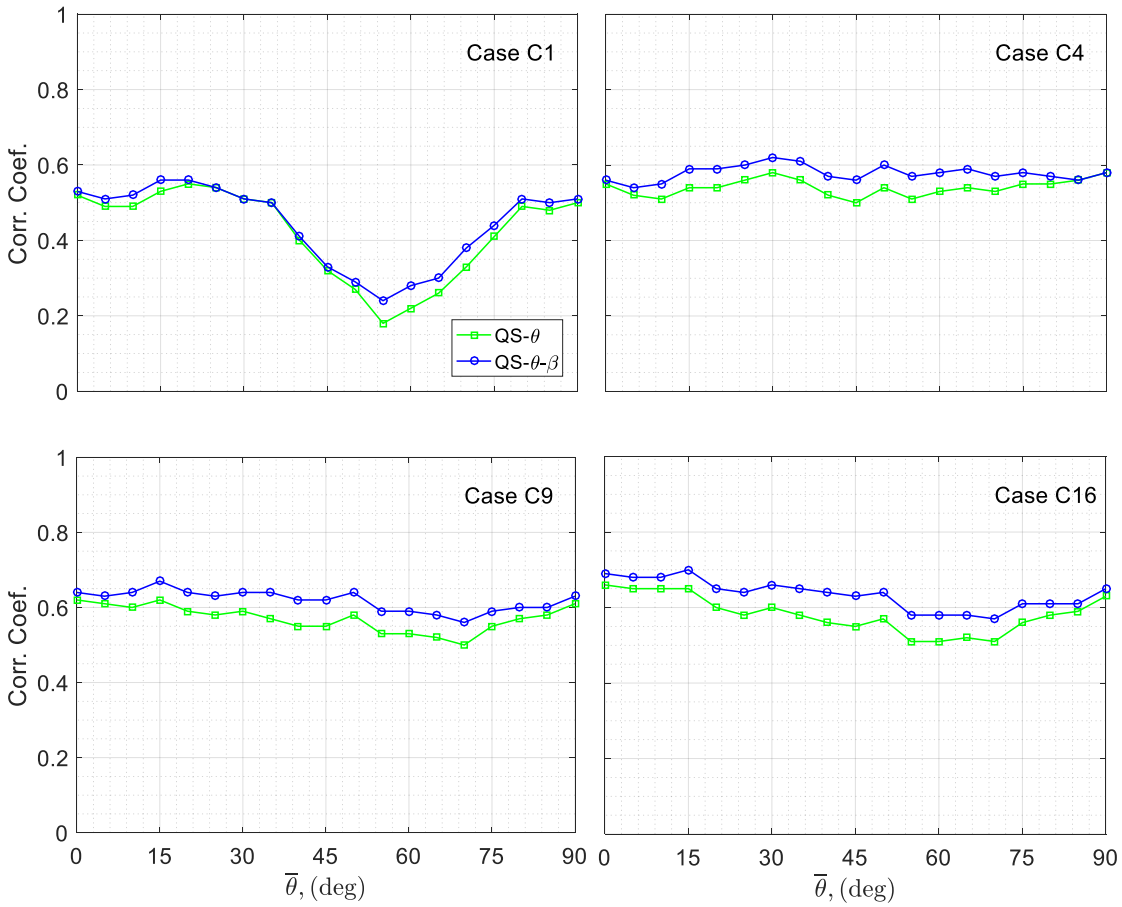

Figure 5-10: Zero-time-lag correlation coefficient between measured and QS-predicted *Cp* for cases C1, C4, C9, and C16.

The differences between the QS-θ and QS-θ-β models can also be observed in terms of correlation coefficients in Figure 5-10. Generally, the QS-θ-β model gives slightly better correlated predictions than QS-θ model, with the magnitudes of the differences depending on wind azimuth. The differences become more uniform for area-averages. Because of the better performance of the QS-θ-β model, it is selected for analyses for the following sections.

5.3.4 Statistics of measured and estimated pressures

In this section, the statistics of *Cp* time histories obtained from measurements and the QS-θ-β model are compared. Figure 5-11 (a) shows the PDF of the measured and predicted values for case C1 with a mean wind direction of 15°. This wind direction is selected arbitrarily for the demonstration of applying the statistical method, although it coincides with the maximum mean suction at point C1 (see Figure 5-2). Of note, the statistical method based on the QS theory described in Section 5.2, was used to obtain the PDF and is denoted as 'QS-statistics'. These results are compared to those obtained directly from the estimated time history (using wind vector with the QS assumption), labeled as 'QS-TH'. The nearly equivalent values of the QS-TH and QS-statistics validate the use of the statistical method. Thus, the results using the method in Section 5.2 (QS-statistics) are presented in what follows, eliminating the need for calculating the time histories.

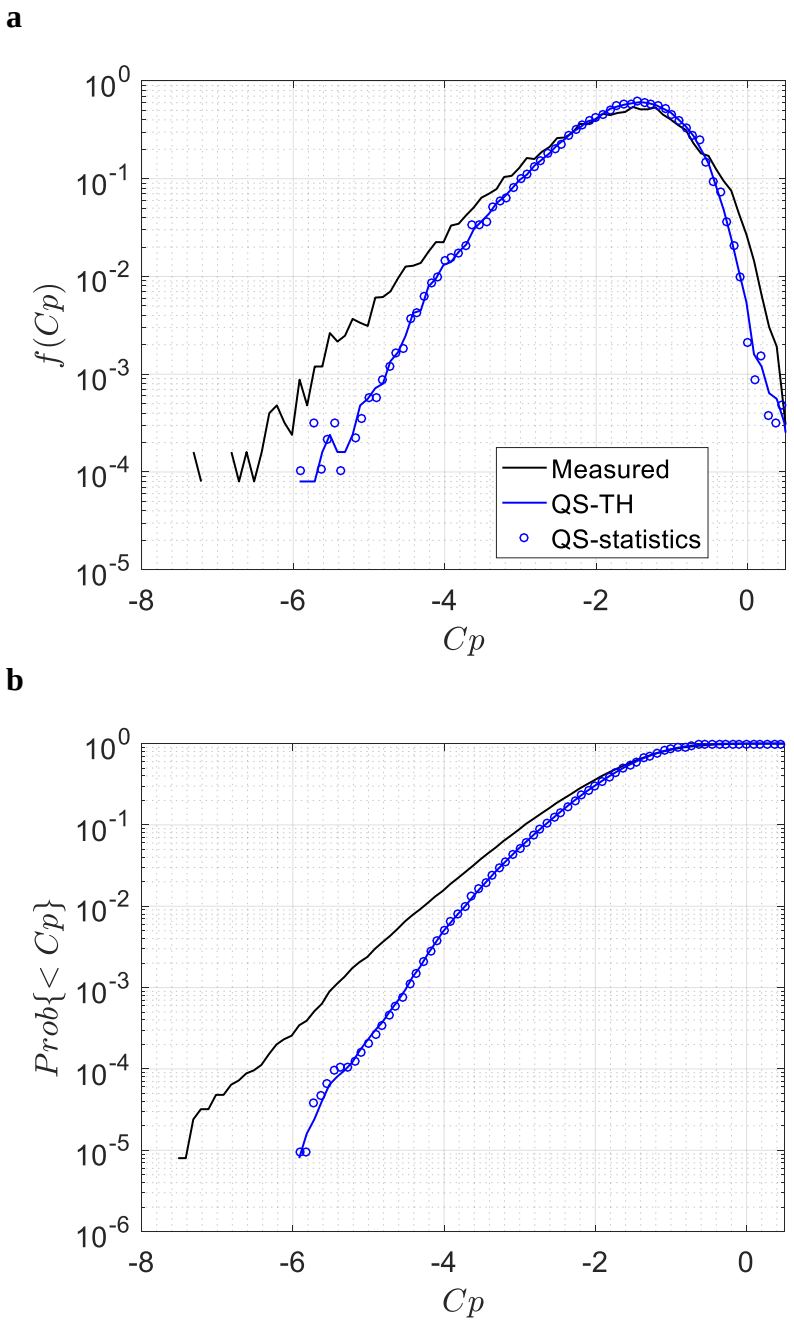

Figure 5-11: (a) PDF and (b) CDF of Cp obtained from measurement and QS-θ-β model for case C1 for mean wind azimuth $\bar{\theta} = 15$.

Figure 5-11 indicates that the QS-θ-β model underestimates the peak values at tails of the distribution, consistent with the observations from the Cp time-series segments shown in Figure 5-9. Figure 5-11 (b) further shows that the corresponding cumulative density

functions (CDF), $\text{Prob}\{< Cp\}$, which is the probability of a pressure coefficient below a given value, is able to predict the probability of exceedance up to 0.3 but underestimates the values for probabilities of exceedance below 0.3. If a probability of exceedance of 0.01% is selected as the reference, the corresponding estimated peak value, $Cp = -5.2$, is 19% lower than the measured peak, $Cp = -6.4$.

Although the statistical method derived in Section 5.2 is for point pressures, it can easily be extended to area-averaged pressures. This is done by simply replacing $Cp_{\text{inst}}(\theta, \bar{\beta})$ and $B(\theta)$ with the appropriate area averaged values, $\sum_i Cp_{\text{inst},i}(\theta, \bar{\beta}) \cdot A_i / A$ and $\sum_i B_i(\theta) \cdot A_i / A$, respectively, in Eq. (5-3), where A_i / A denotes the weight for *i*-th pressure tap within the specified region of total area A. Figure 5-12 depicts the CDFs of four area-averaged coefficients obtained from measurements and prediction for a mean wind direction of 15°. Again, if 0.01% is selected as the reference probability of exceedance, the (QS-θ-β)-predicted peak $Cp = -5.4$ is now 10% less than the measured peak $Cp = -6.0$ for C4. Thus, the underestimation is reduced, compared to the C1 case. The estimates continue to be improved as the total number of taps included in the area increases, and eventually, the (QS-θ-β)-predicted distributions are found to closely match the measurement cases, here for C16 and C-36. The improvement of the QS-θ-β statistical method for area-averaged pressures is consistent with the observations found in QS-θ model by Letchford et al. (1993).

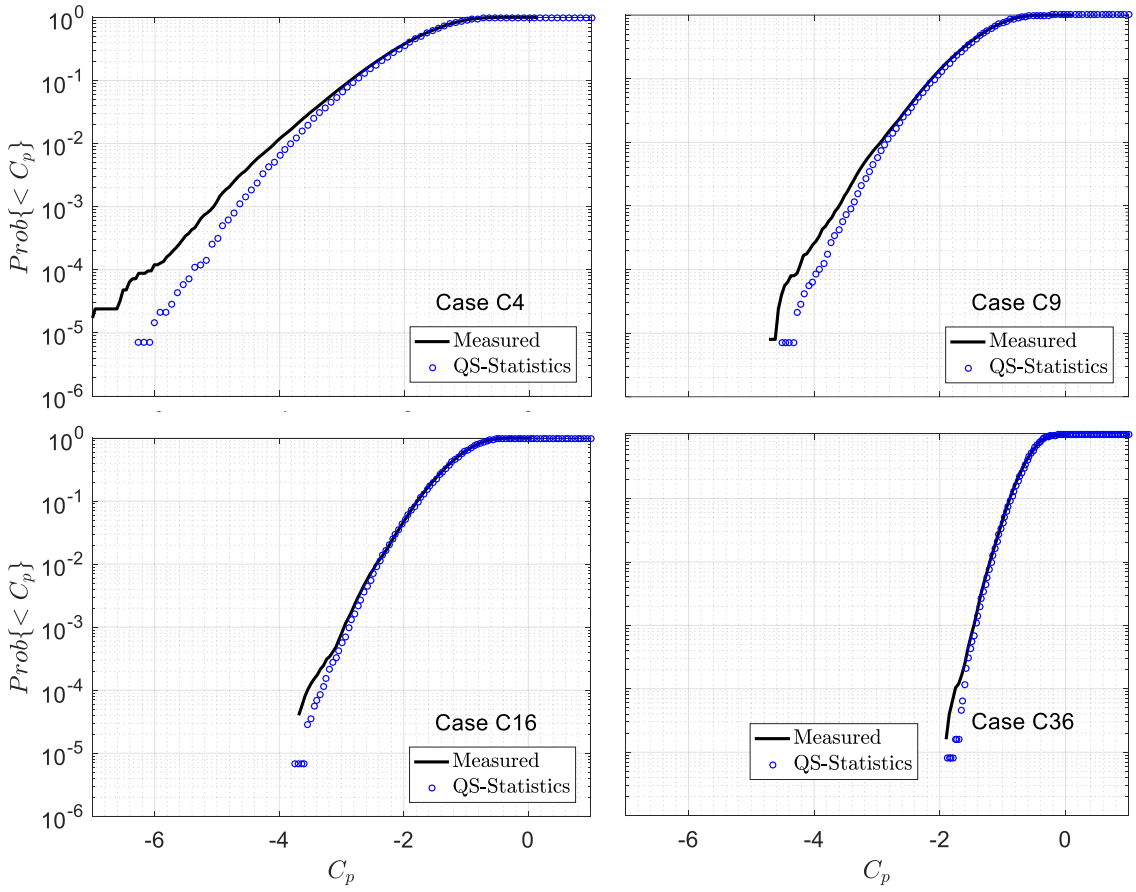

Figure 5-12: CDF of Cp 's obtained from measurement and QS-θ-β model for cases C4, C9, C16, and C36, mean wind azimuth $\bar{\theta} = 15$.

To further investigate the general capability of the QS-θ-β statistical method, the peak pressure coefficients based on the 0.01% probability of exceedance were calculated and compared with measurements in Figure 5-13 for the four area-averages, for all measured mean wind azimuths. For case C4, although the peaks predicted by QS follow the trend observed in measurement, the QS-predicted peaks underestimated the observed values for all wind directions, with larger values for the cases where $\bar{\theta} \leq 15$. As for the results presented in Figure 5-12, the overall level of underestimation of QS-predicted peaks was reduced when more taps are included in the area-averages. Excellent results are obtained for case C36, although C16 also is very good.

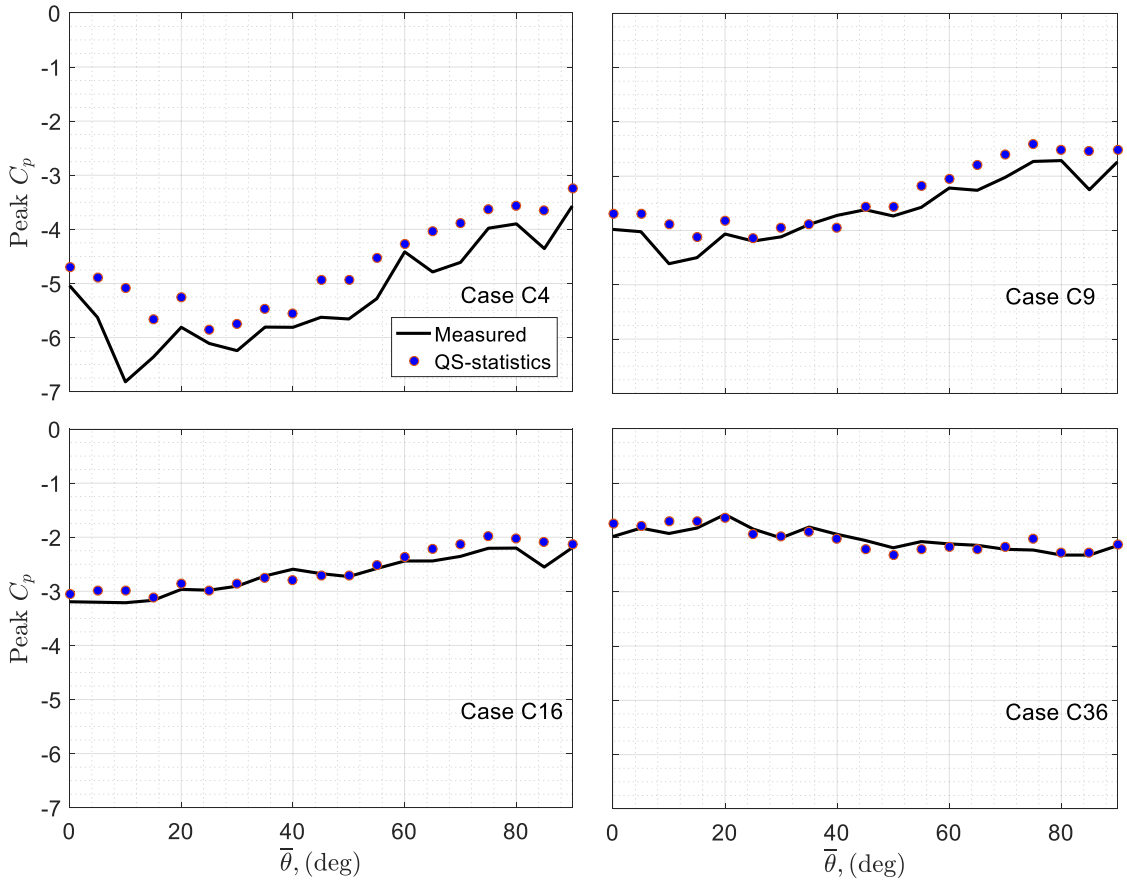

Figure 5-13: Peak *Cp* obtained from measurement and QS-θ-β model for cases C4, C9, C16, and C36.

Finally, some comments are made about the statistical model described in Section 5.2, given by Eqs. (5-11) and (5-12), and the data used herein. First, the joint PDF of the wind vector, $f\left(|\mathbf{u}_{\mathrm{m}}|/u_{\mathrm{ref}}, \theta, \beta'\right)$, should not to be reduced to the individual multiplication, $f\left(|\mathbf{u}_{\mathrm{m}}|/u_{\mathrm{ref}}\right) f(\theta) f(\beta')$, because of a lack of mutual independence between the instantaneous velocity ratio, wind azimuth, and elevation angle. Therefore, the current use of $f\left(|\mathbf{u}_{\mathrm{m}}|/u_{\mathrm{ref}}, \theta, \beta'\right)$ is different from the use of $f\left(|\mathbf{u}_{\mathrm{m}}|/u_{\mathrm{ref}}\right) f(\theta) f(\beta')$ in Richards and Hoxey (2004). However, the velocity ratio and wind azimuth was found to be independent such that the individual multiplication, $f\left(|\mathbf{u}_{\mathrm{m}}|/u_{\mathrm{ref}}\right) f(\theta)$, can replace the

joint pdf, $f\left(\left|\mathbf{u}_{\mathrm{m}}\right|/u_{\mathrm{ref}},\theta\right)$ when the QS-θ model is applied (e.g., Banks and Meroney, 2001; Richards and Hoxey, 2004).

Second, the joint pdf, $f\left(\left|\mathbf{u}_{\mathrm{m}}\right|/u_{\mathrm{ref}},\theta,\beta'\right)$, used in this paper was obtained from a fixed position with respect to the building for each mean wind azimuth, which leads to questions about the possible distortion of measurements due to the building. Measurements showed that there is little difference between the joint pdf of the fluctuating quantities (i.e., $f\left(\left|\mathbf{u}_{\mathrm{m}}\right|/u_{\mathrm{ref}},\theta',\beta'\right)$) measured with and without the building in place, with R^2 values around 95% for all mean wind azimuths. Although there are indeed some small changes of the mean quantities (i.e., $\overline{\left|\mathbf{u}_{\mathrm{m}}\right|}$, $\bar{\theta}$ and $\bar{\beta}$) due to the placement of the building, there is no influence on evaluating the probability distributions based on the formulation described in Eq. (5-11). However, small changes in mean wind speed may be considered in Eq. (5-12) for evaluating the probability distributions of surface pressures.

Third, because the current building can be viewed as a sharp-edged bluff body, the typical pressure coefficients measured on the roof are largely Reynolds number independent (Holmes, 2001). Thus, the statistical model in Eqs. (5-11) and (5-12) is a convenient tool for predicting the probability distributions of roof surface pressure over a range of mean wind speeds, presuming there are no changes in the structure of the wind with wind speed. These invariant joint PDFs of the wind speed vector, $f\left(\left|\mathbf{u}_{\mathrm{m}}\right|/u_{\mathrm{ref}},\theta,\beta\right)$, can be coupled with the instantaneous functions Cp_{inst}, leading to an invariant distribution of Cp, based on Eq. (5-11). Therefore, the PDF of roof surface pressures can be obtained from Eq. (5-12) by simply changing the mean wind speed, $\overline{\left|\mathbf{u}_{\mathrm{m}}\right|}$. Once the PDF of surface pressured is obtained, other statistical quantities, e.g., probability of exceedance, can be derived. For example, Figure 5-14 shows the probability of the building surface pressure exceeding -2 kPa for mean wind speeds ranging from 30 to 170 m/s for the four area-averages (C4, C9, C16, and C36) for a 15° mean wind azimuth. These curves mimic the “fragility” curves, but are simplified examples with the

assumption of a fixed holding strength. Actual fragility curves can be obtained by including the statistics of the panel holding strengths and more accurate failure mechanism; however, the QS statistical model of Eq. (5-11) and (5-12) can be used to simplify the process of accurately modeling the variations of the wind load.

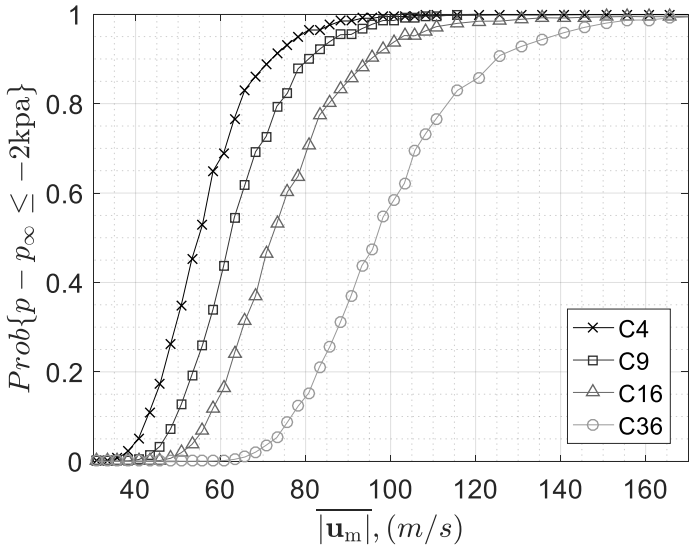

Figure 5-14: Probability of QS-θ-β predicted pressures below -2 kpa for cases C4, C9, C16, and C36 for mean wind azimuth $\bar{\theta} = 15$.

5.4 Summary

The QS model assumes the instantaneous surface pressure as a multiplication of instantaneous dynamic pressure, $0.5\rho|\mathbf{u}_\text{m}|^2$, with the instantaneous function, Cp_inst. This method is applied and extended in this chapter to relate the wind speed to building surface pressure. The effects of wind azimuth and elevation angle are included in the instantaneous function, i.e., $Cp_\text{inst}(\theta, \beta)$, in the QS vector model (QS-θ-β) with a linear effect of wind elevation found to be adequate for the range of fluctuating elevation angle, β', such that $Cp_\text{inst}(\theta, \beta) = Cp_\text{inst}(\theta) + \beta' \cdot dCp_\text{inst}/d\beta$. The gradient $dCp_\text{inst}/d\beta$ is found to vary with respect to wind azimuth so that the functional form is fit with a Fourier series. The instantaneous functions in the model were evaluated from synchronized measurements of building surface pressures and local wind speed vectors. The

experimental method used here eliminates the need to tilt the building model, which was required in the procedures suggested by the previous work, thereby facilitating a process for establishing the QS-θ-β model. The main conclusions are as follows:

(i) Upward-acting winds (i.e., $\beta' > 0$) are generally associated with higher magnitudes of Cp_{inst} while the downward-acting winds (i.e., $\beta' < 0$) are generally associated with lower magnitudes of Cp_{inst}. The effect of the elevation angle can be as large as the effect of wind azimuths for certain mean incident wind angles.

(ii) Higher dynamic pressures, however, are generally associated with downward wind in the atmospheric boundary layer, leading to a suppression process of the actual observed peaks because of this. These observations are consistent with previous published works. By contrast, tornadoes, which can have significant upwardly directed winds, could have significantly increased wind loads as a result of this.

(iii) A statistical method that uses the QS-θ-β model was also derived and validated. With this method, the probability density function (PDF) of building surface pressures is formulated as a double integral of the joint PDF between instantaneous wind speed ratio, wind azimuth, and elevation angle, $f\left(|\mathbf{u}_{\text{m}}|/u_{\text{ref}}, \theta, \beta\right)$.

(iv) Because no mutual independence is found between $|\mathbf{u}_{\text{m}}|/u_{\text{ref}}$, θ, and β, the joint PDF used here is not further reduced to $f\left(|\mathbf{u}_{\text{m}}|/u_{\text{ref}}\right)f(\theta)f(\beta)$, a formulation that has been used in previous works. Furthermore, the direct use of joint PDF of wind turbulence in our formulation offers a more straightforward approach when compared to the procedures used in previous works.

(v) Peak pressures were predicted by applying this method and compared to the measured values for all mean incident wind angles. Underestimation of peak pressures was observed for point pressures on the roof. The accuracy of peak prediction increases as the number of points included in area-averages increases. More specifically, the mean level of error (underestimation) was found be about 30% for a single pressure tap, while

this reduces to < 5% for area-averages of 16 and 36 taps (on the current building with the current tap layout).

(vi) The proposed QS-θ-β model is found to perform well for roof pressure estimation when relatively large areas of the roof are considered for this typical low-rise building.

Chapter 6

6 Estimation of roof pressure fluctuations for different upstream turbulence conditions in atmospheric boundary layer flow using a quasi-steady model

In this chapter, the effect of upstream turbulence on roof surface pressure fluctuations is investigated using the quasi-steady (QS) models introduced in Chapter 5. As discussed in Chapter 5, the QS model performs better in estimating the pressures averaged over an area rather than obtained at a point location. Hence, regions of roof panel areas near the roof corner, i.e., C9 and C16, and near the leading edge, i.e., L9 and L16, shown in Figure 6-1, are used mainly for analyses in this chapter. However, pressures at the point location C1 are also included for the preliminary discussions.

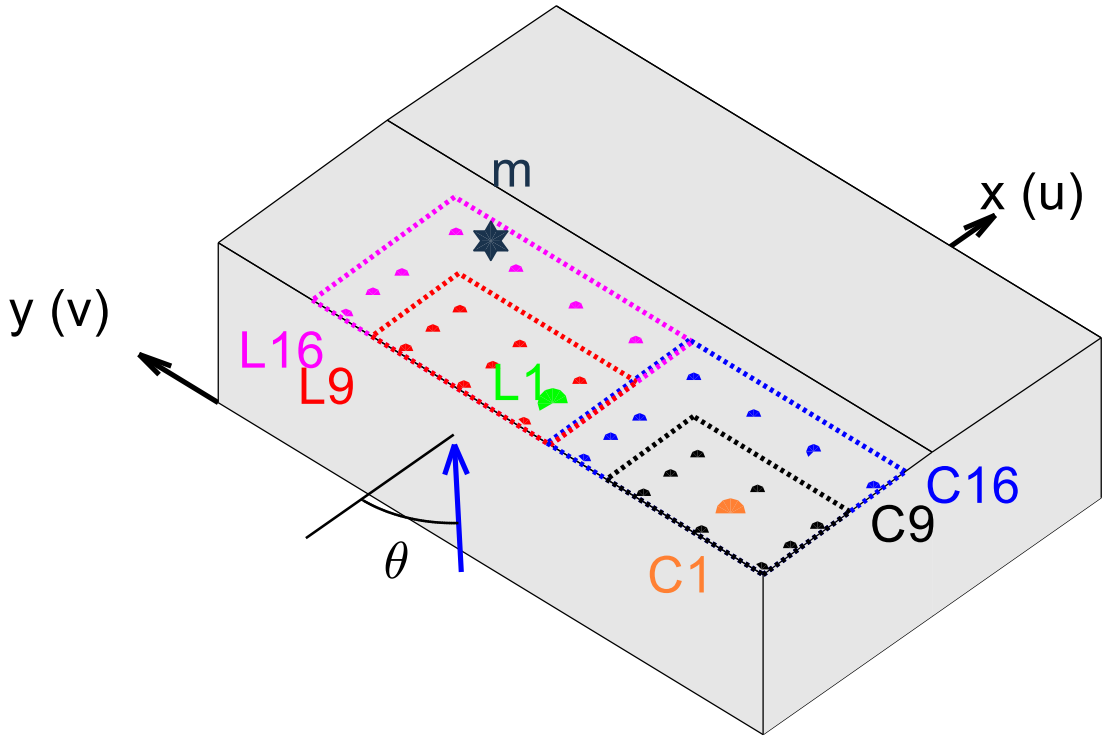

Figure 6-1: Roof panel areas used for pressure averaging.

6.1 Characteristics of ABL turbulence generated by the six upstream terrain conditions

The quasi-steady (QS) estimation of fluctuating roof surface pressures is directly related to the three-dimensional turbulent flow measured at point *m*, as demonstrated in Chapter 5. Hence, in addition to the stream-wise turbulence characteristics measured at roof height (see Figure 2-1), the three-dimensional turbulent velocity vectors measured at point *m* (at height 2*H* without building in place) are further characterized by the spectra and probability density function (PDF) and shown in Figure 6-2.

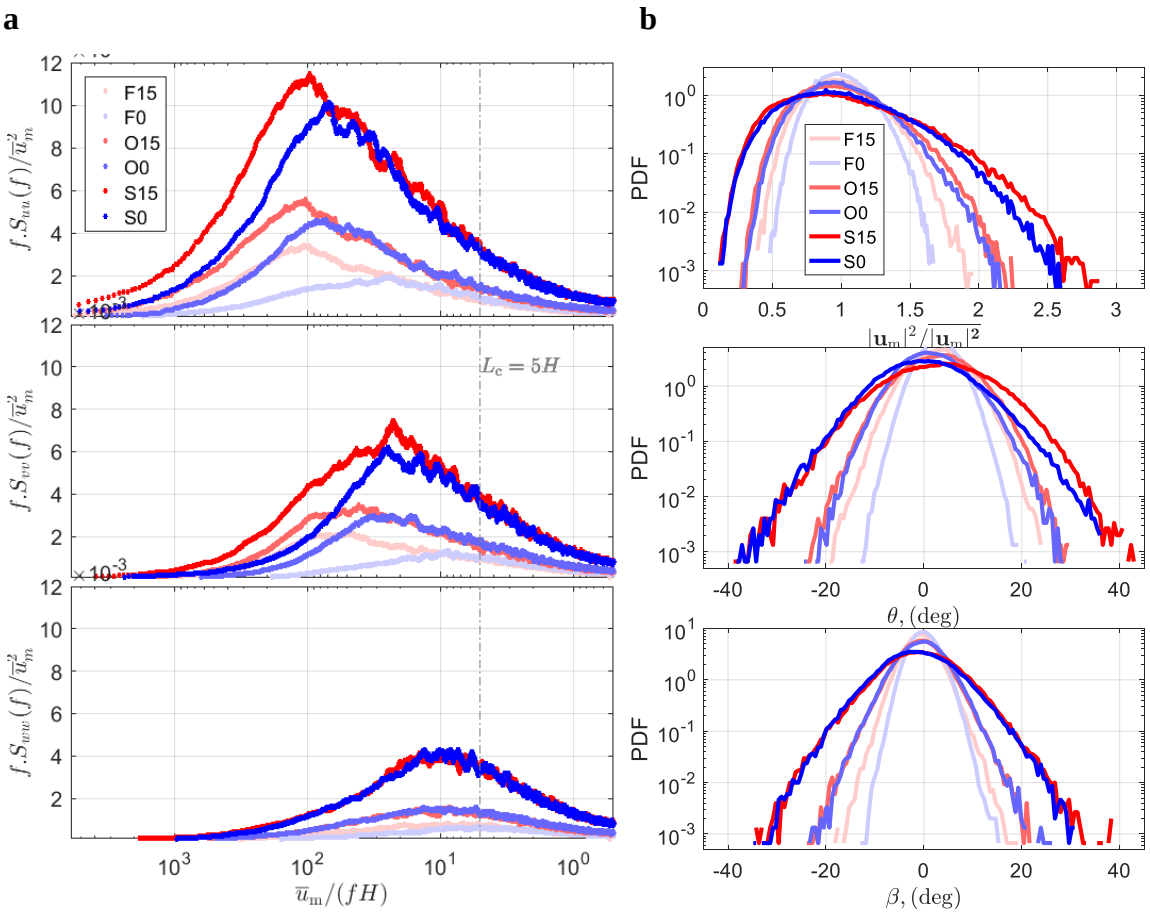

Figure 6-2: Turbulence characteristics of three velocity components measured at location *m* for the six upstream terrain conditions without building in place: (a) Reduced spectra of u-, v- and w-components of velocity; (b) Probability density function (pdf) of $|\mathbf{u}_m|^2/\overline{|\mathbf{u}_m|^2}$, $\boldsymbol{\Theta}$ and $\boldsymbol{\beta}$.

From the spectra shown in Figure 6-2 (a), the turbulence intensities of the three velocity components (i.e., the total area under the spectra) are strongly related to the roughness level of the upstream terrain conditions. Adding the 15-inch barrier at the upstream end of the wind tunnel increases the intensity of the larger length scale turbulence for *u*- and *v*-components of the flow. However the *w*-component fluctuation seems to be unchanged by adding the upstream barrier. The PDF of the wind vector used in the QS model, i.e., the velocity square ratio, $f\left(|\mathbf{u}_{\mathrm{m}}|^2 \Big/ \overline{|\mathbf{u}_{\mathrm{m}}|^2}\right)$, the azimuth angle, $f(\theta)$, and the elevation angle, $f(\beta)$, are shown in Figure 6-2 (b). These PDF's directly reflect the magnitudes of the turbulence intensities represented by the spectra plots, however the variations of turbulence length scales are masked.

6.2 Use of large length scale turbulence in the quasi-steady model

In Chapter 5, the predictions of the roof surface pressure fluctuation for building in terrain S15 are done by the QS model established in same terrain condition. By following the same procedure demonstrated in Chapter 5, the QS model can be established on each of the six terrain conditions with the corresponding ABL turbulences characteristics (shown in Figure 6-2). The resultant instantaneous functions, $Cp_{\mathrm{inst}}(\theta)$, for the QS models (denoted as QS-θ) are shown in Figure 6-3 for the point location, C1, near the roof corner (see Figure 6-1). The conditionally-averaged values of the instantaneous function, $\langle Cp_{\mathrm{inst}} | \theta, \beta \rangle$, which are obtained from the instantaneous pressure and velocity measurement, are also shown for mean wind azimuths ranging from $\bar{\theta} = 0$ to 90 , with an increment of 15 . Note that the data presented in Figure 6-3 are similar to what have been presented in Figure 5-3 but represent a summarized view for the performance of the QS model for each of the wind directions and terrain conditions.

Generally, the measured $\langle Cp_{\mathrm{inst}} | \theta, \beta \rangle$ are matched better to the QS-θ curve for $\bar{\theta} > 20$, with relatively poor performance for $\bar{\theta} \le 20$. Positive elevation angles, i.e., the upward wind directions, generally lead to higher magnitudes of $\langle Cp_{\mathrm{inst}} \rangle$ for all wind azimuths,

with degree of influence depending on the wind azimuth. These general observations are consistent to what have been found in terrain S15 and discussed in Section 5.3.3. However, some differences in the performance of the QS model can be observed for different upstream terrain conditions. Relatively better matches of the modeled $Cp_{\text{inst}}(\theta)$ curve to the measured $\langle Cp_{\text{inst}} | \theta, \beta \rangle$ can be observed for the terrains with larger turbulent length scales. Apparent examples can be found by comparing the $\langle Cp_{\text{inst}} | \theta, \beta \rangle$ loci measured at $\bar{\theta} = 30$. That is, the slopes of the measured $\langle Cp_{\text{inst}} | \theta, \beta \rangle$'s match better to the QS-Θ model for terrains F15 and O15 than that of terrains F0 and O0.

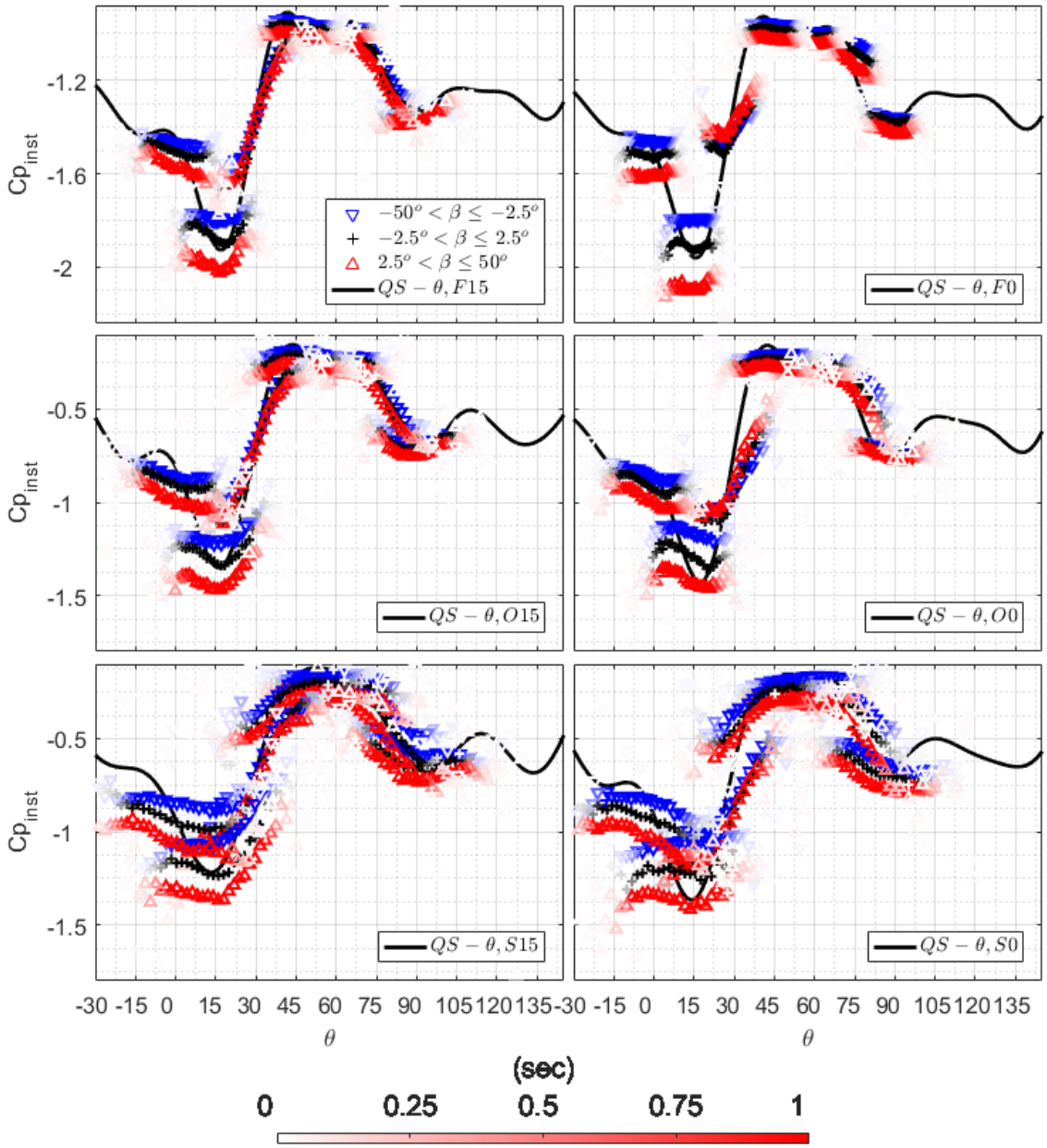

Figure 6-3: The instantaneous function $Cp_{\text{inst}}(\theta)$ of the QS model established from each of the six upstream terrain conditions, along with the conditionally averaged values $\langle Cp_{\text{inst}} | \theta, \beta \rangle$ obtained from instantaneous velocity and pressure measurement at mean wind azimuths $\overline{\theta} = 0$,15 ,30 ,45 ,60 ,75 and 90 , for tap location C1.

The results in Figure 6-3 implies that better performance of the QS-prediction can be observed in cases where the upstream turbulence has larger length scales. In other words, it is the large length scales of upstream turbulence that are expected to be represented by the QS model in predicting the roof surface pressure fluctuation. This expectation can again be seen by reviewing the coherence between the measured and QS-estimated roof surface pressures (see Figure 5-8) and the associated discussion in Section 5.3.3. In order to filter out the large scale turbulence, the moving average technique is applied to smooth the raw time series of each velocity component in this chapter, i.e.,

$$\mathbf{u}_s(t) = \frac{1}{N_s} \sum_{i=1-Ns/2}^{Ns/2} \mathbf{u}(t + i \cdot \Delta t), \tag{6-1}$$

where N_s denotes the temporal window size used in smoothing; $\mathbf{u}_s(t)$ denotes the smoothed version of the raw velocity vector $\mathbf{u}(t)$ at time t; Δt denotes the time step increment and equal to the inverse of the sampling rate, i.e., $1/f_s$. This moving average technique is relatively straightforward and has been used as a low pass-filter for signal processing, e.g., the low-pass filter for the pressure signals used in Asghari-Mooneghi et al. (2016). No time-lag of the smoothed signals is observed by using the moving-averaging technique of Eq. (6-1). This provides an advantage as compared to other types of low-pass filters that generate a time-lag of the smoothed signals, e.g., the Butter-Worth filter used in Banks and Meroney (2001).

It is also worthwhile to see the frequency response of moving-average filter of Eq. (6-1), as it is directly related to the re-distribution of turbulence energy along the frequency, or alternatively, the length scale axis (e.g., Figure 6-2 (a)) for the smoothed velocities. If the cut-off length, L_c, is specified in order to extract turbulence energy of length scale larger than the cut-off length, the corresponding window size used in moving-average Eq. (6-1) can be calculated, i.e.,

$$N_s = \frac{L_c f_s}{\bar{u}_{\mathrm{m}}}, \tag{6-2}$$

where f_s denotes the sampling rate of the velocity signal and $\overline{u}_{\mathrm{m}}$ is the mean stream-wise velocity measured at location *m* (see Figure 6-1). Once the window size and the sampling rate are established, the theoretical frequency response of the moving averaged filter can be determined (see e.g., Asghari Mooneghi et al., 2016), i.e.,

$$H\left(f/f_s\right)=\frac{\sin\left(N_s\pi f/f_s\right)}{N_s\sin\left(\pi f/f_s\right)} \quad \text{for} \quad 0<f\le f_s/2\,, \tag{6-3}$$

where $H(f)$ denotes the response at frequency, f. The corresponding ratio of the spectra of the smoothed signal to the spectra of the raw signal is in fact the squared values of the frequency response. Figure 6-4 shows an example of the spectra ratio (i.e., transfer function) for the smoothed velocity obtained by applying cut-off length equal to 5 building height, i.e., $L_c = 5H$. Note that for length scales larger than 20 times of the cut-off length (100 *H*), the energy level is unchanged for smoothed velocity. For length scales smaller than 20 L_c, however, the spectra ratio start to decrease and down to zero at the length scale equivalent to the cut-off length.

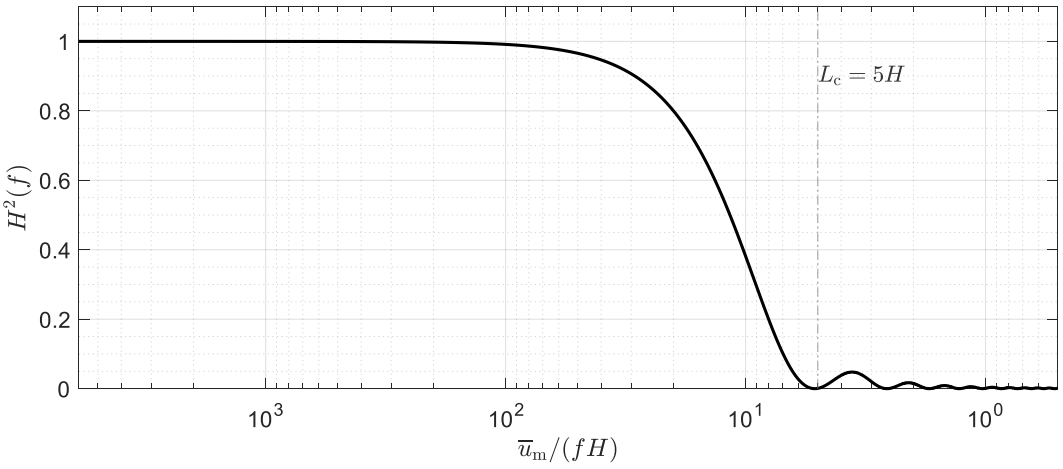

Figure 6-4: The ratio of spectra of smoothed velocity to the spectra of raw velocity with cut-off length (L_c) equal to 5 building height.

By reviewing the coherence between the QS-predicted and measured roof surface pressure fluctuations shown in Figure 5-8, it is found that the coherence decreased to zero

for the multiple area cases near the roof corner at length scale of 5*H*. Hence, the poorly correlated part of the QS-prediction on the small-length-scale pressure fluctuation can be removed by applying moving average on the raw velocity with L_c = 5 *H*. The performance of the QS-model with smoothed velocities is examined again for point location C1 by comparing the measured $\langle Cp_{\text{inst}} | \theta, \beta \rangle$ to the QS function $Cp_{\text{inst}}(\theta)$. As shown in Figure 6-5, there clearly improved matches between $\langle Cp_{\text{inst}} | \theta, \beta \rangle$ and $Cp_{\text{inst}}(\theta)$, as compared to the results obtained from raw velocity signals (see Figure 6-3). Better matches between $\langle Cp_{\text{inst}} | \theta \rangle$ and $Cp_{\text{inst}}(\theta)$ as a result of low-pass filtering the velocity signals were also reported by Banks and Meroney (2001), although the 5-th order Butter-Worth low-pass filtered was used in their approach.

Note that the effect of the upward wind direction (i.e., the positive elevation angle) on the measured values of $\langle Cp_{\text{inst}} | \theta, \beta \rangle$ is generally not altered by using moving averaged velocities with L_c = 5*H*, as can be observed by comparing the results shown in Figure 6-5 to those in Figure 6-3. However, if the cut-off length is further increased, the effects of wind elevation angle may not be observed because the length scale of most of the vertical velocity fluctuation may be smaller than the cut-off length (see an example of the comparison between the cut-off length and fluctuation length scale in Figure 6-2 (a)).

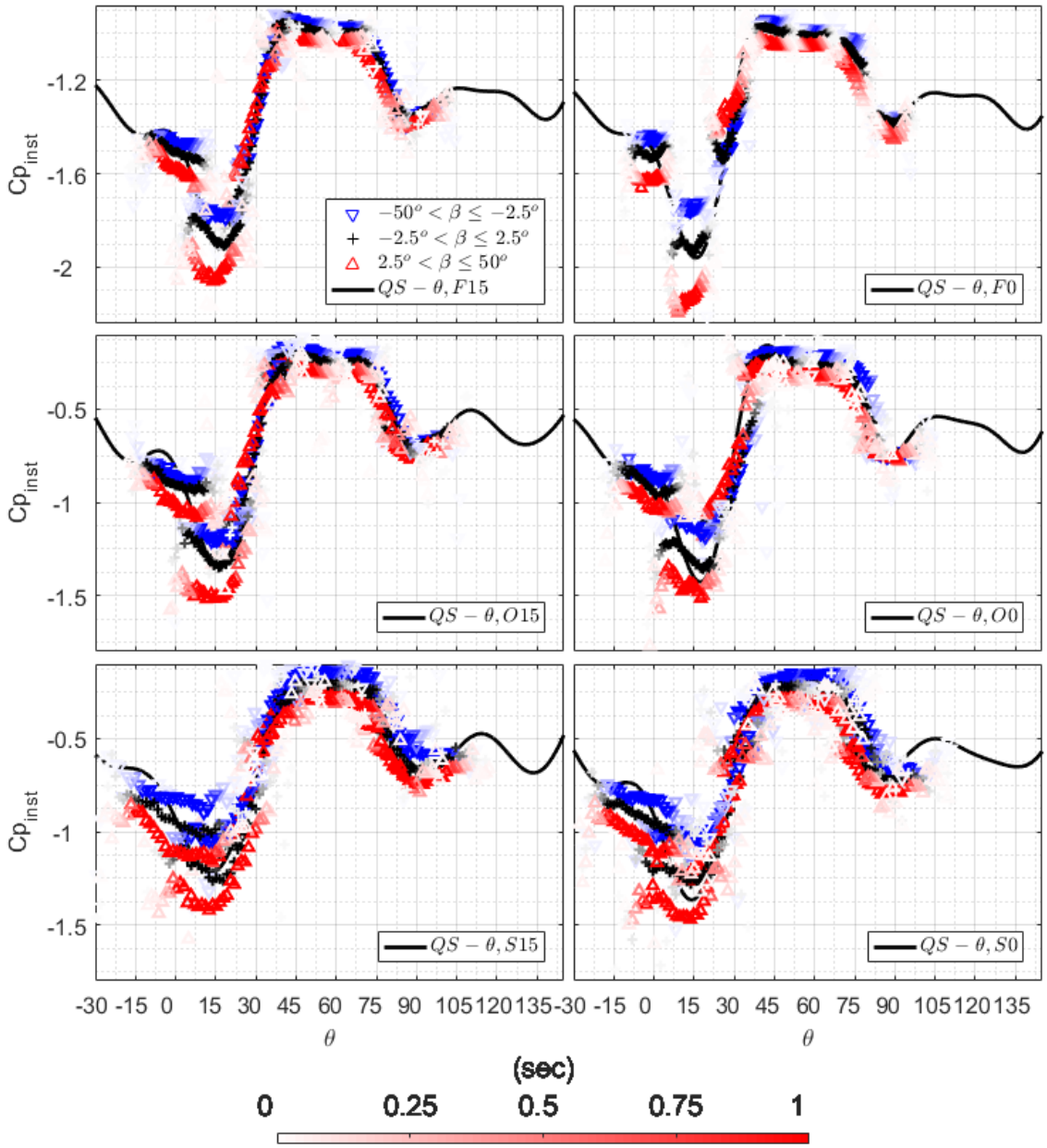

Figure 6-5: The instantaneous function $Cp_{\text{inst}}(\theta)$ of the QS model established from each of the six upstream terrain conditions, along with the conditionally averaged values $\langle Cp_{\text{inst}} | \theta, \beta \rangle$ obtained from moving averaged velocities (with $L_c = 5H$) and pressure measurements at mean wind azimuths $\bar{\theta} = 0$,15 ,30 ,45 ,60 ,75 and 90 , for tap location C1.

As shown by Letchford et al. (1993) and the investigation in Chapter 5, the QS-model more accurately predicts the roof surface pressure fluctuations on a panel area, than for a point location. Because of this, the focus of the following discussions are switched to the panel areas specified in Figure 6-1. Pressures obtained from the panel areas including 9 taps near the roof corner (C9) and near the leading edge of the long wall (L9) are considered. Note also that the QS model established in terrain O0 is now selected for predicting pressures under other terrain conditions for the following discussions. Though the appropriate use of the QS theory should be based on the QS-model established under the identical upstream turbulence condition. These 'cross-terrain' applications of the QS-model are based on the assumption that the variation of upstream turbulence characteristics does not have any significant aerodynamic effects. The justification of this statement is deferred to the beginning of the next section. However, this assumption is applied for the remainder of the discussion in this section.

In order to examine the effects of the smoothed velocities, the coherence between the measured and QS-predicted, area-averaged roof surface pressures is first investigated. Pressures obtained from the roof panel C9 and mean wind azimuth $\bar{\theta} = 15$ provide the first set of results, as shown in Figure 6-6 (a); The second set of results, as shown in Figure 6-6 (b), are obtained from panel area L9 and $\bar{\theta} = 0$. QS-predictions for pressures induced by upstream turbulence conditions F0, O0 and S15 are discussed for brevity. For QS-predictions using instantaneous velocity signals (see green dots in Figure 6-6), the coherence values are maximum for length scales larger than 100 *H* and start to decay for length scale smaller than 100 *H*, vanishing at the cut-off scale of 5*H*. Applying the moving average to the instantaneous velocities using cut-off length $L_c = 5H$ and QS-Θ-β model leads to almost identical coherence values (see black lines in Figure 6-6).

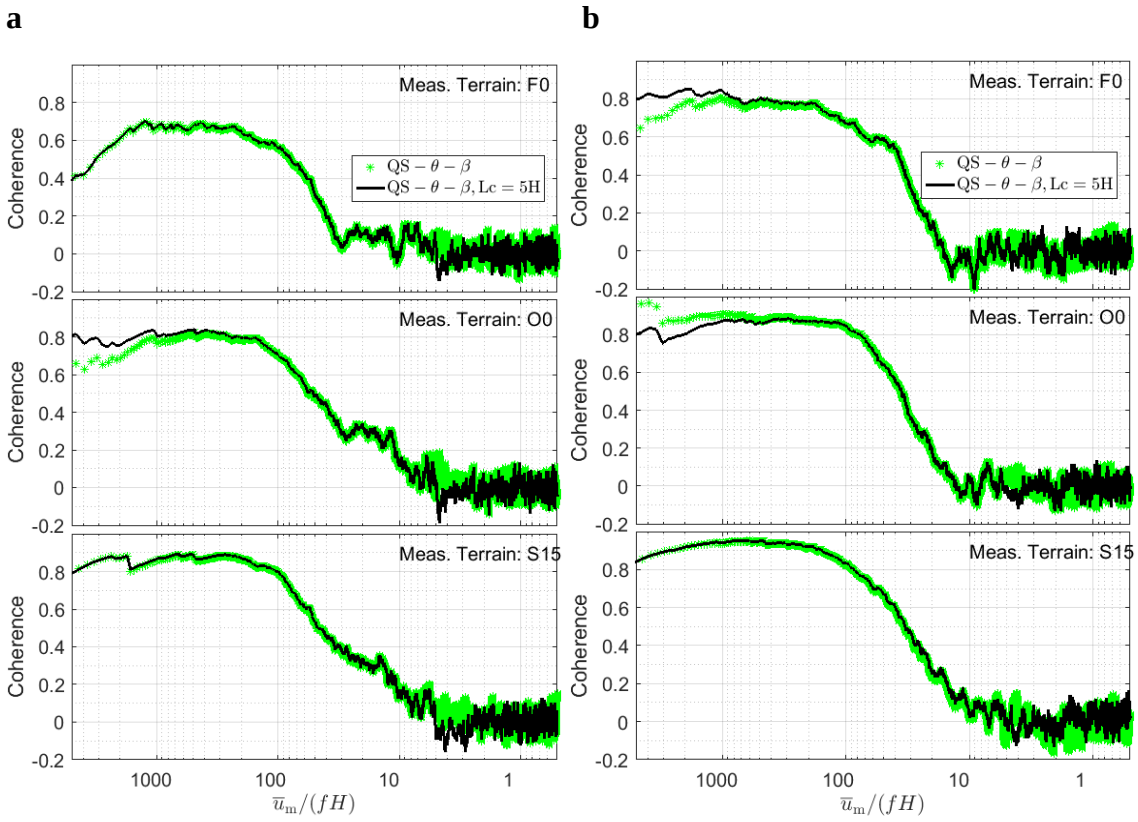

Figure 6-6: The coherence between the measured and predicted area averaged pressures (QS-θ-β model established in O0, with $L_c = 5H$ and without filter): (a) roof area C9, $\overline{\theta} = 15$; (b) roof area L9, $\overline{\theta} = 0$.

Figure 6-7 further shows the time-lag correlation coefficients of the QS-prediction for scenarios used in Figure 6-6. It shows that the maximum correlation coefficient of prediction can be improved by up to 10% via using the smoothed velocities in the QS model. This observation indicates that the improved correlation of the predicted pressures are the results of removing non-physical predictions obtained from the small-scale turbulence while retaining the good predictions obtained from the large-scale turbulence.

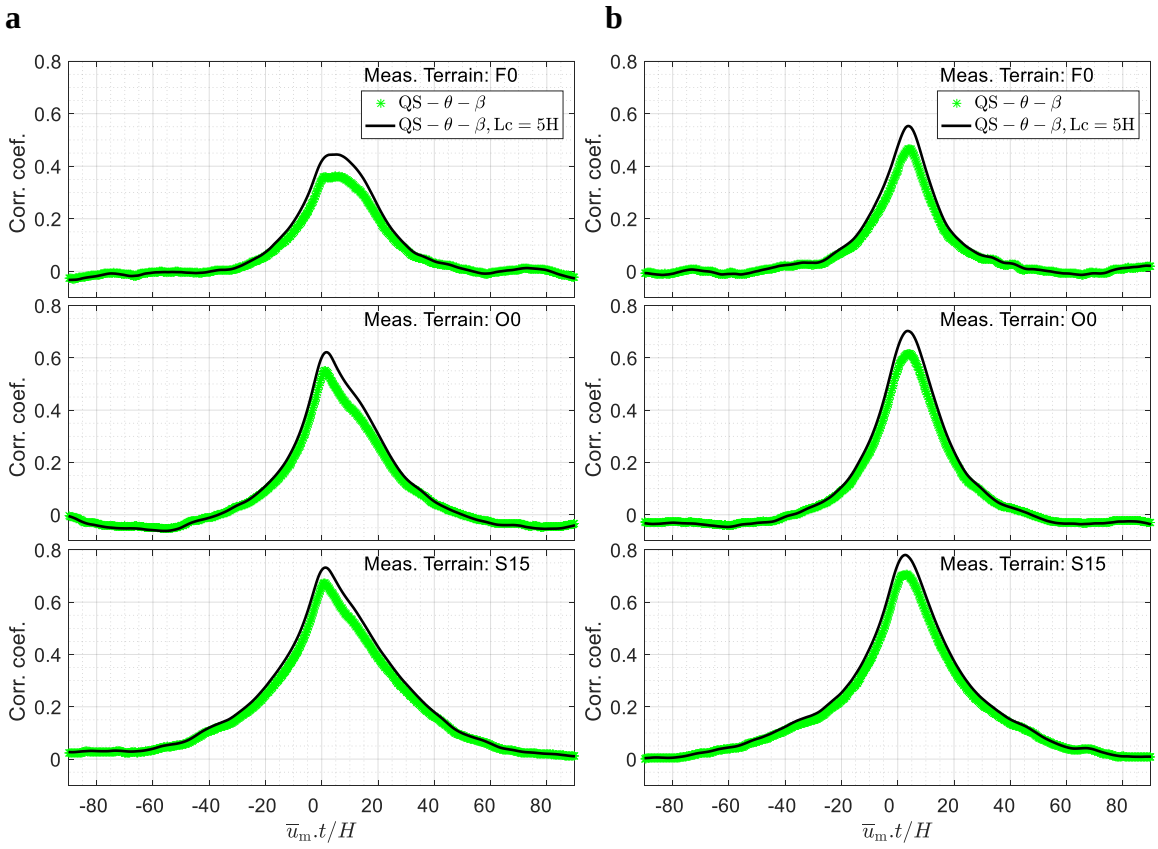

Figure 6-7: The time-lag correlation coefficients between the measured and predicted area averaged pressures (QS-*Θ*-*β* model established in O0, with $L_c = 5H$ and without filter): (a) roof area C9, $\overline{\theta} = 15$; (b) roof area L9, $\overline{\theta} = 0$.

Figure 6-8 shows the ratio of QS-predicted spectra to the measured spectra of the fluctuating pressures (i.e. transfer functions) for the same scenarios used in Figure 6-6. For the predictions using instantaneous velocities (see green dots), the spectral ratios are generally near unity for length scales larger than 10*H*. However, the use of instantaneous velocities in the QS model generally overestimate the pressure fluctuations for length scales smaller than 10*H*, and could be more than twice of the actual fluctuation for length scale less than 1*H*. By using the smoothed velocities in the QS model, the results for the spectral ratios are also plotted using the black lines. As can be observed, the uncorrelated (see Figure 6-6) and overestimated (Figure 6-8) small-length-scale fluctuations predicted using instantaneous velocities are eliminated by the low-pass filter of the moving average.

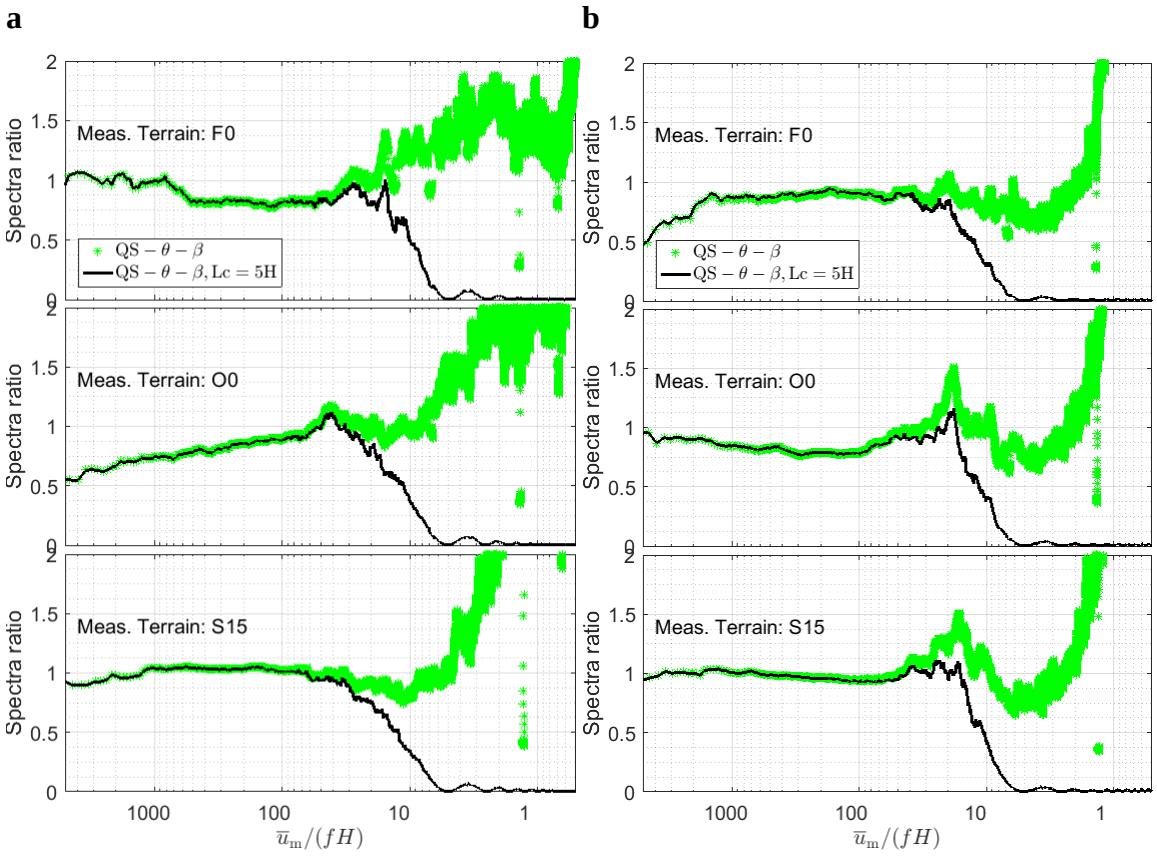

Figure 6-8: The ratio of QS-predicted pressure spectra to the measured pressure spectra. (Note: QS-θ-β model established in O0, with $L_c = 5H$ and without filter). (a) roof area C9, $\overline{\theta} = 15$; (b) roof area L9, $\overline{\theta} = 0$.

Although the use of smoothed velocities in the QS-model improves the correlation coefficients between the predicted and measured pressures (see Figure 6-7), the significant missing portion of the small length scale fluctuation (see Figure 6-8) may raise the question of overall underestimation of the predicted pressure fluctuation. In order to check this drawback, the probability density function (PDF) of the measured and QS-predicted pressures (with both of the instantaneous and smoothed velocities) of the same scenarios are further shown in Figure 6-9. It shows that using the smoothed velocities in the QS model leads to slightly underestimated tail values of the PDFs of the predicted pressures. This implies that the small-length-scale pressure fluctuations account for a relatively minor portion of the overall fluctuation for the area-averaged pressures and, hence, ignoring small-length-scale fluctuations in the QS model does not

lead to significant underestimation of the predictions. Note also that both of the QS-predicted PDF's nearly agree the PDF of the measured pressures.

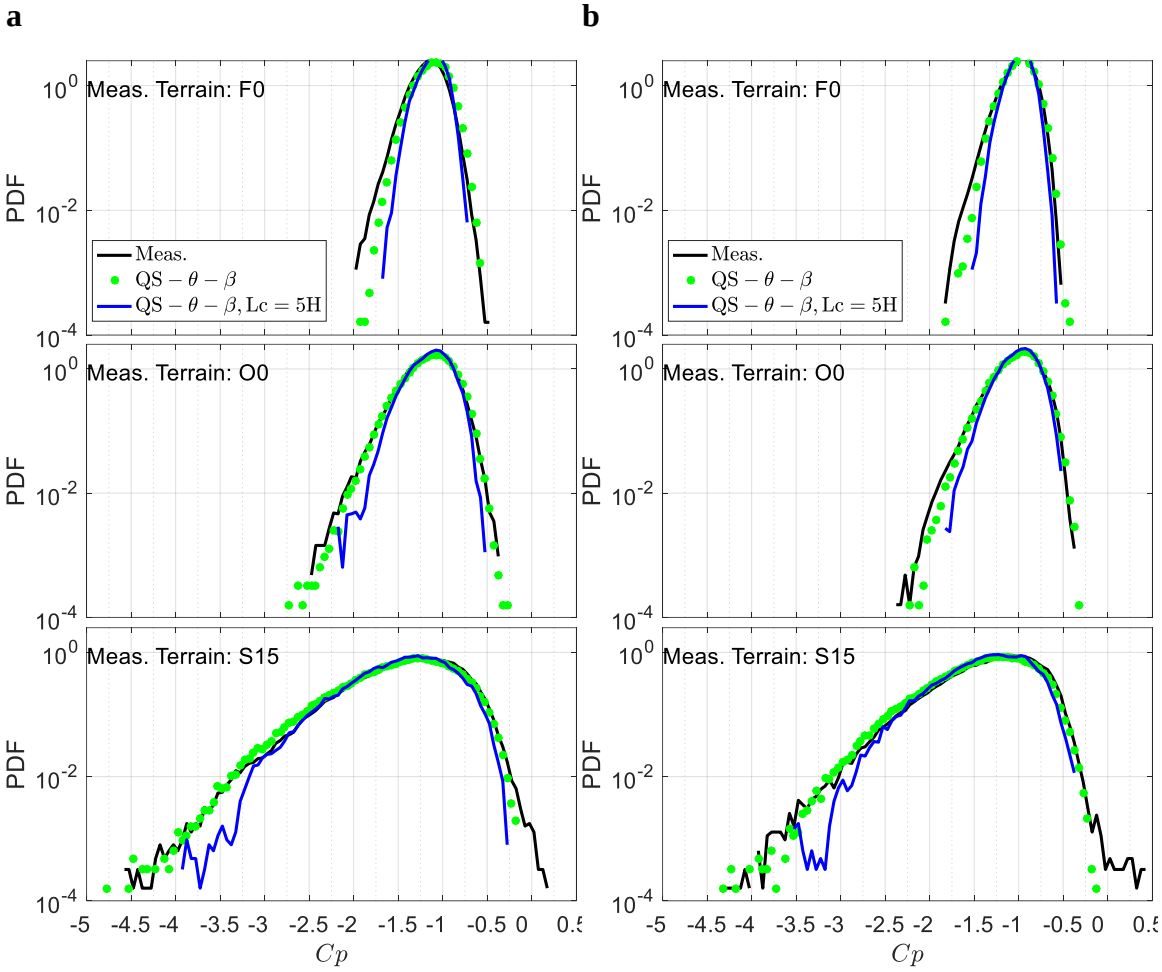

Figure 6-9: The PDF of measured and predicted area averaged pressures (QS-*Θ*-*β* model established in O0, with L_c = 5*H* and without filter): (a) roof area C9, $\bar{\theta} = 15$; (b) roof area L9, $\bar{\theta} = 0$.

6.3 Estimation of roof surface pressure fluctuations under different ABL turbulence conditions

In the typical application of the QS theory, the model used in prediction should be established under the identical upstream turbulence condition. However, it would be more convenient and practically valuable if the QS model established in one turbulence condition could also be applicable for other turbulence conditions. However, this assumption requires that the variation of the upstream turbulences do not significantly alter the aerodynamic mechanisms such that the use of the instantaneous function, i.e., $Cp_{\text{inst}}(\theta,\beta)$, established in one turbulence condition can be used for another.

In this section, the QS model established in upstream terrain condition O0 is used for estimating the fluctuating pressures induced by turbulence generated from other terrain conditions. The selection of terrain O0 is simply based on its median degree of roughness level among the six terrains. In order to justify the selection, the two critical functions in the QS model that account for the variation of wind azimuth, i.e., $Cp_{\text{inst}}(\theta)$, and elevation, i.e., $B(\theta)=\langle dCp_{\text{inst}}/d\beta \mid \theta\rangle$, established under the six upstream terrain conditions are plotted in Figure 6-10 and Figure 6-11, respectively, for each panel area shown in Figure 6-1. Note that the procedures in obtaining the $Cp_{\text{inst}}(\theta)$'s and $B(\theta)$'s are already demonstrated in Chapter 5. As shown in Figure 6-10, the $Cp_{\text{inst}}(\theta)$ curves obtained from each of the six upstream terrains generally collapse, although small differences between each other can be observed. Similar conclusion can be observed for the $B(\theta)$ function shown in Figure 6-11, except for terrain F0. Upstream terrain F0 seems to produce higher magnitudes of $B(\theta)$'s for all of the selected panel areas. In summary, the selection of terrain O0 for establishing the QS-model should be appropriate for the pressure predictions for other upstream terrain conditions.

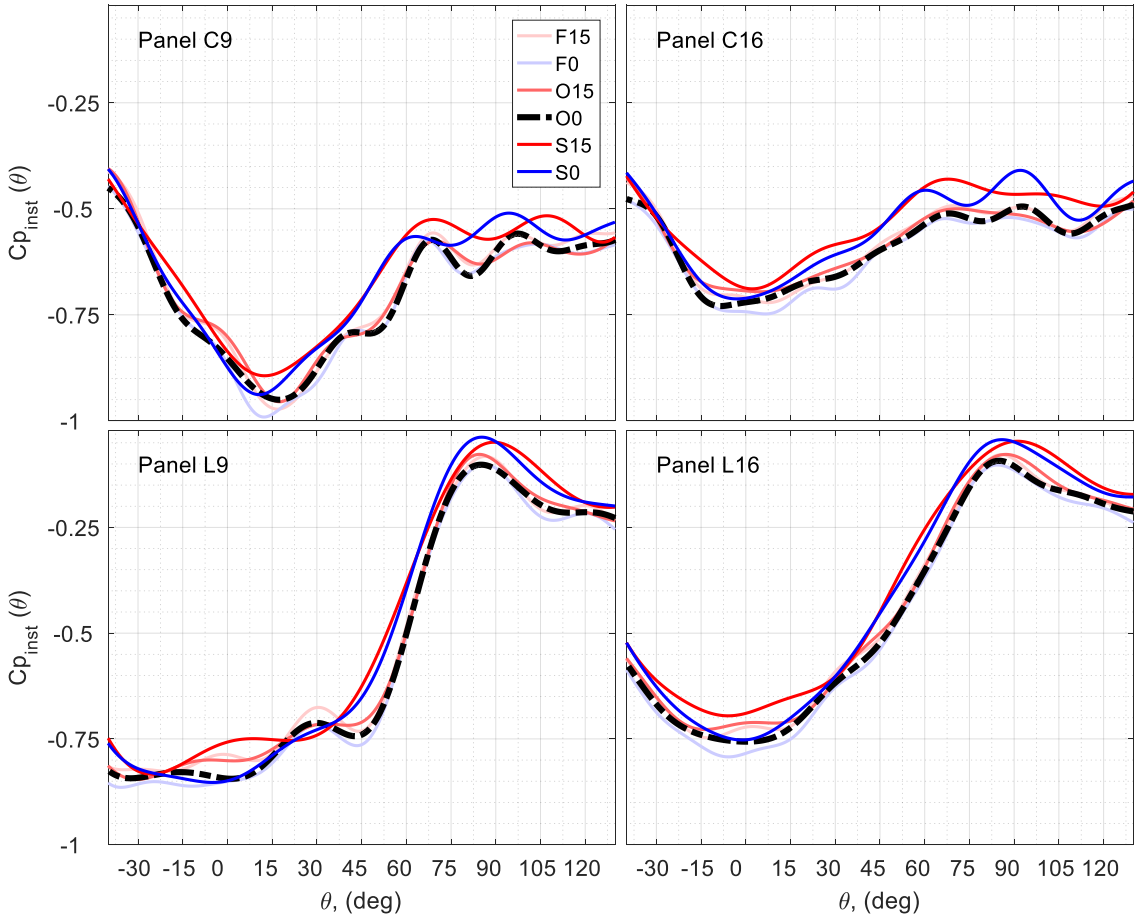

Figure 6-10: Instantaneous function $Cp_{\text{inst}}(\theta)$ used in the QS model obtained from the six upstream terrain conditions for panel areas C9, C16, L9 and L16.

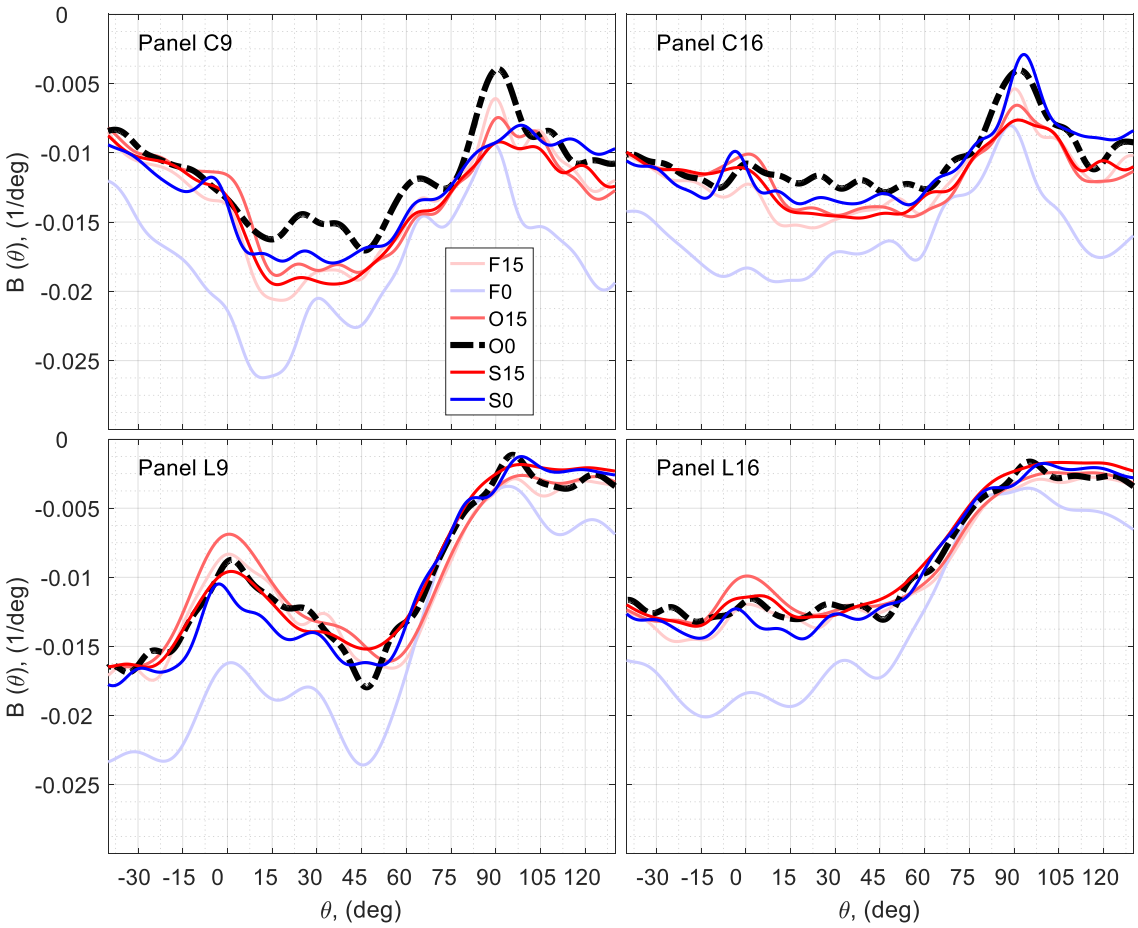

Figure 6-11: $B(\theta)$ (or $\langle dCp_{\text{inst}}/d\beta\,|\,\theta\rangle$) function in the QS model obtained from the six upstream terrain conditions.

In order to quantify the pressure fluctuations, the root mean square, rms(Cp), and the peaks, |min(Cp)|, of the measured and QS-estimated pressures are presented for panel areas C9, C16, L9 and L16 in Figures 6-12, 6-13, 6-14 and 6-15, respectively. Note that the peak values are defined so that the probability of exceedance is equal to 0.01%. The rms values shown in the figures are amplified by 4 times, for visibility. The correlation coefficients between the measured and QS-predicted pressures are also attached in these figures.

For area-averaged pressures measured on the corner panels, i.e., C9 in Figure 6-12 and C16 in Figure 6-13, the fluctuations are nearly uniform for all mean wind azimuths being considered. For the leading edge panels, i.e., L9 in Figure 6-14 and L16 in Figure 6-15,

however, the pressure fluctuations are higher for the separated flow scenarios (i.e., $\bar{\theta} \le 60$) while being reduced for reattached flow scenarios (i.e., $\bar{\theta} > 60$). Increased pressure fluctuations are mainly due to the increased levels of upstream turbulence intensity (Figure 6-2), as can be observed for all panel cases (i.e., Figures 6-12 to 6-15). Increased length scales in the upstream turbulence, on the other hand, can increase the pressure fluctuations as well, although the degree of influence is less than that of turbulence intensity. In fact, increasing turbulence length scales can increase the spatial correlation of point pressures and, hence, enhance the overall fluctuations of the area-averaged pressures. To further visualize this statement, the spatial, zero time lag correlation coefficients between pressures measured at tap C1 and other locations on the building surface are shown in Figure 6-16 for mean azimuth $\bar{\theta} = 15$. Similar plots are generated for tap location L1 and shown Figure 6-17 for $\bar{\theta} = 0$. It can be clearly seen that, as the turbulence length scale increases, the area of high spatial correlation expands for the region near the target tap location.

The zero time lag correlation coefficients (Corr. Coef.) between the QS-predicted and measured pressures are attached in Figures 6-12 to 6-15 as well, where the level axes are attached on the right hand side of these plots. Note that the smoothed velocities with L_c = 5H are used in the QS-model for pressure predictions. For roof corner panels, i.e., C9 in Figure 6-12 and C16 in Figure 6-13, near uniform correlations can be found for all mean wind azimuths being considered. For the leading edge panels, i.e., L9 in Figure 6-14 and L16 in Figure 6-15, higher correlations can be found for separated flow scenarios (i.e., $\bar{\theta} \le 60$). The correlation starts to decrease as the mean wind azimuth further increases for $\bar{\theta} > 60$, reaching the minimum value for the reattached flow scenario, i.e., $\bar{\theta} = 0$. Recall that the surface pressures under the reattached flows are dominated by the ambient static pressure just above the roof, as shown in Section 4.3.2. Hence, the low correlation of the QS-prediction for pressures governed by the reattached flows can be partially due to the missing consideration of the instantaneous static pressures above the panel. Increasing length scale of the upstream turbulence improves the correlation of the QS-predicted pressures, as can be seen for all panel cases shown in Figures 6-12 to 6-15. This again demonstrates that the QS model performance improves in capturing the effects

of large-length-scale turbulence. Pressures averaged over larger panels areas (i.e. C16 and L16) have higher correlation to the QS-predictions. Shorter distances from the probe location, *m*, to the target panel area (see Figure 6-1) also improve the correlation of the QS-prediction, although the influence is minor for the current panel cases being examined.

The rms and peak of the QS-predicted pressures are also shown in Figures 6-12 to 6-15 for all panel cases. The overall fluctuations represented by rms(*Cp*)'s agree well with the QS-predictions. Hence, the QS model used here can account for most of the effects of the upstream turbulence on area-averaged surface pressure fluctuations. The overall trends of the QS-predicted peak pressures, i.e., |min(*Cp*)|'s, generally match the measured values. However, some underestimations can be found for the QS-predicted peaks. Relatively significant underestimation of the QS-predicted peak pressures can be found for the separated flow scenarios in suburban terrains (i.e., S0 and S15), i.e., up to 20% of underestimation for C9 and L9 and 15% of underestimation for C16 and L16. These underestimations may be in part due to the missing consideration of the small scale vortices generated from the leading edges. However, the effects of small-scale vortices are reduced as the panel area increases. As can be seen for larger panel cases (i.e., C16 and L16), the QS-predicted peaks matched better to the measured values and the degree of underestimations are reduced.

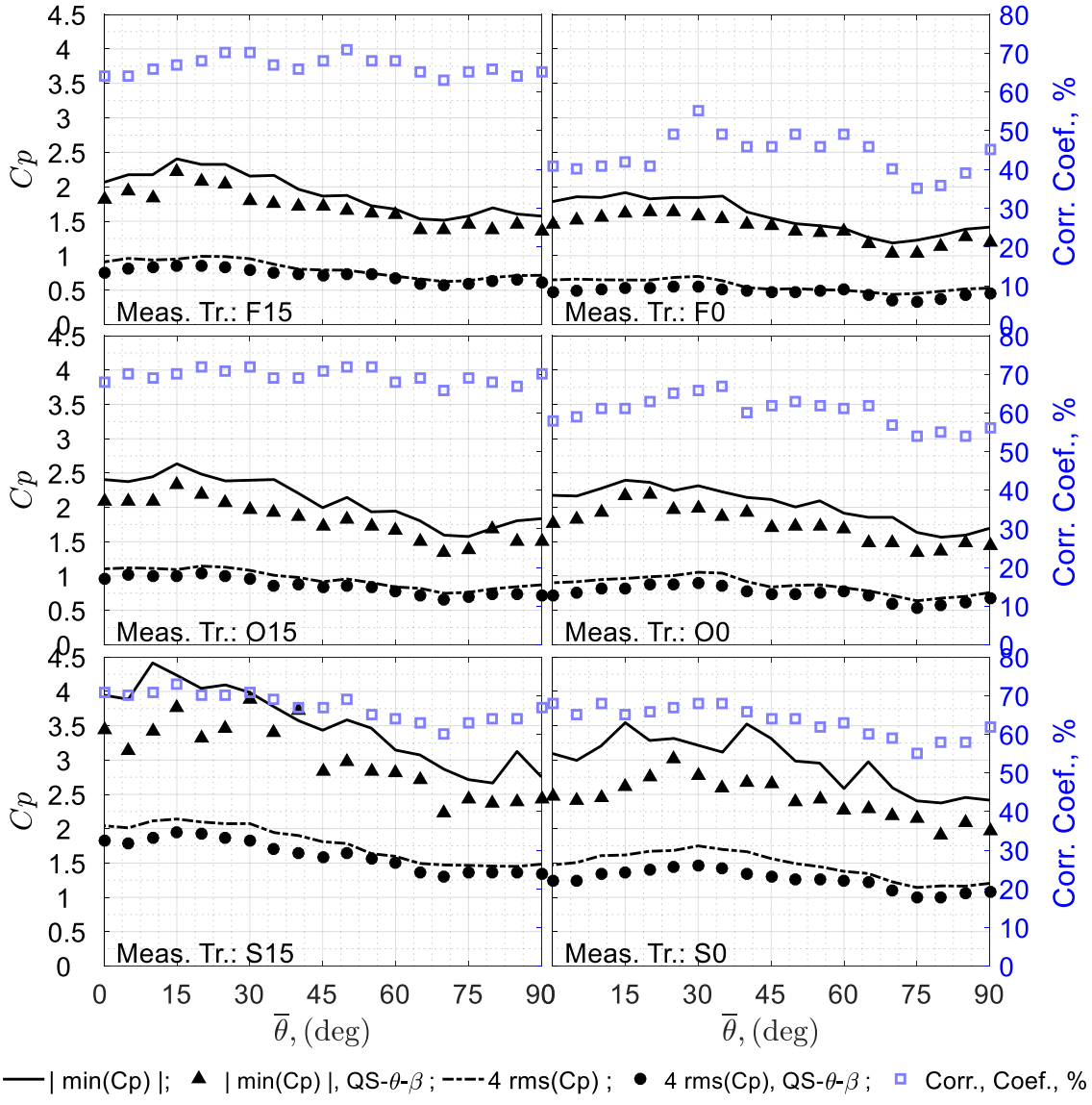

Figure 6-12: Peaks and 4 times of root mean squares (rms) of the measured and the QS-Θ-β estimated Cp over area C9 (with L_c = 5 H), along with the correlation coefficient (right hand side y-axis) between measurements and the QS model.

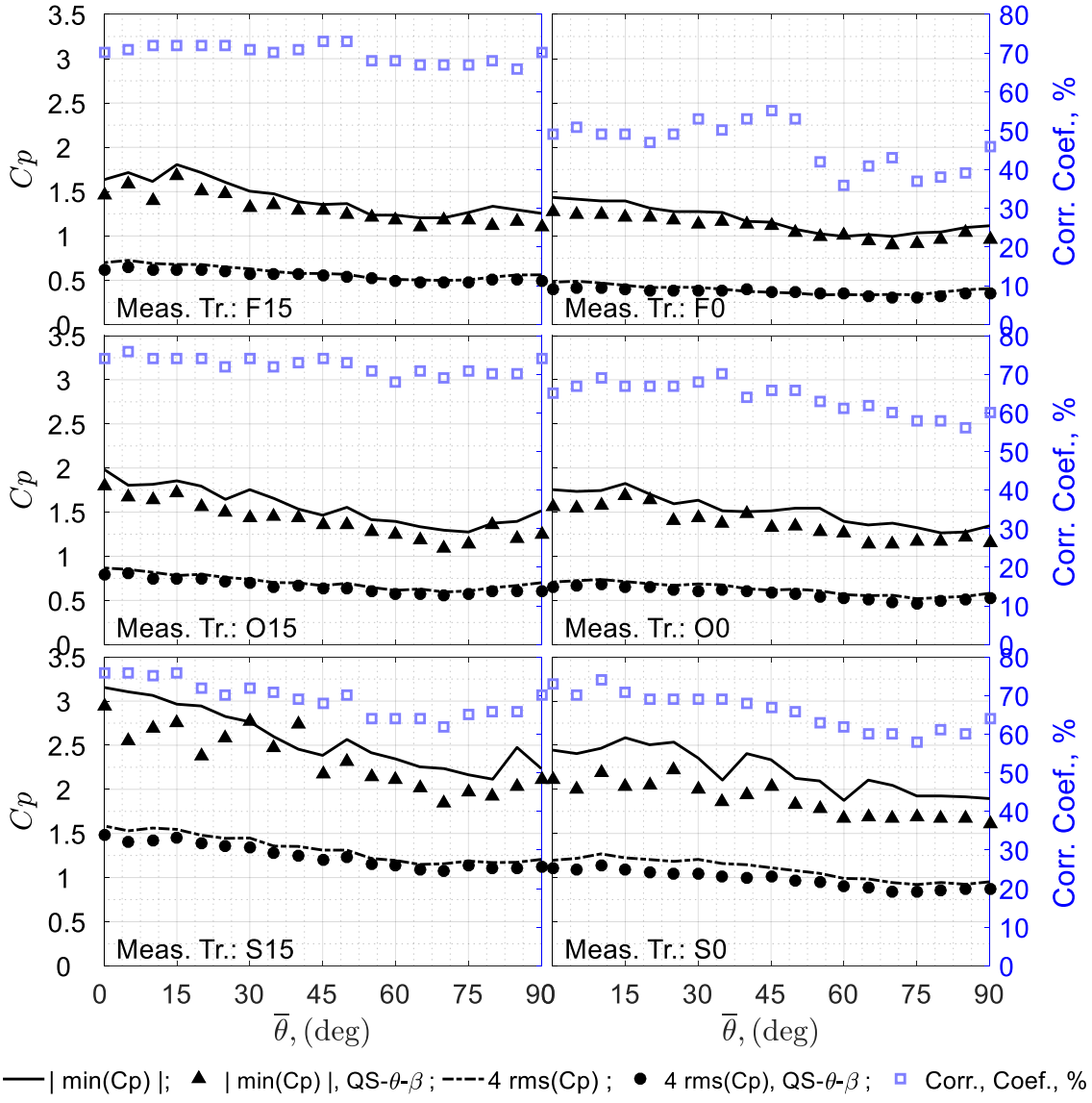

Figure 6-13: Peaks and 4 times of root mean squares (rms) of the measured and the QS-Θ-β estimated Cp over area C16 (with L_c = 5 H), along with the correlation coefficient (right hand side y-axis) between measurements and the QS model.

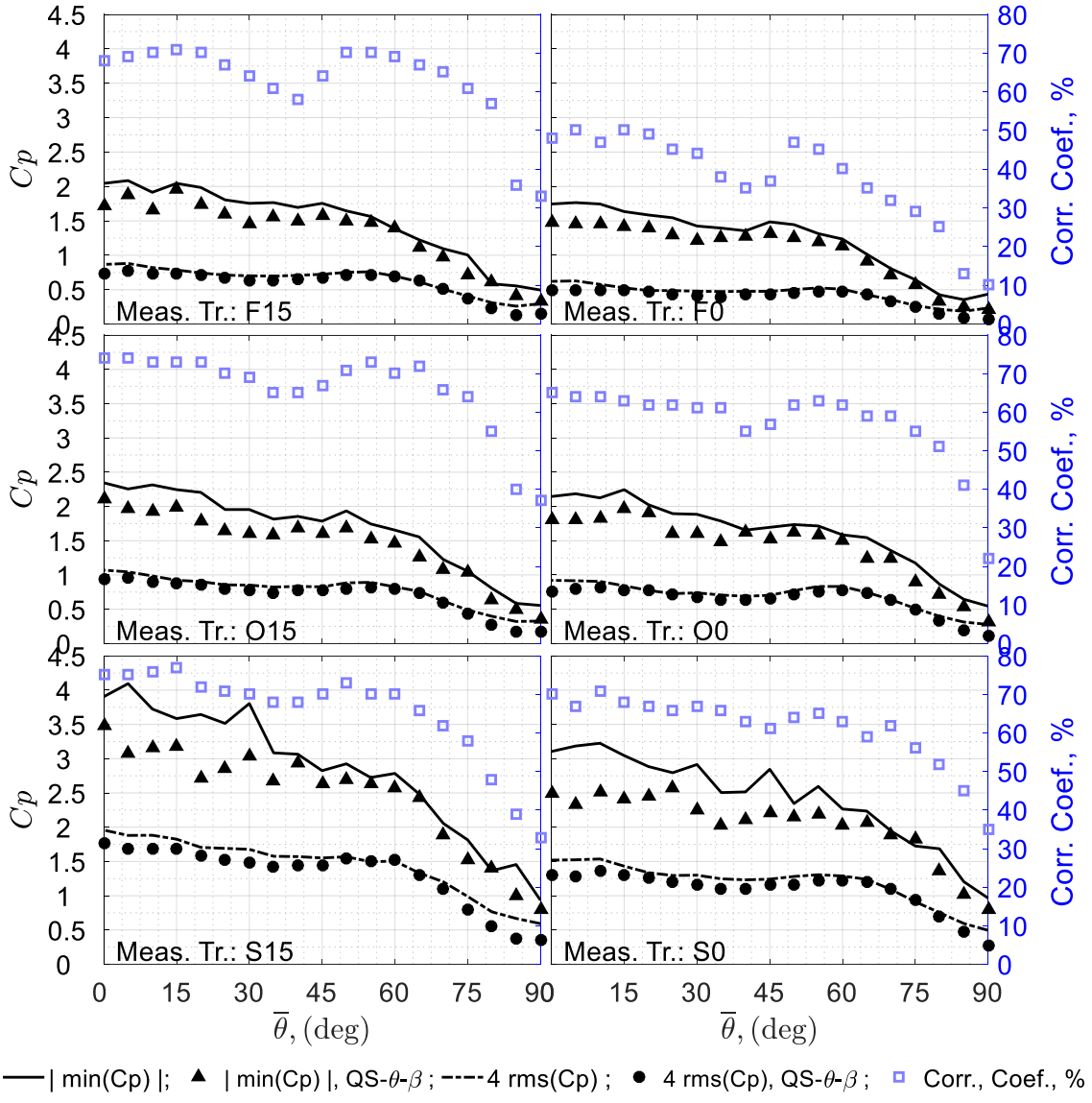

Figure 6-14: Peaks and 4 times of root mean squares (rms) of the measured and the QS-Θ-β estimated Cp over area L9 (with L_c = 5 H), along with the correlation coefficient (right hand side y-axis) between measurements and the QS model.

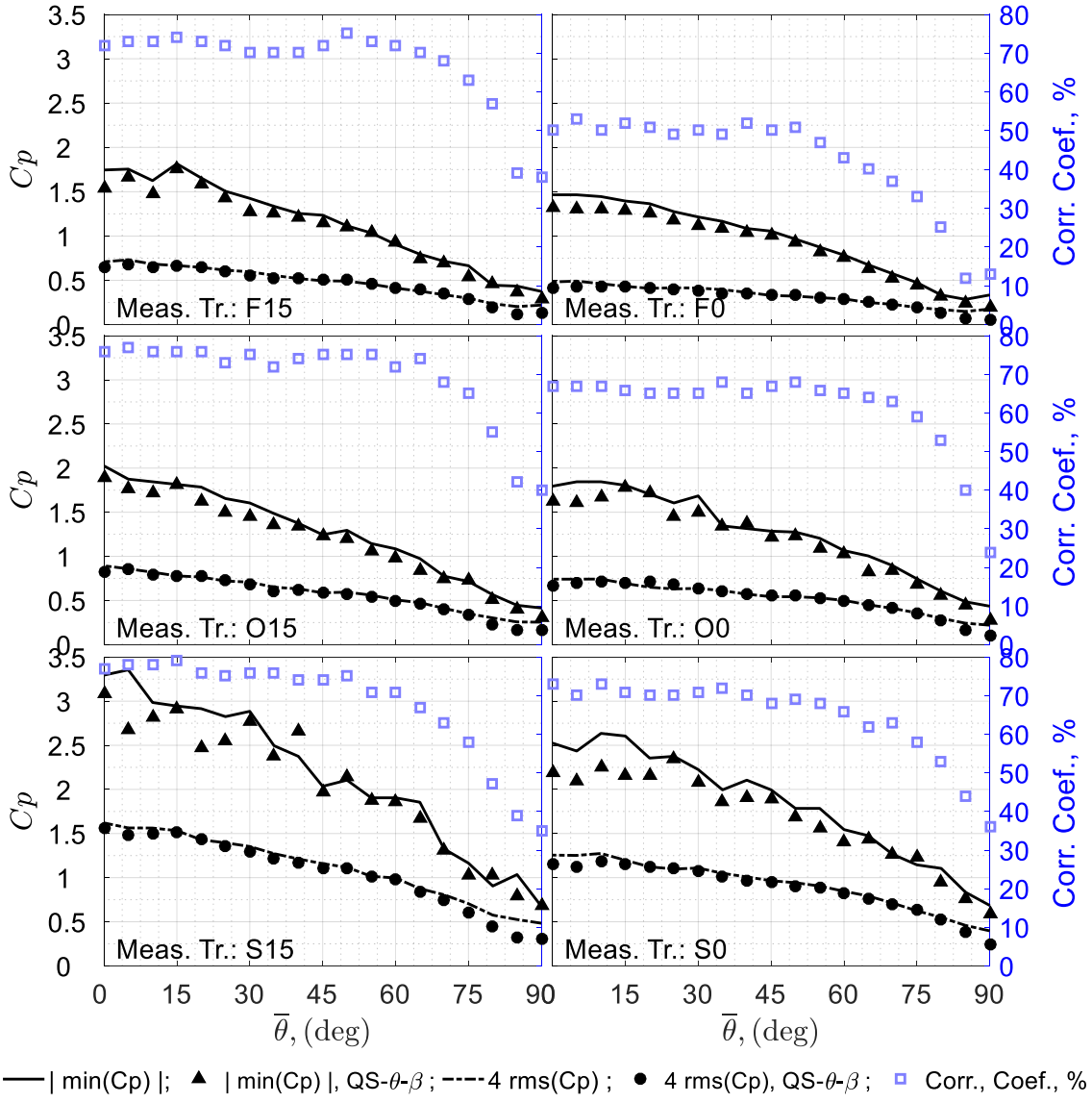

Figure 6-15: Peaks and 4 times of root mean squares (rms) of the measured and the QS-Θ-β estimated Cp over area L16 (with L_c = 5 H), along with the correlation coefficient (right hand side y-axis) between measurements and the QS model.

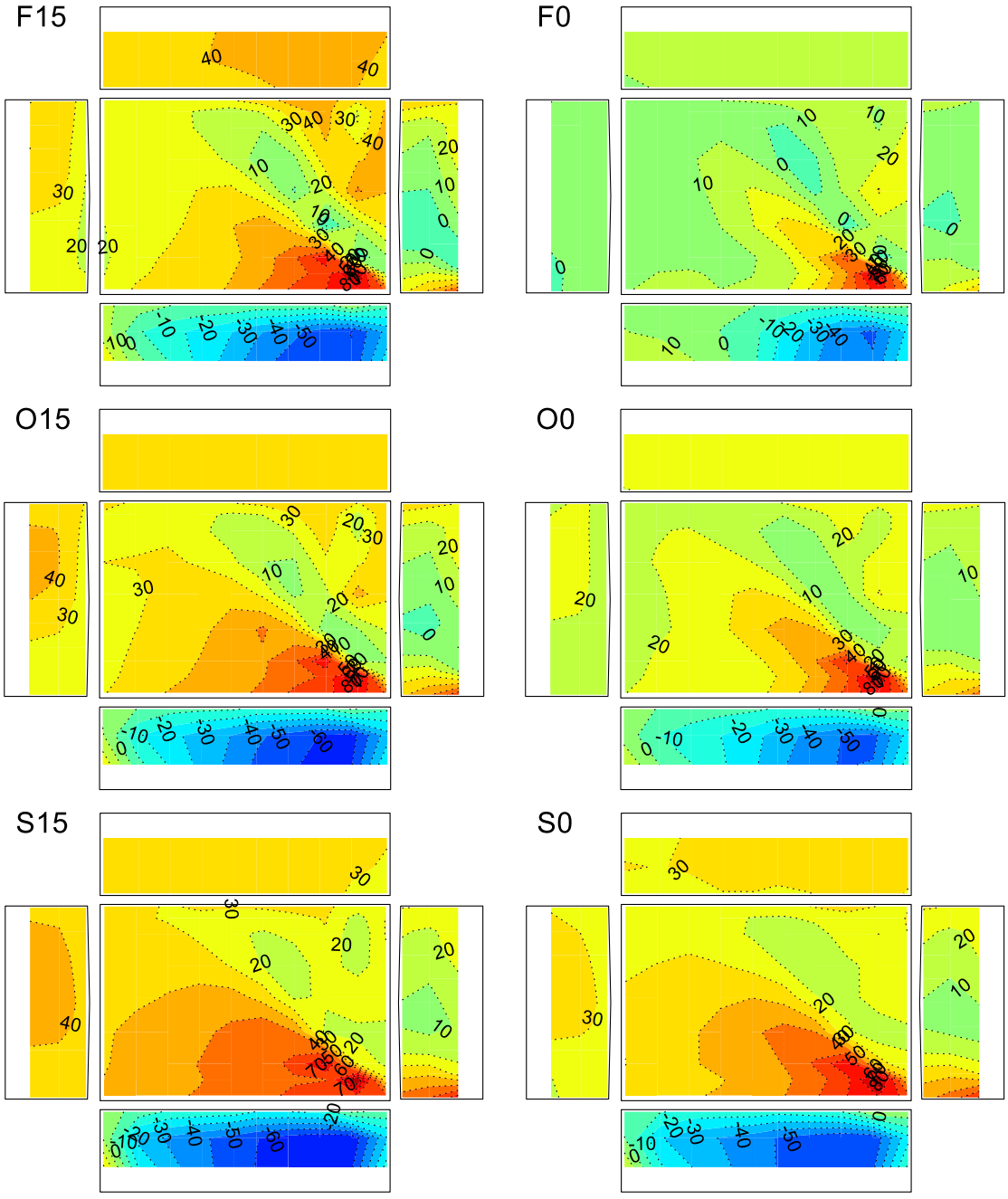

Figure 6-16: Contour of zero time lag correlation coefficients (%) between pressures measured at C1 and other surface locations, for all six terrain conditions and mean wind azimuth $\bar{\theta} = 15$.

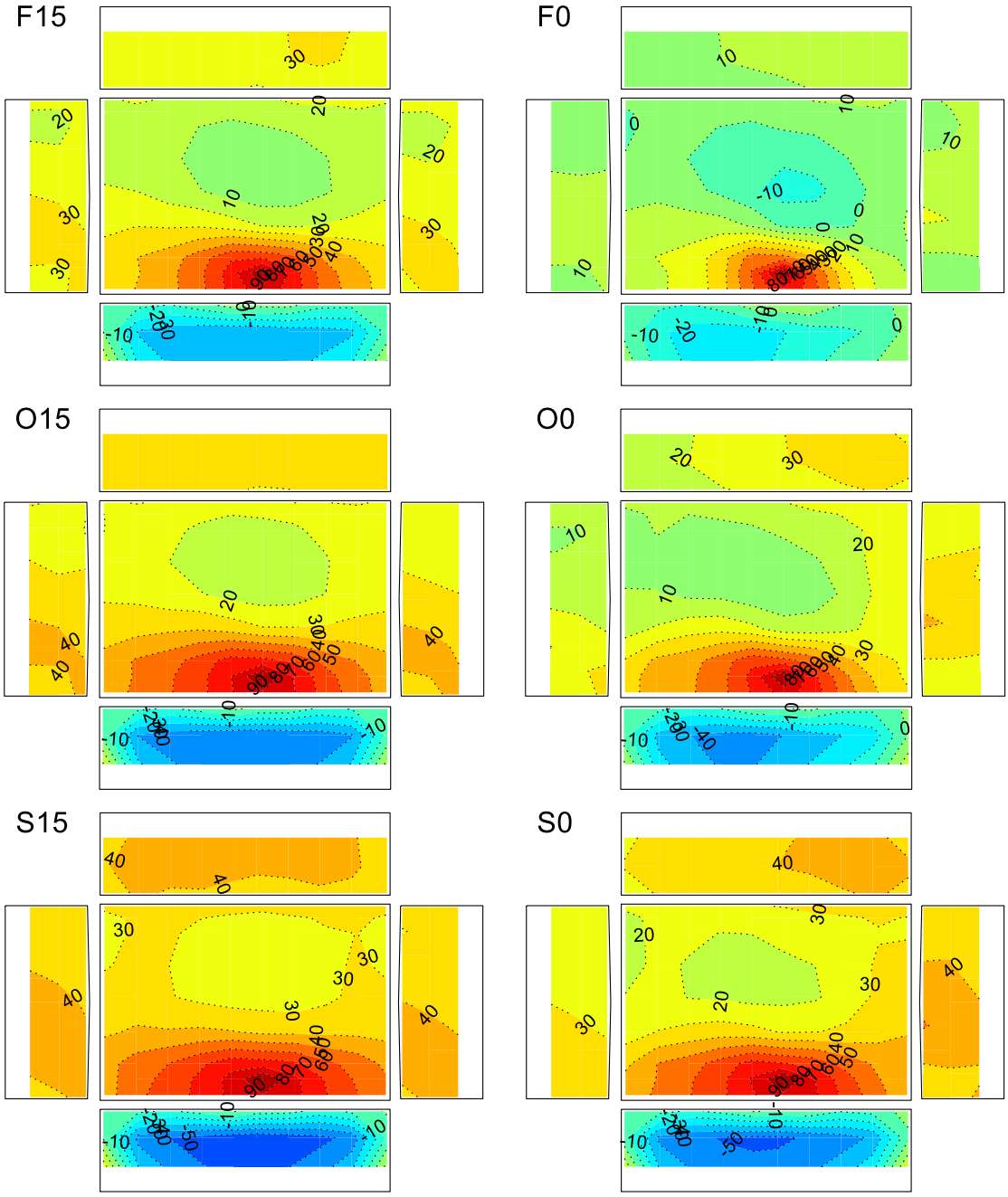

Figure 6-17: Contour of zero time lag correlation coefficients (%) between pressures measured at L1 and other surface locations, for all six terrain conditions and mean wind azimuth $\bar{\theta} = 0$.

6.4 Summary

The quasi-steady (QS) model is known to work better for capturing the effects of large scale turbulence on the roof surface pressure fluctuations. This is due to the fact that small-scale turbulence measured relatively far away from building does not directly influence the pressure fluctuations on the roof. In fact, it is the small-scale vortices separated from the leading edge that correlate more to the surface pressure fluctuations, as shown by Akon (2017). These facts lead to the intent to remove the small-length-scale turbulence in QS- predictions in this chapter, while retaining the information of the large length scale turbulences. Such a procedure is done by applying the moving average to the time series of each velocity component. The use of the smoothed velocities improves the QS-predictions by removing the uncorrelated prediction of small length scale pressure fluctuations. The cut-off length is selected as 5 building heights, for separating the small-length-scale turbulence from the large-length-scale turbulence. Appropriate cut-off lengths can be determined based on the length scale where the coherence between the measured and QS-predicted pressures vanishes.

The wind-induced fluctuating pressures on panels of different areas, near the roof corner and leading edge are examined in this chapter for the six upstream turbulence conditions. It is found that the fluctuation of area-averaged pressures is dominated by the intensity of the upstream turbulence and to a lesser degree by the turbulence length scale. A QS model accounting for the magnitude, azimuth and elevation angles of the instantaneous wind vector is used to predict the fluctuation of the area-averaged pressures. It is found that the instantaneous function (of the QS model) established in terrain O0 is generally consistent with that obtained from other terrain conditions. This implies that the variations of the upstream turbulence do not alter the flow structure significantly so that the mean area-averaged pressure coefficients are nearly similar. Based on this observation, the QS model established from terrain O0 is used to predict the pressure fluctuations induced by turbulences generated from other terrain conditions.

The ‘cross-terrain’ QS-predictions of pressure fluctuations generally works well for the roof panels being examined. The QS prediction of the pressure root mean squares (rms) generally agree well to the measured values. Hence, the QS model used here can account

for most of the effects of the upstream turbulence on pressure fluctuations. However, underestimations up to 20% can be observed for the QS-predicted peak pressures for panels including 9 taps. These underestimations usually happen for panels beneath flow separation. Improved QS-predictions are observed for larger panel areas or, perhaps, by placing the velocity probe closer the target panel (although this has not been examined).

Chapter 7

7 Conclusions and recommendations

7.1 Conclusions

This thesis investigates the effects of the atmospheric boundary layer turbulence (ABL) on the roof surface pressures. For this reason, the six upstream turbulence conditions were generated in the Boundary Layer Wind Tunnel II in University of Western Ontario (UWO) in order to simulate the ABL turbulences featured by different intensities and length scales. The 1/50 geometrically scaled model of the Texas Tech University Wind Engineering Research Field Laboratory (TTU WERFL) building is used for surface pressure measurements in the wind tunnel. The intensities range from 10% to 30% and the integral length scale ranges from 6 to 12 times of the building height for the upstream turbulence near the roof height.

The effects of the atmospheric boundary layer (ABL) turbulence intensity and length scales on the mean separated and reattached flow and roof surface pressure were examined by Akon and Kopp (2016). In Chapter 3, the present work is extended to understand of their observations by further linking the velocity field to the pressure field. Time-resolved particle image velocimetry (TR-PIV) was used to measure the flow field near a typical low-rise building, where surface pressure measurements were also synchronized. Experiments were conducted by Akon (2017) under the six upstream terrain conditions. The main contributions and findings are summarized as follows.

- The Navier-Stokes equations are used to determine the gradient vectors of the mean pressure field from the planar PIV data. The convection-contributed pressure gradients are identified by evaluating the terms associated with mean velocities in the Navier-Stokes equations. The turbulence-contributed pressure gradients, on the other hand, are identified by terms associated with the Reynolds stresses. Effects of upstream turbulence on both the convection- and turbulence-contributed pressure gradients can, hence, be examined.

- In order to obtain the pressure field from the velocity field, the analytical interpolation technique of Ettl et al. (2008) is applied to integrate the mean pressure gradient. The reconstructed pressure fields match Bernoulli's equation well along a streamline away from the body and direct pressure measurement on the surface of the body. Hence, the evaluation of pressure gradient using the Navier-Stokes equations and the corresponding pressure integration technique are validated.

- Akon and Kopp (2016) found that the minimum mean roof surface pressure coefficient, $\min\left(\overline{Cp}\right)$, decreases as the upstream turbulence intensity increases. In the current work, these decreasing $\min\left(\overline{Cp}\right)$'s are directly related to both increased convection- and turbulence-contributed pressure gradients over the windward region of the mean separation bubbles.

- As the upstream turbulence intensity increases, a more rapid pressure recovery can be found for the portion of roof surface on the leeward side of the location of $\min\left(\overline{Cp}\right)$. Such increased surface pressure recovery rates are mainly due to the increased turbulence-contributed pressure gradients near the roof surface.

In Chapter 4, the effects of the upstream turbulences on the area-averaged mean and fluctuating pressures are investigated. Time averaged integral momentum equation is used to relate the near-roof flow fields to the mean area-averaged pressures. On the other hand, a simple quasi-steady model is established for estimating pressure fluctuations. The main goal of this chapter is to derive the physical assumptions embedded in the QS model. The main findings are summarized as follows:

- A time-averaged integral momentum approach is proposed to relate the mean flow and turbulence fields to the area-averaged roof surface pressures. This is done by placing a control volume (CV) directly above the target roof panel, where the mean area-averaged pressure needs to be calculated. This approach is validated by the successful comparison of the estimated and measured mean area-averaged roof surface pressures.

- From the temporal average aspect, the convection term (i.e., the net momentum flux through the CV) dominates the area-averaged pressures for panels beneath the separated flows. For panels under the re-attached flows, the static pressure just above the roof dominates the mean pressures. The effects of turbulence stresses are the same as what has been found in the differential momentum equations. Note that the turbulence stresses play a minor role on affecting the mean area-averaged roof surface pressures, as compared to the convection and pressure terms.

- A simple QS model is established to estimate the instantaneous area-averaged roof surface pressures. This model accounts for the variation of magnitudes and azimuth angles of the instantaneous wind speed measured at the reference location, i.e., one building height above the leading edge. Satisfactory performance of the QS model is found for regions under flow separation.

- The physical assumptions embedded in the QS model are explained from simple algebraic manipulation of the time-averaged integral momentum equation. Two main findings are revealed:

    - The direction of the instantaneous flow field is assumed to be the same as the direction of the mean flow field. This statements holds when the instantaneous wind azimuth measured at the reference point is equivalent to the mean wind azimuth.

    - The magnitude of the instantaneous velocity field is obtained by amplifying the mean velocity field with an uniform rate, $\left|\mathbf{u}_{\mathrm{m}}\right| \Big/ \sqrt{\overline{\left|\mathbf{u}_{\mathrm{m}}\right|^2}}$, where $\mathbf{u}_{\mathrm{m}}$ is the velocity vector measured at the reference point.

- By further comparing the QS assumptions to the instantaneous integral momentum equation, the missing mechanism of the QS-model can be elucidated. Main findings are listed as follows:

    - The ideal scenario for the QS assumption to be true is that the instantaneous flow pattern near the roof exactly matches the mean flow pattern. This ideal scenario

may be better approached if the upstream turbulences have a very large length scale.

- By using a point velocity measurement like a cobra probe, the instantaneous static pressure can be directly measured. Such information may be used to correct the QS assumptions associated with the static pressure above the roof. As compared to the prediction using the typical QS model, the pressure-corrected QS model is found to work better for the regions below the flow re-attachment. However for a roof surface under the flow separation, little improvement can be found by using the pressure-corrected QS model. This is due to the fact that the static pressure on top of the roof dominates the roof surface pressure for the flow re-attachment region while momentum flux contributes more for the flow separation region.

- A missing acceleration term of vertical velocity is identified in the QS model. However, due to little spatial coherence of vertical velocities within the control volume (CV) on top of the roof, using the velocities measured at the reference point overestimates the overall vertical velocity accelerations within the CV. Therefore, adding the acceleration correction to the QS model via a point velocity measurement is not suggested for the practice.

In Chapter 5, the QS model accounts for three-dimensionality of the wind speed vector (measured at one building height above the leading edge) is established and used for estimating the pressure fluctuations. The main conclusions are as follows:

- The QS model assumes the instantaneous surface pressure as a multiplication of instantaneous dynamic pressure, $0.5\rho|\mathbf{u}_{\mathrm{m}}|^2$, with the instantaneous function, Cp_{inst}. The effects of wind azimuth, Θ, and elevation angle, β, are included in the instantaneous function, i.e., $Cp_{\mathrm{inst}}(\theta,\beta)$, in the QS vector model (QS-θ-β). The instantaneous functions in the model were evaluated from synchronized measurements of building surface pressures and local wind speed vectors.

- Upward-acting winds (i.e., $\beta' > 0$) are generally associated with higher magnitudes of Cp_{inst} while the downward-acting winds (i.e., $\beta' < 0$) are generally associated with lower magnitudes of Cp_{inst}. The effect of the elevation angle can be as large as the effect of wind azimuths for certain mean incident wind angles.

- Linear effect of wind elevation is found to be adequate for the range of fluctuating elevation angle, β', such that $Cp_{\text{inst}}(\theta,\beta) = Cp_{\text{inst}}(\theta) + \beta' \cdot dCp_{\text{inst}}/d\beta$. The gradient $dCp_{\text{inst}}/d\beta$ is found to vary with respect to wind azimuth so that the functional form is fit with a Fourier series.

- Higher dynamic pressures, however, are generally associated with downward wind in the atmospheric boundary layer, leading to a suppression process of the actual observed peaks because of this. These observations are consistent with previous published works.

- A statistical method that uses the QS-θ-β model was also derived and validated. With this method, the probability density function (PDF) of building surface pressures is formulated as a double integral of the joint PDF between instantaneous wind speed ratio, wind azimuth, and elevation angle, $f(|\mathbf{u}_{\text{m}}|/u_{\text{ref}}, \theta, \beta)$. This approach is validated by successfully comparing the estimated pressure PDF's to that obtained directly from the velocity time series.

- Because no mutual independence is found between $|\mathbf{u}_{\text{m}}|/u_{\text{ref}}$, θ, and β, the joint PDF used here is not further reduced to $f(|\mathbf{u}_{\text{m}}|/u_{\text{ref}})f(\theta)f(\beta)$, a formulation that has been used in previous works. Furthermore, the direct use of joint PDF of wind turbulence in our formulation offers a more straightforward approach when compared to the procedures used in previous works.

- Peak pressures were predicted by applying the statistical method and compared to the measured values for all mean incident wind angles. Underestimation of peak pressures was observed for point pressures on the roof. The accuracy of peak

prediction increases as the number of points included in area-averages increases. More specifically, the mean level of error (underestimation) was found be about 30% for a single pressure tap, while this reduces to < 5% for area-averages of 16 and 36 taps (on the current building with the current tap layout). Hence, the proposed QS-θ-β model is found to perform well for roof pressure estimation when relatively large areas of the roof are considered for this typical low-rise building.

In Chapter 6 the applicability of QS model in predicting the area-averaged pressure fluctuations induced by the six upstream turbulence conditions are further examined. Fluctuations of area-averaged pressures are investigated for panels near the roof corner and leading edge. Main findings are listed as follows:

- The quasi-steady (QS) model are known to work better for capturing the effects of large scale turbulences on the roof surface pressure fluctuations. Hence, the small length scale turbulences are removed in the QS model by applying the moving average on the time series of each velocity components. The cut-off length is selected as 5 building height, for separating the small length scale of turbulence out from the large scale turbulence. Appropriate cut-off length can be determined based on the length scale where the coherence between the measured and QS-predicted pressures vanishes.

- It is found that the fluctuation of area-averaged pressures is dominated by the intensity of the upstream turbulence and to a lesser degree by the turbulence length scale. However, more spatially coherent pressure fluctuations can be found for upstream turbulences of larger length scale.

- The QS model accounting for the magnitude, azimuth and elevation angles of the instantaneous wind vector is used to predict the fluctuation of the area-averaged pressures. The instantaneous function (of the QS model) established in a moderate roughness condition is generally collapsed with that obtained from the other terrain conditions. This implies that the variations of the upstream turbulence do not alter the flow structure significantly so that the resulted mean area-averaged pressure coefficients are nearly similar. Based on this observation, the QS model established

from the moderate roughness condition is used to predict the pressure fluctuations induced by turbulences generated from other terrain conditions.

- The ‘cross-terrain’ QS-predictions of pressure fluctuations generally works well for the roof panels being examined. The QS predictions of the pressure root mean squares (rms) generally agree well to the measured values. Hence, the QS model used here can account for most of the effects of the upstream turbulence on pressure fluctuations.

- However, underestimations up to 20% can be observed for the QS-predicted peak pressures for panels including 9 taps. These underestimations usually happen for panels beneath flow separation. These underestimations may be due to the missing consideration in the QS model for the small scale vortices generated from the leading edge. Improved QS-predictions are observed for larger panel areas or by placing the velocity probe closer the target panel.

7.2 Recommendations

This thesis demonstrates that the quasi-steady (QS) model is capable for explaining the effects of large length scale upstream turbulences on the fluctuations of the area-averaged roof surface pressures. However, only the flat roof building model (i.e., the 1/50 scaled model for the TTU WERFL building) is examined in this thesis. In this regard, one of the future work can focus on the applicability of the proposed QS model to roofs with more complex geometries, e.g., gable or hip roofs (Gavanski et al, 2011).

As shown by Akon (2017), the small length scale vortices separating from the leading edge of the roof (for wind normal to the building wall) are highly correlated to the point roof surface pressure fluctuations. The QS models discussed in this thesis have not been able to incorporate these effects. Future work regarding this issue may begin with the typical concept used in vortex method (e.g., Spalart, 1998), where the strength of shedding vortices have been studied. Furthermore, the interaction between the upstream turbulence and these shed vortices needs to be studied as well.

In terms of other practical applications, the QS method is anticipated to provide a useful tool for pressure estimation during transient storms (e.g., microbursts, downbursts, tornadoes, etc.). Due to the rapid spatial translation of these types of wind storms, buildings in their path can experience rapid and intense changes of wind speed and direction, especially when compared to the movements and development of large-scale synoptic storms. For example, Kopp and Wu (2017) observed a strong dependence of the building surface pressure patterns on the direction of local wind vectors, as shown in Figure 7-1, for a translating tornado-like vortex passing the building generated in the WindEEE Dome. These storms produce different wind fields that can have features such as upwardly directed gusts correlated with high wind speeds, different vortex structures, and other particular features. Of particular interest is the vertical component of the wind. For example, Blanchard (2013) found that the elevation angle could be more than 20° at the moment when a tornado has its most intense horizontal wind speeds. This contrasts with typical atmospheric surface layers, where gust speeds are generally correlated with downward acting winds. Because the upward wind is generally associated with higher pressure coefficients on roofs, building surface pressures may be amplified in the tornado-induced wind, as compared to typical boundary layer winds, given similar dynamic pressures and that the QS model holds for both scenarios. Further work is required to identify whether the linear relationship between pressure and elevation angle holds, or whether a non-linear contribution may be required in order to maintain accurate estimates of $Cp_{\text{inst}}(\theta,\beta)$.

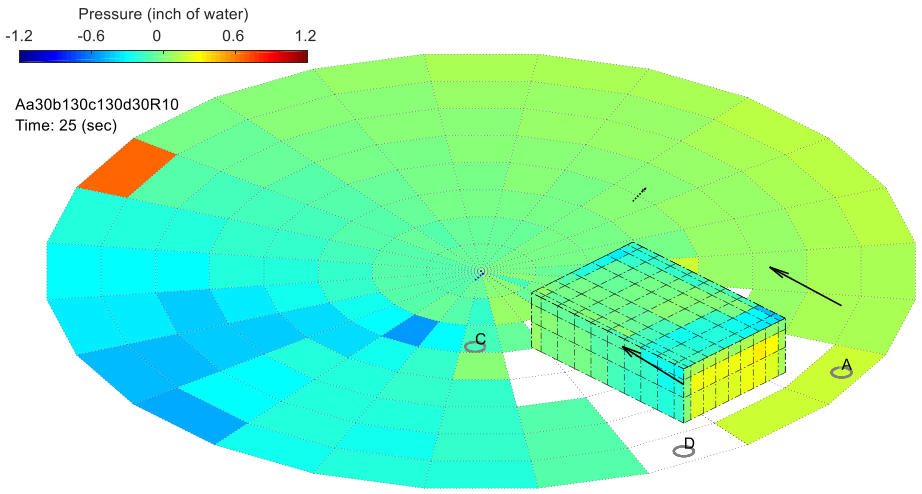

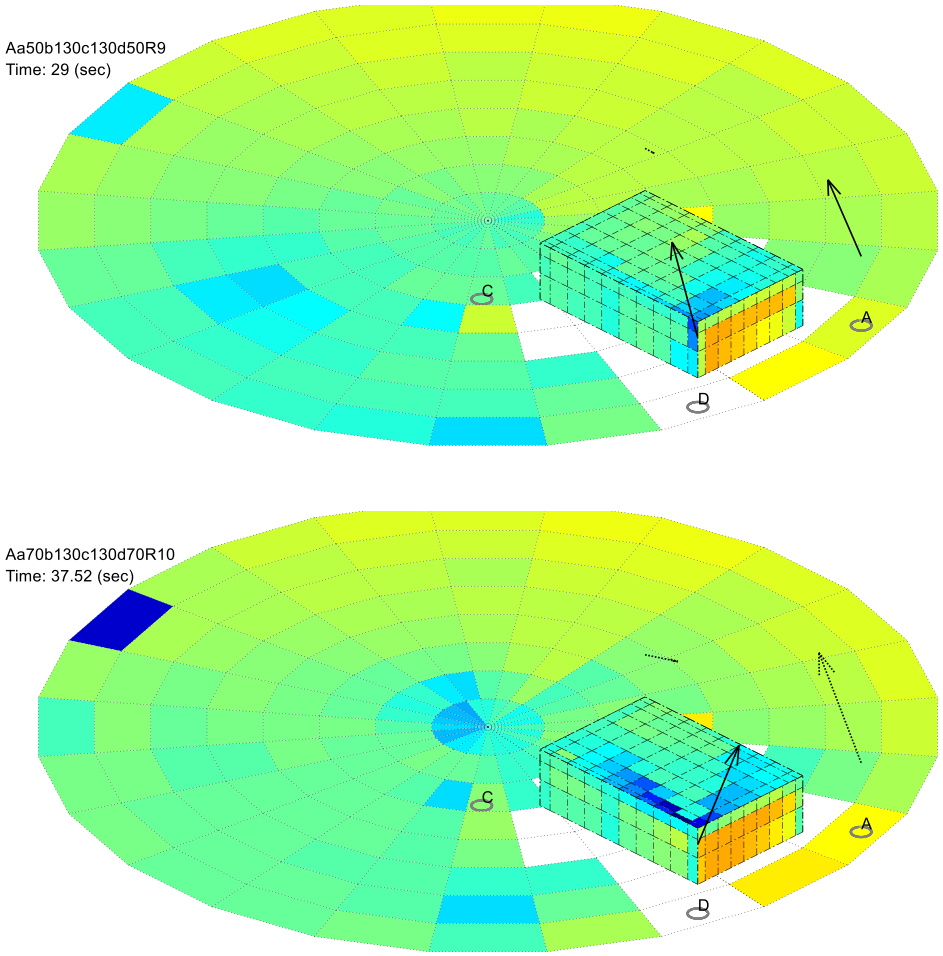

Figure 7-1: Snapshots of ground and building surface pressures (reference to averaged building wall pressures) along with velocity vectors measured near building (Kopp and Wu, 2017). The wind and pressure fields are induced by a translating tornado.

References

Akon, A. F., Kopp, G. A., 2016. Mean pressure distributions and reattachment lengths for roof separation bubbles on low-rise buildings. J. Wind Eng. Ind. Aerodyn. 155, 115-125. DOI: 10.1016/j.jweia.2016.05.008

Akon, A. F., 2017. Effects of turbulence on the separating-reattaching flow above surface-mounted, three dimensional bluff bodies (Dissertation). The University of Western Ontario.

Amini, M. O., van de Lindt, J. W., 2014. Quantitative insight into rational tornado design wind speeds for residential wood-frame structures using fragility approach. J. Struct. Eng. 140 (7), 04014033. DOI: 10.1061/(ASCE)ST.1943-541X.0000914

Asghari Mooneghi, M., Irwin, P., Chowdhury, A. G., 2016. Partial turbulence simulation method for predicting peak wind loads on small structures and building appurtenances. J. Wind Eng. Ind. Aerodyn. 157, 47-62. DOI: 10.1016/j.jweia.2016.08.003

Banks, D., Meroney, R. N., 2001. The applicability of quasi-steady theory to pressure statistics beneath roof-top vortices. J. Wind Eng. Ind. Aerodyn. 89, 569 – 598. DOI: 10.1016/S0167-6105(00)00092-1

Baur, T., Kőngeter, J., 1999. PIV with high temporal resolution for the determination of local pressure reductions from coherent turbulent phenomena. 3rd Int. Workshop on Particle Image Velocimetry (Santa Barbara, USA) 101-106.

Blanchard, D. O. (2013). A comparison of wind speed and forest damage associated with 470 tornadoes in northern Arizona. Weather and Forecasting. 28, 408 – 417. DOI: 10.1175/WAF-D-12-00046.1

de Kat, R., van Oudheusden, B. W., Scarano, F., 2008. Instantaneous planar pressure field determination around a square-section cylinder based on time-resolved stereo-PIV. 14th Int Symp. on Applications of Laser Techniques to Fluid Mechanics (Libson, Portugal).

de Kat, R., van Oudheusden, B. W., 2012. Instantaneous plannar pressure determination from PIV in turbulent flow. Exp. Fluids 52 (2012), 1089-1106. DOI: 10.1007/s00348-011-1237-5

Ettl, S., Kaminski, J., Knauer, M. C., Häusler, G., 2008. Shape reconstruction from gradient data. Applied Optics, 47 (12), 2091 - 2097. DOI: 10.1364/AO.47.002091

Gartshore, I. S., 1973. The effects of freestream turbulence on the drag of rectangular two dimensional prism. University of Western Ontario, BLWT Report No. 4-73, 1973.

Gavanski, E., Kordi, B., Kopp, G. A., Vickery, P. J., 2013. Wind loads on roof sheathing of houses. J. Wind Eng. Ind. Aerodyn. 114, 106-121. DOI: 10.1016/j.jweia.2012.12.011

Cook, 1990. The Designer's Guide to Wind Loading of Building Structures, Part 2 Static Structures. UK: Butterworths

Gurka, R., Liberzon, A., Herfetz, D., Rubinstein, D., Shavit, U., 1999. Computation of pressure distribution using PIV velocity data. Proc. Int. Workshop on PIV (Santa Babara, USA) 671-676.

Hillier, R., Cherry, N. J., 1981. The effects of stream turbulence on separation bubbles. J. Wind Eng. Ind. Aerodyn. 8 (1-2), 49–58. DOI: 10.1016/0167-6105(81)90007-6

Ho, T.C.E., Surry, D., Morrish, D., Kopp, G.A., 2005. The UWO contributions to the NIST aerodynamic database for wind loads on low buildings: Part1. Archiving format and basic aerodynamic data. J. Wind Eng. Ind. Aerodyn. 93 (1), 1–30. DOI: 10.1016/j.jweia.2004.07.006

Holmes, J. D., 2007. Wind Loading of Structures. New York, New York: Taylor & Francis.

He, W. X., Hong, H. P., 2012. Probabilistic characterization of roof panel uplift capacity under wind loading. Can. J. Civ. Eng. 39 (12), 1285-1296. DOI: 10.1139/l2012-114

Irwin, P. A., 2008. Bluff body aerodynamics in wind engineering. J. Wind Eng. Ind. Aerdyn. 96 (6-7), 701 – 712. DOI: 10.1016/j.jweia.2007.06.008

Jaw, S. Y., Chen, J. H., Wu, P. C., 2009. Measurement of pressure distribution from PIV experiments. Journal of Visualization. 12 (1), 27-35. DOI: 10.1007/BF03181940

Kawai, H., 1983. Pressure fluctuations on square prisms – applicability of strip and quasi-steady theories. J. Wind Eng. Ind. Aerodyn. 13, 197–208. DOI:10.1016/0167-6105(83)90141-1

Kiya, M., Sasaki, K., 1983a. Structure of a turbulent separation bubble. Journal of Fluid Mechanics. 137, 83-113. DOI: 10.1017/S002211208300230X

Kiya, M., Sasaki, K., 1983b. Free stream turbulence effects on a separation bubble. J. Wind Eng. Ind. Aerodyn. 14 (1-3), 375–386. DOI: 10.1016/0167-6105(83)90039-9

Kopp, G. A., Hong, E., Gavanski, E., Stedman, D., Sills, D. M. L., 2016. Assessment of wind speeds based on damage observations from the Angus (Ontario) Tornado of 17 June 2014. DOI: 10.1139/cjce-2016-0232

Kopp, G. A., Mans, C., Surry, D., 2005. Wind effects of parapets on low buildings: Part 4. Mitigation of corner loads with alternative geometries. J. Wind Eng. Ind. Aerodyn. 93 (11), 873-888. DOI: 10.1016/j.jweia.2005.08.004

Kopp, G.A., Wu, C-H, 2017. A framework for the aerodynamics of low-rise buildings in tornadoes: Can boundary layer wind tunnels give us everything we need? The 13th Americas Conference on Wind Engineering (13ACWE), Gainesville, Florida USA, May 21-24, 2017.

Kordi, B., Taczuk, G., Kopp, G.A., 2010. Effects of wind direction on the flight trajectories of roof sheathing panels under high winds. Wind and Structures 13 (2), 145–167. DOI: 10.12989/was.2010.13.2.145

Kurtulus, D. F., Scarano, F., David, L., 2007. Unsteady aerodynamic forces estimation on a square cylinder by TR-PIV. 42 (2), 185-196. DOI: 10.1007/s00348-006-0228-4

Lander, D. C., Letchford, C. W., Amitay, M., Kopp, G. A., 2016. Influence of the bluff body shear layers on the wake of a square prism in a turbulent flow. Physical Review Fluids 1, 044406. DOI: 10.1103/PhysRevFluids.1.044406

Levitan, M. L., Mehta, K. C., 1992a. Texas Tech field experiments for wind loads part 1: building and pressure measuring system. J. Wind Eng. Ind. Aerodyn. 43 (1-3), 1565–1576. DOI: 10.1016/0167-6105(92)90372-H

Levitan, M. L., Mehta, K. C., 1992b. Texas Tech field experiments for wind loads part II: meteorological instrumentation and terrain parameters. J. Wind Eng. Ind. Aerodyn. 43 (1-3), 1577–1588. DOI: 10.1016/0167-6105(92)90373-I

Letchford, C. W., Iverson, R. E., and McDonald, J. R., 1993. The application of the quasi-steady theory to full scale measurements on the Texas Tech Building. J. Wind Eng. Ind. Aerodyn. 48, 111–132. DOI:10.1016/0167-6105(93)90284-U

Minor, J.E., 1994. Windborne debris and the building envelope. J. Wind Eng. Ind. Aerodyn. 53 (1–2), 207–227. DOI: 10.1016/0167-6105(94)90027-2

Murai, Y., Nakada, T., Suzuki, T., Yamamoto, F., 2007. Particle tracking velocimetry applied to estimate the pressure field around a Savonius turbine. Meas. Sci. Techonl. 18, 2491-2503. DOI: 10.1088/0957-0233/18/8/026

Nakamura, Y., Ozono, S., 1987. The effects of turbulence on a separated and reattaching flow. J. Fluid Mech. 178, 477-490. DOI: 10.1017/S0022112087001320

Oh, J. H., Kopp, G. A., Inculet, D. R., 2007. The UWO contribution to the NIST aerodynamic database for wind loads on low buildings: Part 3. Internal pressures. J. W. Eng. Aerodyn. 95, 755 – 779. DOI: 10.1016/j.jweia.2007.01.007

Papoulis, A., and Pillai, S. U. (2002). Probability, Random Variables and Stochastic Processes, 4th Edn. New Delhi: McGraw Hill Inc.

Pratt, R. N., Kopp, G. A., 2014. Velocity field measurements above the roof of a low-rise building during peak suctions. J. Wind Eng. Aerodyn. 133, 234-241. DOI: 10.1016/j.jweia.2014.06.009

Robertson, A. P., 1991. Effect of eaves detail on wind pressures over an industrial building. J. Wind Eng. Ind. Aerodyn. 38 (2-3), 325-333. DOI: 10.1016/0167-6105(91)90051-W

Roshko, A., Lau, J. C., 1965. Some observations on transition and reattachment of a free shear layer in incompressible flow. Proceedings of the Heat Transfer and Fluid Mechanics Institute.

Saathoff, P. J., Melbourne W. H., 1997. Effects of free-stream turbulence on surface pressure fluctuations in a separation bubble. J. Fluid Mech. 337, 1-24. DOI: 10.1017/S0022112096004594

Sciacchitano, A., Wieneke, B., 2016. PIV uncertainty propagation. Meas. Sci. Technol. 27, 084006. DOI: 10.1088/0957-0233/27/8/084006.

Sharma, R. N., Richards, P. J., 1999. The influence of Reynolds stresses on roof pressure fluctuations. J. Wind. Eng. Ind. Aerodyn. 83 (1-3), 147-157. DOI: 10.1016/S0167-6105(99)00068-9

Sharma, R. N., Richards, P. J., 2004. The multi-stage process of windward wall pressure admittance. J. Wind Eng. Aerodyn. 92 (14-15), 1191-1218. DOI: 10.1016/j.jweia.2004.07.004

Spalart P. R., 1998. Vortex methods for separated flows. NASA Technical Memorandum 100068. Ames Research Center, California, USA.

Sparks, P.R., Schiff, S.D., Reinhold, T.A., 1994. Wind damage to envelopes of houses and consequent insurance losses. J. Wind Eng. Ind. Aerodyn. 53 (1–2), 145–155. DOI: 10.1016/0167-6105(94)90023-X

Stenabaugh, S. E., Iida, Y., Kopp, G. A., Karava, P., 2015. Wind loads on photovoltaic arrays mounted parallel to sloped roofs on low-rise buildings. J. Wind Eng. Ind. Aerodyn. 139, 16 – 26. DOI: 10.1016/j.jweia.2015.01.007

Taylor, Z. J., Gurka, R., Kopp, G. A., 2014. Effects of leading edge geometry on the vortex shedding frequency of an elongated bluff body at high Reynolds numbers. J. Wind Eng. Ind. Aerodyn. 128, 66–75. DOI: 10.1016/j.jweia.2014.03.007

Tieleman H. W., 1993. Pressures on surface-mounted prisms: The effects of incident turbulence. 49 (1–3), 289-299. DOI: 10.1016/0167-6105(93)90024-I

Tieleman, H. W., 2003. Wind tunnel simulation of wind loading on low-rise structures: a review. J. Wind Eng. Ind. Aerodyn. 91, 1627-1649. DOI: 10.1016/j.jweia.2003.09.021

Tieleman H. W., Surry, D., Lin, J. X., 1994. Characteristics of mean and fluctuating pressure coefficients under corner (delta wing) vortices. J. Wind Eng. Ind. Aerodyn. 52, 263-275. DOI: 10.1016/0167-6105(94)90052-3

Tieleman, H. W., Surry, D., Mehta, K. C., 1996. Full/model-scale comparison of surface pressures on the Texas Tech experimental building. J. Wind Eng. Ind. Aerodyn. 61 (1), 1-23. DOI: 10.1016/0167-6105(96)00042-6

Uematsu, Y., Isyumov, N., 1998. Peak gust pressures acting on the roof and wall edges of a low-rise building. J. Wind Eng. Ind. Aerodyn. 77 & 78, 217-231. DOI: 10.1016/S0167-6105(98)00145-7

van de Lindt, J. W., Pei, S., Dao, T., Graettinger, A., Prevatt, D.O., Gupta, R., and Coulbourne, W., 2013. Dual-objective-based tornado design philosophy. Journal of Structural Engineering. 139, 251 – 263. DOI: 10.1061/(ASCE)ST.1943-541X.0000622

van de Lindt, J.W., Graettinger, A., Gupta, R., Skaggs, T., Pryor, S., Fridley, K.J., 2007. Performance of wood-frame structures during Hurricane Katrina. Journal of Performance of Constructed Facilities. 21 (2), 108–116. DOI: 10.1061/(ASCE)0887-3828(2007)21:2(108)

van Oudheusden, B. W., Scarano, F., Roosenboom, E. W. M., Casimiri, E. W. F., Souverein, L. J., 2007. Evaluation of integral forces and pressure fields from planar velocimetry data for incompressible and compressible flow. Exp. Fluids. 43, 153-162. DOI: 10.1007/s00348-007-0261-y

van Oudheusden, B. W., 2013. PIV-based pressure measurement. Meas. Sci. Techonl. 24, 032001. DOI: 10.1088/0957-0233/24/3/032001

Wind Science and Engineering Center (WSEC), 2006. A recommendation for an enhanced Fujita scale. Texas Tech University, Lubbock, Texas.

Wu, F., Sarkar, P. P., Mehta, K.C., Zhao, Z., 2001. Influence of incident wind turbulence on pressure fluctuations near flat-roof corners. J. Wind Eng. Ind. Aerodyn. 89, 403-420. DOI: 10.1016/S0167-6105(00)00072-6

Wu, C.-H., Kopp, G. A., 2016. Estimation of wind-induced pressures on a low-rise building using quasi-steady theory. Frontiers Built Env., 2(5). DOI: 10.3389/fbuil.2016.00005.

Appendices

Appendix A: Correlation analyses for velocities measured near the building model

In this section, the correlations between velocities measured at different locations near the TTU model building are investigated. The motivation of this analyses arises from the heavy reliance on the instantaneous velocity measurements in the quasi-steady (QS) model for prediction of the instantaneous building surface pressures. If the measurements cannot represent the instantaneous velocities near the building, then the QS predicted pressures produce little insight for actual physical mechanism.

In order to specify the relative distances between the velocity probes, the origin of the global coordinate is fixed at the center of the turntable in the wind tunnel (see Figure A 1). The positive x-coordinate is aligned with the main stream direction (u-component of the velocities) whereas the positive z-coordinate denotes the vertical distance from the tunnel floor. The y-coordinate denotes the transverse distance and its positive direction follows the right hand rule and the x- and z-coordinates. In the wind-speed and pressure measurements regarding the QS applications in this thesis, a total three Cobra probes are involved in measurements, i.e., the 'L-shaped' probe with serial number #289 and two straight probes #311 and #313. Corba probe #289 was placed at one building height above the middle roof leading edge of the longer wall, as shown in Figure A 1 (a) and (b). Note that this probe (#289) was fixed with respect to the building, such that the probe is on the positive y-coordinate for mean wind azimuth $\bar{\theta} = 90$ and on the negative x-coordinate for $\bar{\theta} = 0$. The straight probe #311 was placed at the building height and away from the corner with a side and a upstream distance being $|\Delta y| = 3H$ and $|\Delta x| = 3H$, respectively, for the setup of mean azimuth $\bar{\theta} = 90$, as shown in Figure A 1 (a). The other straight probe #313 was placed at a mirrored location (with respect to x-coordinate) of probe #311. Note that these two straight probes did not change their positions when the building is rotated in the wind tunnel testing (e.g., see the unchanged locations for $\bar{\theta} = 0$ in Figure A 1 (b)).

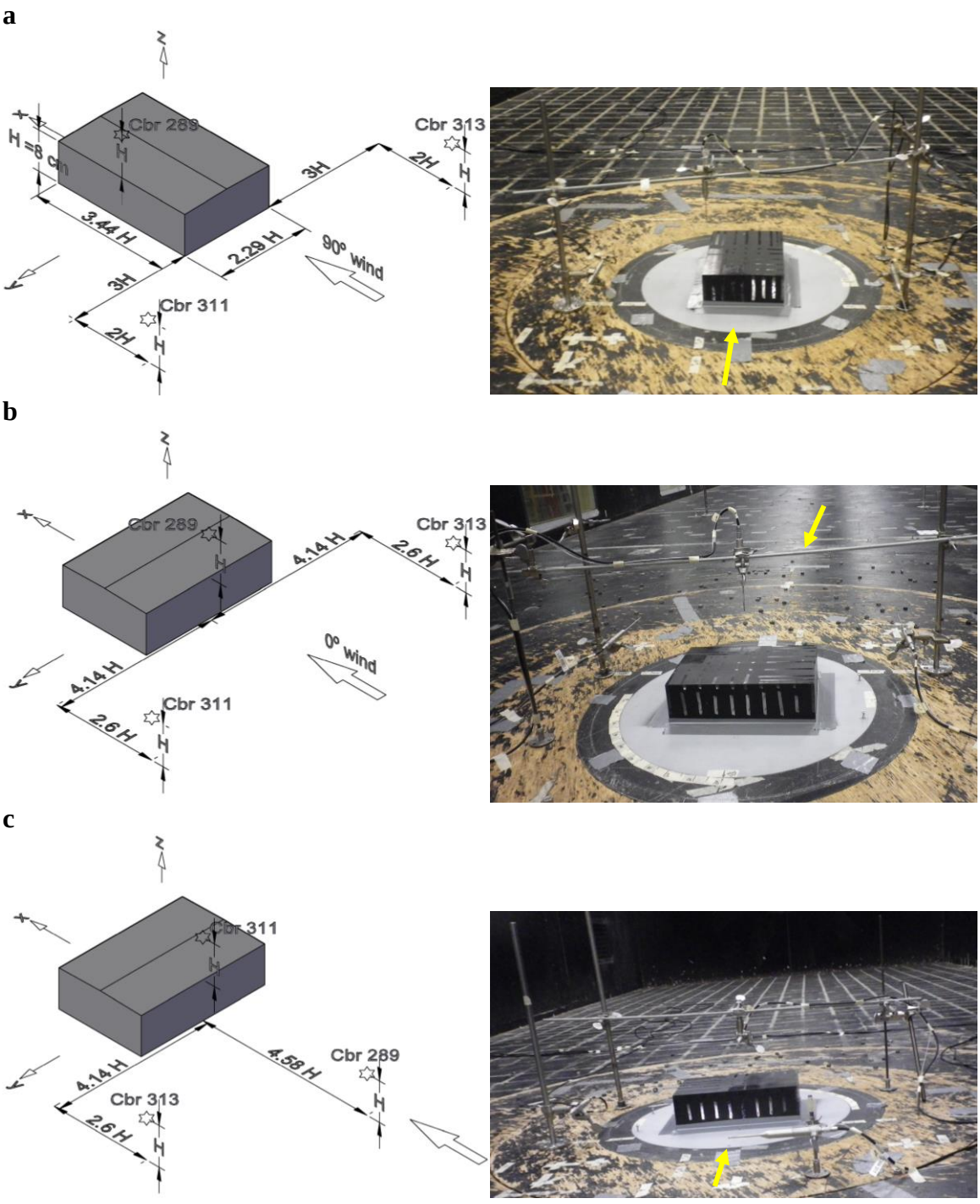

Figure A 1: Cobra probe locations with respect to the building model: (a) Typical measurement at $\bar{\theta} = 90$; (b) Typical measurement at $\bar{\theta} = 0$; (c) Additional measurement with an upstream probe.

Based on the probe setups for mean wind azimuths $\bar{\theta} = 90$ shown in Figure A 1 (a) and $\bar{\theta} = 0$ in Figure A 1 (b), three combinations of relative distances between probes are used for the correlation analyses. The largest separation in the transverse direction, i.e., $|\Delta y| = 8.29H$, can be observed between the straight probes #311 and #313, where H denotes the building height of 8 cm. The second large transverse separation can be observed between probes #311 and #289, i.e., $|\Delta y| = 4.14H$, for mean wind azimuth of $\bar{\theta} = 0$. The third large transverse separation, i.e., $|\Delta y| = 3H$, can be observed between the same probes (i.e., #311 and #289) for mean wind azimuth of $\bar{\theta} = 90$. The fourth case is obtained by adding an additional setup, as shown in Figure A 1 (b), where the angled probe #289 was placed at the upstream location of the roof top probe #311 for a distance of $|\Delta x| = 4.58H$. The summary of these cases are shown in Table A 1. As the case number increases, the transverse distance decreases while stream-wise distance increases. The relative vertical distances are either zero or 1*H*.

Table A 1: Relative distances between the two probes for correlation study.

Case	Selected two probes	Relative distance, $\|\mathbf{x}_a - \mathbf{x}_b\|$	Notes
(i)	#311 #313	$\|\Delta x\|/H = 0$ $\|\Delta y\|/H = 8.28$ $\|\Delta z\|/H = 0$	Figure A 1 (a), (b)
(ii)	#311 #289	$\|\Delta x\|/H = 2.6$ $\|\Delta y\|/H = 4.14$ $\|\Delta z\|/H = 1$	Figure A 1 (b)
(iii)	#311 #289	$\|\Delta x\|/H = 3.72$ $\|\Delta y\|/H = 3$ $\|\Delta z\|/H = 1$	Figure A 1 (a)
(iv)	#289 #311	$\|\Delta x\|/H = 4.58$ $\|\Delta y\|/H = 0$ $\|\Delta z\|/H = 1$	Figure A 1 (c)

The time lag correlation coefficients and coherences are calculated for the various probe separations summarized in Table A 1 and large length scale turbulence conditions (i.e., F15, O15 and S15 shown in Figure 2-1). For stream-wise and transverse component of

the velocities shown respectively in Figure A 2 and Figure A 3, the results show that the correlation drops quickly as the transverse separation between probes increases. On the other hand, increasing the stream-wise separation has restively minor effects on the correlations. For the results of the vertical velocity components shown in Figure A 4, the spatial correlations are the smallest for as compared to that of the stream-wise and transverse components. Significant correlation of the vertical velocities can only be observed when the probes are aligned with the main stream direction. All these results imply the fact that the turbulent eddies are transported along the main stream direction.

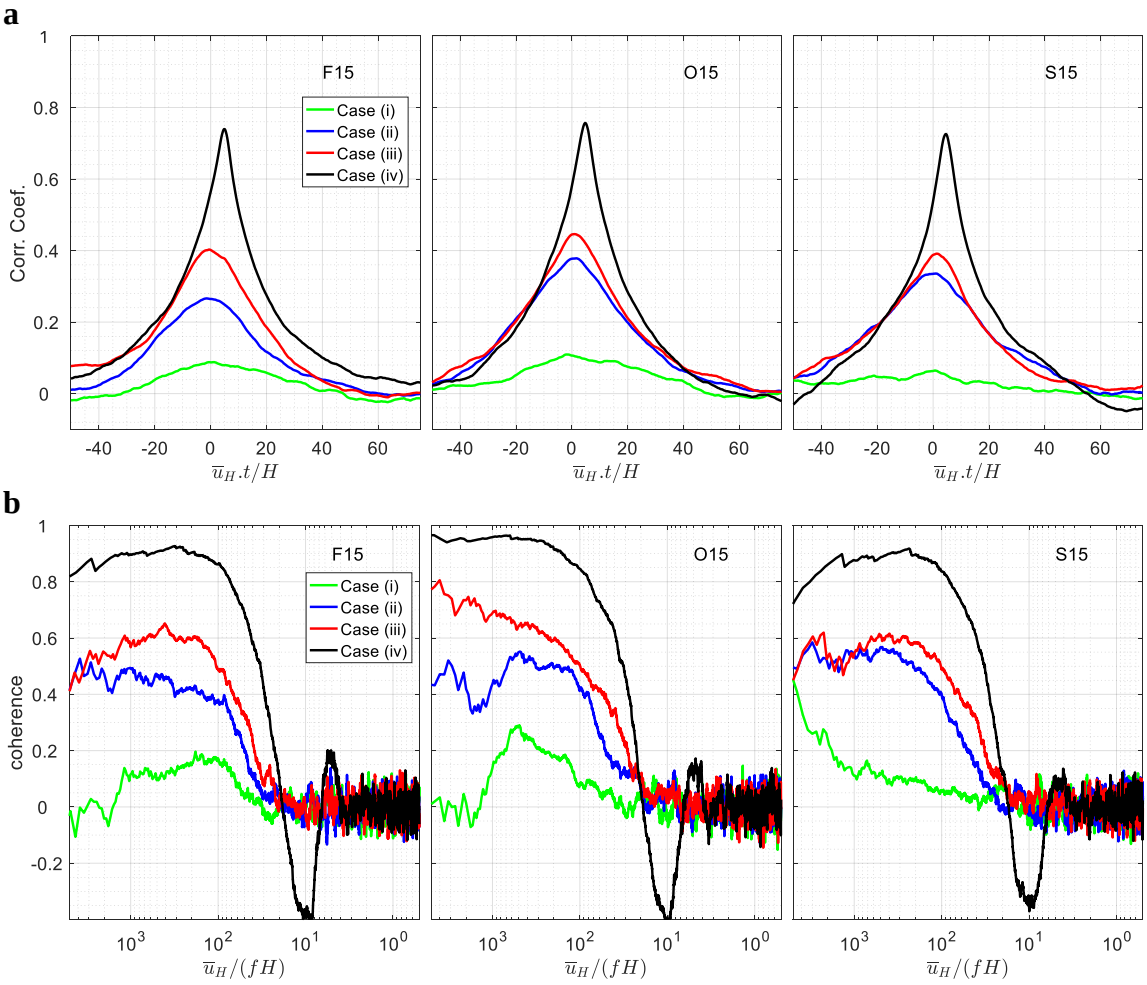

Figure A 2: (a) Time-lag correlation coefficient and (b) coherence between u-velocity components measured at two locations (specified in Table A 1) for the three upstream roughness conditions F15, O15 and S15.

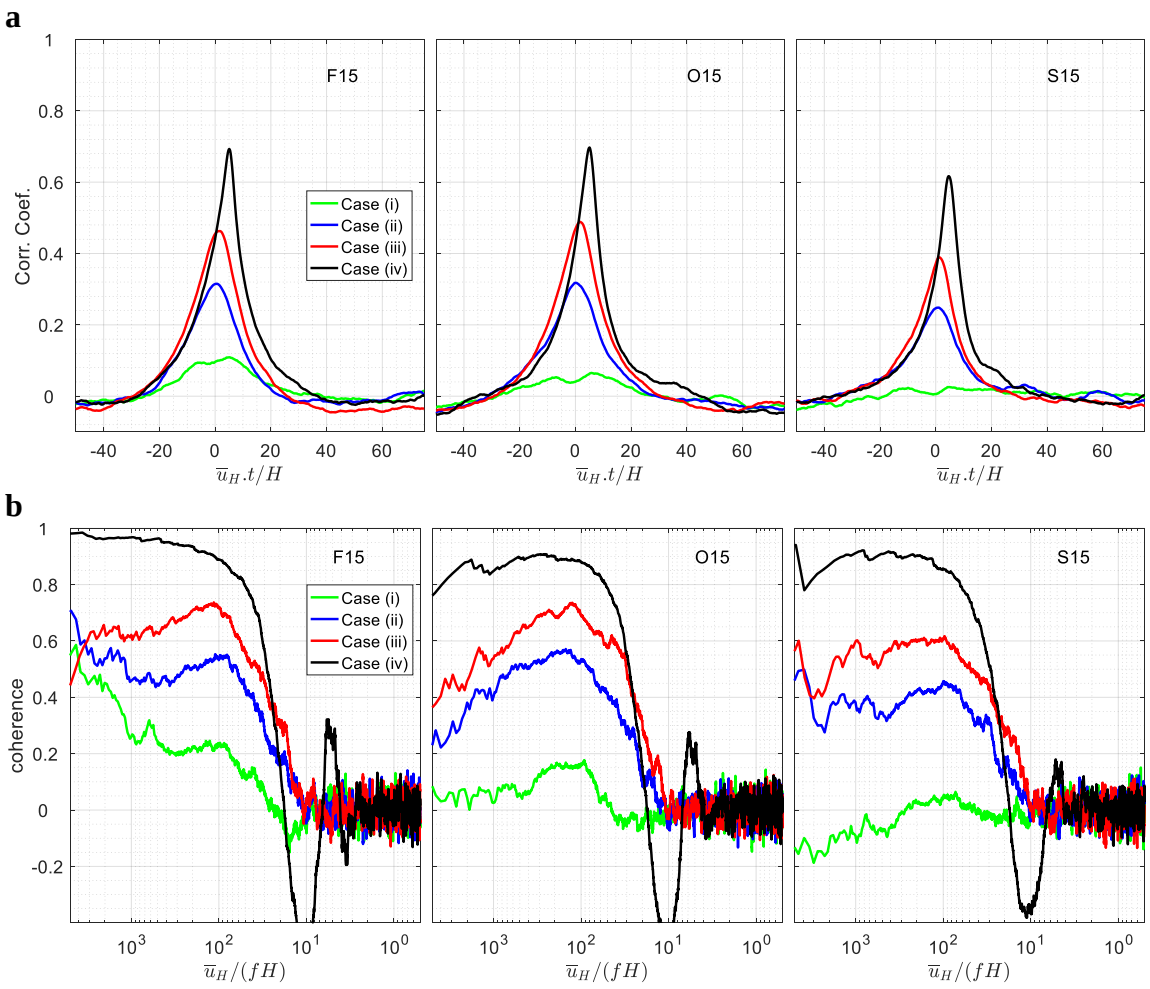

Figure A 3: (a) Time-lag correlation coefficient and (b) coherence between v-velocity components measured at two locations (specified in Table A 1) for the three upstream roughness conditions F15, O15 and S15.

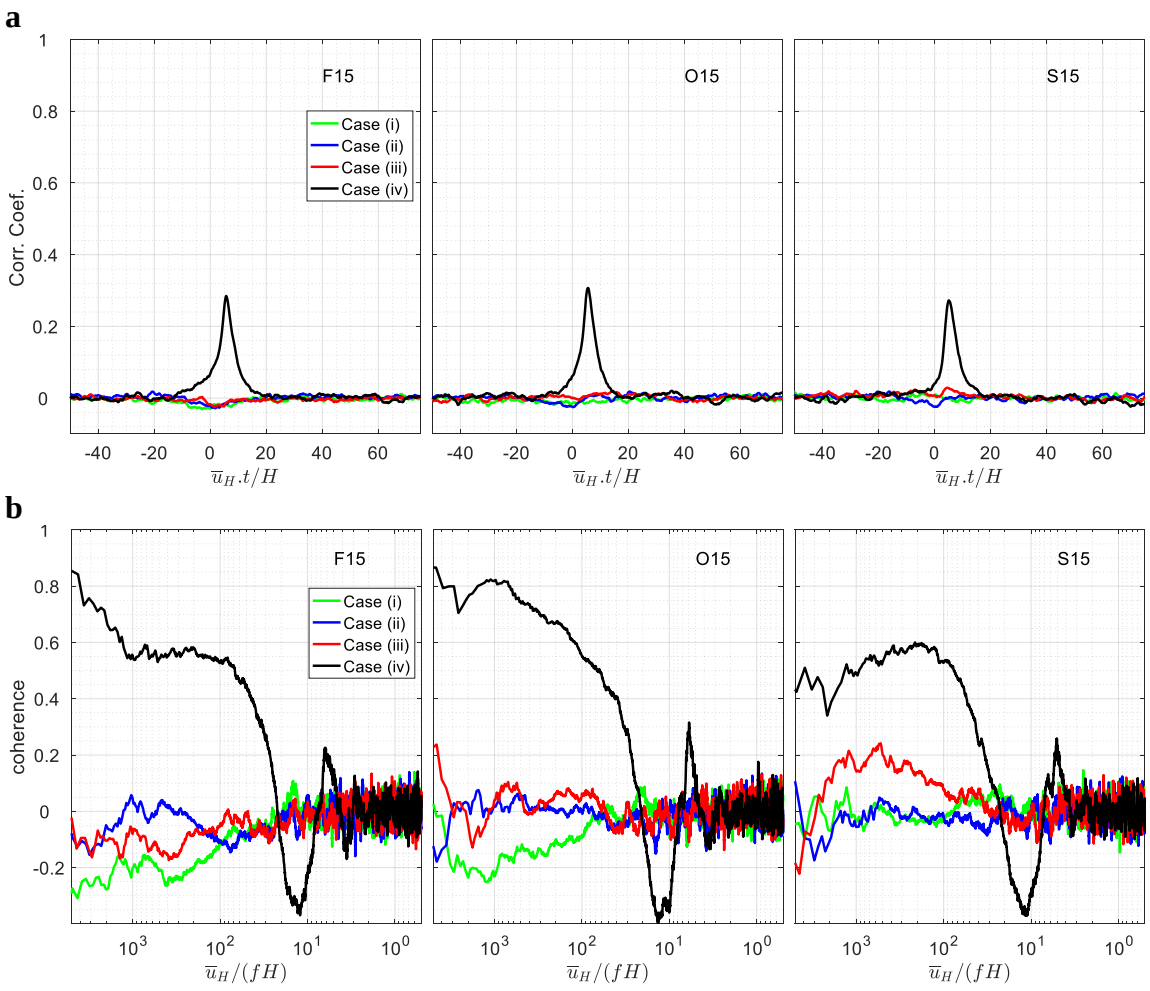

Figure A 4: (a) Time-lag correlation coefficient and (b) coherence between w-velocity components measured at two locations (specified in Table A 1) for the three upstream roughness conditions F15, O15 and S15.

Appendix B: Synchronization of point velocity and pressure measurements

For the velocity-pressure studies regarding the quasi-steady (QS) theory, the original building surface pressures were logged by the system that was independent from that of wind velocities measured from the Cobra probes. Manually triggering the logging process was conducted for the velocity-pressure measurements. The Turbulent Flow Instrument (TFI) that was used to log the velocities, record the signals first. This procedure is followed by the pressure logs. Because of this manual operation, there may exist a time lag, Δt_{lag}, between the velocity and pressure recordings, as shown in Figure B 1 (a). The sign and magnitude of the time lag can also vary for different sets of measurement.

In order to synchronize the two logging systems, the sampling rate was first set to be identical for both of the TFI and Pressure data acquisition systems. The second step is to determine the time lag between two logging systems. This is done by first distributing a common signal into both of the systems, as schematically shown in Figure B 1 (a). The time lag correlation coefficients between the common signals measured in TFI, u'_{TFI}, and in the pressure system, u'_{PSS}, are then calculated. i.e.,

$$\text{Corr.Coef.} = \frac{\overline{u'_{\text{PSS}}(t)\,u'_{\text{TFI}}(t+\Delta t)}}{\left(\overline{u'_{\text{PSS}}} \cdot \overline{u'_{\text{TFI}}}\right)^{0.5}}, \qquad \text{(B-1)}$$

where *t* denotes time and Δt denotes the time lag. Note that the common signals that are involved in correlation analyses are fluctuating components (i.e., deviations from the mean). The measurement time lag can be determined by identifying the time lag corresponding to the maximum correlation coefficient, as schematically shown by Figure B 1 (b).

The total available length of the "synchronized" data is $T - \Delta t_{\text{lag}}$, where *T* denotes the the original sampling duration, as can be easily observed from Figure B 1. The common signals used for these synchronization processes are the stream-wise velocities measured

by the Pitot tube near the wind tunnel ceiling. The use of random signals such as the turbulent velocities has the advantage that there is only one maximum in the time lag correlation coefficients.

a

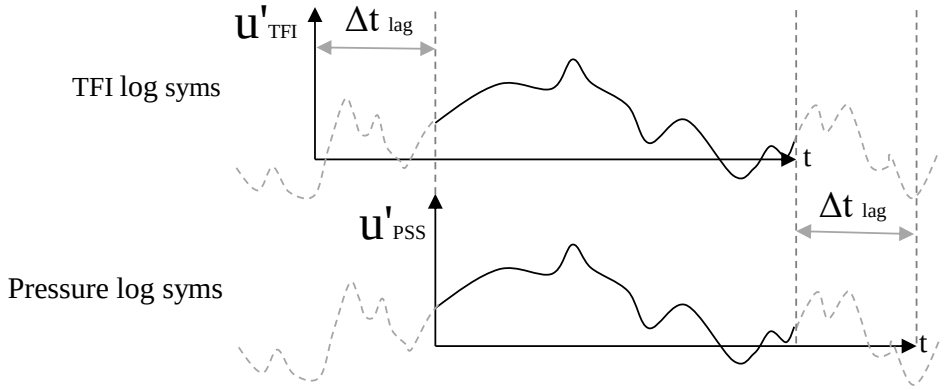

b

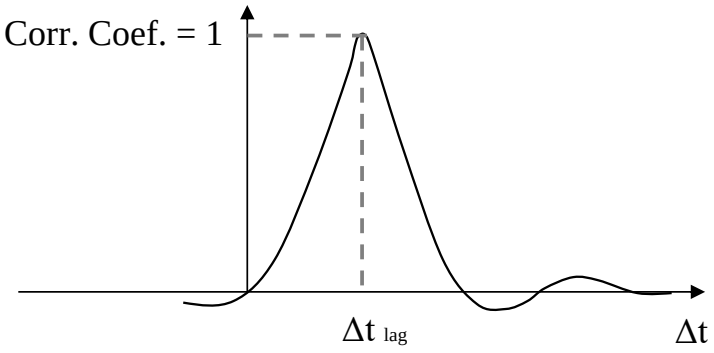

Figure B 1: (a) Schematic recordings of a common signal using TFI and Pressure logging systems; (b) Schematic time lag correlation coefficients between the common signals measured at the two systems.

Appendix C: Use of symmetrical layout of pressure taps and building geometry in pressure measurements

In order to establish a quasi-steady model that capturing the effect of all possible wind azimuths (see Figure 5-2 for an example), building surface pressure measurements need to be conducted for all mean wind azimuths in wind tunnel. These measurement work can be greatly reduced if the building geometry and tap layout are in symmetry. Given a roof of rectangular planar shape, as shown in Figure C 1 for example, wind tunnel measurements only need to be conducted for the wind azimuths within the first quadrant, i.e., $0 \le \theta \le 90$ (as shown by the solid blue vector in Figure C 1). The measured pressures not only capture the building aerodynamics due to the first quadrant wind, but also include the information due to wind azimuths of the remainder range, $90 \le \theta \le 360$. In order to extract these implicit information due to other wind azimuths, empirical comparison is required to identify the scenarios where the relative wind direction with respect to tap location is similar. This section provides a systematic approach to identify the case of symmetry.

Consider a rectangular planar roof shape shown in Figure C 1 and the origin of the Cartesian coordinate, *o*, placed at the center of symmetry, with x- and y-axis aligned with the short and long walls respectively. The roof region and wind directions are divided into the four quadrant, i.e., I, II, III and IV, as labeled in Figure C 1, based on the location of the origin. The upstream wind velocity vector, **u**, of fixed magnitude is assumed to be two-dimensional. This vector is placed at the origin as well, with component u and v aligning with x- and y-coordinate, respectively. The azimuth of wind vector is defined based on the polar coordinate system, i.e., $\theta = 0$ for **u** lying on the positive x-axis and $\theta = 90$ for **u** lying on the positive y-axis. For an arbitrary pressure tap labeled as ① in Figure C 1, its location on the roof, $\mathbf{x}_1 = x_1\mathbf{i} + y_1\mathbf{j}$, is defined with respect to the origin as well.

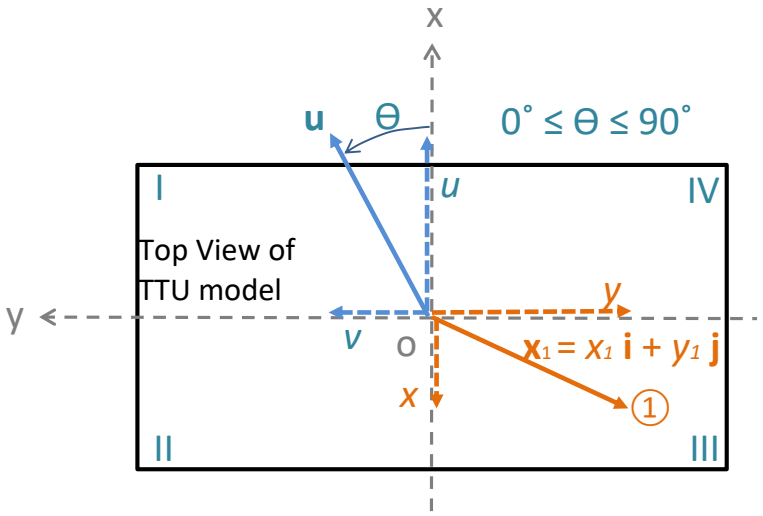

Figure C 1: The unit vector of wind direction and the location vector of a tap with respect to a Cartesian coordinate located at the center of symmetry for a rectangular roof.

The mean pressures, for example, measured at tap ① represent the results obtained from the first quadrant winds, i.e., $0 \le \theta \le 90$. In this case, the relative wind direction to the tap location can be characterize by the inner product, i.e.,

$$\mathbf{u} \cdot \mathbf{x}_1 = u\, x_1 + v\, \mathrm{y}_1 \quad \text{for} \quad u \ge 0 \text{ and } v \ge 0. \tag{C-1}$$

By using the same magnitude of wind speed but reversing the direction of *u*-component in Figure C 1, as shown in the left plot in Figure C 2 (a), the wind azimuth is now $180 - \theta$ and is confined to the 2nd quadrant, i.e., $90 \le (180 - \theta) \le 180$. The inner product between the velocity and tap location vectors is now $\mathbf{u} \cdot \mathbf{x}_1 = -u\, x_1 + v\, \mathrm{y}_1$. Because there is no measurement conducted for the 2nd quadrant wind azimuth, $(180 - \theta)$, the goal now is to determine an equivalent tap location such that the inner product is unchanged for measurement under azimuth θ. This can be done by simply interchanging the sign between the *u*-component of real velocity vector and the *x*-component of tap location, $\mathbf{x}_1$, in the inner product, i.e.,

$$\begin{aligned}\mathbf{u}\cdot\mathbf{x}_1 &= -u\,x_1 + v\,y_1 \\ &= u\left(-x_1\right) + v\,y_1 = u\,x_2 + v\,y_2 = \mathbf{u}\cdot\mathbf{x}_2\end{aligned} \quad \text{for wind azimuth } 180^\circ - \theta. \qquad \text{(C-2)}$$

Based on Eq. (C-2), it is clear that the tap location, $\mathbf{x}_2$, measuring the equivalent pressures due to the 2nd quadrant wind, $\left(180^\circ - \theta\right)$, can be obtained by simply reversing the sign of the *x*-component of the original tap location, i.e., $x_2 = -x_1$ and $y_2 = y_1$. Such tap location is labeled as ② in the right plot of Figure C 2 (a), along with the wind vector of azimuth θ.

Similar to the second quadrant wind, the equivalent tap location ③, $\mathbf{x}_3$, for the third quadrant wind azimuth $\left(180^\circ + \theta\right)$ can be determined by calculating the inner product between the real velocity vector and the original tap location (as shown in left plot in Figure C 2 (b)), i.e.,

$$\begin{aligned}\mathbf{u}\cdot\mathbf{x}_1 &= -u\,x_1 - v\,y_1 \\ &= u\left(-x_1\right) + v\left(-y_1\right) = u\,x_3 + v\,y_3 = \mathbf{u}\cdot\mathbf{x}_3\end{aligned} \quad \text{for wind azimuth } 180^\circ + \theta. \qquad \text{(C-3)}$$

From Eq. (C-3), it is clear that the tap location ③ can be obtained by interchanging the signs of both *x*- and *y*- components of the original tap location, i.e., $x_3 = -x_1$ and $y_3 = -y_1$ (see the right plot of Figure C 2 (b)). The equivalent tap location ④, $\mathbf{x}_4$, for the fourth quadrant wind azimuth $\left(360^\circ - \theta\right)$ can be also determined by taking the inner product between the real wind velocity vector and tap location (see left plot in Figure C 2 (c)), i.e.,

$$\begin{aligned}\mathbf{u}\cdot\mathbf{x}_1 &= u\,x_1 - v\,y_1 \\ &= u\,x_1 + v\left(-y_1\right) = u\,x_4 + v\,y_4 = \mathbf{u}\cdot\mathbf{x}_4\end{aligned} \quad \text{for wind azimuth } 360^\circ - \theta. \qquad \text{(C-4)}$$

Hence, $\mathbf{x}_4$ is the mirrored location of $\mathbf{x}_1$ about y-coordinate, i.e., $x_4 = x_1$ and $y_4 = -y_1$.

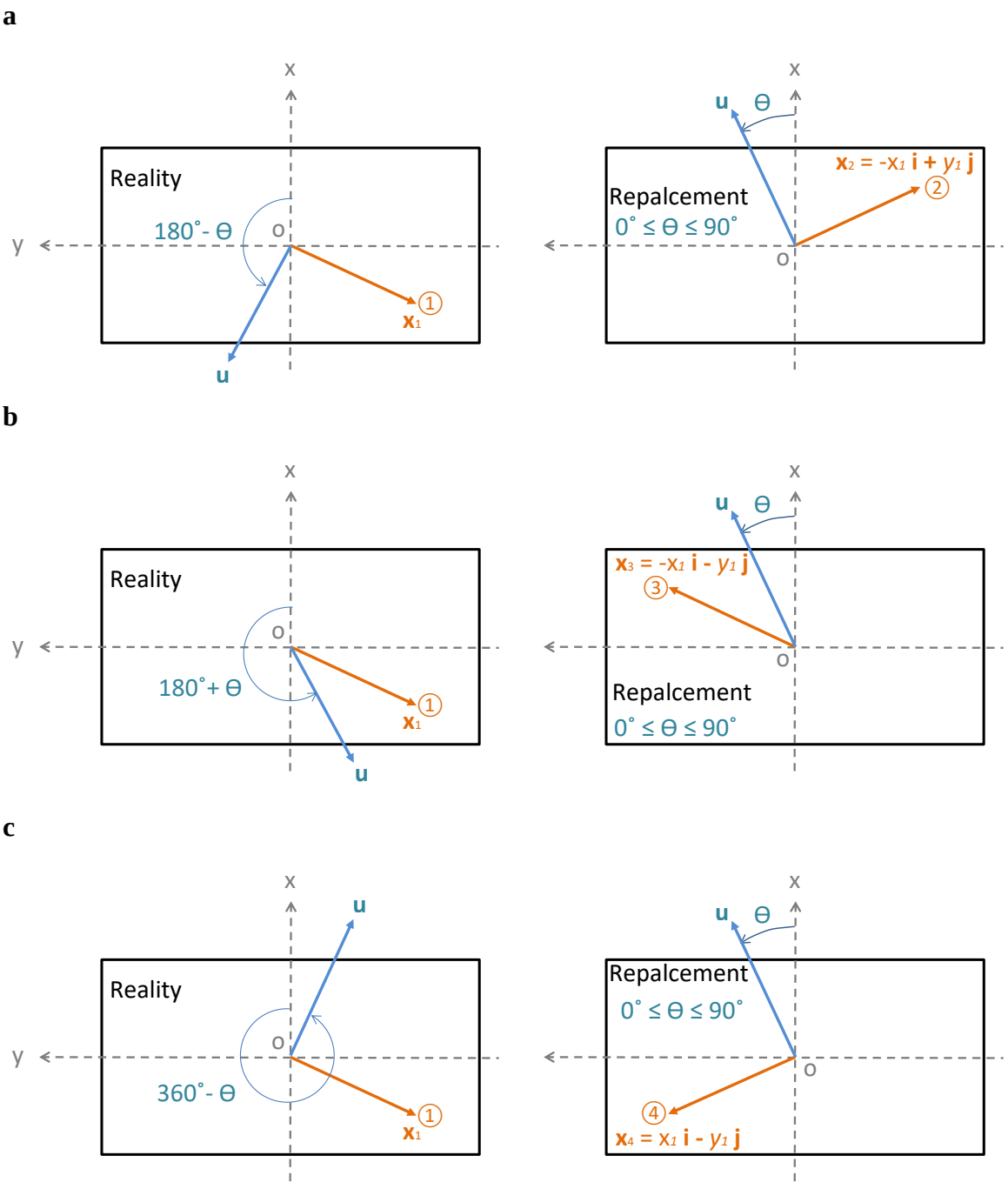

Figure C 2: Equivalent tap locations for measurement wind directions between 0˚ and 90˚ for real wind directions: (a) $90 \le \theta \le 180$ **, (b)** $180 \le \theta \le 270$ **and (c)** $270 \le \theta \le 360$ **.**

An arbitrary tap ① located within the quadrant III region measures the pressures under the first quadrant wind azimuths, $90 \le \theta \le 180$, as shown in Figure C 1. The

corresponding equivalent tap locations for measurements of other quadrant wind azimuths are derived from Eqs. (C-1) to (C-4) and further shown in for Figure C 2. Following the rules established in Eqs. (C-1) to (C-4), the equivalent tap locations for all possible tap locations are further summarized in Figure C 3.

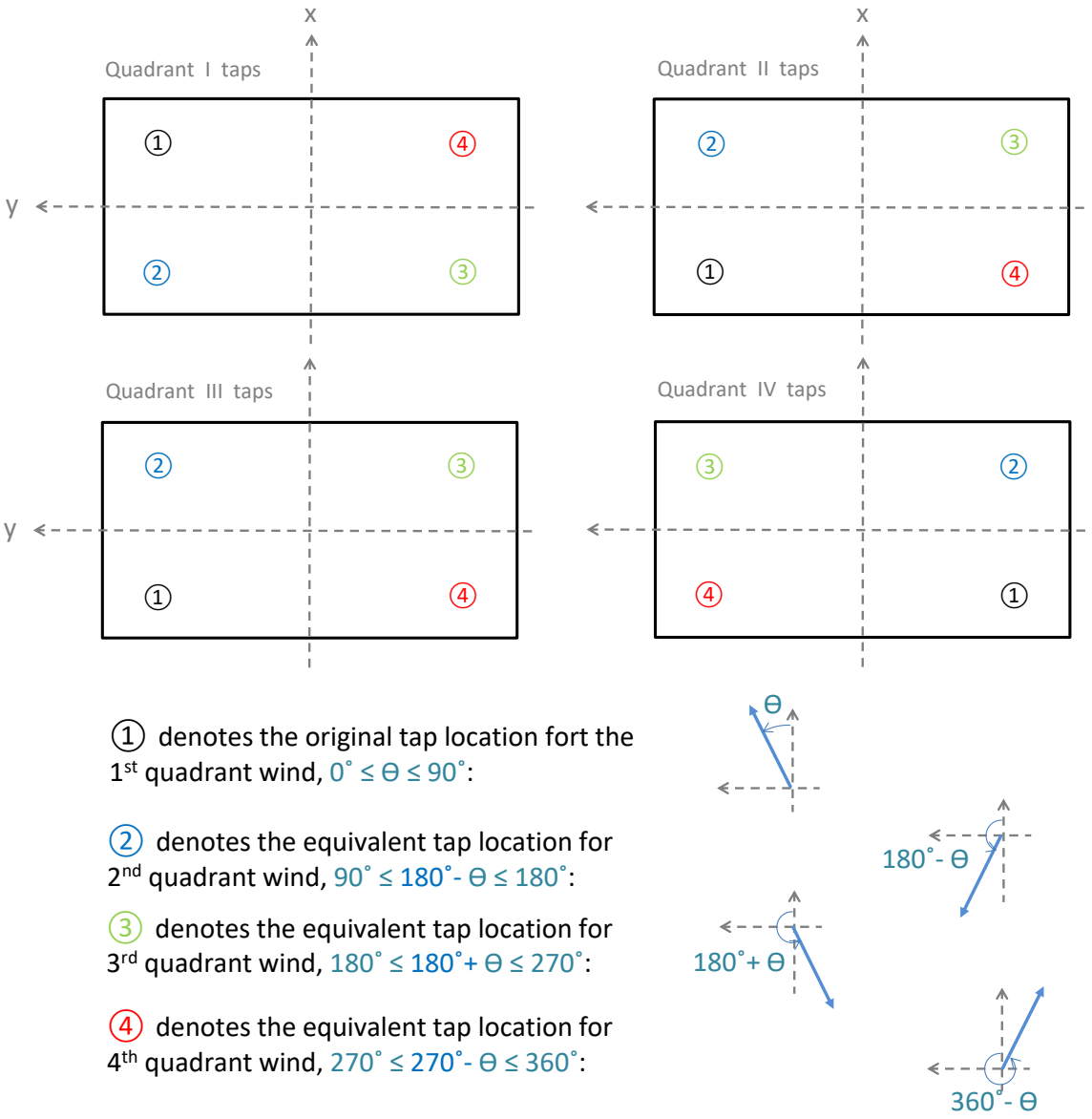

Figure C 3: Summary of the equivalent tap locations for measurement wind azimuths within the first quadrant, $0 \le \theta \le 90$ **.**

An example of utilizing the symmetric property given in Figure C 3 is applied for determining the spatial $\overline{Cp}$ distribution over the entire building surface for wind azimuth $\overline{\theta} = 60$. The results are shown in Figure C 4 for $\overline{Cp}$ measured in terrain 'O15' (see Section 2.1). Note that $u_{\text{ref}} = u_H$ for defining the pressure coefficient.

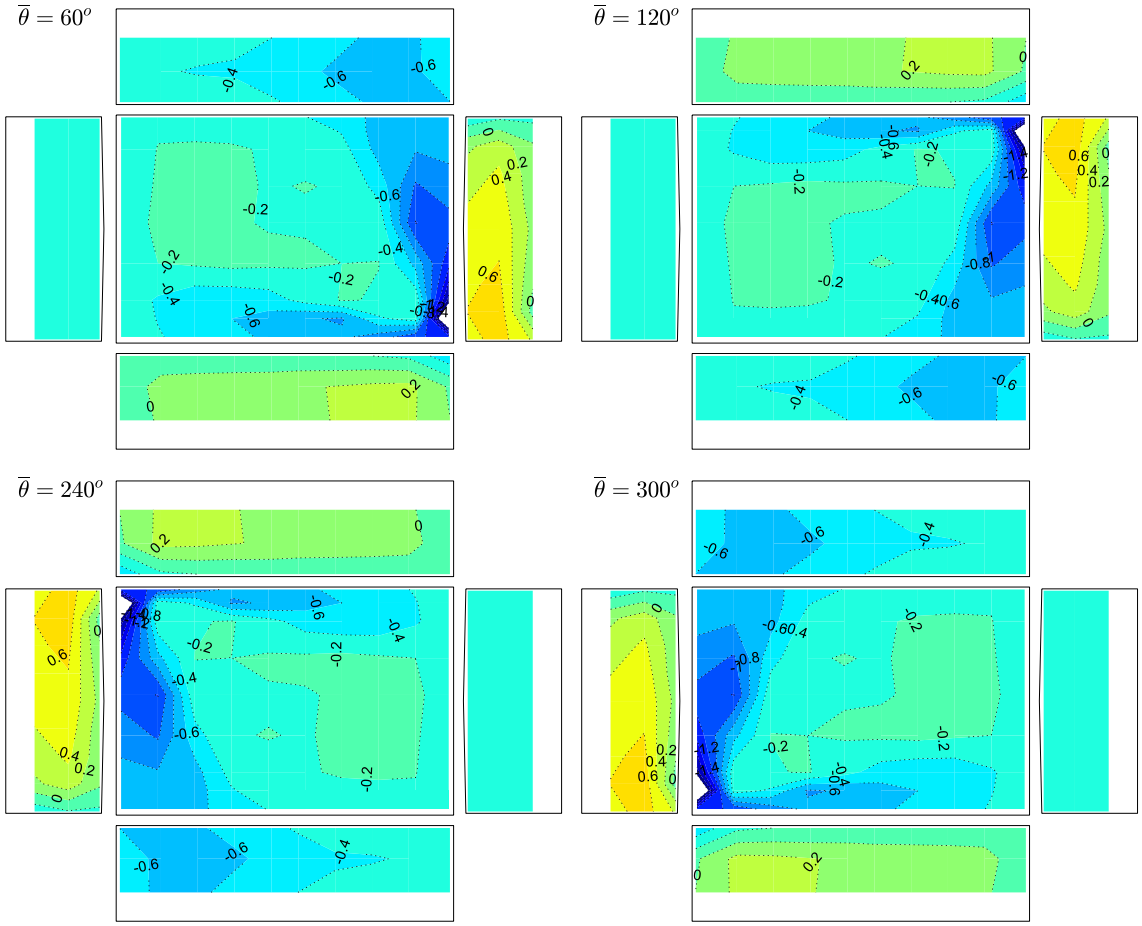

Figure C 4: $\overline{Cp}$ measured at $\overline{\theta} = 60$ and corresponding symmetric results for $\overline{\theta} = 120$, 240 and 300 .

Detailed $\overline{Cp}$ distributions as results of utilizing the symmetric property (Figure C 3) are further shown in Figure C 5 for the roof corner tap C1 and leading edge tap L1 (see Figure 6-1). Continuous $\overline{Cp}$ distribution can be found for both cases. Near symmetric pattern can be found for $\overline{Cp}$ measured at L1.

a

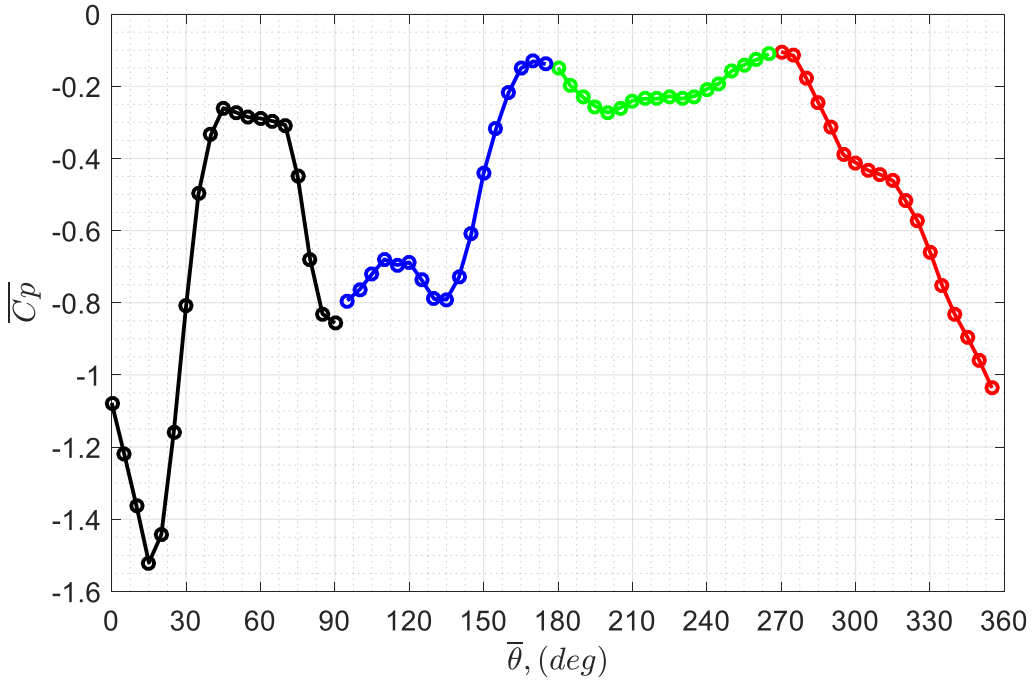

b

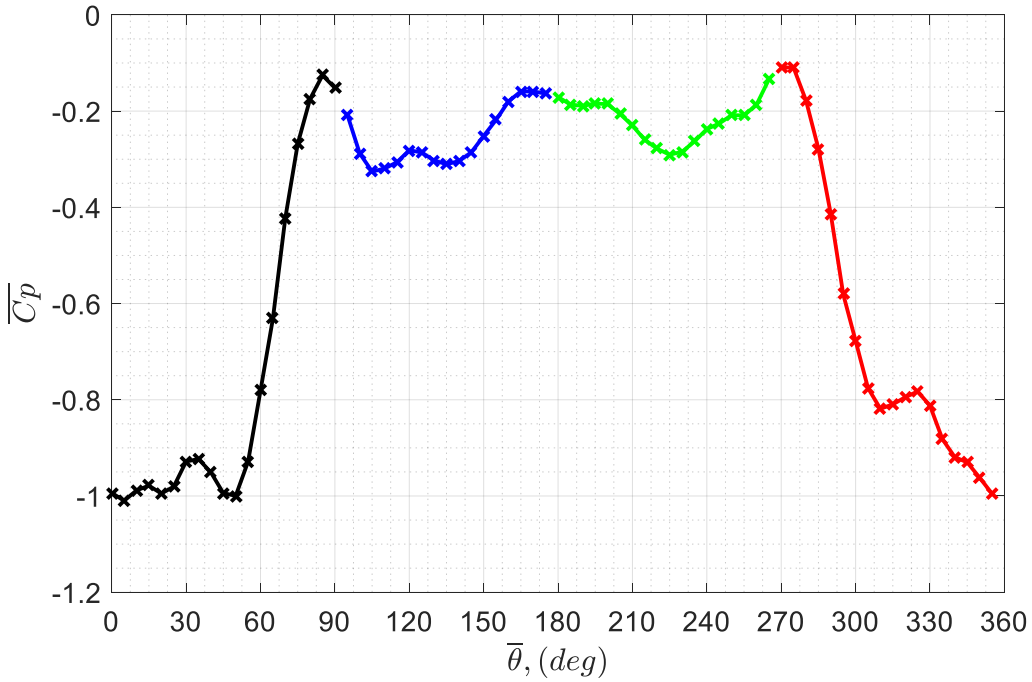

Figure C 5: $\overline{Cp}$ distribution for entire range mean wind azimuths at taps: (a) C1 and (b) L1 (see Figure 6-1).

Appendix D: Effects of the cobra probes on the pressure distributions on the building model

In this thesis, the synchronized measurements of building surface pressures and local velocities are done by placing the three Cobra probes near the building model. Examples of such setups are shown in Figure A 1 (a) and (b) for measurements at $\bar{\theta} = 90$ and 0 respectively. Because of the placement of Cobra probes are close to the building, the surface pressures measured on the building model may be affected. In order to see the degree of influence, the building surface pressures measured with and without the Cobra probes are examined.

Spatial distributions of $\overline{Cp}$ on the building surface measured with and without Cobra probes at mean wind azimuths $\bar{\theta} = 0$, 30° and 90° are shown in Figures D 1, D 2 and D 3, respectively, for terrains F0, O0 and S15 (see Section 2.1). Measurements of $\bar{\theta} = 30$ are selected because of the widest building projection width normal to the main stream direction and , hence, may be affected more by the two side probes (see Cobra #311 and #313 in Figure A 1 (a) and (b)). On the other hand, measurements of $\bar{\theta} = 0$ and 90° are selected because they are bounding scenarios of building orientations. Figures D 4, D 5 and D 6 further shows the $\mathrm{rms}(Cp)$ for the probe effects on the overall pressure fluctuations. Both mean and rms Cp distributions are very similar for measurements obtained with and without Cobra probes, indicating the influences due to the setups of these probes are not significant.

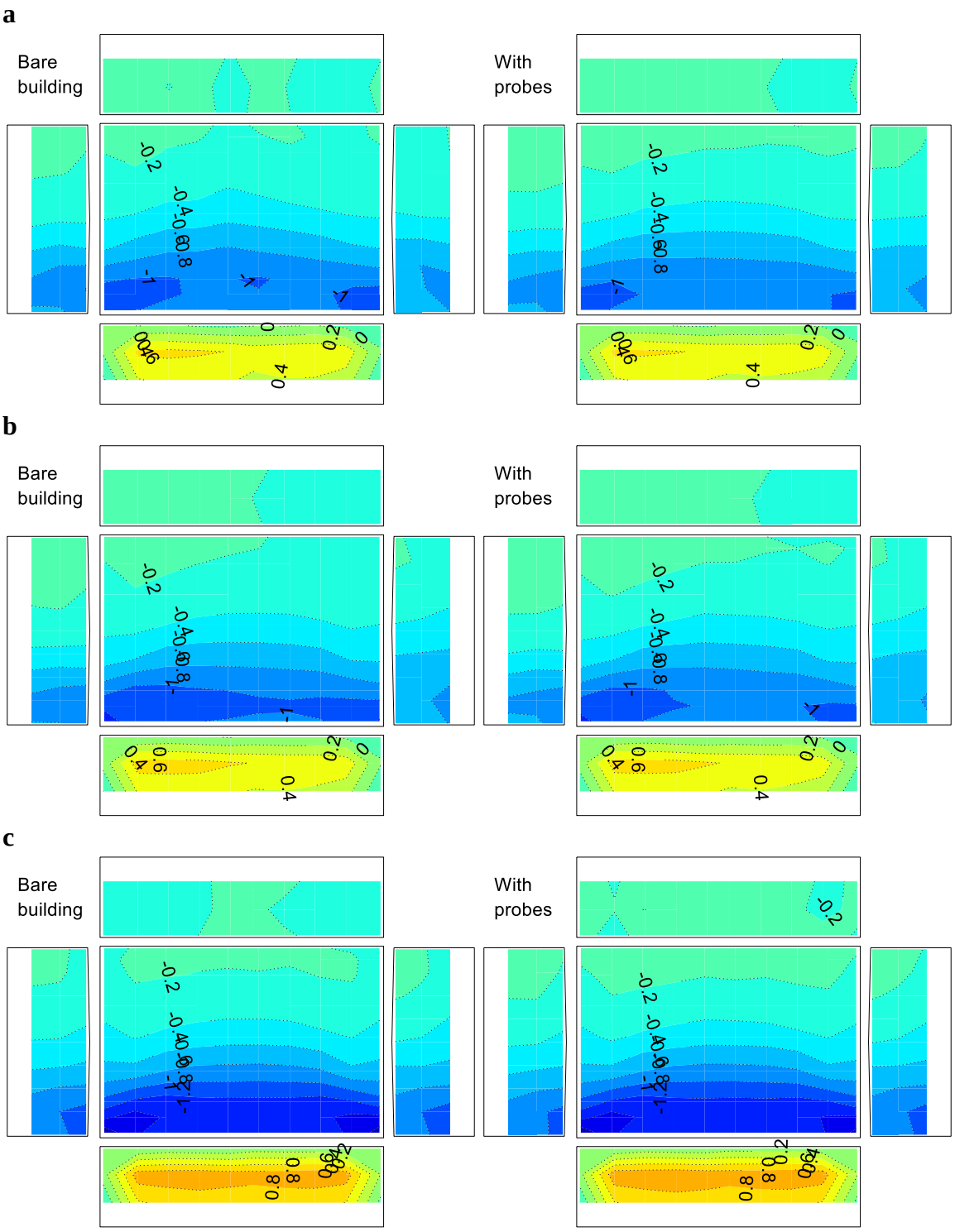

Figure D 1: Building surface $\overline{Cp}$ contour measured at $\bar{\theta} = 0$ with and without cobra probes for terrains (a) F0, (b) O0 and (c) S15.

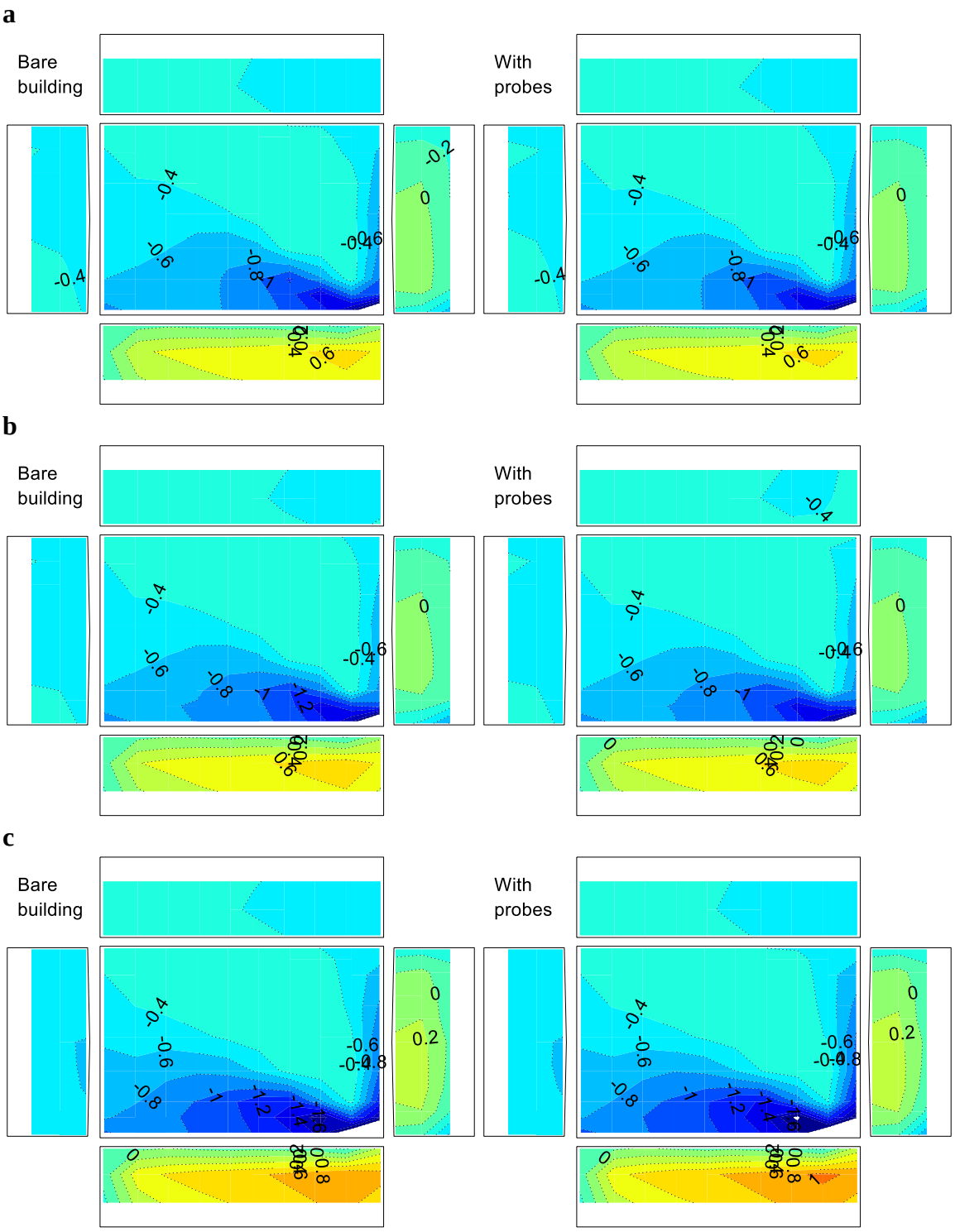

Figure D 2: Building surface $\overline{Cp}$ contour measured at $\bar{\theta} = 30$ with and without cobra probes for terrains (a) F0, (b) O0 and (c) S15.

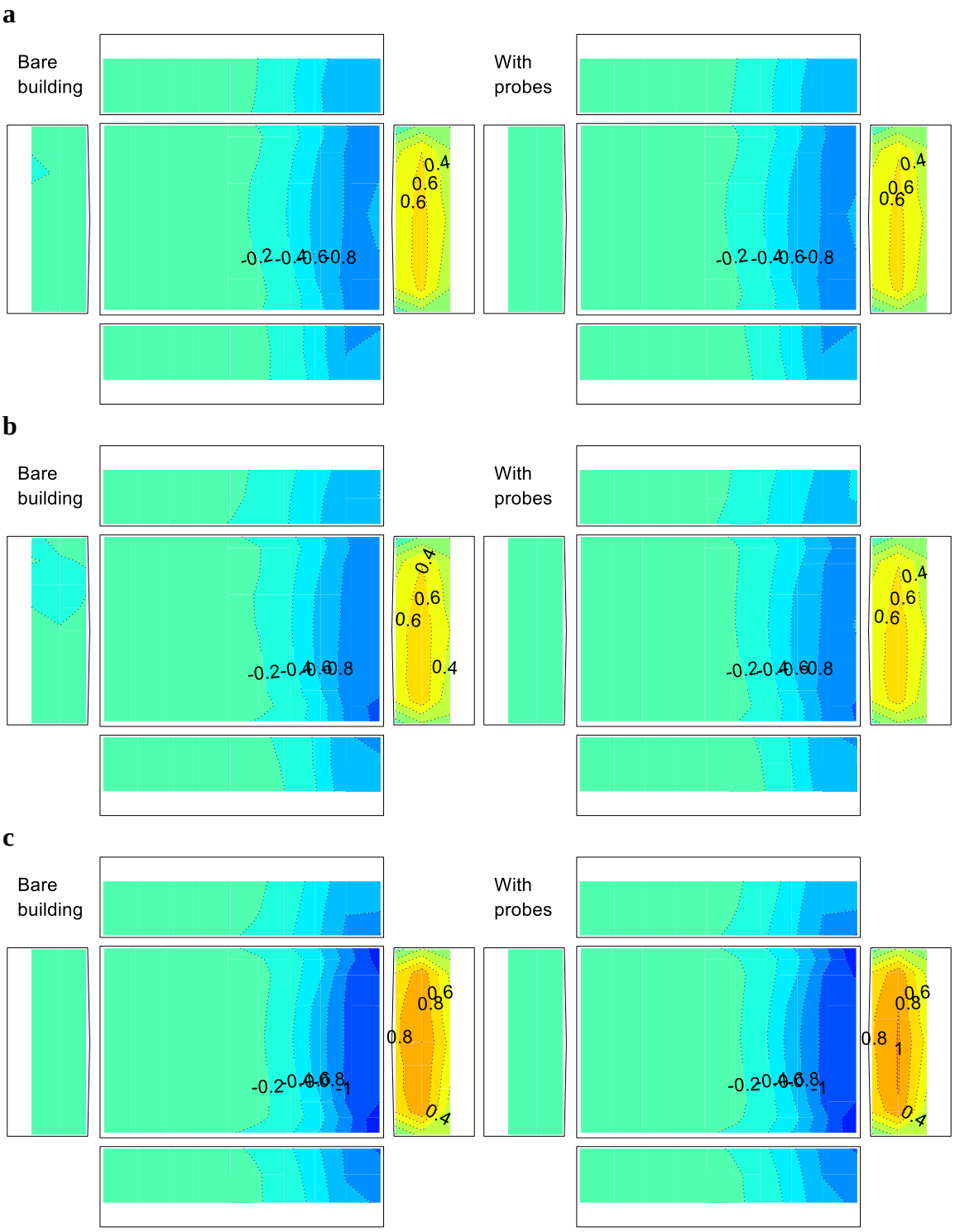

Figure D 3: Building surface $\overline{Cp}$ contour measured at $\bar{\theta} = 90$ with and without cobra probes for terrains (a) F0, (b) O0 and (c) S15.

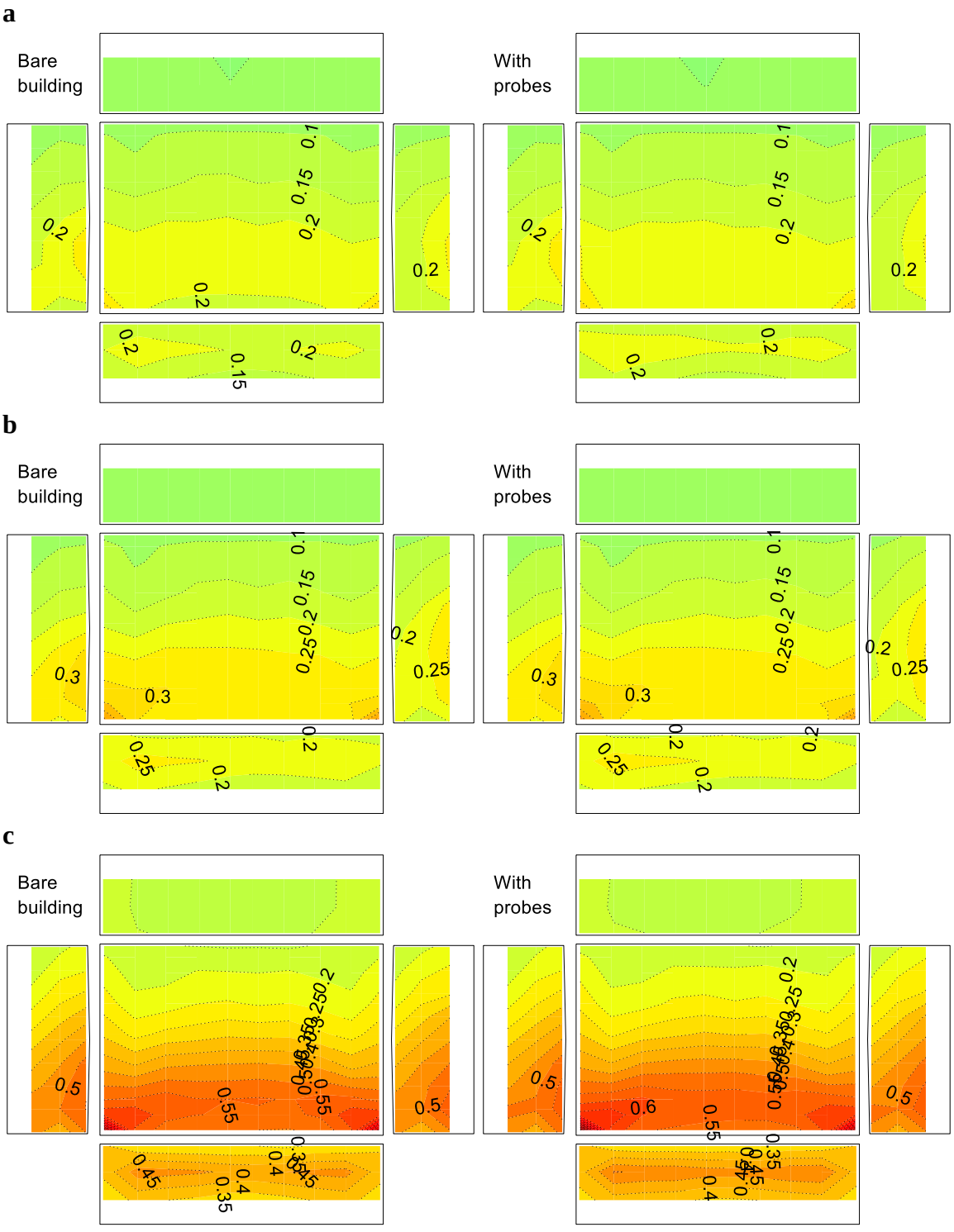

Figure D 4: Building surface $\mathrm{rms}(\mathrm{Cp})$ contour measured at $\bar{\theta} = 90$ with and without cobra probes for terrains (a) F0, (b) O0 and (c) S15.

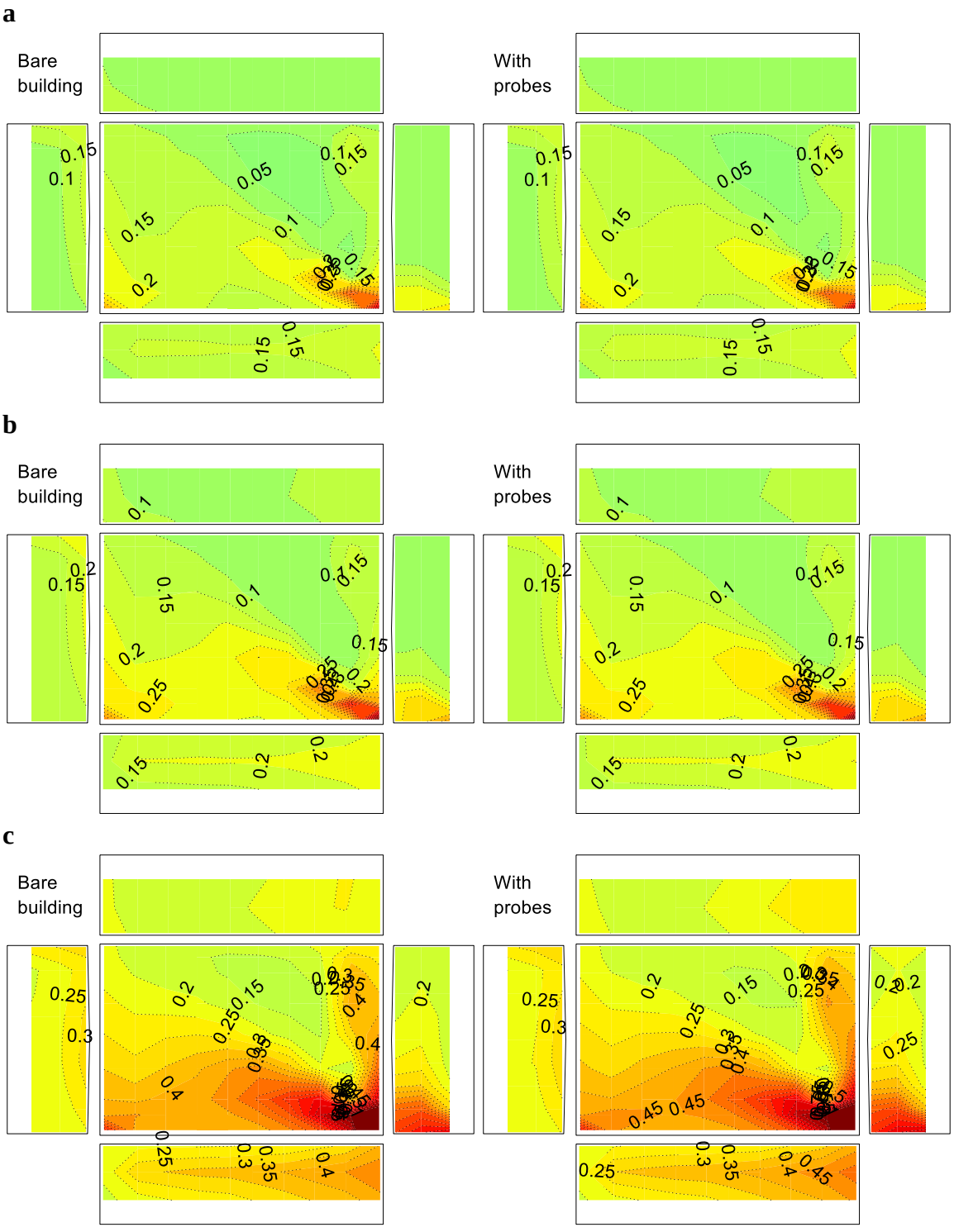

Figure D 5: Building surface $\mathrm{rms}(\mathrm{Cp})$ contour measured at $\bar{\theta} = 30$ with and without cobra probes for terrains (a) F0, (b) O0 and (c) S15.

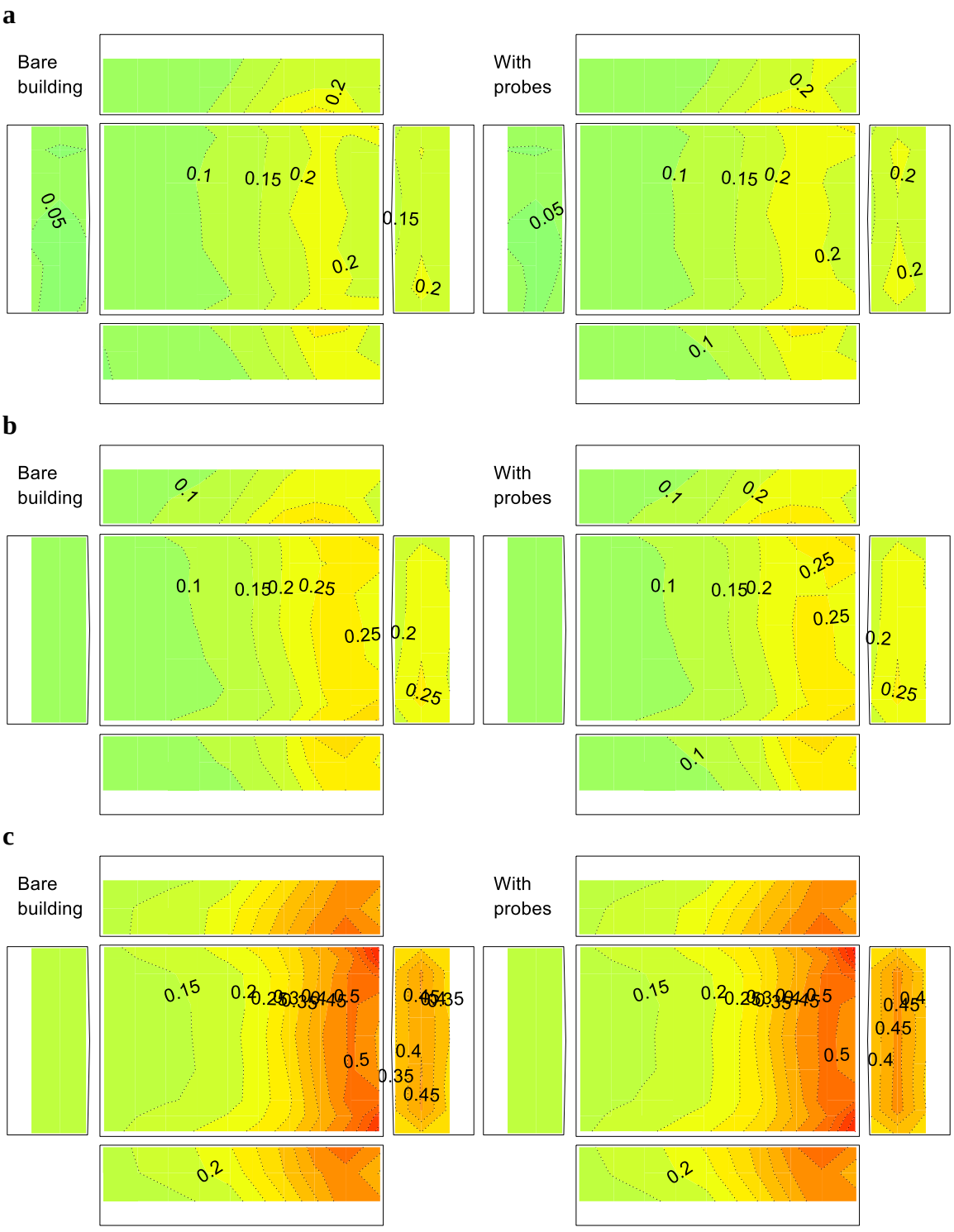

Figure D 6: Building surface $\mathrm{rms}(\mathrm{Cp})$ contour measured at $\bar{\theta} = 90$ with and without cobra probes for terrains (a) F0, (b) O0 and (c) S15.

Curriculum Vitae

Name: Chieh-Hsun Wu

Post-secondary Education and Degrees:
Tamkang University
New Taipei City, Taiwan,
2002-2006 B.A.

Colorado State University
Fort Collins, Colorado, USA
2009-2012 M.A.

The University of Western Ontario
London, Ontario, Canada
2013-2017 Ph.D.

Related Work Experience
Teaching Assistant
The University of Western Ontario
2013-2017

Publications:

Wu, C.-H., 2012. Application of model reduction tools in analysis of wind-induced pressures on low-rise buildings. Master thesis, Colorado State University, CO, USA.

Wu, C.-H., Kopp, G. A., 2015. Applicability of quasi-steady theory on building point pressures. Proceedings of the 25th Canadian Congress of Applied Mechanics, London, Ontario, Canada.

Wu, C.-H., Kopp, G. A., 2016. Estimation of wind-induced pressures on a low-rise building using quasi-steady theory. Frontiers of Built Environment, 2(5). DOI: 10.3389/fbuil.2016.00005.

Kopp, G.A., Wu, C-H, 2017. A framework for the aerodynamics of low-rise buildings in tornadoes: Can boundary layer wind tunnels give us everything we need? The 13th Americas Conference on Wind Engineering (13ACWE), Gainesville, Florida USA, May 21-24, 2017.

Wu, C.-H., Akon, A. F., Kopp, G. A., 2016. Evaluation of mean pressure field above a roof using PIV data and a 2D interpolation algorithm. 8th International Colloquium on Bluff Body Aerodynamics and Applications. ID: 225.

Wu, C.-H., Akon, A. F., Kopp, G. A., 2016. Evaluation of mean pressure field above a roof using PIV data and a 2D interpolation algorithm. 24th International Congress of Theoretical and Applied Mechanics, Montreal, Quebec, Canada.

Romanic, D., Refan, M., Wu, C.-H., Micheal, G., 2016. Oklahoma tornado risk and variability: A statistical model. International Journal of Risk Disaster Reduction, 16, 19-32. DOI: 10.1016/j.ijdrr.2016.01.011

Wu, C.-H., Kopp, G. A., 2016. Wind loads on the roof-top equipment of low-rise buildings. Phase 4: Effects of equipment dimensions. Boundary Layer Wind Tunnel project technical report, London, ON, Canada.